2024
Volume 7
Issue 1
ISSN: 2578-1995(Online)

CHARACTERIZATION AND APPLICATION OF NANOMATERIALS

https://systems.enpress-publisher.com/index.php/CAN

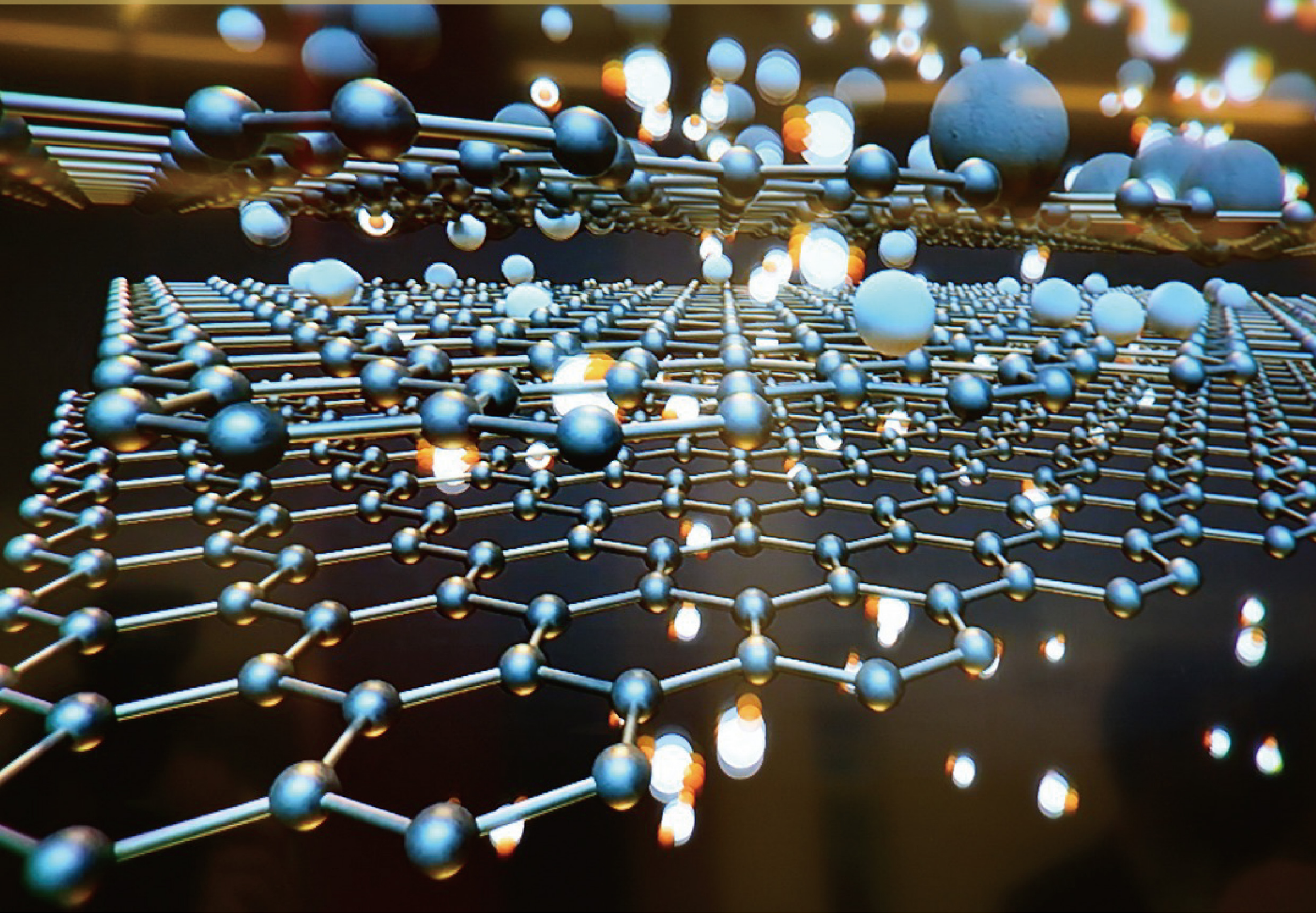

CAN

ISSN 2578-1995

EnPress Publisher

Editorial Board

Editor-in-Chief

Associate Editor

Editorial Board Members

Samy Mohamed Shaban
Egyptian Petroleum Research Institute
Egypt

Volume 7 Issue 1·2024

Characterization and Application of Nanomaterials

Editor-in-Chief

Prof. Francesco Tornabene

University of Salento, Italy

EnPress Publisher

2024 | Volume 7 | Issue 1

Characterization and Application of Nanomaterials

https://systems.enpress-publisher.com/index.php/CAN

Contents

Articles

Reviews

EnPress Publisher

Characterization and Application of Nanomaterials 2024, 7(1), 3587.
https://doi.org/10.24294/can.v7i1.3587

Article

Mo-doped titanate nanofibers from hydrothermal syntheses for improving bone scaffold

Yang Tian[1,2,†], Lu Zhang[3,†], Yiting Xiao[4,†], Trenton Collins[5], Abdussamad Akhter[5], Yan Huang[6], Z. Ryan Tian[1,2,3,5,*]

[1] Department of Materials Science and Engineering, University of Arkansas, Fayetteville, AR 72701, USA.
[2] Institute for Nanoscience and Engineering, University of Arkansas, Fayetteville, AR 72701, USA.
[3] Department of Cell and Molecular Biology, University of Arkansas, Fayetteville, AR 72701, USA.
[4] Department of Biological and Agricultural Engineering, University of Arkansas, Fayetteville, AR 72701, USA.
[5] Department of Chemistry and Biochemistry, University of Arkansas, Fayetteville, AR 72701, USA.
[6] Department of Animal Science, University of Arkansas, Fayetteville, AR 72701, USA.
*** Corresponding author:** Z. Ryan Tian, rtian@uark.edu
[†]*These authors contributed equally to this work.*

CITATION

Tian Y, Zhang L, Xiao Y, et al. Mo-doped titanate nanofibers from hydrothermal syntheses for improving bone scaffold. Characterization and Application of Nanomaterials. 2024; 7(1): 3587. https://doi.org/10.24294/can.v7i1.3587

ARTICLE INFO

Received: 9 December 2023
Accepted: 9 January 2024
Available online: 18 January 2024

Abstract: A longstanding interest in bone tissue engineering is the development of new bio-scaffolds that can be manufactured on a large scale with high throughput at low cost. Here, we report a low-cost and systematically optimized hydrothermal synthesis for producing Mo-doped potassium titanate nanofibers with high structural purity. This new nanosynthesis is based on bone tissue growth on an undoped titanate nanowires-entangled scaffold, as previously reported by our team. The morphological and structural characterization data suggest that the crystal structure of Mo-doped titanate nanofibers closely resembles that of the undoped ones. This resemblance is potentially valuable for assessing the role of Mo dopants in engineering bone tissue.

Keywords: nanosynthesis; titanate nanofiber; bone scaffold; molybdenum dopant

1. Introduction

Exploiting new methods for synthesizing biocompatible nanowires with novel structures and surface properties is critical to the development of new tissue engineering scaffolds. The nanowires-entangled scaffolds with well-tuned surface chemistry (e.g., the surface energy, protein adsorption, and pore structure) can facilitate a programmable release of growth hormones, drugs, and nutrients to promote the osteoblast cells adhesion, proliferation, and differentiation, thus-upgrading the bio-scaffolds versatilities [1]. Further, doping valve metal atoms in the nanowire structure or on the nanowire surface can enhance the scaffold's radio-opacity to boost the orthopedic X-ray imaging's contrast, i.e., resolution [2–6]. Under these inspirations, this work has successfully doped and optimized the nanowire analogs of natural bone scaffold, in a series of systematic syntheses for doping the scaffold nanowire rationally using different valve metals in different doping ratios. Thus, varied properties of the nanowires, such as aspect ratio, surface chemistry, and the chemical environment of the doping atoms, are anticipated to provide new insights into the role of valve metals in bone implants [1].

Titanium dioxide (TiO_2) has been attracting enormous interest in both nanomaterial chemistry and orthopedic nanomedicine. The TiO_2-based nanosyntheses have typically resulted in a clay-like layered titanate structure in the nanowire [7] or nanotube [8] morphologies, with the edge-sharing [TiO_6] octahedra in the negatively charged layer and the cations intercalating in between the layers, which can promote the hydroxyapatite nucleation and formation on the nanowire surface quickly in a simulated body fluid (SBF) [9]. In a hydrothermal treatment, the TiO_2 powders (regardless of the rutile or anatase phase) originally suspended in an aqueous KOH solution can quickly start to form the K-titanate of one-dimensional (1D) nanowires [10]. The resultant layered 1D-nanostructure can act like a cation “reservoir”, facilitating the ion-exchange of K^+ with other cations in the body fluids. This allows for an autonomous, real-time balance of cations *in situ*, on which the bone tissue growth can be promoted. Here, the K-titanate, in a hypotonic condition with respect to the plenty of calcium (Ca^{2+}) ions nearby, can prompt the ion-exchange of K^+ ions with the Ca^{2+} in SBF. Subsequently, the phosphate anions in the body fluid, including $(PO_4)^{3-}$, $(HPO_4)^{2-}$, and $(H_2PO^4)^-$, can support the interactions with the Ca^{2+} ions on the titanate surface. This interaction results in the formation of hydrated calcium phosphate, commonly referred to as hydroxyapatite, which is a vital component of natural bone and essential for establishing an osteogenic/osteoconductive environment [9].

In addition, nanomaterials containing valve metals such as Molybdenum (Mo), Zirconium (Zr), Niobium (Nb), or Tantalum (Ta) can help improve the osteointegration [10–16]. Here, the Mo ions can promote the immunomodulation and facilitate bone repair by comodulating the balance between bone formation and resorption, showing a good potential to help regenerate bones [12]. Further, the Mo-based nanomaterials syntheses in literature should be optimized to meet the need for large-scale productions. Moreover, doping the relatively expensive valve metals on or in the low-cost titanate scaffold nanowire can reduce the cost and the valve metals cytotoxicity to the bone tissue. In this work, we systematically conducted nanosynthesis to produce long and pristine Mo-doped titanate nanofibers with the good feasibility for mass-production of the new orthopedic implants. The doping ratio was optimized using the structural, morphological, and chemical characterizations data from the scanning electron microscopy with an energy-dispersive elemental analyzer (SEM-EDX), X-ray diffraction (XRD), and X-ray photoelectron spectroscopy (XPS).

2. Materials and methods

2.1. Nanowire synthesis

The Mo-doped potassium titanate nanowires were prepared following a protocol in literature [10,17–20] with some modifications. Briefly, in a Teflon cup containing 50 mL water solution of 10M KOH, 500 mg of TiO_2 powder (Aeroxide P25) was added in and stirred for about 5 min with a Teflon-coated magnetic stirring bar on an electrical stirrer. Thereafter, Molybdenum oxide powder (from Alfa Aesar) was mixed into the Teflon cup to form a mixture upon stirring. Here, the weight ratio of Mo-dopant to titanate was in the range of 1%–4%.

Next, the mixture containing Teflon cup was sealed in an autoclave container, heated in an oven at 240 °C for 72 h and then cooled down in air. The white powdery product was collected, water-washed to pH = 7, and oven-dried at 60 °C for the characterizations. To keep the nanowire lattice intact, it is important to do the water-washing step carefully, as detailed separately below.

2.2. Characterizations

The SEM-EDX analysis was done on the FEI Nova NanoLab 200 to check the nanowires morphology and chemical composition. Typically, a nanowire sample was placed on an aluminum holder to let the sample dry in air, then surface-coated with Au in a plasma sputtering coater. The XRD analysis was performed on the Rigaku MiniFlex II Desktop X-ray diffractometer using monochromatized Cu-Kα ($\lambda = 1.5406$ Å) at 30 kV and 15 mA, in the range of 2θ from 5° to 60° at a speed of 1°/min. The XPS characterization was conducted on the PHI VersaProbe Scanning XPS system to study the chemical environment of Mo.

3. Results and discussions

3.1. Evidence of the novel Mo-doping

The Mo-doped potassium titanate nanowires underwent a self-assembly process, resulting in the formation of a bio-scaffold, as illustrated in **Figure 1**. This self-assembled nanofibrous scaffold has pores in the size of tens of microns (**Figure 1(a)**) to support the effective adhesion of osteoblast cells into the pores, while the pore wall (of self-entangled nanowires) is also highly porous (**Figure 1(b)**) to allow the osteoblast cells' nutrients and metabolites to diffuse quickly across.

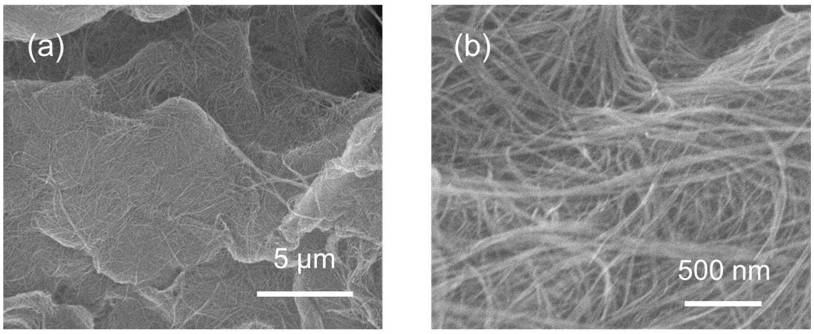

Figure 1. SEM micrographs of Mo-doped potassium titanate.

Upon examination at a higher magnification (**Figure 2(a)**), the clean and well-crystallized long nanowires in self-entangled form can be clearly seen, which is a characteristic of the Mo-doped potassium titanate nanowires. The nanofibers length extends into tens of microns, while retaining their width below 100 nm. In addition, **Figure 2(a)** shows the relatively smooth surface of the high length-to-width ratio (or aspect ratio) nanofibers, suggesting the optimal control over the nanowires' nucleation and 1D-growth in nanoscale, which is crucial for the Mo-dopant's good distribution throughout the crystal lattice of all the nanowires from the "one-pot" nanosynthesis.

In the Energy-Dispersive X-ray (EDX) spectroscopy mapping (**Figure 2(b)**), the Mo dopants exhibit a uniform distribution in the nanofibers. This uniformity in distribution suggests the dopant well-dispersed in the Mo-doped potassium titanate nanowires, which is indicative of a quite precisely controlled nano-synthesis process. In theory, the [MoO_6] octahedron in the nanowire lattice is larger than the [TiO_6]

octahedra [21]. However, this size difference-induced structural distortions were well-tolerated without compromising the overall lattice continuity, as suggested by the EDX mapping in **Figure 2**. Intuitively, the good dispersion of Mo allows each [MoO_6] octahedron to integrate into the lattice without disrupting the structural integrity, thus keeping the framework intact everywhere. In other words, the high dispersion of Mo dopant in the nanofiber structure suggests the optimal doping conditions that support the **Figure 1**.

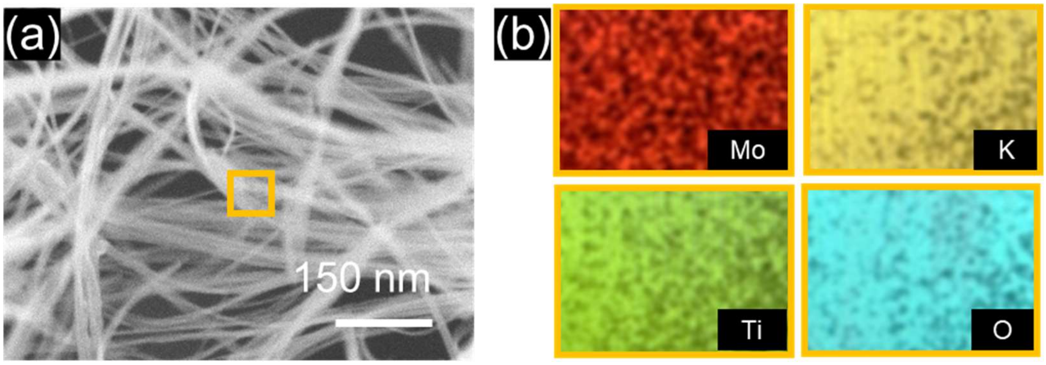

Figure 2. The EDX Mapping of the Mo-doped Potassium Titanate Nanofibers. **(a)** The high-resolution SEM of Mo-doped potassium with the yellow box for EDX mapping. **(b)** The EDX mapping showed that the Mo, K, Ti, and O are evenly distributed on the titanate nanowires.

The nanofiber crystal structure was further characterized using the XRD patterns (**Figure 3**). All the XRD peaks of (200), (110), (310), ($31\bar{2}$), ($40\bar{4}$), and (020) can be assigned to the layered $K_2Ti_6O_{13}$ titanate lattice (JCPDS No. 40-0403). The XRD patterns of titanate nanofibers with various doping ratios were identical and no residual impurity was detected, as evidenced by no extra peaks in the XRD pattern with respect to the XRD detection limit, which again indicates that the larger [MoO_6] octahedron was evenly doped in the titanate crystal structure to maintain the lattice integrity and nanowire structure.

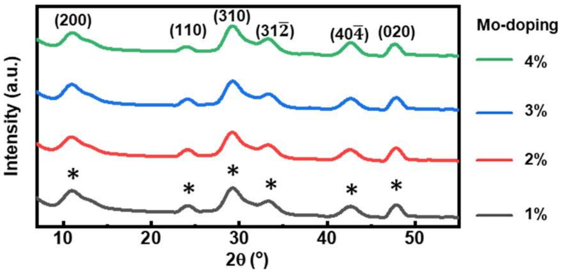

Figure 3. X-Ray diffraction of Mo-doped potassium titanate nanofibers with doping percentage.

Comparing the XRD patterns with and without the Mo-dopants (**Figure 4(a)**), the large Mo-dopant increases the d-space between adjacent titanate sheets by shifting the XRD peak to $d_{(200)} = 8.0919$ Å (or a lower 2-theta angle at $2\theta = 11.03°$). This is in contrast with the undoped nanowire's smaller d-space of $d_{(200)} = 7.7415$ Å at a higher 2-theta angle ($2\theta = 11.43°$). This interlayer spacing expansion is indicative of Mo substitutional doping within the titanate lattice. More specifically, the ionic radius of Mo^{5+} (75 pm) and Mo^{6+} (73 pm) is larger than that of Ti^{4+} (53 pm) which leads to interlayer spacing expansion with $Mo^{5+/6+}$ replacing Ti^{4+} while without destroying the original lattice structure [21]. Equivalently, the Mo dopant's higher content can shift the $d_{(200)}$ peak to a lower diffraction angle. The same shift happened to (110), (310), $(31\bar{2})$, and (020), as shown in **Figure A1**. Moreover, the doped samples XRD patterns show no structural impurity. Apparently, all the XRD peaks are in the same width and can be indexed to that of potassium titanate, matching what our lab reported in literature before [10,17,18].

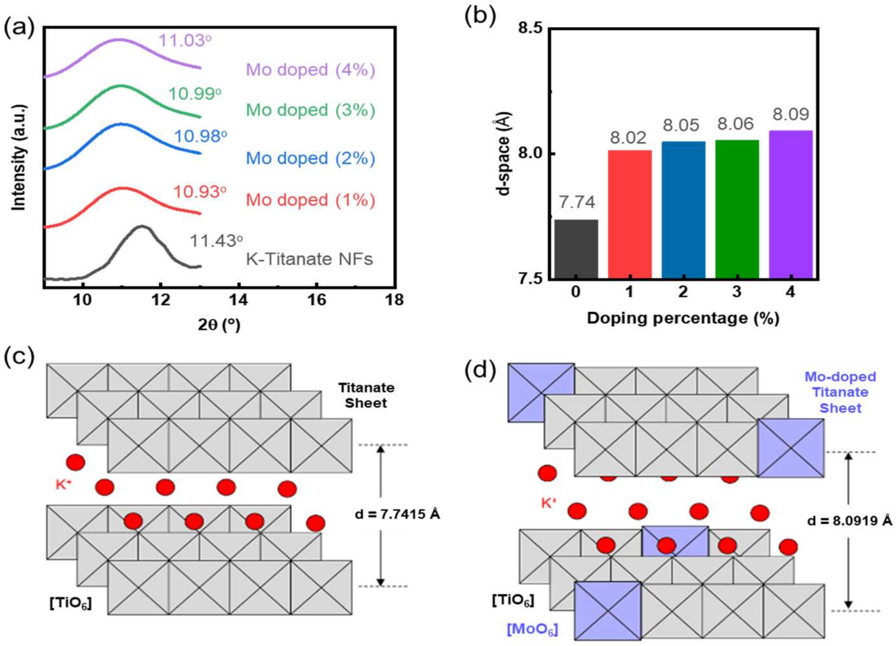

Figure 4. (a) XRD analysis of Mo-doped potassium titanate nanowires with **(b)** d-space. **(c)** and **(d)** the schematics for illustrating the Mo-dopant impact on the titanate crystal structure.

The XPS characterization investigated the chemical environment of the Mo dopant. The Mo $3d_{3/2}$ and $3d_{5/2}$ peaks of the 4% Mo-doped K-titanate nanofibers are presented in **Figure 5**. The peaks observed at 232.5 and 235.7 eV came from the Mo $3d_{5/2}$ and Mo $3d_{3/2}$ of Mo^{6+}, while the peaks at 231.9 and 235.0 eV came from the Mo $3d_{5/2}$ and Mo $3d_{3/2}$ of Mo^{5+} [22]. These characteristic peaks are attributed to Mo-O bonds, indicating the successful integration of Mo into the K-titanate lattice. Obtaining from the ratio of peak area, the atomic percentage of Mo^{6+} is 67.5% while that of Mo^{5+} is 32.5%, showing that Mo^{6+} is the main dopant form in the K-titanate nanofiber crystal lattice.

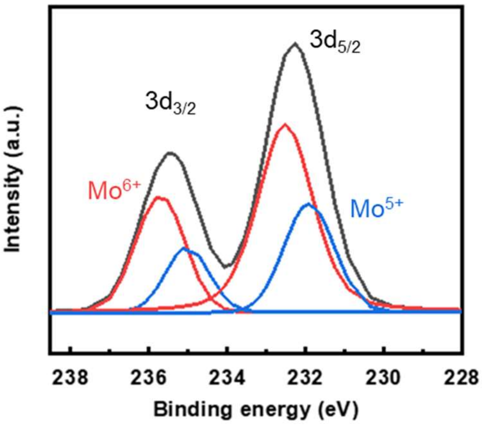

Figure 5. XPS spectroscopy of 4% Mo-doped potassium titanate nanofibers.

3.2. Lessons from the Mo-doping

Evidently, within the K-titanate nanofiber's clay-like layered crystal structure, the Ti^{4+}-based [TiO_6] octahedra were partially substituted by the Mo-based [MoO_6] octahedra, confirming the sterically challenging doping of Mo. Naturally, the larger [MoO_6] compared to [TiO_6] would position itself more easily on the nanofiber surface to reduce perturbations in the [TiO_6]-dominated nanowire crystal lattice. Such surface-exposed [MoO_6] units can be recognized by the osteoblast cell surface to facilitate the bone-tissue adhesion, as supported by the previous studies [12,13]. In this logic, the interlayer K^+ cations near the [MoO_6] could be rapidly substituted by the nearby Ca^{2+} cations in the body fluids. The Ca^{2+} cations' rapid exchange can in turn accelerate the formation of hydrated calcium phosphates, or hydroxyapatite, on the nanowire surface, matching the findings from other research groups using SBF [9,23], which supports this project's logic in the rational design. On this basis, the hydroxyapatite layer on the underlying titanate nanofiber should in turn support the sustained bone tissue adhesion on the hydroxyapatite-supported nanofiber, crafting an optimal osteogenic/osteo- conductive milieu [9], which is under an ongoing verification using the slow and tedious *in vitro* cell-culture experiments. The doping-modified titanate nanofibers surface characteristics has demonstrated a simple approach to existing methodologies in literature, for potentially improving the osteoconductivity of bone-scaffolds [10,12,15,18,24]. Fundamentally, this work found a new and manufacturing-viable route to incorporating Mo into the titanate nanowire matrix, which could be generally applicable to other subfields of the orthopedic nanomedicine.

4. Conclusions

Potassium titanate nanofibers doped with Mo have been successfully fabricated through a simple hydrothermal process, which to the best of our knowledge is quite new, especially in orthopedic nanomedicine. The doping process has been well-controlled to keep the nanowire's morphology, structure, and chemical composition intact. These are indicative of the successful development of an efficient and well-controlled doping method for varying the Mo dopant concentrations while preserving the nanowires lattice. This is critical for further optimizing the nanowires other properties for different applications. To evaluate the influence of this material in the field of bone tissue engineering, nanofibers with different concentrations of Mo-dopant have been investigating *in vitro* to determine their biocompatibility and osteogenic capabilities.

Currently, a critical and logical phase of the follow-up research is in progress, concentrating on the analysis of these nanofibers with systematically varied concentrations of Mo dopants, for specifically assessing these new nanowires biocompatibility and osteogenic potential. The investigation into the interactions between these Mo-doped nanofibers and bone cells is pivotal for acquiring a deeper understanding of their suitability as potential materials for bone implants. The thorough evaluation of the biocompatibility is pivotal to determining these materials viability in for medical applications, especially in the bone tissue regeneration. A forward-thinking strategy to expand upon this research entails the doping of titanate nanowires with, for example, dual oxide dopants. Such a new methodology could pave the way for exploring a broader spectrum of bone implants of new types with the potentially greater physiological adaptability. Comprehending the biocompatible transition metals' doping impact on the physical and chemical properties of these nanowire-based bone implants is crucial and fruitful. This understanding is pivotal for the tailored customization of biomaterials to suit each unique application, ensuring their optimal performance and compatibility.

Finally, developing a diverse and novel family of doped titanate nanofibers, each characterized by distinct compositions and properties, constitutes a strategic approach for enabling researchers to systematically explore how variations in doping influence the material's characteristics and performance. Gathering such data is imperative for the precise optimization of these materials, tailoring them for specific uses in bone tissue engineering or other relevant fields.

Author contributions: Investigation, YT, YX, TC, and AA; writing—original draft preparation, YT, LZ, ZRT; writing—review and editing, YT, LZ, YH, and ZRT. All authors have read and agreed to the published version of the manuscript.

Funding: This work was partially supported from the NSF (Grant #2230853) and NIST (Grant #70NANB22H010).

Conflict of interest: The authors declare no conflict of interest. The funders had no role in the design of the study; in the collection, analyses, or interpretation of data; in the writing of the manuscript, or in the decision to publish the results.

Data availability statement: Applicable for reasonable request.

References

1. Gao C, Wei D, Yang H, et al. Nanotechnology for treating osteoporotic vertebral fractures. International Journal of Nanomedicine. 2015; 10: 5139–5157. doi: 10.2147/IJN.S85037
2. Zhang B, Li J, He L, et al. Bio-surface coated titanium scaffolds with cancellous bone-like biomimetic structure for enhanced bone tissue regeneration. Acta Biomaterialia. 2020; 114: 431–448. doi: 10.1016/j.actbio.2020.07.024
3. Min Q, Liu J, Zhang Y, et al. Dual network hydrogels incorporated with bone morphogenic protein-7-loaded hyaluronic acid complex nanoparticles for inducing chondrogenic differentiation of synovium-derived mesenchymal stem cells. Pharmaceutics. 2020; 12(7): 613. doi: 10.3390/pharmaceutics12070613
4. Wu T, Li B, Wang W, et al. Strontium-substituted hydroxyapatite grown on graphene oxide nanosheet-reinforced chitosan scaffold to promote bone regeneration. Biomaterials Science. 2020; 8(16): 4603–4615. doi: 10.1039/D0BM00523A
5. Oudadesse H, Najem S, Mosbahi S, et al. Development of hybrid scaffold: Bioactive glass nanoparticles/chitosan for tissue engineering applications. Journal of Biomedical Materials Research Part A. 2021; 109(5): 590–599. doi: 10.1002/jbm.a.37043
6. Nie L, Deng Y, Li P, et al. Hydroxyethyl chitosan-reinforced polyvinyl alcohol/biphasic calcium phosphate hydrogels for bone regeneration. ACS Omega. 2020; 5(19): 10948–10957. doi: 10.1021/acsomega.0c00727
7. Aldaadaa A, Qaysi M, Knowles J. Physical properties and biocompatibility effects of doping SiO_2 and TiO_2 into phosphate-based glass for bone tissue engineering. Journal of Biomaterials Applications. 2018; 33(2): 271–280. doi: 10.1177/08853282187888
8. Hashemi A, Ezati M, Mohammadnejad J, et al. Chitosan coating of TiO_2 nanotube arrays for improved metformin release and osteoblast differentiation. International Journal of Nanomedicine. 2020; 15: 4471–4481. doi: 10.2147/IJN.S248927
9. Liang F, Zhou L, Wang K. Apatite formation on porous titanium by alkali and heat-treatment. Surface and Coatings Technology. 2003; 165(2): 133–139. doi: 10.1016/S0257-8972(02)00735-1
10. Cole P, Tian Y, Thornburgh S, et al. Hydrothermal synthesis of valve metal Zr-doped titanate nanofibers for bone tissue engineering. Nano and Medical Materials. 2023; 3(2): 249. doi: 10.59400/nmm.v3i2.249

11. Awasthi GP, Kaliannagounder VK, Maharjan B, et al. Albumin-induced exfoliation of molybdenum disulfide nanosheets incorporated polycaprolactone/zein composite nanofibers for bone tissue regeneration. Materials Science and Engineering: C. 2020; 116: 111162. doi: 10.1016/j.msec.2020.111162
12. Tian B, Li X, Zhang J, et al. A 3D-printed molybdenum-containing scaffold exerts dual pro-osteogenic and anti-osteoclastogenic effects to facilitate alveolar bone repair. International Journal of Oral Science. 2022; 14(1): 1–18. doi: 10.1038/s41368-022-00195-z
13. Vasto S, Baldassano D, Sabatino L, et al. The role of consumption of molybdenum biofortified crops in bone homeostasis and healthy aging. Nutrients. 2023; 15(4): 1022. doi: 10.3390/nu15041022
14. Wu S, Wang J, Jin L, et al. Effects of polyacrylonitrile/MoS_2 composite nanofibers on the growth behavior of bone marrow mesenchymal stem cells. ACS Applied Nano Materials. 2018; 1(1): 337–343. doi: 10.1021/acsanm.7b00188
15. Marins NH, Lee BEJ, e Silva RM, et al. Niobium pentoxide and hydroxyapatite particle loaded electrospun polycaprolactone/gelatin membranes for bone tissue engineering. Colloids and Surfaces B: Biointerfaces. 2019; 182: 110386. doi: 10.1016/j.colsurfb.2019.110386
16. Frandsen CJ, Brammer KS, Noh K, et al. Tantalum coating on TiO_2 nanotubes induces superior rate of matrix mineralization and osteofunctionality in human osteoblasts. Materials Science and Engineering: C. 2014; 37: 332–341. doi: 10.1016/j.msec.2014.01.014
17. Dong W, Cogbill A, Zhang T, et al. Multifunctional, catalytic nanowire membranes and the membrane-based 3D devices. The Journal of Physical Chemistry B. 2006; 110(34): 16819–16822. doi: 10.1021/jp0637633
18. Dong W, Zhang T, Epstein J, et al. Multifunctional nanowire bioscaffolds on titanium. Chemistry of Materials. 2007; 19(18): 4454–4459. doi: 10.1021/cm070845a
19. Xiao Y, Tian Y, Zhan Y, Zhu J. Degradation of organic pollutants in flocculated liquid digestate using photocatalytic titanate nanofibers: Mechanism and response surface optimization. Frontiers of Agricultural Science and Engineering. 2023; 10(3): 492–502. doi: 10.15302/J-FASE-2023503
20. Dong W, Zhang T, McDonald M, et al. Biocompatible nanofiber scaffolds on metal for controlled release and cell colonization. Nanomedicine: Nanotechnology, Biology and Medicine. 2006; 2(4): 248–252. doi: 10.1016/j.nano.2006.10.005
21. Shannon RD. Revised effective ionic radii and systematic studies of interatomic distances in halides and chalcogenides. Acta Crystallographica Section A. 1976; 32(5): 751–767. doi: 10.1107/S0567739476001551
22. Xue D, Luo J, Li Z, et al. Enhanced photoelectrochemical properties from Mo-doped TiO_2 nanotube arrays film. Coatings. 2020; 10(1): 75. doi: 10.3390/coatings10010075
23. Wang X, Liu SJ, Qi YM, et al. Behavior of potassium titanate whisker in simulated body fluid. Materials Letters. 2014; 135: 139–142. doi: 10.1016/j.matlet.2014.07.145
24. de Souza Balbinot G, da Cunha Bahlis EA, Visioli F, et al. Polybutylene-adipate-terephthalate and niobium-containing bioactive glasses composites: Development of barrier membranes with adjusted properties for guided bone regeneration. Materials Science and Engineering: C. 2021; 125: 112115. doi: 10.1016/j.msec.2021.112115

Appendix

XRD analysis of K-titanate NFs with various doping ratio.

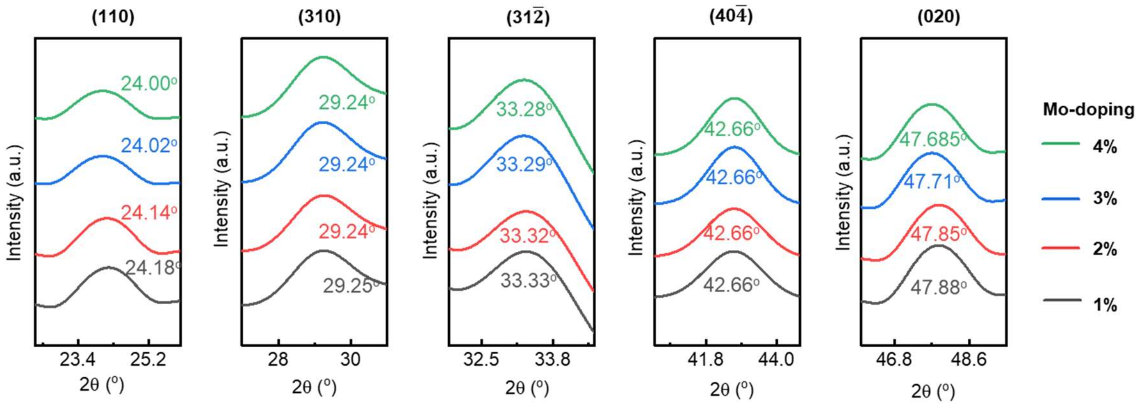

Figure A1. XRD peak shift analysis of K-titanate NFs with various doping ratio.

Characterization and Application of Nanomaterials 2024, 7(1), 5593.
https://doi.org/10.24294/can.v7i1.5593

Article

Green recovery of NaF-Na_2CO_3-NaCl ternary fluxing agent from aluminum dross

Mostafa Mahinroosta[1,2,*], **Ali Allahverdi**[2]

[1] Department of Energy, Materials and Energy Research Center, Karaj 3177983634, Iran
[2] Research laboratory of Inorganic Chemical Process Technologies, School of Chemical Engineering, Iran University of Science and Technology, Tehran 1684613114, Iran
*** Corresponding author:** Mostafa Mahinroosta, mahinroosta2010@gmail.com

CITATION

Mahinroosta M, Allahverdi A. Green recovery of NaF-Na_2CO_3-NaCl ternary fluxing agent from aluminum dross. Characterization and Application of Nanomaterials. 2024; 7(1): 5593. https://doi.org/10.24294/can.v7i1.5593

ARTICLE INFO

Received: 18 December 2023
Accepted: 6 March 2024
Available online: 1 April 2024

Abstract: The present study deliberates the recovery of sodium fluoride (NaF)-natrite (Na_2CO_3)-sodium chloride (NaCl) ternary fluxing agent from hazardous aluminum dross waste using three types of heating methods, including direct heating on a hotplate, heating by a drying oven, and microwave heating. Deionized water was used as a green solvent for the recovery experiments. Investigating the effects of time and temperature on recovery percentage showed that a recovery percentage of around 96.5% can be achieved under time and temperature of 90 min and 95 °C, respectively. The recovered fluxing agent salt was characterized by XRD, FTIR spectroscopy, FESEM, and energy dispersive X-ray spectroscopy (EDS) elemental analysis. Rietveld fitting analysis of phases detected in the XRD patterns showed that the recovered fluxing agent contained 74–81 wt.% NaF, 8–11 wt.% NaCl, and 11–14.7 wt.% Na_2CO_3. The FESEM micrographs revealed that the retrieved salts were in nano scale. The recovered fluxing agent showed different morphologies including needle-like, round shape, and a mixture of both, corresponding to microwave, drying oven, and hotplate heating methods, respectively. The nano-needles exhibited diameter of the tip and base in the range of 39–60 nm and 50–103 nm, respectively.

Keywords: waste; sodium fluoride; needle-like; microwave-assisted; nanostructure

1. Introduction

With a general look at the current situation of the industry in the world, industrial production is associated with challenging issues such as waste accumulation and natural resource depletion. The accumulation of industrial wastes over time generates environmental and public health problems [1]. In recent years, public awareness on improving the quality and preservation of the environment has coerced legislators into passing strict regulations on air and water pollution [2].

Aluminum black dross (ABD) as a hazardous industrial waste is a salty-metallic-oxidic waste of aluminum ingot production process formed in casting units [3,4]. The ABD also contains about 8%–10% of soluble salts, mainly alkali fluorides and chlorides [5,6]. In aluminum production process, a fluxing agent (usually a salt mixture containing sodium and potassium chlorides as well as a small amount of a mineral fluorine compounds (Na_3AlF_6 or CaF_2) is used to protect Al metal from oxidation under favorable conditions (high temperature and the presence of oxygen) [1]. NaF is formed as a result of the disintegration of Na_3AlF_6 (also known as cryolite) which plays the role of an electrolyte in the melting process as well as a fluxing agent in the process of smelting alumina and turning it into metallic aluminum [7,8]. Also, NaF may directly come from the molten salt flux [7].

In Europe, stockpiling of this kind of waste is prohibited because the soluble salts are a major source of surface and groundwater pollution [9] and may have some disadvantages such as cost and safety risks [5,6]. The presence of excess fluoride in drinking water often results in skeletal fluorosis, weakening bone structure, as well as discoloration and speckling of teeth, cancer or adverse effects on the brain and kidney [10]. Also, high levels of sodium in drinking water exacerbate chronic congestive heart failure, blood pressure and hypertension [11]. Therefore, finding an appropriate solution to eliminate or reduce the environmental pollution of the waste is a necessity.

Halite (NaCl), natrite (Na_2CO_3), and NaF are water-soluble and recoverable mineral salts. The recovered salt can be mixed with fresh fluxing agent and returned to aluminum smelting furnace. This is economically beneficial and also reduces the toxicity of the ABD waste [12]. Recently, NaF pellets have been applied for the adsorption of gaseous HF as an impurity in the industrial generation of fluorine gas [13]. Inasmuch as the adsorption of gaseous pollutants can be noticeably enhanced by developing nano-structures [14], the last mentioned application of NaF seems more important.

NaF in a bulk scale is prepared by neutralizing hydrofluoric acid with sodium hydroxide [15]. In nano scale, the synthesis of nanoparticles of sodium halide salts (NaF; NaCl, NaBr, NaI) having sizes of less than 3.0 nm using reverse micelles methods with capping agent has been reported by Abdelkader and Buckner [16].

Sodium carbonate (Na_2CO_3) can be used to remove iron oxide in some stages of aluminum production and cause further purification of aluminum. In addition, sodium carbonate can improve the flotation performance and play a role as a pH regulator [17]. In the aluminum smelting process, sodium carbonate improves the performance of the fluxing agent [18]. Sodium fluoride, sodium chloride, and sodium carbonate can be used as roasting agents in the processes of extracting valuable materials from primary and secondary sources [19–21].

Within the scope of this work, facile green recovery of fluxing agent nanostructures from the ABD is investigated for the first time. The recovery of soluble salts in the form of nanostructures implies to the principles 3 (substances with little or no hazard), 5 (safer solvents and auxiliaries), and 12 (safety considerations) of the twelve principles of green chemistry [22]. After removing the soluble salts from the ABD, its pollution is significantly reduced, and the soluble salt-free residue can be subjected to subsequent processes such as the recovery of alumina as a valuable and widely used material [23,24].

2. Materials and methods

2.1. Materials

The ABD used herein was obtained from Iranian Aluminum Company (Iralco) situated in Markazi province, Iran. The as-received BAD was medium gray in color with the actual and bulk densities of 2.22 and 0.85 g/cm^3, respectively. The mineralogy of the ABD will be discussed in section 3.2. **Figure 1** shows the particle size distribution of the ABD. As seen, about 55% of the ABD particles are below 250 µm, whereas about 90% of which are less than 2.38 mm.

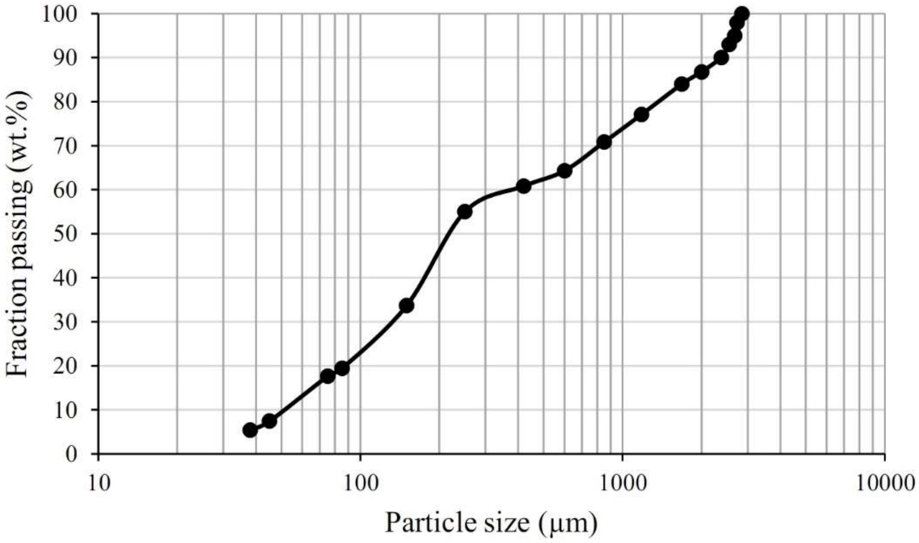

Figure 1. Particle size distribution of ABD.

Table 1 gives oxide composition of the ABD which was determined by X-ray fluorescence (XRF) technique. According to data in **Table 1**, the ABD contains almost 61 and 15 wt.% aluminum oxide and silicon dioxide, respectively. The loss on ignition (LOI) was obtained around 9 wt.% and the remaining 15 wt.% accounts for the other oxides.

Deionized (DI) water (TDS = 5 mg/L) was utilized at all recovery experimental tests as a green solvent.

Table 1. Chemical composition of ABD.

Oxide	**(wt.%)**
Al_2O_3	62.56
SiO_2	7.53
CaO	5.87
Fe_2O_3	2.73
Na_2O	4.68
MgO	1.25
P_2O_5	0.17
SO_3	0.10
K_2O	0.81
TiO_2	0.32
MnO	0.31
Cl	3.35
F	1.32
CuO	0.11
LOI*	8.89

2.2. Methods

2.2.1. Determination of water leachable salt content of ABD

To determine the water leachable salt content of the ABD, the method described in DIN 38414-S4 standard for determination of leachability by water was used. According to this standard, first 100 g of dry ABD sample is loaded into a 2 L beaker and then 1 L of DI water is added. The mixture is then stirred for 24 h. After the mixing time has elapsed, the mixture is filtered through a vacuum filtration system. The filtrate should be transparent at this stage, otherwise it must be re-filtered with a filter paper with a mesh size of 0.45 µm. The determination of the chemical analysis of leachate is performed using inductively coupled plasma atomic emission spectroscopy (ICP-AES). At the end of the experiment, the mass of the leached substance is calculated by the following Equation (1).

$$W_{ES} = (\beta \times V_E)/m_s \quad (1)$$

where, W_{ES} is the mass of the leached substance (in mg/kg), β is the mass concentration of the leached substance (in mg/L), m_s is the dry mass of initial sample (in kg), and V_E is the volume of the filtrate (in L).

2.2.2. Salt recovery experiments

To perform salt recovery experiments, the setup shown in **Figure 2** was used. **Figure 2** shows a three-neck glass reactor, Graham condenser, a water bath for homogenizing the recovery temperature, and a magnetic stirrer. After accurate weighing, 5.00 g of the ABD is loaded into the reactor. Then 100 mL of deionized water is added to it. The rinsing starts at a specified temperature under the stirring speed of 600 rpm. After a certain period of time, the suspension is filtered using a vacuum filtration system.

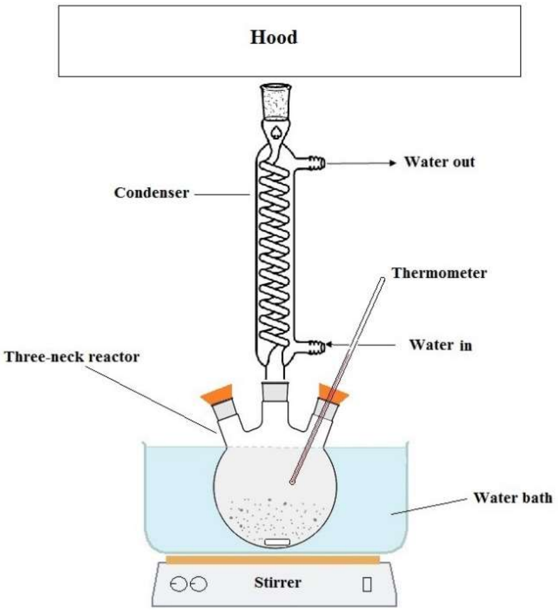

Figure 2. Experimental setup used for salt recovery from ABD.

As illustrated in **Figure 3**, in order to evaporate the water content of the obtained filtrate, three types of heating methods including microwave irradiation, heating by a drying oven (Pars Khazar, OT 650P), and heating by a hotplate (IKA C-MAG HS7

Digital) were applied. The microwave irradiation was provided using a domestic microwave oven (Sapor, 1500 W, 2450 MHz). At the end of the heating, a white solid was achieved. The heating processes were performed at 95 ± 1 °C for 2 h by hotplate and at 95 ± 0.5 °C for 1 h by drying oven. The microwave irradiation continued for a preset time of 15 min.

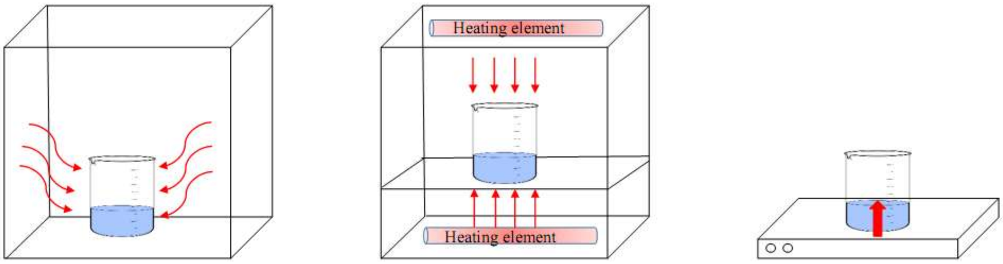

Figure 3. Three types of heating methods (left: microwave irradiation, middle: heating by a drying oven, right: heating by a hotplate).

2.2.3. Characterization methods

To obtain X-ray diffractograms of the samples, Philips Expert System X-ray diffractometer was utilized with CuKα-radiation and Ni-filter at voltage and current of 40 kV and 30 mA, respectively. The XRD analyses were carried out at 2θ angles of 10°–80° (scanning speed: 2 °/min; anti-scatter: 1°; receiving slit: 0.01 mm). Fourier transform infrared spectroscopy (FTIR) spectra of the recovered salts were recorded employing a FTIR spectrometer device (SHIMADZU IR Spectrophotometer 8400 s) in the wavenumber range of 400–4000 cm^{-1}. The spectra were recorded with a sensitivity of 4 cm^{-1} and 64 scans per spectrum taken.

Morphological and elemental analyses were obtained employing two kinds of microscopes including SIGMA VP-500 FESEM microscope (ZEISS) and TESCAN MIRA3 at accelerating voltages of 15 and 10 kV, respectively. For sample preparation, an adequate amount of the recovered salts is adhered on a holder. Then they are coated with a thin layer of gold. The chemical composition of the ABD was determined using a XRF PW2404 device with a measurement range of 20 ppm to 100 wt.%.

3. Results and discussion

3.1. Chemical analysis of leachate

The ICP-AES chemical analysis of the leachate obtained according to DIN 38414-S4 standard is presented in **Table 2**, indicating significant amount of sodium and minor amounts of potassium and aluminum.

Table 2. Chemical analysis of the leachate obtained according to DIN 38414-S4 standard.

Element	Na	K	Al	Ca
Concentration (mg/L)	5662.40	37.23	74.77	ND*
Mass%	98.06	0.64	1.30	-

*ND: not detected.

Based on the data in **Table 2**, the water leachable salt content of the ABD was 5.77 mass%. The pH value of the leachate was around 11.25.

The previous studies [23,24] revealed that the ABD contains aluminum oxide (Al_2O_3), spinel ($MgAl_2O_4$), quartz (SiO_2), diaoyudaoite ($NaAl_{11}O_{17}$), villiaumite (NaF), cryolite (Na_3AlF_6), silicon (Si), aluminum nitride (Al) and iron oxide (Fe_2O_3) as well as minor traces of halite (NaCl), graphite (C), and fluorite (CaF_2). Considering the aforementioned compounds, the presence of sodium in the leachate is majorly due to the dissolution of NaF and NaCl. The presence of aluminum in the leachate originates from the partial hydrolysis of aluminum nitride in water [25,26]. A trace amount of potassium is more likely due to the dissolution of potassium chloride which is used along with sodium chloride as salt flux in melting process of aluminum.

3.2. Effects of time and temperature on salt recovery efficiency

Before performing any salt recovery experiment, the moisture content of the ABD sample was removed in a drying oven at 105 ± 0.5 ℃. This is a necessary step to obtain exact recovery efficiency data. The previous study [24] showed that a drying time of 50 min is enough to completely remove the moisture. In order to investigate the possibility of faster recovery of soluble salts, water leaching of the ABD was carried out at different temperatures and times. In these experiments, the water leaching of the ABD was performed at 25, 45, 65, 85 and 95 ℃ for 30, 60, 90, and 120 min at each temperature. Each experiment was performed twice. The results are depicted in **Figure 4**.

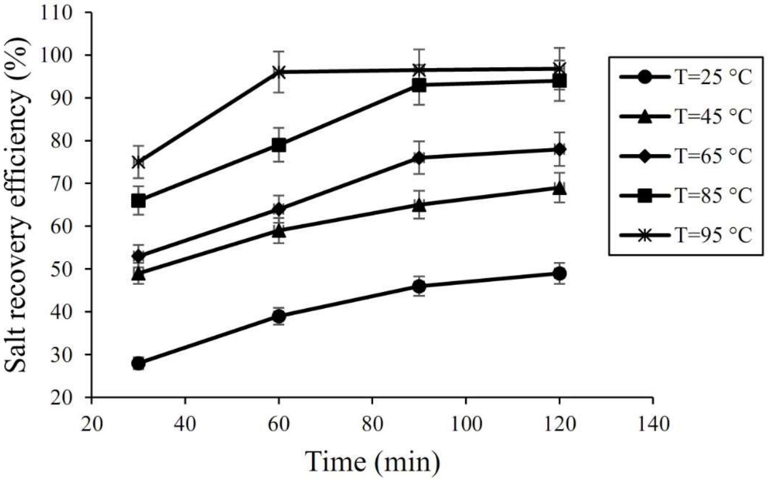

Figure 4. The effects of time and temperature on salt recovery efficiency.

From **Figure 4**, it is clear that the salt recovery efficiency generally increases with increasing temperature and time. Such an enhancement was expected, since the solubility of NaF in water increases with temperature [27]. At 95 ℃, after 60 min, the recovery efficiency is about 96%, and more increase in time does not significantly change the percentage of salt recovery. Also, recovery times of more than 1 h are not practically interesting. **Figure 5** shows the XRD patterns of the raw ABD and water-leached ABD.

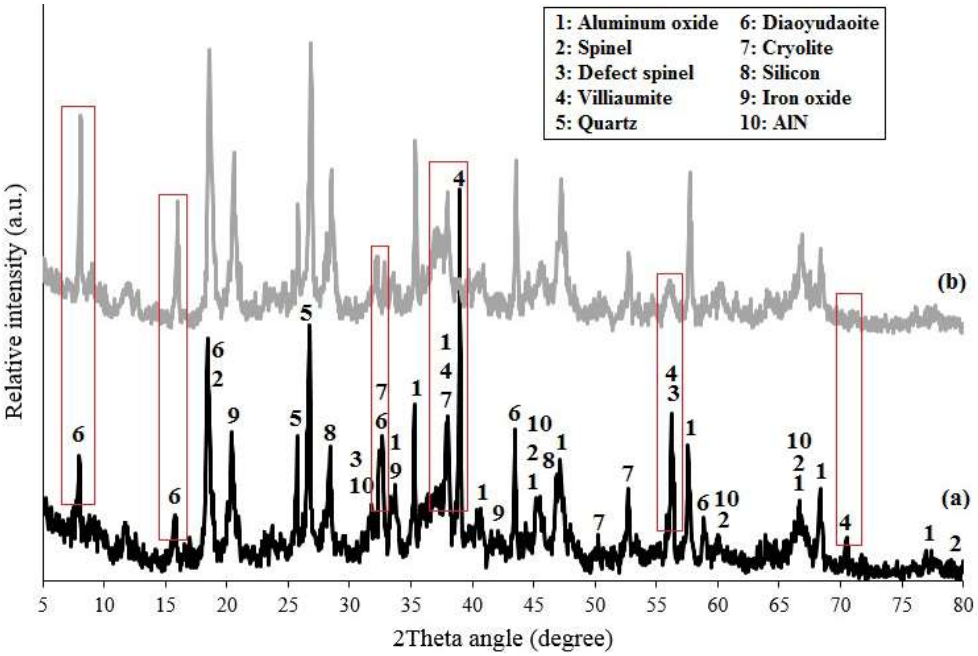

Figure 5. XRD patterns of **(a)** raw ABD and **(b)** water-leached ABD.

Figure 5a shows that the ABD contains aluminum oxide (Al_2O_3), spinel ($MgAl_2O_4$), defect spinel ($Al_{1.83}Mg_{0.87}O_{3.61}$), quartz ($SiO_2$), diaoyudaoite ($NaAl_{11}O_{17}$), villiaumite (NaF), cryolite (Na_3AlF_6), silicon (Si), aluminum nitride (Al) and iron oxide (Fe_2O_3) as well as minor traces of halite (NaCl), graphite (C), and fluorite (CaF_2). Among all these phases, only NaF and NaCl are highly soluble in water. As can be clearly observed from the peaks surrounded by rectangles in **Figure 5**, almost all villiaumite (NaF) has been dissolved in water. Reduced intensity of the diaoyudaoite phase shows that this phase has also partially been dissolved in water. Unfortunately, there is not enough information on the solubility of this material in the literature.

3.3. Characterization of the recovered salts

3.3.1. XRD patterns

Figure 6 presents the X-ray diffractograms of the recovered salts using the mentioned three types of heating methods. The peaks of the recovered salts correspond to those of NaF, NaCl, KCl, AlN, and SiO_2 phases according to the standard cards of ICDD-01-089-2956, ICDD-01-088-2300, ICDD-01-077-2121, ICDD-01-089-3446, and ICDD-01-081-0069, respectively. Because XRD data are substantially qualitative and also due to the proximity of the intensities of some peaks, a reasonable comparison between the three patterns requires the quantification of data and gaining the mass fraction of each phase. To calculate the mass fraction of each phase, the XRD data were quantified applying the Rietveld fitting analysis. The Rietveld fitting analyses were performed using crystallographic information files (CIFs) of villiaumite (NaF), halite (NaCl), and natrite (Na_2CO_3). According to the quantitative data shown in **Figure 6**, the recovered salts consist of predominantly NaF, accounting for 74–81 wt.%. The remaining 20–25 wt.% is dedicated to the presence of sodium chloride and sodium carbonate. The higher amount of NaF improves the performance of fluxing agent. Therefore, according to **Figure 6**, heating by a drying oven is more suitable. In fact, this type of drying method is a type of indirect heating method, which is mainly done through convection.

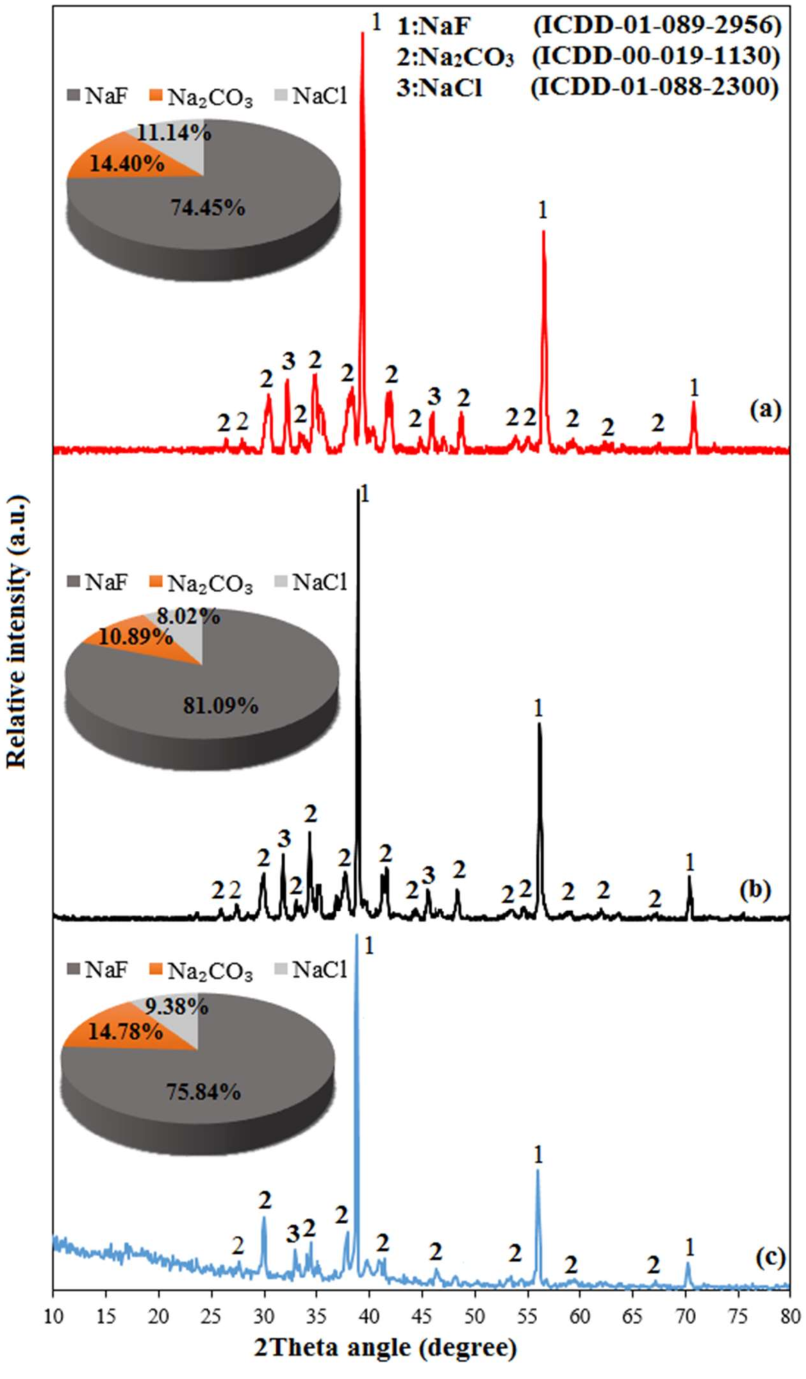

Figure 6. XRD patterns of the recovered salts. Heat source: **(a)** microwave irradiation, **(b)** drying oven, and **(c)** hotplate.

The average crystallite size was obtained using Scherrer equation:

$$L = k\lambda/\beta\cos\theta \tag{2}$$

in which L is the average crystallite size, θ the Bragg's angle, λ the incident X-ray wavelength (λ = 1.541874 Å), and β the full width at half maximum (FWHM) of the peak. β and 2θ values were obtained from each XRD pattern using HighScore Plus software. The results are presented in **Table 3**.

Table 3. Values of 2θ, *β*, and average crystallite size of the recovered salts.

Recovered salt sample	2θ (degree)	*β* (degree)	*β* (rad)	Average crystallite size (nm)
Salt recovered by microwave irradiation	38.9254	0.1653	0.00288	61.9
Salt recovered by drying oven heating	38.9232	0.1968	0.00343	52.0
Salt recovered by hotplate heating	38.7726	0.2952	0.00515	34.5

According to **Table 3**, the salt recovered by hotplate heating has the most minute average crystallite size (34.5 nm) and the salt recovered by microwave irradiation has the largest one (61.9 nm). The larger crystal size of the salt recovered by microwave irradiation is due to the fact that the heating rate is very rapid (only one tenth to one hundredth of the time needed by conventional ways), which leads to the supersaturation of the solution. Crystals in a supersaturated solution can grow faster and become larger [28,29].

3.3.2. FTIR analysis

Figure 7 depicts FTIR spectra of the recovered salts.

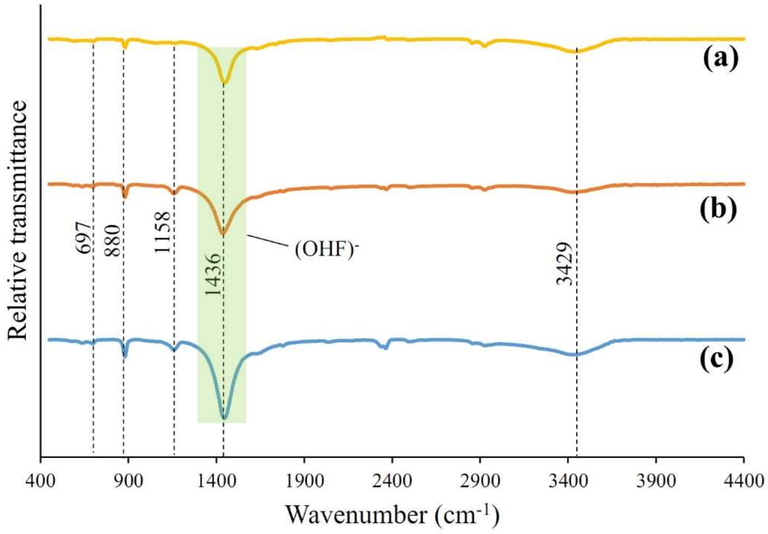

Figure 7. FTIR spectra of the recovered salts. Heat source: **(a)** microwave irradiation; **(b)** drying oven; and **(c)** hotplate.

All three samples show absorption bands at 697, 880, 1158, 1436, 2366, 2924, and 3429 cm^{-1}. The bands observed at 697 and 880 cm^{-1} are assigned to the presence of AlN. This is in agreement with the literature that the main excitation of the Al-N bonds by infrared radiation take place at the range 200-1000 cm^{-1} [30]. The band at 1158 cm^{-1} is caused by the asymmetric stretching of the oxygen atom in the Si-O-Si chain [31]. The absorption band at 1436 cm^{-1} is allocated to $(OHF)^-$ complexes with a hydrogen bond [32,33]. The presence of $(OHF)^-$ complex may be due to some amount of water at the surface of the recovered salts, which dissolves some NaF and produces fluoride ions. Thus, the generated fluoride ions are surrounded by OH groups due to hydrogen bonding. Considering this peak, it is realized that its intensity in the salt recovered by hotplate heating is higher than that in two other samples. The reason may be the formation of more hydrogen bonds and thus the formation of more $(OHF)^-$ complexes. This evidence suggests that the hotplate heating method is less effective in evaporation of water content of the recovered salt compared to other two heating methods. The absorption band at 3429 cm^{-1} shows a small amount of water in the recovered salts.

3.3.3. Microstructural and elemental analyses

To gain appropriate insight into the morphological and elemental information of the recovered salts by three types of heating sources, FESEM/EDS analyses were used. **Figure 8** depicts the FESEM images and corresponding EDS elemental analyses of the recovered salts. **Figure 8a** shows that the evaporation of water of the leached salt from the ABD through heating by a hotplate has caused the formation of a needle-like nanostructure on surfaces of relatively larger particles (a few to several microns) that seems to be amorphous. Observations at high magnification (**Figure 8a1**), however, reveals that the relatively large particles are aggregation of numerous round shape nanoparticles with a diameter in the range of 33–40 nm. As it can be clearly seen from **Figure 8b**, a pure needle-like morphology has emerged due to the removal of water of the leached salt by microwave heating. **Figure 8b1** shows that the needle-like particles grown with different orientations are in nano scale. The nano-needles show diameter of the tip and base in the range of 39–60 nm and 50–103 nm, respectively. This is despite the fact that the evaporation of water of the leached salt through heating by a drying oven has resulted in the formation of aggregates of round shape nanoparticles only. As can obviously be observed from **Figure 8c**, the agglomerates include nanoparticles with the sizes larger than 20 nm (as shown in **Figure 8c1**). All EDS elemental analyses disclosed Na, F, O, Cl, Al, C, Si, and K as the chemistry of the formed nanostructures.

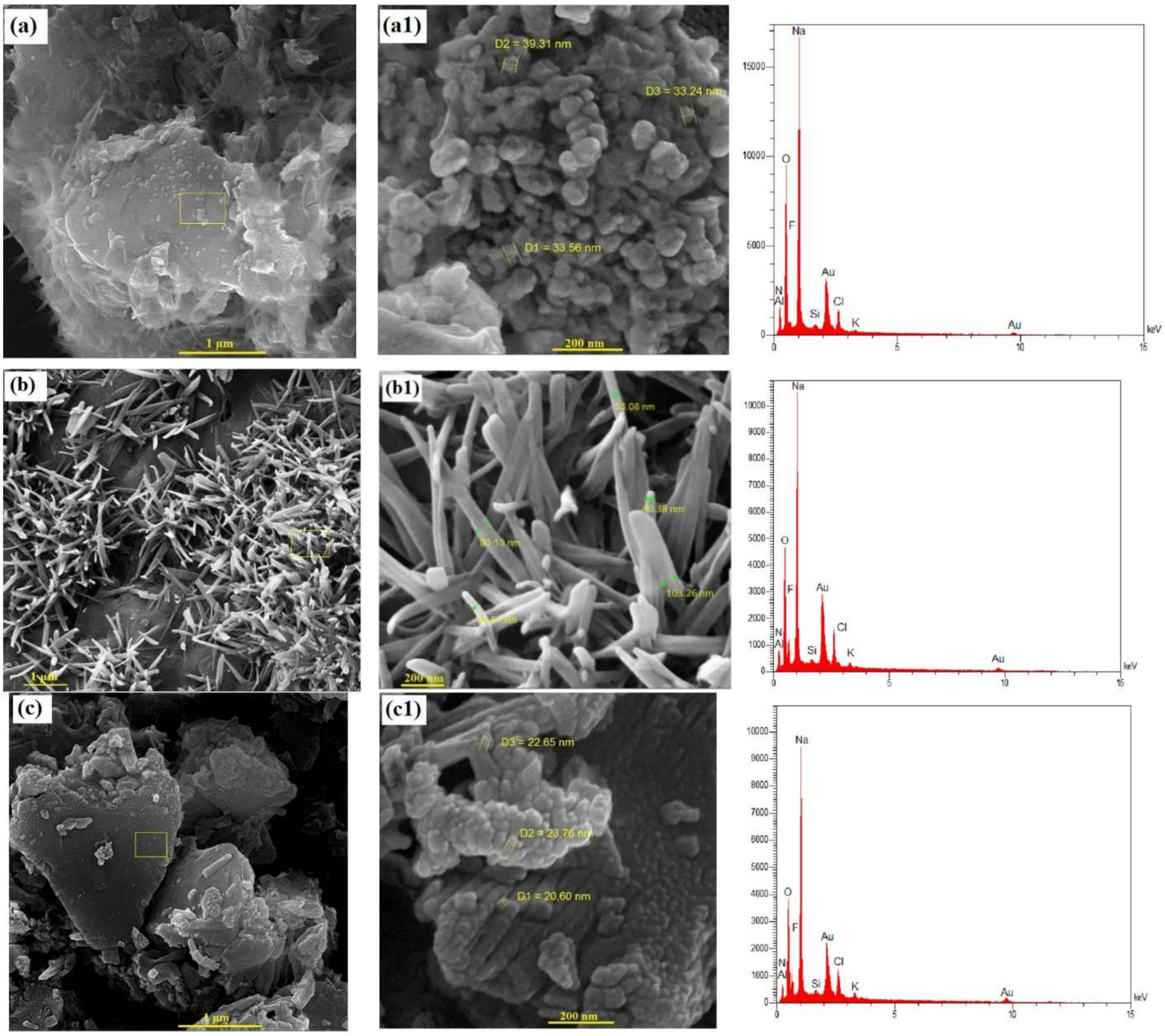

Figure 8. FESEM images and corresponding EDS elemental analyses of the recovered salts. Heat source: **(a, a1)** hotplate; **(b, b1)** microwave irradiation; and **(c, c1)** drying oven.

The mechanism for the formation of different nanostructures can be interpreted as follows:

Water-soluble halides are ionized in water according to the following reaction [16]:

$$NaY_{(solid)} \leftrightarrow Na^{+}_{(aqueous)} + Y^{-}_{(aqueous)} \quad (3)$$

Driving force for the formation of nanostructures of sodium halides or any water-soluble particles is the evaporation of water from a confined space which allows the size and shape control. Considering the type of heating source for evaporation of water of the leached salts, two main parameters that may have a key role in the appearance of different nanostructures are temperature gradient and supersaturation. As shown in **Figure 3**, heating through a hotplate causes the temperature of regions from the solution close to the hot plate to be higher than the temperature of the surface regions of the solution in the vicinity of the air. This results in the formation of a sharp temperature gradient in the solution, which in turn leads to a different evaporation rate and, ultimately, a different crystallization rate. The heat generated by a drying oven with heating elements embedded in top and bottom of the oven chamber creates a milder temperature gradient compared to the previous heating state. Consequently, the evaporation rate and the rate of crystallization are more uniform. As a result, morphology is expected to be more uniform. Also, the nanoparticles obtained by drying oven and hotplate heating methods tend to severe agglomeration [28] and this is clear in **Figure 8a,c**. The microwave heating as a green heating method, has a mechanism fundamentally different from the common heating methods. This difference is significant from two perspectives: firstly, in common heating methods, i.e., conduction, convection, and radiation, heat is supplied through an external source. While in microwave heating, heat generated from microwave energy is absorbed by the material depending on its position in the microwave field. Secondly, common heating methods produce a sharp temperature gradient in the material, while the microwave heating method does not create any temperature gradient and the temperature of the whole material is almost the same. In addition, microwaves deliver heat uniformly and simultaneously throughout the bulk of a material and also have the potential to penetrate deeply into material bulk [34,35]. As another important reason, experimental results have revealed that the crystal characteristics such as size distribution, crystal morphology and degree of agglomeration are also strongly influenced by the degree of supersaturation at the beginning of crystallization [29,36]. The crystals in a relatively high supersaturated solution focus on extending along the longitudinal direction. With the progress of the process, the supersaturation descends around the tips of the crystals and this causes the tips have a smaller diameter than the bases. As a result, a more orderly and uniform structure is expected.

4. Conclusions

In the present work, NaF-Na_2CO_3-NaCl ternary fluxing agent ternary was recovered from aluminum black dross as a hazardous solid waste. Despite a significant reduction in waste toxicity, the recovery of fluxing agent in the form of a nanostructured salt can provide economic benefits. The recovery process was performed using water as a green solvent followed by the evaporation of water. The heat for the evaporation process was supplied using three sources of heating including a hotplate, microwave irradiation, and a drying oven. Investigating the effects of time and temperature revealed that a recovery efficiency of 96.5% can be achieved under optimum temperature and time of 95 ℃ and 90 min, respectively. The recovered fluxing agent salt was found to contain more than 74 wt.% of NaF by employing the Rietveld fitting analysis. Microstructural study by FESEM disclosed that the ternary fluxing agent has been recovered in the form of highly aggregated round shape nanoparticles, needle-like nanoparticles, and a combination of both.

Author contributions: Conceptualization, MM; methodology, MM; software, MM; validation, MM and AA; formal analysis, MM; investigation, MM and AA; resources, MM and AA; data curation, MM and AA; writing—original draft preparation, MM; writing—review and editing, MM and AA; visualization, MM; supervision, AA; project administration, MM and AA; funding acquisition, MM and AA. All authors have read and agreed to the published version of the manuscript.

Conflict of interest: The authors declare no conflict of interest.

References

1. Xiao Y, Reuter MA, Boin UDO. Aluminium Recycling and Environmental Issues of Salt Slag Treatment. Journal of Environmental Science and Health, Part A. 2005; 40(10): 1861-1875. doi: 10.1080/10934520500183824
2. Tsakiridis PE, Oustadakis P, Agatzini-Leonardou S. Aluminium recovery during black dross hydrothermal treatment. Journal of Environmental Chemical Engineering. 2013; 1(1-2): 23-32. doi: 10.1016/j.jece.2013.03.004
3. Dash B, Das BR, Tripathy BC, et al. Acid dissolution of alumina from waste aluminium dross. Hydrometallurgy. 2008; 92(1-2): 48-53. doi: 10.1016/j.hydromet.2008.01.006
4. Sarker MdSR, Alam MdZ, Qadir MdR, et al. Extraction and characterization of alumina nanopowders from aluminum dross by acid dissolution process. International Journal of Minerals, Metallurgy, and Materials. 2015; 22(4): 429-436. doi: 10.1007/s12613-015-1090-2
5. Unlü N, Drouet MG. Comparison of salt-free aluminum dross treatment processes. Resour Conserv Recycl. 2002; 36. doi: 10.1016/S0921-3449(02)00010-1
6. Yoshimura HN, Abreu AP, Molisani AL, et al. Evaluation of aluminum dross waste as raw material for refractories. Ceramics International. 2008; 34(3): 581-591. doi: 10.1016/j.ceramint.2006.12.007
7. Narayanan R, Sahai Y. Chemical Interactions of Dross with Water and Water Vapor in Aluminum Scrap Remelting. Materials Transactions, JIM. 1997; 38(1): 85-88. doi: 10.2320/matertrans1989.38.85
8. Das BR, Dash B, Tripathy BC, et al. Production of η-alumina from waste aluminium dross. Minerals Engineering. 2007; 20(3): 252-258. doi: 10.1016/j.mineng.2006.09.002
9. Shinzato MC, Hypolito R. Solid waste from aluminum recycling process: characterization and reuse of its economically valuable constituents. Waste Management. 2005; 25(1): 37-46. doi: 10.1016/j.wasman.2004.08.005
10. Harrison PTC. Fluoride in water: A UK perspective. Journal of Fluorine Chemistry. 2005; 126(11-12): 1448-1456. doi: 10.1016/j.jfluchem.2005.09.009
11. World Health Organization. Sodium in drinking-water, background document for development of WHO guidelines for drinking-water quality, 2nd ed. World Health Organization; 1996.
12. Bruckard WJ, Woodcock JT. Recovery of valuable materials from aluminium salt cakes. International Journal of Mineral Processing. 2009; 93(1): 1-5. doi: 10.1016/j.minpro.2009.05.002
13. Afzal S, Rahimi A, Ehsani MR, et al. Experimental study of hydrogen fluoride adsorption on sodium fluoride. Journal of Industrial and Engineering Chemistry. 2010; 16(1): 147-151. doi: 10.1016/j.jiec.2010.01.004
14. Fryxell GE, Cao G. Environmental Applications of Nanomaterials. Imperial College Press; 2011. doi: 10.1142/p814
15. Lailach G, Bulan A, Buss G. Process for the preparation of sodium fluoride. US6251358B1, 1998.
16. Abdelkader E, Buckner SW. Synthesis of NaX (X = F, Cl, Br, I) Nanoparticles. Soft Nanoscience Letters. 2013; 3(1): 22-27. doi: 10.4236/snl.2013.31005
17. Kupka N, Rudolph M. Role of sodium carbonate in scheelite flotation—A multi-faceted reagent. Minerals Engineering. 2018; 129: 120-128. doi: 10.1016/j.mineng.2018.09.005
18. Kientzler P, Löbbers K, Michard L. Improved modifying flux for molten aluminium. EP2231887A1, 2013.
19. Dang H, Chang Z, Wu X, et al. Na_2SO_4–NaCl binary eutectic salt roasting to enhance extraction of lithium from pyrometallurgical slag of spent lithium-ion batteries. Chinese Journal of Chemical Engineering. 2022; 41: 294-300. doi: 10.1016/j.cjche.2021.09.008
20. Huang J, Wang Y, Zhou G, et al. Investigation on the Effect of Roasting and Leaching Parameters on Recovery of Gallium from Solid Waste Coal Fly Ash. Metals. 2019; 9(12): 1251. doi: 10.3390/met9121251
21. Wu H, Yan H, Liang Y, et al. Rare earth recovery from fluoride molten-salt electrolytic slag by sodium carbonate roasting-hydrochloric acid leaching. Journal of Rare Earths. 2023; 41(8): 1242-1249. doi: 10.1016/j.jre.2022.07.001
22. Anastas PT, Warner JC. Green Chemistry: Theory and Practice. Oxford University Press; 1998.
23. Mahinroosta M, Allahverdi A. A promising green process for synthesis of high purity activated-alumina nanopowder from secondary aluminum dross. Journal of Cleaner Production. 2018; 179: 93-102. doi: 10.1016/j.jclepro.2018.01.079
24. Mahinroosta M, Allahverdi A. Enhanced alumina recovery from secondary aluminum dross for high purity nanostructured γ-alumina powder production: Kinetic study. Journal of Environmental Management. 2018; 212: 278-291. doi: 10.1016/j.jenvman.2018.02.009

25. Bowen P, Highfield JG, Mocellin A, et al. Degradation of Aluminum Nitride Powder in an Aqueous Environmet. Journal of the American Ceramic Society. 1990; 73(3): 724-728. doi: 10.1111/j.1151-2916.1990.tb06579.x
26. Fukumoto S, Hookabe T, Tsubakino H. Hydrolysis behavior of aluminum nitride in various solutions. J Mater Sci. 2000; 35. doi: 10.1023/A:1004718329003
27. Reynolds JG, Belsher JD. A Review of Sodium Fluoride Solubility in Water. Journal of Chemical & Engineering Data. 2017; 62(6): 1743-1748. doi: 10.1021/acs.jced.7b00089
28. Wang B, Zhang W, Zhang W, et al. Progress in Drying Technology for Nanomaterials. Drying Technology. 2005; 23(1-2): 7-32. doi: 10.1081/drt-200047900
29. Sarig S, Eidelman N, Glasner A, et al. The effect of supersaturation on the crystal characteristics of potassium chloride. Journal of Chemical Technology and Biotechnology. 1978; 28(10): 663-667. doi: 10.1002/jctb.5700281004
30. Balasubramanian C, Bellucci S, Cinque G, et al. Characterization of aluminium nitride nanostructures by XANES and FTIR spectroscopies with synchrotron radiation. Journal of Physics: Condensed Matter. 2006; 18(33): S2095-S2104. doi: 10.1088/0953-8984/18/33/s25
31. Roy Chowdhuri A, Takoudis CG, Klie RF, et al. Metalorganic chemical vapor deposition of aluminum oxide on Si: Evidence of interface SiO_2 formation. Applied Physics Letters. 2002; 80(22): 4241-4243. doi: 10.1063/1.1483903
32. Bryukvina LI, Khulugurov VM, Parfianovich IA. Infrared vibrational spectra of radiatively induced absorption of NaF: OH crystals. Opt Spectrosc. 1987; 63(1).
33. Cheng J, Guo R, Wang QM. Zinc oxide single-crystal microtubes. Applied Physics Letters. 2004; 85(22): 5140-5142. doi: 10.1063/1.1825067
34. Cheng J, Agrawal D, Zhang Y, et al. Fabricating transparent ceramics by microwave sintering. Am Ceram Soc Bull. 2000; 79(9).
35. Liu XY, Bennema P. Theoretical consideration of the growth morphology of crystals. Physical Review B. 1996; 53(5): 2314-2325. doi: 10.1103/physrevb.53.2314
36. Ma M, Ye W, Wang XX. Effect of supersaturation on the morphology of hydroxyapatite crystals deposited by electrochemical deposition on titanium. Materials Letters. 2008; 62(23): 3875-3877. doi: 10.1016/j.matlet.2008.05.009

Characterization and Application of Nanomaterials 2024, 7(1), 4671.
https://doi.org/10.24294/can.v7i1.4671

Article

Influence of green synthesized aluminum oxide nanoparticle concentration on wear and coefficient of friction of vegetable oil-based lubricants

Stephen Yebosoko Tsado[1], Tijani Jimoh Oladejo[2], Uzoma Gregory Okoro[1], Daniel Ipilakyaa Tertsegha[3], Ibrahim Ogu Sadiq[1], Joseph Abutu[4], Emmanuel Ogo Onche[5], Antwi Afari Acheampong[6], Alhassan Sullaiman[6], Ebenezer Adu Kyeremeh[6], Sunday Albert Lawal[1,6,*]

[1] Department of Mechanical Engineering, Federal University of Technology Minna, Minna 920101, Nigeria
[2] Department of Chemistry, Federal University of Technology Minna, Minna 920101, Nigeria
[3] Department of Mechanical Engineering, Joseph Sarwuan Tarka University, Makurdi 970101, Nigeria
[4] Department of Mechanical Engineering, Taraba State University, Jalingo 660213, Nigeria
[5] Department of Mechanical Engineering, University of Abuja, Giri 900105, Nigeria
[6] Department of Mechanical Engineering, University of Mines and Technology Tarkwa, Tarkwa 000031, Ghana
*** Corresponding author:** Sunday Albert Lawal, lawalsunday@futminna.edu.ng

CITATION

Tsado SY, Oladejo TJ, Okoro UG, et al. Influence of green synthesized aluminum oxide nanoparticle concentration on wear and coefficient of friction of vegetable oil-based lubricants. Characterization and Application of Nanomaterials. 2024; 7(1): 4671.
https://doi.org/10.24294/can.v7i1.4671

ARTICLE INFO

Received: 18 February 2024
Accepted: 26 March 2024
Available online: 18 April 2024

Abstract: Green manufacturing is increasingly becoming popular, especially in lubricant manufacturing, as more environmentally friendly substitutes for mineral base oil and synthetic additives are being found among plant extracts and progress in methodologies for extraction and synthesis is being made. It has been observed that some of the important performance characteristics need enhancement, of which nanoparticle addition has been noted as one of the effective solutions. However, the concentration of the addictive that would optimised the performance characteristics of interest remains a contending area of research. The research was out to find how the concentration of green synthesized aluminum oxide nanoparticles in nano lubricants formed from selected vegetable oils influences friction and wear. A bottom-up green synthesis approach was adopted to synthesize aluminum oxide (Al_2O_3) from aluminum nitrate ($Al(NO_3)_3$) precursor in the presence of a plant-based reducing agent—*Ipomoea pes-caprae*. The synthesized Al_2O_3 nanoparticles were characterized using TEM and XRD and found to be mostly of spherical shape of sizes 44.73 nm. Al_2O_3 nanoparticles at different concentrations—0.1 wt%, 0.3 wt%, 0.5 wt%, 0.7 wt%, and 1.0 wt%—were used as additives to castor, jatropha, and palm kernel oils to formulate nano lubricants and tested alternately on a ball-on-aluminum (SAE 332) and low-carbon steel Disc Tribometer. All the vegetable-based oil nano lubricants showed a significant decrease in the coefficient of friction (CoF) and wear rate with Ball-on-(aluminum SAE 332) disc tribometer up to 0.5wt% of the nanoparticle: the best performances ($e_{COF} = 92.29$; $e_{WR} = 79.53$) came from Al_2O_3-castor oil nano lubricant and Al_2O_3-palm kernel oil; afterwards, they started to increase. However, the performance indices displayed irregular behaviour for both COF and Wear Rate (WR) when tested on a ball-on-low-carbon steel Disc Tribometer.

Keywords: nanoparticles; green synthesized; wear; coefficient of friction; lubricants

1. Introduction

In recent times, vegetable oils have been identified as a favorite substitute for mineral oils as base oils in lubricant formulations. This is because vegetable oils possess high biodegradability and lubricity and, hence, can return to nature upon consumption after their useful lives. This property of vegetable oils makes them environmentally friendly alternatives to mineral oil-based lubricants. Researchers have carried out studies using vegetable oils as the base oil for lubricants while using various nanoparticle additives to improve its tribological performance [1–3]. Vegetable oils comprise the chemical composition of molecules of triacylglycerol made up of esters derived from glycerol and long chains of polar fatty acids [4]. Other vegetable oils are also composed of esters of glycerin and long-chain fatty acids (triglycerides), which have molecular structure with three long-chain fatty acids attached at the hydroxyl groups via ester linkages [5]. The chemical structure of a typical vegetable oil is shown in **Figure 1**.

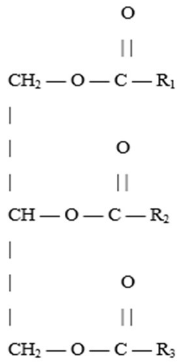

Figure 1. Chemical structure of triglyceride of a typical vegetable oil [5].

Other parameters that are determined through the process of formulating the oil-based lubricants are the acid value, saponification, and free fatty acid of the oil [6,7]. Nanoparticles ranging between 1 nm and 100 nm have all three external dimensions in the nanoscale, and their longest and shortest axes do not have a significant difference, typically being a factor of at least 3. Some examples are nonporous Pd NPs (0D), graphene nanosheets (2D), Ag nanorods (1D), polyethylene oxide nanofibers (1D), urchin-like ZnO nanowires (3D), and WO3 nanowire network (3D) [8]. Nanoparticles demonstrate desirable physical and optical characteristics such as shape and size, which makes them suitable to confine their electrons and produce quantum effects. These properties help in a complete description of its behavioural and operational functionalities, which deal with the size, shape, surface properties, crystallinity, and dispersion state [9]. The use of nanomaterials as additives to oil-base lubricants to produce nano lubricants with improved tribological properties has been gaining research attention in the industry in recent times [10]. This is essentially a result of their anti-wear, extreme pressure, and friction-modifying properties. Although there are different types of nanomaterials used in the formulation of nano lubricants, about 72% of nano lubricants are formulated using metal-containing nanomaterials as lubricant additives [11]. Among the various metallic nanoparticles that could be used as additives to lubricants, the Cu nanoparticles have received wide research attention for their superior performance in comparison with other metallic nanoparticles [12].

Metal nanoparticles are produced by the addition of reducing agents, while metal oxide nanoparticles are manufactured by the addition of oxidizing/precipitating agents during their synthesis [13]. Generally, when compared with metal-containing nanoparticles, the metal oxide nanoparticles are larger in size. Metal oxide nanoparticles have been shown to improve the viscosity of lubricants at low temperatures and the rolling effect of the lubricant at high temperatures, with deposition of the metal oxide nanoparticles on the interacting surfaces leading to improved anti-wear performance [11]. Utilizing metal oxide nanoparticles will improve the nano lubricant properties. These properties include the nanoparticle size, morphology/shape, surface functionalization, and nanoparticle concentration. In synthesizing the nanoparticles, the green synthesis method was used for this work. This is a bottom-up approach of the two methods of synthesizing. The other method, the top-down approach, emphasizes the preparation of nanoparticles from the process of breaking down complex metal ions through physical, chemical, or thermal methods [14], which is more costly to undertake.

Several nanoparticles have been used as additives to vegetable oils to investigate their effect on the tribological properties of lubricating oils. The major parameters varied are the size, shape, and concentration of the nanoparticles. Among other nanoparticles investigated, Al_2O_3 nanoparticles, a metal oxide nanoparticle, have the potency of improving the tribological performance of base oils. Also, most nanoparticles investigated are chemically synthesized, and this becomes a subject of interest and consideration when considering potential impacts on the environment on a large scale. Therefore, the investigation of the tribological performance of green synthesized Al_2O_3 nanoparticles as additives to vegetable oils for the development of nano lubricants as alternatives to mineral oil-based lubricants holds considerable potential in eco-friendly lubrication.

2. Materials and methods

The materials used in the study are vegetable oils, aluminum oxide (Al_2O_3) nanoparticles, aluminum nitrate ($Al(NO_3)_3$) salt, beach morning glory (stem) (*Ipomoea pes-caprae*), aluminum SAE 332 disc, low carbon steel disc, and distilled water. The vegetable oils are palm kernel oil (PKO), jatropha oil, and castor oil, and they were all locally sourced off the shelf. The aluminum oxide nanoparticles were synthesized based on the green synthesis method, as summarized in **Figure A1**. The Aqueous Leave Extract (ALE) was produced based on the hot extraction method as presented in **Figure 2**. This involves mixing a milled leaf in distilled water at a ratio 1 g to 20 mL in a beaker and heating the mixture to a temperature range of 60–80 °C for 1 h. The mixture is allowed to cool to room temperature and afterwards filtered using a Whatman-grade 540 filter paper. The ALE was further used in the synthesis of Al_2O_3 nanoparticles using a 0.1 M $Al(NO_3)_3$ solution as a precursor. The extracts were used to synthesize Al_2O_3 nanoparticles within 5 min of extraction. In synthesising the Al_2O_3 nanoparticles, an aqueous solution of 0.1 M $Al(NO_3)_3$ was prepared by dissolving 4.8286 g of the salt into 200 mL of distilled water. The mixture was stirred for 5 min at room temperature using the magnetic stirrer at a stirring speed of 300–320 rpm to ensure proper dissolution of all salt particles in the mixture. Using a ratio of 1:4 for the aqueous solution and plant extract, respectively, the plant extract was poured into the beaker with the stirring bar and placed on the magnetic stirrer. The temperature of the stirrer was set at 60 °C, and the speed was set at 320 rpm. UV-Visible adsorption spectra analysis was conducted to determine the wavelength and absorption of the synthesized mixture using the UV-Vis spectrophotometer. The result of the analysis gave the size distribution of the Al_2O_3 nanoparticles. Synthesized Al_2O_3 nanoparticles were further subjected to drying and calcination in order to obtain dried and powdered nanoparticles. The synthesized mixture was centrifuged at a rotational speed of 8000 rpm to remove excess moisture content and impurities that may be less dense compared to the precipitate using a high-speed refrigerated centrifuge. The resulting mixture was further subjected to freeze drying using a freeze dryer. The freeze dryer removed moisture content and produced the powdered Al_2O_3 nanoparticles. Furthermore, in order to get rid of residual moisture content and impurities, the dried nanoparticles were calcined at a temperature of 700 °C for 1 h using an electric oven.

Figure 2. Plant extraction process.

The characterization of the Al_2O_3 nanoparticles was done based on transmission electron microscopy (TEM) to determine the particle size distribution and morphology of the synthesized Al_2O_3 nanoparticles and X-ray diffraction analysis (XRD) to determine the structure of the synthesized Al_2O_3 nanoparticles. Vegetable oils comprising of palm kernel oil, jatropha oil, and castor oils at 0 wt% concentration of nanoparticles were characterised to serve as control experiments of the vegetable oils before addition of the nanoparticles. The properties examined are dynamic viscosity @24 °C (mPa/s), dynamic viscosity @40 °C, dynamic viscosity @100 °C, kinematic viscosity @40 °C (m^2/s), kinematic viscosity @100 °C, density (g/cm^3), specific gravity, flash point (°C), fire point (°C), pour point (°C), cloud point, smoke point, acid value (KOH/g), saponification (KOH/g), and free fatty acids (FFA). The oils were tested using a rotor labeled "3" at a rotational speed of 60 rpm. To determine the smoke point, flash point, and fire point, a volume of the oil sample was poured into a 5 mL crucible, placed on a heating element, and temperatures were taken at smoke, flash, and fire conditions. Furthermore, cloud and pour points were determined using a freezer with temperatures taken at cloud and pour conditions. The acid value, saponification, and free fatty acid of the oils were determined by the use of 25 mol of methanol that was prepared, and n-hexane was added in a ratio of 1:1.

The study adopted the two-step method in the preparation of the lubricants. The nanoparticles synthesized and characterized were dispersed into the base oil. The base vegetable oils used are palm kernel oil (PKO), jatropha oil (JO), and castor oil (CO). 50 g of nano lubricants were prepared by dispersing dry powder nanoparticles of size 44.73 nm at concentrations of 0.1 wt%, 0.3 wt%, 0.5 wt%, 0.7 wt%, and 1.0 wt% into the vegetable oils as shown in **Table 1**. The mixture was stirred for 10 min at a speed of 300–320 rpm and a stirring temperature of 60–80 °C using a magnetic stirrer. The nanoparticles were weighed using a chemical weighing balance. A total of 18 samples were prepared, including control samples.

Table 1. Mixture ratio for preparation of nano lubricants.

Nanoparticle concentration (g)	PKO (g)	JO (g)	CO (g)
0	50	50	50
0.05	49.95	49.95	49.95
0.15	49.85	49.85	49.85
0.25	49.75	49.75	49.75
0.35	49.65	49.65	49.65
0.5	49.5	49.5	49.5

The concentration was computed using the Equation (1).

$$\text{Mass (wt\%)} = \frac{\text{Mass of solute (NPs)}}{\text{Mass of solution (Oil + NPs)}} \times 100\% \qquad (1)$$

The tribological test for the formulated nano lubricants was done using a ball-on-disc tribometer to determine the coefficient of friction (COF) and wear rate of the nano lubricants formulated. The parameters for the tribological tests used are shown in **Table 2**. A total of 38 metal disc samples of 30 mm diameter each were prepared from aluminum (SAE 332) and low-carbon steel. The samples were cast from the waste piston and engine block. They were further machined into discs of 30 mm diameter, polished, and etched to improve the surface finishing. The chemical composition of aluminum SAE 332 and low-carbon steel discs is presented in **Tables 3** and **4,** respectively.

Table 2. Parameters for the tribological tests.

S/N	Parameter	Value
1	Track radius	5 mm
2	Linear speed	10 cm/s
3	Normal load	8 N
4	Run time	1500 s
5	Linear distance	150 m
6	Acquisition rate	10 Hz
7	Dimension of ball	6 mm
8	Disc diameter	30 mm
9	Temperature	29 ℃
10	Humidity	55%
11	Stop condition	4775 laps

Table 3. Chemical compositions of aluminum SAE 332 disc.

Element	Si	Cu	Mg	Al
% Composition	9.5	3.0	1.0	86.5

Table 4. Chemical compositions of low carbon steel disc.

Element	**C**	**Si**	**Mn**	**P**	**S**	**Cr**	**Mo**	**Ni**	**Cu**	**Co**	**Fe**
% Composition	0.105	0.034	1.450	<0.005	<0.127	0.082	0.005	0.208	0.336	0.023	97.757

To identify the phase of the Al_2O_3 nanoparticle samples, the result of the XRD analysis was compared with the positions and intensities of the already known crystallographic structure of the same material.

In the process of characterization of the vegetable oils, the total quantity of NaOH added to the solution to turn it purple-like was observed as recorded as the titer value. The titer value was substituted into Equation (2) to determine the acid value. Half the acid value is the FFA, as shown in Equation (3). The reverse order of this process is used to determine the saponification value. The value of the density was obtained using a specific gravity bottle. The mass and volume of the oil were obtained, and the density was obtained using Equation (4). In the determination of the coefficient of friction (COF), the value of the COF was computed by the InstrumX software based on the principle of Equation (5). This value was recorded for each test carried out. The scar made on the aluminum SAE 332 and low-carbon steel discs represented the wear track for the determination of the wear rate. The diameter of the outer and inner wear tracks is measured. The difference gives the wear volume, which is used to compute the specific wear rate using Equation (6). The size of the diameter is indicative of the lubricant's ability to resist wear. The efficiencies of the nano lubricants were determined by comparing performance and results obtained for the coefficient of friction and the wear rate with the results obtained for the control samples (i.e., samples of vegetable oils at 0% nanoparticle concentration). Equations (7) and (8) were used to ascertain the efficiency of the prepared and tested nano lubricants for the coefficient of friction and wear rate, respectively.

$$\text{Acid value} = \frac{\text{Titer value } \times \text{Concentration of NaOH} \times \text{Molar mass of NaOH}}{\text{Mass of oil}} \tag{2}$$

$$\text{FFA} = \frac{\text{Acid value}}{2} \tag{3}$$

$$\text{Density} = \frac{\text{Mass}}{\text{Volume}} \tag{4}$$

$$\text{COF} = \frac{T\sqrt{6}}{2Wr} \tag{5}$$

$$\text{Specific wear rate} = \frac{\text{Wear volume}}{\text{Load} \times \text{Sliding distance}} \tag{6}$$

$$\varepsilon_{\text{COF}} = \frac{\text{COF}_{\text{CS}} - \text{COF}_{\text{NL}}}{\text{COF}_{\text{CS}}} \times 100\% \tag{7}$$

$$\varepsilon_{\text{WR}} = \frac{\text{WR}_{\text{CS}} - \text{WR}_{\text{NL}}}{\text{WR}_{\text{CS}}} \times 100\% \tag{8}$$

where: T = Frictional torque (kg/mm); W = Applied load (kg), r = Distance from centre of contact surface on the lower ball to the rotation axis (mm), ε_{CoF} = Efficiency of lubricant for coefficient of friction, ε_{WR} = Efficiency of lubricant for wear rate, COF_{NL} = Coefficient of friction of nano lubricant, COF_{CS} = Coefficient of friction of control sample, WR_{NL} = Wear rate of nano lubricant, WR_{CS} = Wear rate of control sample.

3. Results and discussion

The results of the phytochemical screening of plant extract for green synthesis revealed a high presence of tannins, saponins, flavonoids, glycosides, and alkaloids. This is presented in **Table 5**. (++ imply high presence of phytochemicals in the plant extract.) **Figure 3** shows the one-factor graphs, whose plots indicate the effect of each parameter varied on the size of the synthesized Al_2O_3 nanoparticles. The parameters are volume of plant extract (*A*), volume of aqueous solution (*B*), temperature (*C*), speed (*D*), and time (*E*). The graphs show that only volume of the extract and volume of the solution have significant impact on the particle size.

Table 5. Phytochemical screening of *Ipomoea pes-caprae*.

Plant metabolite	**Extract content**
Tannins	++
Flavonoids	++
Saponins	++
Glycosides	++
Alkaloids	++

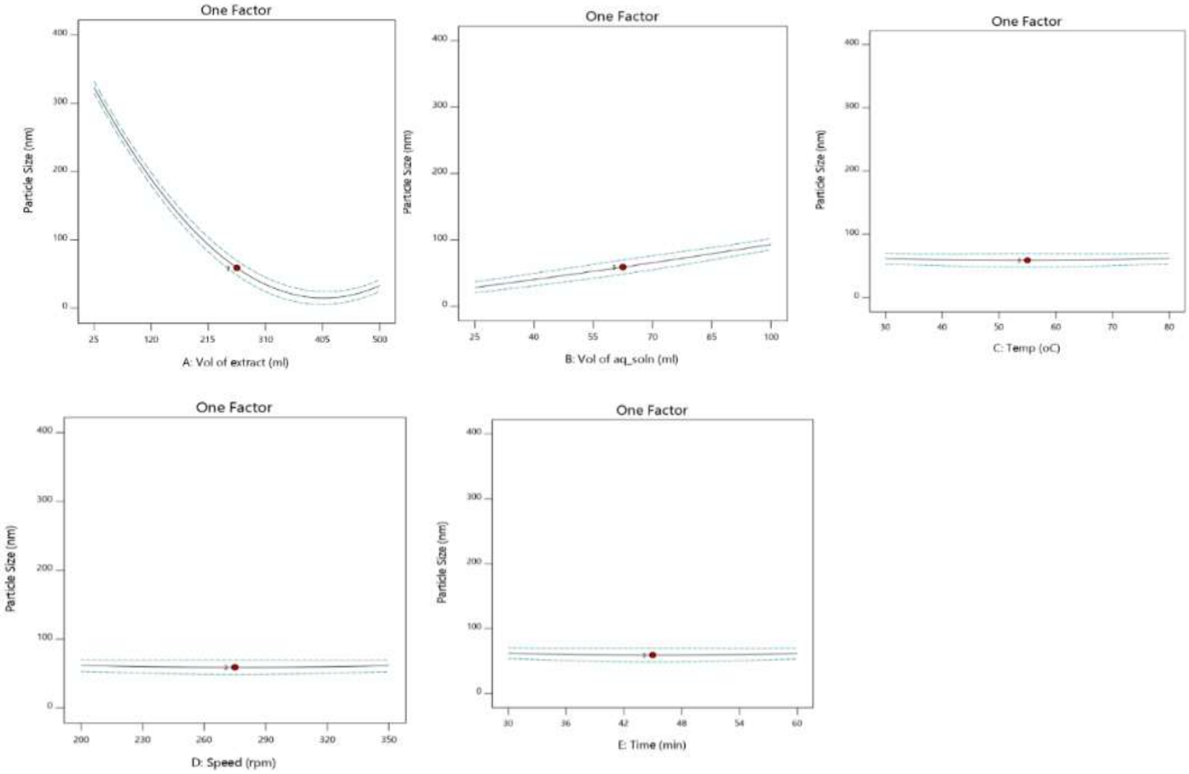

Figure 3. One-factor graphs (A–E).

The result of the UV-Vis analysis is shown in **Figure 4**. A strong and conspicuous absorption peak is observed at 283.00 nm. This confirms the formation of Al_2O_3 nanoparticles in agreement with Selma et al. [15] The result of the nanosizing shows peaks at 9.142 nm, 44.73 nm, and 1210.00 nm corresponding to 10.9% vol, 88.9% vol, and 0.2% vol, respectively, of the synthesized nanoparticles, as shown in **Figure 5**. The result of the nanosizing indicates a close correlation with the predictions from the

DoE using Design Expert software, with the various DoE responses as shown in **Table 6**, which compares the results of the predicted and the actual results of the experiment. The result shows the predicted mean from the DoE to be 44.78 nm, while the experimented mean is 44.73 nm from the nanosizing analysis. A percentage difference of 0.12% was recorded.

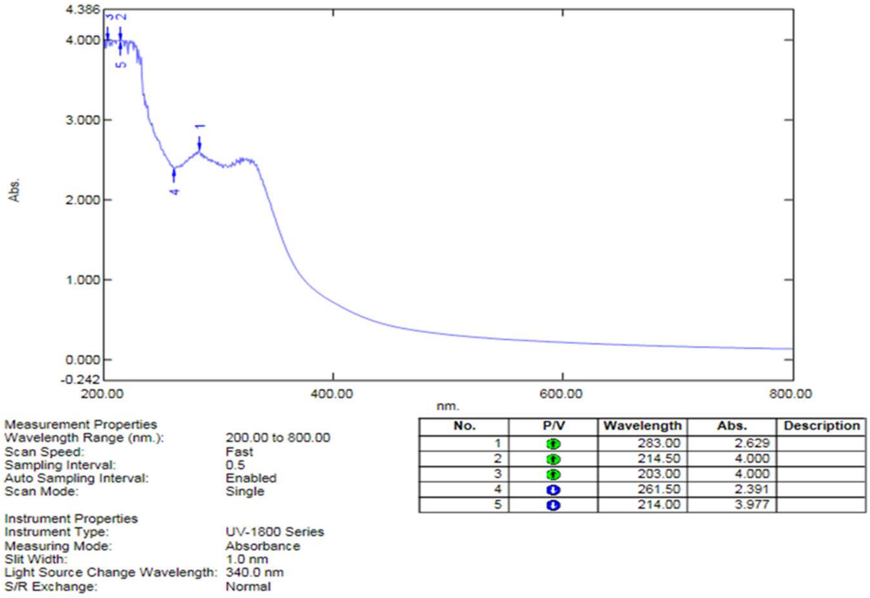

Measurement Properties
Wavelength Range (nm.): 200.00 to 800.00
Scan Speed: Fast
Sampling Interval: 0.5
Auto Sampling Interval: Enabled
Scan Mode: Single

Instrument Properties
Instrument Type: UV-1800 Series
Measuring Mode: Absorbance
Slit Width: 1.0 nm
Light Source Change Wavelength: 340.0 nm
S/R Exchange: Normal

No.	P/V	Wavelength	Abs.	Description
1	●	283.00	2.629	
2	●	214.50	4.000	
3	●	203.00	4.000	
4	●	261.50	2.391	
5	●	214.00	3.977	

Figure 4. UV-Vis analysis of synthesized Al_2O_3 nanoparticles.

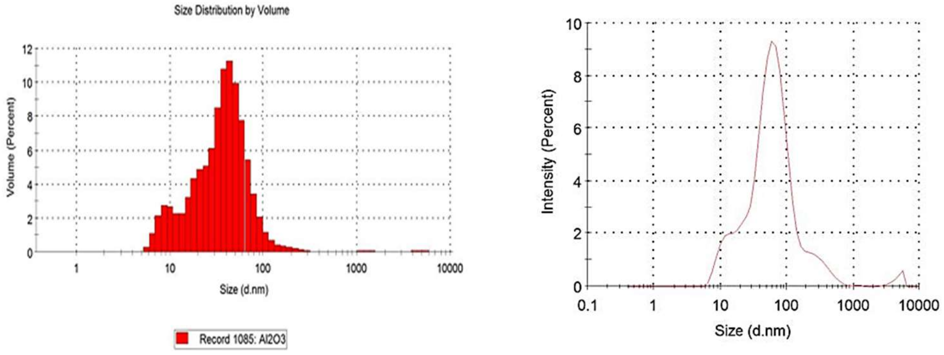

(a) **(b)**

Figure 5. (a) Al_2O_3 nanoparticles size distribution (nanosizing); **(b)** Al_2O_3 nanoparticles size distribution by intensity.

Table 6. Comparison of Predicted and Experimented responses.

Response	Predicted mean	Experimental mean	Difference	% Difference
Particle size	44.784 nm	44.73 nm	0.054	0.12

The characterization of Al_2O_3 nanoparticles through the transmission electron microscopy (TEM) micrographs shows spherically shaped nanoparticles with size distributions of 2 nm as shown in **Figure 6a**, 20 nm in **Figure 6b**, and 50 nm as shown in **Figure 6c**. Furthermore, **Figure 6d** presents the selected area electron diffraction (SEAD), which shows bright continuous diffraction rings, indicating the formation of amorphous Al_2O_3 nanoparticles.

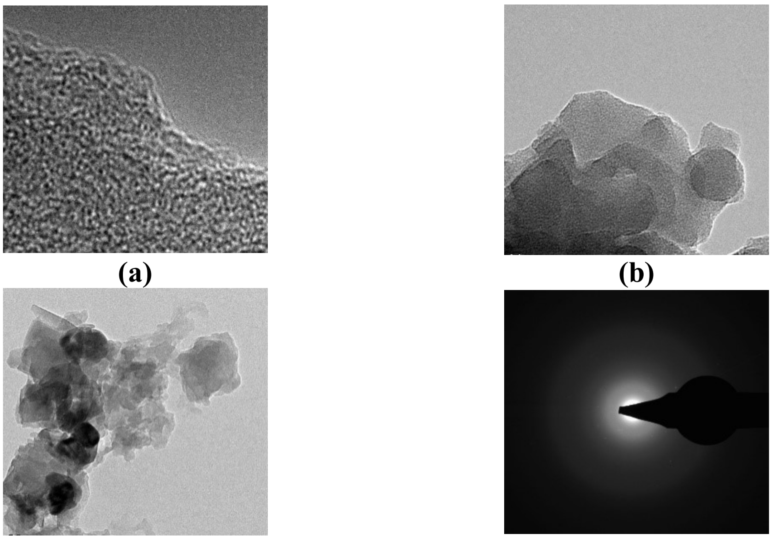

Figure 6. TEM micrographs at **(a)** 2 nm; **(b)** 20 nm; and **(c)** 50 nm; and **(d)** SAED.

Figure 7 shows the X-ray diffraction (XRD) analysis, with observed peaks recorded over a wide range of Bragg angle 2θ ($20° \leq 2\theta \leq 80°$). This confirmed the formation of Al_2O_3 nanoparticles by the transformation of Al to Al_2O_3 using $Al(NO_3)_3$ salt as precursor and *Ipomoea pes-caprae* plant extract as reducing agent. The results of the tribological test for COF of the nano lubricants on low-carbon steel and aluminum SAE 332 discs are presented in **Figures 8–10**. All nano lubricants of castor oil, jatropha oil and PKO have significantly lower COF on aluminum SAE 332 discs compared to PKO without Al_2O_3 nanoparticles. **Figure 8** (L) shows that nano lubricants with 0.5 wt% and 1.0 wt% have significantly lower COF on aluminum SAE 332 discs compared to castor oil without Al_2O_3 nanoparticles.

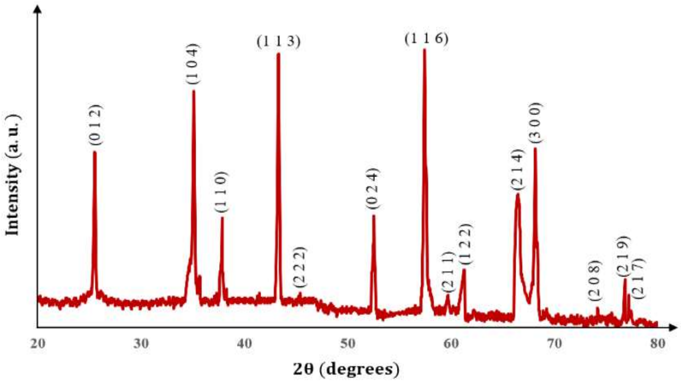

Figure 7. XRD Pattern of Al_2O_3 NPs using *Ipomoea pes-caprae* extract.

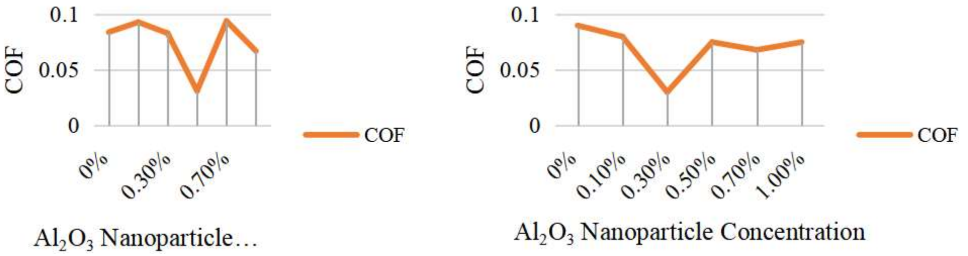

Figure 8. COF of castor oil (L) and jatropha oil (R) on aluminum SAE 332 discs.

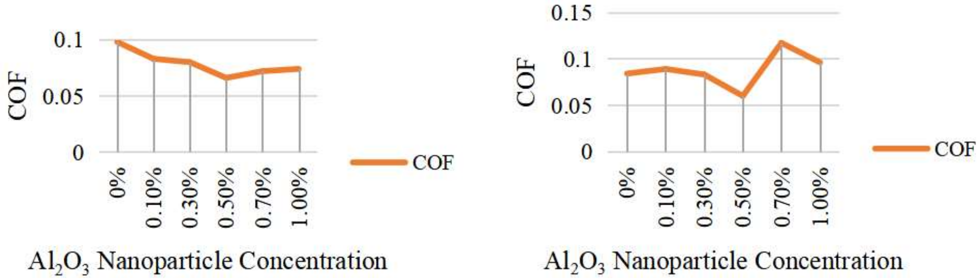

Figure 9. COF of Palm kernel oil on aluminum SAE 332 discs (L) and COF of castor oil on Low carbon steel disc (R).

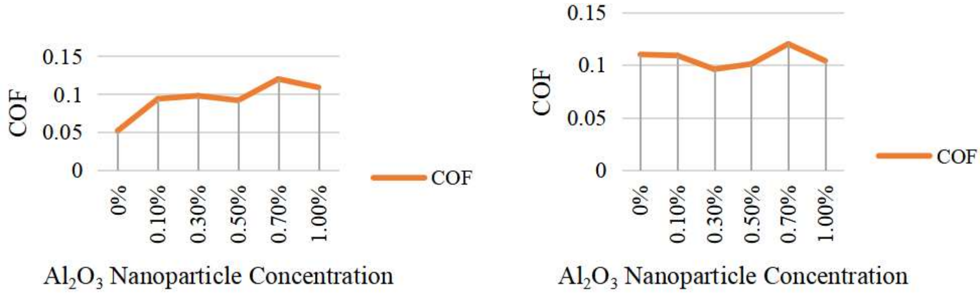

Figure 10. COF of jatropha oil on low carbon steel disc (L) and COF of PKO on low carbon steel disc (R).

Figure 8 (R) shows that nano lubricant with 0.3 wt% Al_2O_3 nanoparticles concentration gave the most desirable result with COF of 0.030 against a COF of 0.090 at 0 wt% concentration.

Figure 9 (L) shows that nano lubricant with 0.5 wt% Al_2O_3 nanoparticles concentration gave the most desirable result with COF of 0.066 against a COF of 0.098 at 0 wt% concentration and **Figure 8** (R) shows a significantly lower COF was observed at 0.5 wt% Al_2O_3 nanoparticles, beyond which the nano lubricant demonstrated higher COF compared to castor oil at 0 wt% Al_2O_3 nanoparticles.

Figure 10 (L) shows that the nano lubricants demonstrated significantly higher COF compared to jatropha oil without Al_2O_3 nanoparticles, making jatropha oil demonstrate better performance in inhibiting friction on low-carbon steel discs compared to samples with Al_2O_3 nanoparticle additives. **Figure 9** (R) shows nano lubricant with 0.3 wt% demonstrated significantly lower COF on low-carbon steel discs compared to castor oil without Al_2O_3 nanoparticles. The results of the tribological test for wear rate of the nano lubricants on low-carbon steel and aluminum SAE 332 discs are presented in **Figures 11–13**.

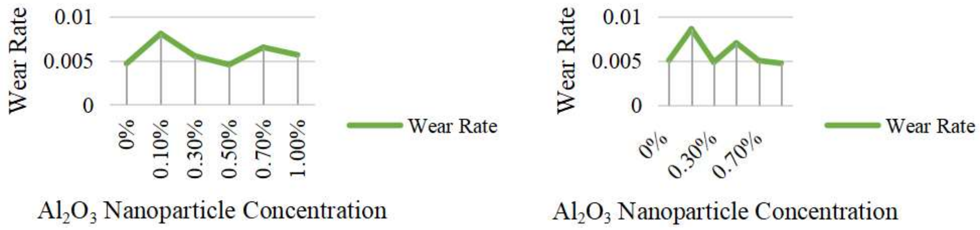

Figure 11. Wear rate of castor oil (L) and jatropha oil (R) on aluminium SAE 332 discs.

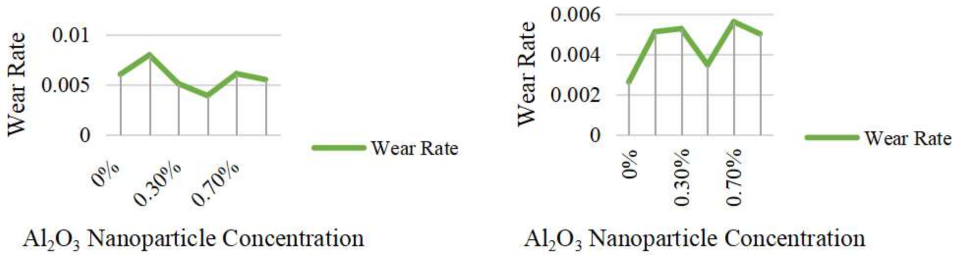

Figure 12. Wear rate of palm kernel oil on aluminium SAE 332 discs (L) and wear rate of castor oil on low carbon disc (R).

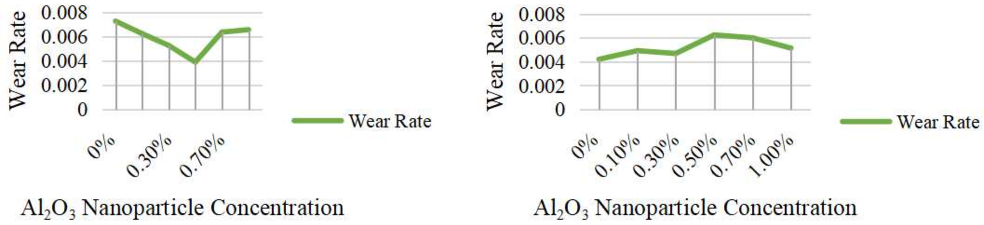

Figure 13. Wear rate of jatropha oil (L) and palm kernel oil (R) on low carbon steel disc.

Figure 11 (L) shows that the nano lubricant with 0.5 wt% demonstrated a slightly lower wear rate on aluminum SAE 332 discs compared to castor oil without Al$_2$O$_3$ nanoparticles. **Figure 11** (R) shows that the addition of Al$_2$O$_3$ nanoparticles at 0.1 wt% and 0.5 wt% concentrations significantly increased the wear rate, and the nano lubricant with 1.0 wt% Al$_2$O$_3$ nanoparticle concentration demonstrated a wear rate of 0.004727 mm^{3}N^{-1}m^{-1}, compared to the wear rate of 0.005064 mm^{3}N^{-1}m^{-1} at 0 wt% concentration.

Figure 12 (L) shows that nano lubricant with a 0.5 wt% Al$_2$O$_3$ nanoparticle concentration gave the most desirable result with a wear rate of 0.003915 mm^{3}N^{-1}m^{-1}, compared to a wear rate of 0.006037 mm^{3}N^{-1}m^{-1} at a 0 wt% concentration. **Figure 12** (R) shows that all nano lubricant formulated demonstrated a higher wear rate compared to castor oil without Al$_2$O$_3$ nanoparticles, with a wear rate of 0.002627 mm^{3}N^{-1}m^{-1}.

Figure 13 (L) shows a steady reduction in wear rate upon addition of Al$_2$O$_3$ nanoparticles to jatropha oil was observed from 0.1 wt% to 0.5 wt%, demonstrating the lowest wear rate. **Figure 13** (R) shows that all nano lubricant formulated demonstrated a higher wear rate compared to castor oil without Al$_2$O$_3$ nanoparticles with a wear rate of 0.004191 mm^{3}N^{-1}m^{-1}. On the efficiency of the base oils and nano lubricants, the efficiency of castor oil, jatropha oil, and PKO with nano lubricants on COF on aluminum SAE 332 discs has the nano lubricant with 0.5 wt% Al$_2$O$_3$ nanoparticles had the highest efficiency with 92.29%, 0.3 wt% Al$_2$O$_3$ nanoparticles recorded the highest efficiency of 92.54% and 0.5 wt% Al$_2$O$_3$ nanoparticles recorded the highest efficiency of 83.58%, respectively. The computation of the efficiency of oils and the nano lubricants with castor oil, jatropha oil, and PKO as base oils on COF using a low-carbon steel disc has the nano lubricant with 0.5 wt% Al$_2$O$_3$ nanoparticles recording the highest efficiency of 87.80%, while jatropha oil without Al$_2$O$_3$ nanoparticle additives recorded the highest efficiency of 89.43%, with the closest nano lubricant recording an efficiency of 81.30 at 0.5 wt% Al_2O_3 nanoparticle concentration and the nano lubricant with 0.3 wt% Al_2O_3 nanoparticles recorded the highest efficiency of 80.49% for PKO. The computation of the efficiency of castor oil, jatropha oil, and PKO and the nano lubricants with the oils as base oils on wear rate using aluminum SAE 332 discs has the nano lubricant with 0.5 wt% Al_2O_3 nanoparticles had the highest efficiency with 76.20% for the castor oil, while the nano lubricant with 1.0 wt% Al_2O_3 nanoparticles recorded the highest efficiency of 75.29% jatropha oil and the nano lubricant with 0.5 wt% Al_2O_3 nanoparticles recorded the highest efficiency of 79.53% for PKO. The computation of the efficiency of the oils and the nano lubricants with castor oil without Al_2O_3 nanoparticle additive recorded the highest efficiency of 64.65%, while jatropha oil with 0.5 wt% Al_2O_3 nanoparticle concentration recorded the highest efficiency of 47.65%, and for PKO, all nano lubricant had lower efficiency compared to PKO without Al_2O_3 nanoparticle additives with an efficiency of 43.61%.

4. Conclusion

Al_2O_3-castor oil nano lubricant significantly reduced COF on aluminum SAE 332 and low-carbon steel from 0.084 without Al_2O_3 nanoparticles to 0.031 and from 0.084 to 0.060 at 0.5 wt%, respectively. Al_2O_3—jatropha nano lubricant reduced COF on aluminum SAE 332 from 0.090 without Al_2O_3 nanoparticles to 0.030 when Al_2O_3 nanoparticles were added at 0.3 wt%. On low-carbon steel, an increase in COF was recorded across all concentrations of Al_2O_3 nanoparticles. Similarly, Al_2O_3—palm kernel oil on aluminum SAE 332 demonstrated a reduction in COF from 0.098 to 0.066 at concentrations of 0.5 wt%. On low-carbon steel, the COF mostly increased. The test for the wear rate of Al_2O_3—castor nano lubricant indicated an increase in wear rate on aluminum SAE 332 and low-carbon steel. Similarly, Al_2O_3—jatropha nano lubricant on aluminum SAE 332 demonstrated an increase in wear rate. However, on low-carbon steel, the wear rate reduced from 0.007265 without Al_2O_3 nanoparticles to 0.003891 at 0.5 wt% Al_2O_3 nanoparticle additives. Al_2O_3—PKO nano lubricant on aluminum SAE 332 demonstrated a reduction in wear rate from 0.006037 without Al_2O_3 nanoparticles to 0.003915 at 0.5 wt% of Al_2O_3 nanoparticles. On low-carbon steel, however, the wear rates increased across all concentrations.

Author contributions: Conceptualization, SYT, TJO and SAL; methodology, SYT, and TJO; software, UGO; validation, JA, IOS and EOO; formal analysis, DIT and AAA; investigation, AS and EAK; resources, SAL; data curation, SAL and UGO; writing—original draft preparation, SYT; writing—review and editing, SAL and UGO; visualization, JA; supervision, SAL and TJO; project administration, SAL; funding acquisition, SYT and SAL. All authors have read and agreed to the published version of the manuscript.

Conflict of interest: The authors declare no conflict of interest.

References

1. Dai W, Kheireddin B, Gao H, et al. Roles of nanoparticles in oil lubrication. Tribology International. 2016; 102: 88-98. doi: 10.1016/j.triboint.2016.05.020

2. Ghaednia H, Hossain MS, Jackson RL. Tribological Performance of Silver Nanoparticle–Enhanced Polyethylene Glycol Lubricants. Tribology Transactions. 2016; 59(4): 585-592. doi: 10.1080/10402004.2015.1092623
3. Hwang Y, Lee JK, Lee JK, et al. Production and dispersion stability of nanoparticles in nanofluids. Powder Technology. 2008; 186(2): 145-153. doi: 10.1016/j.powtec.2007.11.020
4. Mohan D, Pittman CU, Bricka M, et al. Sorption of arsenic, cadmium, and lead by chars produced from fast pyrolysis of wood and bark during bio-oil production. Journal of Colloid and Interface Science. 2007; 310(1): 57-73. doi: 10.1016/j.jcis.2007.01.020
5. Lawal SA, Choudhury IA, Nukman Y. Application of vegetable oil-based metalworking fluids in machining ferrous metals—A review. International Journal of Machine Tools and Manufacture. 2012; 52(1): 1-12. doi: 10.1016/j.ijmachtools.2011.09.003
6. Salimon J, Abdullah BM, Salih N. Saponification of Jatropha curcas Seed Oil: Optimization by D-Optimal Design. International Journal of Chemical Engineering. 2012; 2012: 1-6. doi: 10.1155/2012/574780
7. Mahesar SA, Sherazi STH, Khaskheli AR, et al. Analytical approaches for the assessment of free fatty acids in oils and fats. Anal Methods. 2014; 6(14): 4956-4963. doi: 10.1039/c4ay00344f
8. Jeevanandam J, Barhoum A, Chan YS, et al. Review on nanoparticles and nanostructured materials: history, sources, toxicity and regulations. Beilstein Journal of Nanotechnology. 2018; 9: 1050-1074. doi: 10.3762/bjnano.9.98
9. Griffis C, Wilson T, Schneider J, Pierpont P. Unmanned Aircraft System Propulsion Systems Technology Survey. Available online: https://commons.erau.edu/cgi/viewcontent.cgi?article=1042&context=publication (accessed on 2 January 2024).
10. Trofymov I, Svyryd M, Matveyeva O, Sydorenko O. Influence of electromagnetic treatment of fuels and oils on the formation of wear resistance of friction pairs. In: Selected Aspects of Providing the Chemmotological Reliability of the Engineering. National Aviation University; 2019. pp. 141-153. doi: 10.18372/38236
11. Dai C, Zhang A, Liu M, et al. Hollow Alveolus-Like Nanovesicle Assembly with Metal-Encapsulated Hollow Zeolite Nanocrystals. ACS Nano. 2016; 10(8): 7401-7408. doi: 10.1021/acsnano.6b00888
12. Kart HH, Yildirim H, Ozdemir Kart S, et al. Physical properties of Cu nanoparticles: A molecular dynamics study. Materials Chemistry and Physics. 2014; 147(1-2): 204-212. doi: 10.1016/j.matchemphys.2014.04.030
13. Rastogi A, Zivcak M, Sytar O, et al. Impact of Metal and Metal Oxide Nanoparticles on Plant: A Critical Review. Frontiers in Chemistry. 2017; 5. doi: 10.3389/fchem.2017.00078
14. NadaroĞLu H, Güngör AA, Nce S. Synthesis of Nanoparticles by Green Synthesis Method Synthesis of Nanoparticles by Green Synthesis Method. International Journal of Innovative Research and Reviews. 2017; 1(1): 6-9.
15. Selma MA, Sarya DMA, Wafaa KK. Characterization of Laser Ablated Nanostructured Al_2O_3/p-Solar Cells. Iraqi Journal of Applied Physics. 2015; 11(1): 29-32.

Appendix

Figure A1. Graphical abstract.

Characterization and Application of Nanomaterials 2024, 7(1), 4912.
https://doi.org/10.24294/can.v7i1.4912

Article

Enhancing the thermal properties of paraffin wax as latent heat storage material using hybrid nanomaterials

A. A. El-Sebaii[1], S. Aboul-Enein[1], M. R. I. Ramadan[1], N. Samy[1], A. R. El-Sayed[2], S. M. Shalaby[2,*]

[1] Physics Department, Faculty of Science, Tanta University, Tanta 31511, Egypt
[2] Engineering Physics and Mathematics Department, Faculty of Engineering, Tanta University, Tanta 31511, Egypt
*** Corresponding author:** S. M. Shalaby, saleh.shalaby@f-eng.tanta.edu.eg

CITATION

El-Sebaii AA, Aboul-Enein S, Ramadan MRI, et al. Enhancing the thermal properties of paraffin wax as latent heat storage material using hybrid nanomaterials. Characterization and Application of Nanomaterials. 2024; 7(1): 4912. https://doi.org/10.24294/can.v7i1.4912

ARTICLE INFO

Received: 29 February 2024
Accepted: 25 March 2024
Available online: 18 April 2024

Abstract: Paraffin wax is the most common phase change material (PCM) that has been broadly studied, leading to a reliable optimal for thermal energy storage in solar energy applications. The main advantages of paraffin are its high latent heat of fusion and low melting point that appropriate solar thermal energy application. In addition to its accessibility, ease of use, and ability to be stored at room temperature for extended periods of time, Nevertheless, improving its low thermal conductivity is still a big, noticeable challenge in recently published work. In this work, the effect of adding nano-Cu_2O, nano-Al_2O_3 and hybrid nano-Cu_2O-Al_2O_3 (1:1) at different mass concentrations (1, 3, and 5 wt%) on the thermal characteristics of paraffin wax is investigated. The measured results showed that the peak values of thermal conductivity and diffusivity are achieved at a wight concentration of 3% when nano-Cu_2O and nano-Al_2O_3 are added to paraffin wax with significant superiority for nano-Cu_2O. While both of those thermal properties are negatively affected by increasing the concentration beyond this value. The results also showed the excellence of the proposed hybrid nanoparticles compared to nano-Cu_2O and nano-Al_2O_3 as they achieve the highest values of thermal conductivity and diffusivity at a weight concentration of 5.0 wt%.

Keywords: thermal characteristics; phase change materials; paraffin wax; hybrid nanocomposites

1. Introduction

Paraffin wax (PW) is one of the most important materials used as phase change materials (PCMs) in the thermal energy storage system [1]. A lower thermal conductivity is considered the main disadvantage of PCMs, which causes a lower heat transfer rate during the charging and discharging processes. Many studies have been conducted to overcome this property, such as adding metallic or nonmetallic nanoparticles with high thermal conductivity [2], inserting fins [3], fibrous materials [4], macro-micro and nano-encapsulations [5,6], metal foams [7], carbon nanotubes [8].

The above-mentioned techniques used to improve the thermal conductivity of the PW include the addition of high-conductive nanomaterials, which is the simplest and most practicable technique. The influence of adding nano-graphite (NG) on the PW thermal conductivity was experimentally studied by Li [9]. The results showed that the thermal conductivity of the composite PCMs with 1% and 10% NG is 2.89 times and 7.41 times that of pure paraffin. Nano-Silicon nitride (Si_3N_4) at different mass fractions (1, 2, 3, 4, 5, 10 wt%) was studied by Yang et al. [10] to enhance the thermal properties of PW. They observed an improvement of 35% in thermal conductivity and also found an improvement in thermal diffusivity, reaching 47% at 10 wt% Si_3N_4

additional fraction. Wang et al. [11] experimentally studied the effect of dispersing copper oxide (CuO) as a nanomaterial at different mass fractions of 0.3, 0.6, 0.9, and 1.2% into the PW. They concluded that the thermal conductivity of nanocomposite PCMs with a weight fraction of 1.2% had improved by 24.4%. Pise et al. [12] experimentally evaluated the improvement of thermal performance of PW integrated with nano-alumina (Al_2O_3) particles at various mass concentrations of nanoparticles of 1, 3, and 5%. They reported that the thermal performance of paraffin wax is enhanced up to 14% compared to pure paraffin. Another experimental study concerning the thermophysical properties of Al_2O_3 nanoparticles/paraffin emulsions with two mass fractions of 5 wt% and 10 wt% [13]. The measured results showed that the increase in thermal conductivity is nonlinear with the increase in nanoparticle mass fraction. Yanqi et al. [14] examined how interfacial thermal resistance and particle size affected the thermal conductivity of paraffin/expanded graphite (EG) composites. They found that the increase in thermal conductivity is directly correlated with larger particle sizes. The small EG particles have less of an enhancement in thermal conductivity because interfacial thermal resistance predominates in their impact on the composite thermal conductivity. Sari et al. [15] also examined the paraffin/EG composite material and revealed that the thermal conductivity of the composite increased to 0.82 W/mK at 10 wt% EG. Huang et al. [16] investigated the enhancement of thermal conductivity of paraffin composites using non-equilibrium molecular dynamics simulation. The simulation results indicated that the thermal conductivity of PW is significantly enhanced by adding graphene oxide, which is more efficient than graphene. Maher et al. [17] investigated the effect of the addition of nanosilicon carbide (SiC) and nanosilver (Ag)-based paraffin composites on the thermal characteristics of PCM. The results revealed that the thermal conductivity of the paraffin/SiC composite improved by 58.2%, which is much higher than the thermal conductivity of the paraffin/Ag composite, which improved by 31.2% at the same mass fraction of 15 wt%. Qusay et al. [18] found that the thermal conductivity of the PW is improved by 18.2% when adding 3 wt% of nano-SiC into the PW. The impact of silver nanoparticles on the thermal conductivity of the PW was experimentally studied by Pradeep et al. [19]. Their results showed that thermal conductivity increases with the increase of the mass concentration of Ag nanoparticles. Sahan et al. [20] concluded experimental research evaluating the effect of adding nanomagnetite (Fe_3O_4) on the thermal properties of PW. They found that the thermal conductivity increased by 48% and 67% when adding 10 wt% and 20 wt% nano magnetite, respectively.

According to several studies, PCM could benefit from the addition of two or more hybrid nanoparticles [21–23]. When hybrid nanoparticles are used instead of single nanoparticles, the researchers conclude that the thermal conductivity increases at the same additional mass fraction compared to individual nanoparticles. From this point forward, several practical, numerical, and experimental investigations focus on the use of hybrid nanoparticles. Kumar et al. [24] studied the influence of hybrid nanoparticles containing SiO_2 and CeO_2 nanoparticles on the thermo-physical characteristics of the PW as PCM with various mass fractions (0.5, 1.0, and 2.0 wt%). They observed that the highest paraffin's thermal conductivity (0.298 W/m K) is achieved at 2.0 wt%. Kalbande et al. [25] carried out the addition of CuO and multi-walled carbon nanotubes (MWCNT) hybrid nanoparticles into the PW for thermal energy storage applications. They found that the thermal conductivity of nano-enhanced paraffin wax (PCM) was 6.125% higher than that of pure paraffin wax. Harikrishnan et al. [26] investigated the effect of dispersed hybrid nanoparticles CuO-TiO_2 into PW, which includes several mass concentrations of 0.25%, 0.5%, 0.75%, and 1 wt% to improve its thermal performance. They reported that the optimum studied concentration of hybrid nano-phase change material (HnPCM) is 1.0 wt%, and the improvement of thermal conductivity reaches 46.81% compared to pure paraffin. Ibrahim et al. [27] added nano-TiO_2, nano-MgO, and a 50% mixture of the two kinds into PW at different mass fractions of 0.25%, 0.5%, 0.75%, and 1 wt% to find the maximum thermal storage characteristics of PCM. They observed that the highest enhancement is achieved when adding 1% of the nanoparticles, and the thermal conductivity at this fraction is 4.6%, 3.9%, and 4.6% for nano-TiO_2, nano-MgO, and hybrid nanoparticles, respectively.

In this work, the experimental investigations were conducted thoroughly to analyze the variation of thermo-physical properties of paraffin wax based as PCM under the influence of various weight concentrations (1%, 3%, 5%) of the nanoparticles, namely: Cu_2O and Al_2O_3. It is very important to mention here that Cu_2O nanoparticles are used for the first time, as authors know, to improve the thermal properties of paraffin wax. A thorough investigation into the impact of additional hybrid nanoparticles on the thermo-physical properties of paraffin is also rare in the literature. Therefore, the hybrid nanoparticles were also prepared by mixing equal masses of Cu_2O and Al_2O_3 to study their effect on the thermo-physical characteristics of the PCM. It was found that the hybrid nanoparticles at a mass fraction of 5.0 wt% presented significant potential for enhancing the thermal storage properties of the paraffin wax.

2. Experimental work

In this study, the effect of adding Cu_2O, Al_2O_3 nanoparticles, and hybrid Cu_2O-Al_2O_3 nanoparticles into PW under different mass fraction concentrations (1%, 3%, 5%) on its thermal characteristics has been studied. To determine the accurate weights of pure PW, Cu_2O, Al_2O_3, and hybrids of the two nanoparticles, a digital balance with an accuracy of 0.0001 g was employed. Using a water path, 100 g of pure PW was melted at a melting point of 56 ℃ in order to prepare a specific PW/nanocomposite to obtain paraffin/nano-Cu_2O (NPCM-1), paraffin/nano-Al_2O_3 (NPCM-2) and paraffin/hybrid nano-Cu_2O-Al_2O_3 (1:1) (NPCM-3) as shown in **Table 1**. After the completely melted PW, nano-Cu_2O, nano-Al_2O_3 and hybrid nanoparticles were added to the PW individually under continuous stirring for around 15 min to reduce the precipitation of the droplet's nano-additives into the PW and make the mixture homogenous. These steps were repeated at each of the nano-additives with various mass concentrations (1%, 3%, 5%). All samples are allowed to cool at room temperature and then shaped into a disc shape in the press designed for this process, where all prepared samples of PW, NPCM-1, NPCM-2, and NPCM-3 were impressed at 15 mm diameter and 3 mm thickness, as shown in **Figure 1**. The thermal properties of PW before and after adding the nano-additive materials were measured using the

Hot Disc Transient (Hot Disc TPS 500 S). Repeating the test twice produces more accurate, very flexible, fast, non-destructive, and reliable thermal properties of PW before and after adding the nano-additive materials, including thermal conductivity, thermal diffusivity, and specific heat. The size of the samples must be determined when a suitable disc radius for a particular material has been chosen and the best test times for the disc and material combination are known. Taking into consideration that the nickel spiral sensor 7577 has a has a radius of 2.1 mm with Kapton insulation sandwiched between two sample portions to ensure tight contact with the sensor to minimize the amount of air gap. More details about Al_2O_3 nanoparticle preparation and characterization can be found elsewhere [28]. While Cu_2O nanoparticles are purchased from Qualikems Fine Chem Pvt. Ltd., Vadodara, Gujarat, India.

Table 1. Sample labelling and compositions.

S. No.	Sample label	Composition (wt%)
1	Pure paraffin	100 PW
2	1% NPCM-1	99 PW + 1.0 Nano-Cu_2O
3	3% NPCM-1	97 PW + 3.0 Nano-Cu_2O
4	5% NPCM-1	95 PW + 5.0 Nano-Cu_2O
5	1% NPCM-2	99 PW + 1.0 Nano-Al_2O_3
6	3% NPCM-2	97 PW + 3.0 Nano-Al_2O_3
7	5% NPCM-2	95 paraffin+ 5.0 Nano-Al_2O_3
8	1% NPCM-3	99 PW +0.5 Nano-Cu_2O + 5.0 Nano-Al_2O_3
9	3% NPCM-3	97 PW + 1.5 Nano-Cu_2O + 1.5 Nano-Al_2O_3
10	5% NPCM-3	95 PW + 2.5 Nano-Cu_2O + 2.5 Nano-Al_2O_3

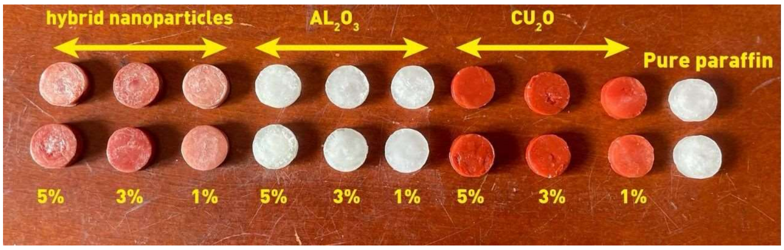

Figure 1. Photograph of the prepared paraffin nanocomposites.

3. Results and discussions

In this section, the measured values of different thermal properties of the prepared samples of pure paraffin and nanocomposites are presented, discussed, and evaluated. The compromise between adding individual or hybrid nanoparticles into the PW is also of great interest in this section.

Figure 2 shows the variation of the thermal conductivity of NPCM-1, NPCM-2, and NPCM-3 with the concentrations. For samples NPCM-1 and NPCM-2, it was observed that the thermal conductivity of samples NPCM-1 and NPCM-2 reaches its peak value of 0.2760 W/m K and 0.2708 W/m K at 3.0% mass fraction of nano-Cu_2O and nano-Al_2O_3, respectively, with an improvement of 10.98% and 9.27% compared to the measured value for pure PW (0.2457 W/mK). But such a tendency is declined at 5.0 wt% for both samples. The improvement of thermal conductivity is calculated as:

$$percentage\ of\ improvement = \frac{k_{nanocomposit}\qquad {}_{pure\,paraffin\,wax}}{k_{nanocomposite}} \times 100,$$

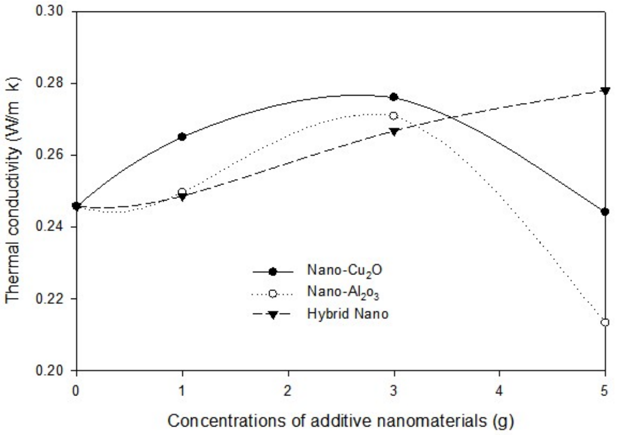

Figure 2. The thermal conductivity of the NEPCMs at different concentrations of 1.0, 3.0 and 5.0 wt%.

The improvement of thermal conductivity of the PW is primarily because these additive nanomaterials have higher thermal conductivity and the combination performance of the nano-additives into the paraffin wax to enable the use of phase-change heat at higher temperatures to enhance the released rate of heat in paraffin. The results of **Figure 2** also show that the thermal conductivity of PW/nano-Cu_2O is higher than that of PW/nano-Al_2O_3 at all studied mass concentrations. While it is higher than those values measured for PW/hybrid nanoparticles except at a mass fraction of 5.0%. This situation of decline happens at higher concentrations (>3%) in NPCM-1 and NPCM-2 samples due to the poor combination between the nano-additives and paraffin, which causes an interfacial thick layer [29], hence augmenting the interface thermal resistance between the paraffin and nano-additives. This layer is unable to contribute to the phase change temperature as phase change does not take place in the interface layer, so it decreases the thermal storage unit volume. Furthermore, the thicker thermal storage layer also diminishes the heat conduction performance of the NEPCMs. The same non-linear trend of thermal conductivity of nano Cu–paraffin composites has been reported by Lin and Al-Kayiem [30]. The results reveal that the increased mass percentage of nanoparticles in the base material may form their repressible agglomeration due to the prevailing cohesive forces, which would account for the diminished slope in the magnitude of thermal conductivity at the upper mass fractions. The phenomenon of an increase and sudden decrease in thermal conductivity of nano-Al_2O_3 was also reported by Arshad et al. [31] due to randomly molecule motion within the disordered microstructure of paraffin in the liquid phase.

The hybrid nano-Cu_2O and nano-Al_2O_3 show different effects as shown in **Figure 2**, where the thermal conductivity increases with incrusting the mass fraction (under the studied values) to reach 0.2780 W/m K at a mass concentration of 5.0% compared to 0.2441 W/mK and 0.2133 W/mK for nano-Cu_2O and nano-Al_2O_3, respectively. This improvement achieved by adding hybrid nanomaterials is considered the best among the studied cases, reaching 11.62% compared to pure paraffin. Keep in mind that this improvement was achieved at a higher concentration (5.0%). The results of **Figure 2** also show that the improvement percentages of the thermal conductivity of paraffin/nano-Cu_2O, paraffin/nano-Al_2O_3 and paraffin/hybrid nanoparticles at 1.0 wt% are 7.28%, 1.56%, and 1.17%, respectively, compared to pure paraffin. While these improvements reached 10.98%, 9.27%, and 7.87%, respectively, at a mass concentration of 3.0% compared to pure paraffin. The results also showed a drop of 0.65% and 13.19% in the thermal conductivity of PW/nano-Cu_2O and PW/nano-Al_2O_3 at 5.0 wt%, respectively. **Figure 2** also shows that the thermal conductivity improvement for PW/nano-Cu_2O is higher by about 5.8% and 1.88% than for PW/nano-Al_2O_3 and PW/hybrid nanoparticles, respectively, at mass fraction 1%, while these percentages increase to 6.19% and 3.37%, respectively, when mass fraction 3.0 wt% is used. On the other hand, the thermal conductivity of PW/hybrid nanoparticles at 5 wt% is higher than the corresponding measured values of PW/nano-Cu_2O and PW/nano-Al_2O_3, which are 12.19% and 23.27%, respectively.

Among the physical properties, thermal diffusivity is considered one of the most important properties because it measures the facility of a material to conduct thermal energy, corresponding to its ability to store thermal energy. Considering the fact that thermal diffusivity has a great significance in thermal management, this property was investigated in the current study, as shown by the results presented in **Figure 3**. This figure shows that the thermal diffusivity of samples NPCM-1 and NPCM-2 reach their maximum values of 0.1595 m^2/s and 0.1252 m^2/s at 3.0% mass fraction of nano-Cu_2O and nano-Al_2O_3, respectively, compared to 0.1130 m^2/s for pure paraffin. So the maximum improvements achieved by adding nano-Cu_2O and nano-Al_2O_3 are 29.15% and 9.74%, respectively, compared to pure paraffin. Accordingly, the thermal conductivity is directly proportional to the thermal diffusivity, so the behavior observed in thermal diffusivity is the same in thermal conductivity. Increasing the mass fraction of nano additives causes an increase in the thermal diffusivity except at concentrations of 5.0 wt% for each of the nano-Cu_2O and nano-Al_2O_3 where the decline occurs, decreasing to 0.1006 and 0.0692 m^2/s, respectively, in comparison to pure paraffin.

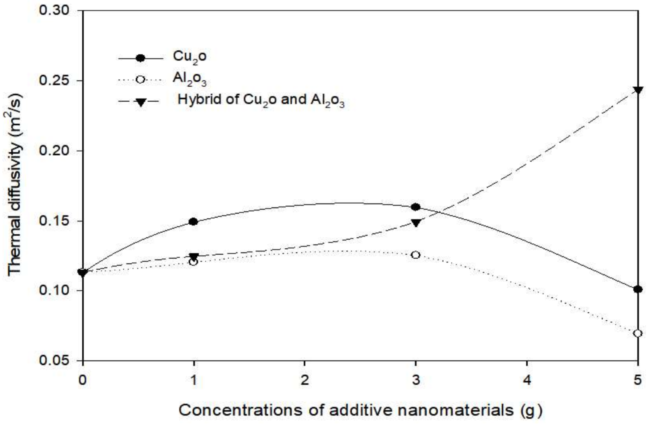

Figure 3. The thermal diffusivity of the NEPCMs at different concentrations of 1.0, 3.0 and 5.0 wt%.

From the results of **Figure 3**, the thermal diffusivity enhanced to 0.1245 m^2/s, 0.1493 m^2/s and 0.2440 m^2/s at 1.0, 3.0, and 5.0 wt%, respectively. In comparison to nano-Al_2O_3 and hybrid nano, the paraffin wax/nano-Cu_2O composite exhibits a percentage improvement of 19.21% and 16.39% at a weight concentration of 1% and 21.50% and 6.39% at a weight concentration of 3%, respectively, as shown in **Figure 3**. However, the hybrid nano has a percentage rise of 58.77% and 71.64% greater than nano-Cu_2O and nano-Al_2O_3 at a weight concentration of 5.0%, respectively. This means that the higher the dispersion of suspended nanoparticles, the higher the thermal diffusivity, which accelerated heat transmission from the top to the bottom of the nanocomposite. The limited dispersion of suspended nanoparticles will affect the value of thermal diffusivity, which will create a reduced heat transfer rate even though the ratio of added nanoparticles is higher. The comparison between the thermophysical properties of all established samples is summarized in **Table 2**.

Table 2. Enhanced thermal properties of the pure paraffin wax.

Samples	Thermal conductivity (W/mk)	Percentage of enhancement (%)	Thermal diffusivity(m^2/s)	Percentage of enhancement (%)
Pure paraffin	0.2457	-	0.1130	-
1% NPCM-1	0.2650	7.28	0.1489	24.11
3% NPCM-1	0.2760	10.98	0.1595	29.15
5% NPCM-1	0.2441	-	0.1006	-
1% NPCM-2	0.2496	1.56	0.1203	6.07
3% NPCM-2	0.2708	9.27	0.1252	9.74
5% NPCM-2	0.2133	-	0.0692	-
1% NPCM-3	0.2486	1.17	0.1245	9.24
3% NPCM-3	0.2667	7.87	0.1493	24.31
5% NPCM-3	0.2780	11.62	0.2440	53.69

The specific heat is the only measured property that decreased with the nano-Cu_2O, nano-Al_2O_3 and hybrid additions into PW as it is inversely proportional to the thermal conductivity and diffusivity as shown in the following equation:

$$\alpha = \frac{k}{\rho c_p} m^2/_{s}.$$

where α and k are thermal diffusivity (m^2/s), and thermal conductivity (W/m k), respectively, ρ is the density (Kg/m^3) and c_p is specific heat (J/m^3k).

The reduction rates as shown in **Figure 4** were 15.52%, 20.88%, 2.31%, and 2.80% for the addition of nano-Cu_2O and nano-Al_2O_3 at concentrations of 1.0 and 3.0 wt%, respectively, in comparison to pure paraffin. According to the decrease in thermal conductivity and also thermal diffusivity for nano-Cu_2O and nano-Al_2O_3 at 5.0 wt%, the specific heat increased to 2.427 J/m^3k, 3.081 J/m^3k, respectively, which equals 2.1739 J/m^3k for pure paraffin. As shown in **Figure 4** the peak reduction percentage is 48.43%, compared to pure paraffin in the case of hybrid nanoparticles at 5.0 wt%. Since the specific heat capacity of nano-Cu_2O is lower than that of nano-Al_2O_3 by about 13.52%, 18.60%, and 21.23% at 1.0, 3.0, and 5.0 wt%, respectively. The same conclusion is revealed by Kok [32]. The author integrated paraffin wax as

PCM with alumina (Al_2O_3) and copper oxide (CuO). His results showed that copper oxide has a lower specific heat capacity than alumina. Also, the influence of the occupied volume variation of nanoparticles immersed into the paraffin was studied by Sushobhan and Kar [33]. Their results agree with the present work since the specific heat of the composites decreased by increasing the volume fraction of nanomaterials through the composite.

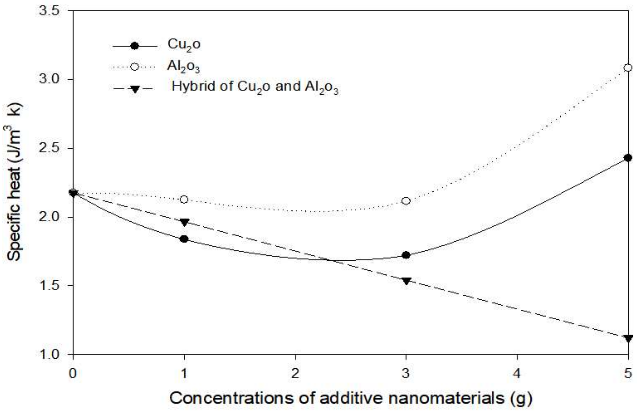

Figure 4. The specific heat of the NEPCMs at different concentrations of 1.0, 3.0 and 5.0 wt%.

From the above results, the hybrid nano-Cu_2O-Al_2O_3 paraffin wax composite at a concentration of 5 wt% is the best among the studied NEPCMs in this work for thermal energy storage systems because it has the highest thermal conductivity and diffusivity. It also has the lowest specific heat, which is considered a good feature in this case as it quickly reaches the melting point.

4. Conclusions

In this study, high-thermal-conductive nano-additives materials were used to prepare NEPCMs by adding different concentrations of Cu_2O, Al_2O_3, and a mixture of the two oxides in a ratio of 1:1 into the paraffin wax. In general, adding high thermally conductive nano-additives increases the thermal conductivity and thermal diffusivity of the paraffin nano-oxide composites while decreasing the specific heat in comparison to pure paraffin. The peak values of thermal conductivity and diffusivity are achieved at a weight concentration of 3.0% when nano-Cu_2O and nano-Al_2O_3 are added to paraffin wax with significant superiority for nano-Cu_2O. While both of those thermal properties are negatively affected by increasing the concentration beyond this value. The results also showed the excellence of the proposed hybrid nanoparticles compared to nano-Cu_2O and nano-Al_2O_3, as they achieved the highest values of thermal conductivity and diffusivity at a weight concentration of 5.0 wt%. It also has the lowest specific heat among the studied samples at a weight concentration of 5.0%. Increasing the weight concentration in the case of hybrid nanoparticles may lead to more improvement in the thermal properties. So, it is strongly recommended for future work to study the proposed hybrid nanoparticles of paraffin wax at higher weight concentrations.

Author contributions: Conceptualization, SMS, AAES and MRIR; methodology, SAE; software, ARES; formal analysis, NS; investigation, NS; data curation, NS; writing—original draft preparation, NS; writing—review and editing, SMS; visualization, ARES; supervision, AAES, SAE, MRIR, SMS; project administration, AAES. All authors have read and agreed to the published version of the manuscript.

Acknowledgments: This paper is based upon work supported by Science, Technology and Innovation Funding Authority (STIFA), Capacity building project, Code: 42922.

Conflict of interest: The authors declare no conflict of interest.

References

1. He B, Setterwall F. Technical grade paraffin waxes as phase change materials for cool thermal storage and cool storage systems capital cost estimation. Energy Conversion and Management. 2002; 43(13): 1709-1723.
2. Wang J, Xie H, Xin Z, et al. Enhancing thermal conductivity of palmitic acid based phase change materials with carbon nanotubes as fillers. Solar Energy. 2010; 84(2): 339-344. doi: 10.1016/j.solener.2009.12.004
3. Shi S, Niu J, Wu Z, et al. Experimental and numerical investigation on heat transfer enhancement of vertical triplex tube heat exchanger with fractal fins for latent thermal energy storage. International Journal of Heat and Mass Transfer. 2022; 198: 123386. doi: 10.1016/j.ijheatmasstransfer.2022.123386
4. Fukai J, Hamada Y, Morozumi Y, Miyatake O. Improvement of thermal characteristics of latent heat thermal energy storage units using carbon-fiber brushes: Experiments and modeling. International Journal of Heat and Mass Transfer. 2003; 46(23): 4513-4525.
5. Ahmed F, Mahmood M, Waqas A, et al. Thermal analysis of macro-encapsulated phase change material coupled with domestic gas heater for building heating. Sustainable Energy Technologies and Assessments. 2021; 47: 101533. doi: 10.1016/j.seta.2021.101533
6. Rehman OA, Palomba V, Verez D, et al. Experimental evaluation of different macro-encapsulation designs for PCM storages for cooling applications. Journal of Energy Storage. 2023; 74: 109359. doi: 10.1016/j.est.2023.109359
7. Wang Z, Zhang H, Dou B, et al. Effect of copper metal foam proportion on heat transfer enhancement in the melting process of phase change materials. Applied Thermal Engineering. 2022; 201: 117778. doi: 10.1016/j.applthermaleng.2021.117778
8. Leong KY, Hasbi S, Ku Ahmad KZ, et al. Thermal properties evaluation of paraffin wax enhanced with carbon nanotubes as latent heat thermal energy storage. Journal of Energy Storage. 2022; 52: 105027. doi: 10.1016/j.est.2022.105027
9. Summers EK, Lienhard JH. Experimental study of thermal performance in air gap membrane distillation systems, including the direct solar heating of membranes. Desalination. 2013; 330: 100-111. doi: 10.1016/j.desal.2013.09.023
10. Yang Y, Luo J, Song G, et al. The experimental exploration of nano-Si_3N_4/paraffin on thermal behavior of phase change materials. Thermochimica Acta. 2014; 597: 101-106. doi: 10.1016/j.tca.2014.10.014
11. Wang J, Li Y, Wang Y, et al. Experimental investigation of heat transfer performance of a heat pipe combined with thermal energy storage materials of CuO-paraffin nanocomposites. Solar Energy. 2020; 211: 928-937. doi: 10.1016/j.solener.2020.10.033
12. Pise AT, Waghmare AV, Talandage VG. Heat Transfer Enhancement by Using Nanomaterial in Phase Change Material for Latent Heat Thermal Energy Storage System. Asian Journal of Engineering and Applied Technology. 2013; 2(2): 52-57. doi: 10.51983/ajeat-2013.2.2.667
13. Ho CJ, Gao JY. Preparation and thermophysical properties of nanoparticle-in-paraffin emulsion as phase change material. International Communications in Heat and Mass Transfer. 2009; 36(5): 467-470. doi: 10.1016/j.icheatmasstransfer.2009.01.015
14. Zhao Y, Jin L, Zou B, et al. Expanded graphite – Paraffin composite phase change materials: Effect of particle size on the composite structure and properties. Applied Thermal Engineering. 2020; 171: 115015. doi: 10.1016/j.applthermaleng.2020.115015
15. Sarı A, Karaipekli A. Thermal conductivity and latent heat thermal energy storage characteristics of paraffin/expanded graphite composite as phase change material. Applied Thermal Engineering. 2007; 27(8-9): 1271-1277. doi: 10.1016/j.applthermaleng.2006.11.004

16. Huang YR, Chuang PH, Chen CL. Molecular-dynamics calculation of the thermal conduction in phase change materials of graphene paraffin nanocomposites. International Journal of Heat and Mass Transfer. 2015; 91: 45-51. doi: 10.1016/j.ijheatmasstransfer.2015.07.110
17. Maher H, Rocky KA, Bassiouny R, et al. Synthesis and thermal characterization of paraffin-based nanocomposites for thermal energy storage applications. Thermal Science and Engineering Progress. 2021; 22: 100797. doi: 10.1016/j.tsep.2020.100797
18. Jawad QA, Mahdy AMJ, Khuder AH, et al. Improve the performance of a solar air heater by adding aluminum chip, paraffin wax, and nano-SiC. Case Studies in Thermal Engineering. 2020; 19: 100622. doi: 10.1016/j.csite.2020.100622
19. Pradeep N, Paramasivam K, Rajesh T, et al. Silver nanoparticles for enhanced thermal energy storage of phase change materials. Materials Today: Proceedings. 2021; 45: 607-611. doi: 10.1016/j.matpr.2020.02.671
20. Şahan N, Fois M, Paksoy H. Improving thermal conductivity phase change materials—A study of paraffin nanomagnetite composites. Solar Energy Materials and Solar Cells. 2015; 137: 61-67. doi: 10.1016/j.solmat.2015.01.027
21. Mhedheb T, Hassen W, Mhimid A, et al. Parametric analysis of a solar parabolic trough collector integrated with hybrid-nano PCM storage tank. Case Studies in Thermal Engineering. 2023; 51: 103652. doi: 10.1016/j.csite.2023.103652
22. Hayat MA, Yang Y, Li L, et al. Preparation and thermophysical characterisation analysis of potential nano-phase transition materials for thermal energy storage applications. Journal of Molecular Liquids. 2023; 376: 121464. doi: 10.1016/j.molliq.2023.121464
23. Manoj Kumar P, Mylsamy K, Alagar K, et al. Investigations on an evacuated tube solar water heater using hybrid-nano based organic phase change material. International Journal of Green Energy. 2020; 17(13): 872-883. doi: 10.1080/15435075.2020.1809426
24. Pasupathi MK, Alagar K, P MJS, et al. Characterization of Hybrid-nano/Paraffin Organic Phase Change Material for Thermal Energy Storage Applications in Solar Thermal Systems. Energies. 2020; 13(19): 5079. doi: 10.3390/en13195079
25. Kalbande VP, Fating G, Mohan M, et al. Experimental and theoretical study for suitability of hybrid nano enhanced phase change material for thermal energy storage applications. Journal of Energy Storage. 2022; 51: 104431. doi: 10.1016/j.est.2022.104431
26. Harikrishnan S, Deepak K, Kalaiselvam S. Thermal energy storage behavior of composite using hybrid nanomaterials as PCM for solar heating systems. Journal of Thermal Analysis and Calorimetry. 2013; 115(2): 1563-1571. doi: 10.1007/s10973-013-3472-x
27. Ibrahim SI, Ali AH, Hafidh SA, et al. Stability and thermal conductivity of different nano-composite material prepared for thermal energy storage applications. South African Journal of Chemical Engineering. 2022; 39: 72-89. doi: 10.1016/j.sajce.2021.11.010
28. Abosheiasha HF, Mansour DEA, Darwish MA, et al. Synthesis and investigation of structural, thermal, magnetic, and dielectric properties of multifunctional epoxy/$Li_{0.5}Al_{0.35}Fe_{2.15}O_4/Al_2O_3$ nanocomposites. Journal of Materials Research and Technology. 2022; 16: 1526-1546. doi: 10.1016/j.jmrt.2021.11.149
29. Mahian O, Kolsi L, Amani M, et al. Recent advances in modeling and simulation of nanofluid flows-Part I: Fundamentals and theory. Physics Reports. 2019; 790: 1-48. doi: 10.1016/j.physrep.2018.11.004
30. Lin SC, Al-Kayiem HH. Evaluation of copper nanoparticles – Paraffin wax compositions for solar thermal energy storage. Solar Energy. 2016; 132: 267-278. doi: 10.1016/j.solener.2016.03.004
31. Arshad A, Jabbal M, Yan Y. Thermophysical characteristics and application of metallic-oxide based mono and hybrid nanocomposite phase change materials for thermal management systems. Applied Thermal Engineering. 2020; 181: 115999. doi: 10.1016/j.applthermaleng.2020.115999
32. Kok B. Examining effects of special heat transfer fins designed for the melting process of PCM and Nano-PCM. Applied Thermal Engineering. 2020; 170: 114989. doi: 10.1016/j.applthermaleng.2020.114989
33. Sushobhan BR, Kar SP. Thermal Modeling of Melting of Nano based Phase Change Material for Improvement of Thermal Energy Storage. Energy Procedia. 2017; 109: 385-392. doi: 10.1016/j.egypro.2017.03.035

Characterization and Application of Nanomaterials 2024, 7(1), 5300.
https://doi.org/10.24294/can.v7i1.5300

Article

Synthesis, characterization and analytical prospects of cellulose-derived nanoparticles of Ferric-oxide (Fe_2O_3/cellulose) and Copper-oxide (CuO_x)

Sana Ullah Khan[1], Ali Khan[2], Amir Hassan[3,*], Beena Abbas[3]

[1] Department of Chemistry, Government Post Graduate College, Mardan 23200, Pakistan
[2] Department of Chemical and Materials Engineering, Chang Gung University, Taoyuan 333, Taiwan
[3] Faculty of Natural Sciences, Novosibirsk State University (NSU), 630090 Novosibirsk, Russia
*** Corresponding author:** Amir Hassan, amirhassan741@gmail.com, a.khassan1@g.nsu.ru

CITATION

Khan SU, Khan A, Hassan A, Abbas B. Synthesis, characterization and analytical prospects of cellulose-derived nanoparticles of Ferric-oxide (Fe_2O_3/cellulose) and Copper-oxide (CuO_x). Characterization and Application of Nanomaterials. 2024; 7(1): 5300. https://doi.org/10.24294/can.v7i1.5300

ARTICLE INFO

Received: 18 March 2024
Accepted: 29 April 2024
Available online: 29 May 2024

Abstract: Our environment has been significantly impacted by man-made pollutants, primarily due to industries making substantial use of synthetic chemicals, resulting in significant environmental consequences. In this research investigation, the co-precipitation approach was employed for the synthesis of cellulose-based ferric oxide (Fe_2O_3/cellulose) and copper oxide nanoparticles (CuO_x-NPs). Scanning electron microscopy (SEM) analyses were conducted to determine the properties of the newly synthesised nanoparticles. Furthermore, the synthesized nanoparticles were employed for eliminating chromium from aqueous media under various conditions, including temperature, contact time, adsorbent concentration, adsorbate concentration, and pH. Additionally, the synthesised materials were used to recover Cr(VI) ions from real samples, including tap water, seawater, and industrial water, and the adsorptive capacity of both materials was evaluated under optimal conditions. The synthesis of Fe_2O_3/cellulose and CuO_x-NPs proved to be effective, as indicated by the outcomes of the study.

Keywords: nanocomposites; cellulose-derived NPs; (Fe_2O_3/cellulose); (CuO_x-NPs) and SEM

1. Introduction

Heavy metal ions, which are transported into aquatic environments via industrial effluents, affect aquatic life. They are harmful because of their hazardous bio-accumulative nature. One of the most hazardous heavy metal contaminants is chromium Cr(VI), which has been utilized extensively and on a massive scale in a number of sectors, including metal cleaning, dyes, leather, textiles, and plating. Cr(VI) is a transition metal, steel-gray, lustrous, stiff, and having a brittle appearance [1–4]. Cr(VI) has a high degree of oxidation resistance even at high temperatures. Cr(VI) is exceedingly poisonous and carcinogenic; therefore, its excess presence in food, water, or the environment may seriously harm the biota. For this reason, several environmental protection agencies have established a chromium limit that is acceptable as long as no acute or long-term effects on human health have been documented. According to the World Health Organization (WHO 1958), 0.05 mg/L of chromium is the maximum level that should be present in water. The Maximum Contaminant Limit (MCL) and Maximum Contaminant Limit Goal (MCLG) for chromium in water were both set at 0.1 parts per million (ppm) by the United States Environmental and Protection Agency (US EPA) in 2012 (100 ppb). The Maximum Contaminant Limit (MCL) for chromium in drinking water is 0.05 mg/L, according to a 2013 report from the California Department of Public Health. The public health objective for Cr(VI) is 0.02 ppb; however, the maximum contamination level is established at 10 ppb [4,5]. The quick removal of Cr(VI) ions from contaminated water has been focused on for the last few decades, and numerous techniques have been utilized, such as electrochemical deposition, ion exchange, adsorption, biological methods, and membrane separation. Adsorption separation is the fastest, most practical, and least expensive method for the quick removal of harmful pollutants. The adsorptive removal of Cr(VI) ions from wastewater has occasionally been accomplished using a variety of adsorbents, including zeolite, activated carbon, metal oxides, waste industrial material, and nano-composites, etc. For the quick removal of heavy Cr(VI) ions, a variety of metal oxide nanostructures have been employed, including cellulose-based iron oxide nanoparticle composites, titanium oxides, aluminum oxides, and copper oxides [6,7].

In the present research investigations, synthesised Fe_2O_3/Cellulose nano-composites and CuO_x-NPs are being characterised and used for the direct removal of Cr(VI) ions from an aqueous environment. Additionally, the adsorption properties of these adsorbents are being compared. The results obtained suggest that the synthesised Fe_2O_3/cellulose and CuO_x-NPs are useful for adsorption and can potentially be used multiple times without losing their effectiveness.

2. Materials and methods

2.1. Materials

The used papers served as a source of cellulose and were purchased from the local market. All of the reagents utilised in the experiment were of analytical grade. Iron(III) oxide, sodium hydroxide, copper chloride, copper nitrates, and urea were acquired from the commercial supplier Sigma-Aldrich.

2.2. Synthesis of Fe_2O_3/cellulose nanocomposite

Synthesis of Fe_2O_3/cellulose using the precipitation method involves a two-stage process. During the initial phase, previously utilised copy paper was fragmented into smaller segments, subjected to three rounds of washing with distilled water, and afterwards immersed in a solution containing 40% H_2SO_4. The mixture was subjected to filtration and afterwards washed four times with distilled water. Following this, the mixture was dried in an oven maintained at a temperature of 50 ℃. In addition, a quantity of 3.3 g of dried material was introduced into a solution containing NaOH, thiourea, and urea at a temperature of 261.15 Kelvin. The solution was then stirred for a duration of 25 min in an environment saturated with nitrogen [8]. During the second stage of the experiment, a solution containing 15 mL of $Fe_2Cl_3.6H_2O$ (weighing 13.51 g) and $FeCl_2.4H_2O$ (weighing 4.97 g) was prepared. This solution was then added drop by drop to the cellulose solution and vigorously stirred for a duration of 180 min at room temperature. The composite material that was synthesised underwent a filtration process, followed by rinsing with distilled water, ethanol, and acetone. The synthesised substances were further dried in an oven at a temperature of 323.15 K and thereafter stored.

2.3. Synthesis of CuO_x-NPs

Copper oxide nanoparticles (CuO_x-NPs) were synthesised utilising the precipitation method, employing copper chloride ($CuCl_2$) and copper nitrate ($Cu(NO_3)_2.3H_2O$) as precursor materials. To initiate the experiment, every precursor was initially dissolved in 100 millilitres of distilled water to achieve a concentration of 0.1 M. Subsequently, a 0.1 M NaOH solution was gradually introduced into the mixture under constant stirring until the pH level reached 14, resulting in the formation of black precipitates indicative of the presence of N_2 gas. The black precipitate was collected and later subjected to washing procedures until the pH was adjusted to 7.0. Distilled water was used initially, followed by a wash with 100% ethanol. The yields were thereafter subjected to a drying process at a temperature of 80 °C for a duration of 16 h, as indicated in references [9,10]. Subsequently, the synthesised materials passed through a calcination process at a temperature of 500 ℃ for a duration of 4 h.

2.4. Characterization and batch adsorption study

The synthesised materials, which are Fe_2O_3/Cellulose and CuO_x-NPs, were subjected to comprehensive characterization using essential analytical techniques. In order to determine the characteristics of the freshly synthesised nanoparticles, the morphological and elemental analyses were investigated through the JSM-IT800 Schottky Field Emission Scanning Electron Microscope, JEOL Ltd. Investigation involved the utilisation of synthesised materials for the purpose of conducting an adsorption study. To establish the standard stock solution of chromium (VI) ions with a concentration of 500 parts per million (ppm), a mass of 0.5 g of chromium was solubilized in 1000 mL of distilled water. The initial concentrated solution was subjected to additional dilution in order to attain the desired concentrations, employing the dilution formula denoted as $C_1V_1 = C_2V_2$. A solution was prepared and supplemented with 0.1 g of copper oxide nanoparticles (CuO-NPs) and iron (III) oxide (Fe_2O_3) composite. The specimen underwent agitation for approximately 30 minutes within a water bath shaker. Subsequently, the sample was subjected to filtration in order to isolate any remaining Cr(VI) species. The quantification of Cr(VI) was accomplished using Atomic Absorption Spectroscopy (AAS) through the application of Equation (1).

$$q_e\left(\frac{mg}{g}\right) = \frac{C_o - C_e}{W} \times V \tag{1}$$

Initial and equilibrium concentrations of chromium (VI) metal, denoted as C_o and C_e ($mg.L^{-1}$) respectively, are of interest in this context. Additionally, the quantity of chromium (VI) adsorbed at equilibrium, represented as qe (mg/g), and the volume of the solution, denoted as V (mL), are also relevant parameters. The influence of different parameters on the adsorption process was investigated, encompassing temperature, initial concentration, contact time, ionic strength, and pH. The identical methodology was also employed to explore the efficacious elimination of hexavalent chromium (Cr(VI)) from a true sample.

3. Results and discussion

3.1. Characterization

The synthesis of Fe_2O_3/Cellulose and CuO-NPs was achieved using the co-precipitation method, and the SEM analysis conclusively validates the successful synthesis of these nanomaterials, as shown in **Figure 1**. SEM analysis reveals a densely packed surface with Cr(VI) ions attached to the adsorbent materials. This observation corresponds to favorable electrostatic interactions and efficient metal adsorption in the acidic environment due to the presence of elevated hydronium ions (H+). Conversely, under extremely acidic conditions, SEM images show a weakened and less stable adsorbent surface due to surface oxidation processes. This phenomenon aligns with the decrease in metal adsorption observed in these conditions. This shift adversely affects the attachment of chromium oxyanions to the adsorbent surface. The SEM analysis also suggests that at higher pH levels, the presence of an increased concentration of hydroxyl groups (OH−) in the solution leads to repulsion between chromium oxyanions and OH− ions, reducing the availability of adsorption sites and competition for these sites.

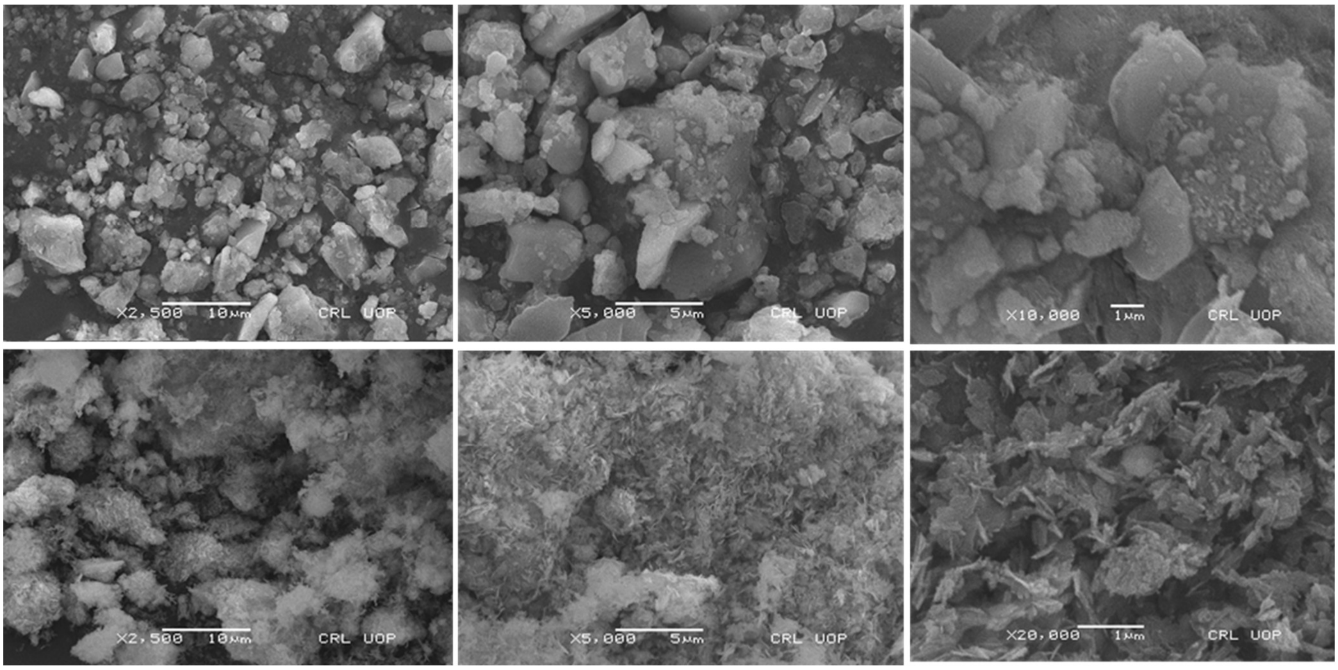

Figure 1. SEM analyses of CuO_x nanoparticles (I-III) and FeO_x nanoparticles (IV-VII).

3.2. Effect of pH adsorption and contact time

The adsorption behavior of Cr(VI) ions onto the surfaces of Fe_2O_3/cellulose and CuO_x nanoparticles (NPs) was investigated across a pH range spanning from 2.0 to 10.0, utilizing a fixed concentration of 300 mg/L. The experimental outcomes are presented graphically in **Figure 2a**. The adsorption of Cr(VI) ions on Fe_2O_3/cellulose and CuO_x-NPs displays a significant dependency on pH. Maximum adsorption of Cr(VI) ions was observed at pH values of 2.0 and 4.0. This phenomenon can be attributed to the elevated concentrations of hydronium ions (H+) present on the adsorbent surface within an acidic environment, thereby intensifying the electrostatic interactions between the negatively charged chromium ions and the protonated sorbent.

This enhanced interaction enhances the efficiency of metal adsorption. However, it should be noted that the adsorbent surface experiences a weakening and loss of stability under extremely acidic conditions, primarily due to surface oxidation processes, which in turn diminishes the capacity for metal adsorption. These observations are consistent with the fact that CuO_x nanoparticles possess a nearly neutral point of zero charge, around 6.9. Consequently, as the pH level rises from its optimal value (pH 3.5) towards the alkaline range, the degree of protonation of the CuO_x nanoparticles surface gradually decreases. Beyond this point, the surface acquires a net negative charge, rendering it less favorable for the attachment of chromium oxyanions. Moreover, at higher pH levels, the concentration of hydroxyl groups (OH^-) in the solution increases, leading to repulsion between chromium oxyanions and OH^- ions, resulting in competition for the limited available adsorption sites. This competition reduces the removal efficiency of Cr(VI) ions from the solution [11,12].

To establish the optimal experimental conditions for the adsorption of Cr(VI) ions onto CuO_x nanoparticles (CuO_x-NPs) and Fe_2O_3/cellulose composites, we conducted contact time experiments. The findings demonstrated that equilibrium for Cr(VI) ion adsorption on CuO_x-NPs was attained after 120 min, while equilibrium for adsorption on Fe_2O_3/cellulose was reached within 60 min, as illustrated in **Figure 2b**. Initially, the rapid adsorption of Cr(VI) ions was facilitated by the abundance of unoccupied binding sites on the surfaces of CuO_x-NPs and Fe_2O_3/cellulose composites, coupled with a substantial concentration gradient between the adsorbate and the solid phase of the synthesized materials. However, with prolonged contact time, the number of available active sites for adsorption diminished, and there was an increase in repulsive forces between the ions that had already adsorbed onto the adsorbent surface and those still in the solution. Consequently, the adsorption of Cr(VI) ions proceeded more slowly as the system approached equilibrium due to ion competition for the limited accessible binding sites [13,14].

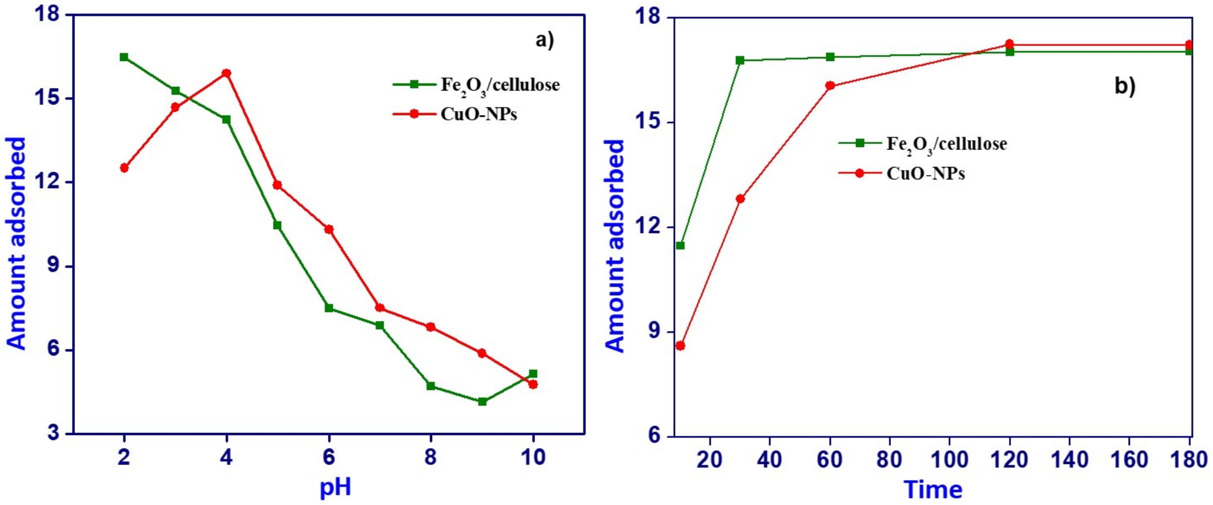

Figure 2. (a) Influence of pH on Cr adsorption; and **(b)** Impact of Contact Time on Cr adsorption using Fe_2O_3/cellulose and CuO-NPs.

3.3. Effect of adsorbent dosage and adsorbate concentration

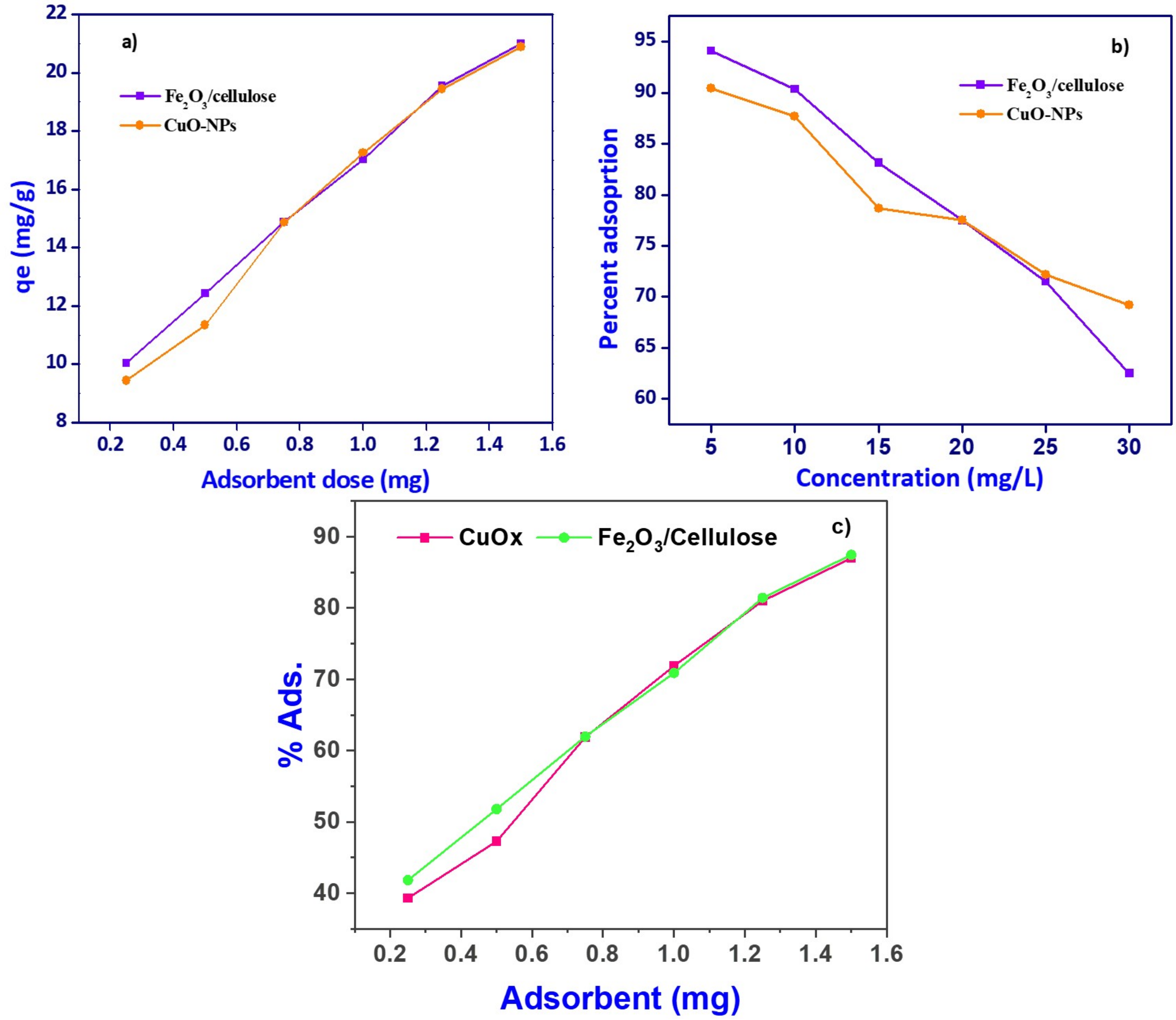

Figure 3. (a) Influence of adsorbent on Cr adsorption; and **(b)** effect of adsorbate concentration on Cr adsorption; **(c)** dose dependent adsorbent removal efficiency, using Fe_2O_3/cellulose and CuO_x-NPs.

Table 1. Various adsorbent utilized for Cr(VI) adsorption.

S. No	Adsorbent type	Q_{max} (mg/g)	Percent, %	Reference
1	N77 cation exchange resins	35.38 mg/g	95	[15]
2	SKN1 cation exchange resins	46.34 mg/g	95	[15]
3	carbon aerogel electrodes	-	94.69	[16]
4	C1 activated carbon	-	98.86	[17]
5	C2 activated carbon	-	98.6	[17]
6	C3 activated carbon	-	93	[17]
7	Al electrodes	-	97.76	[18]
8	Chemical Precipitation Method	-	99.74	[18]
9	Eucalyptus bark (EB)	-	99	[19]
10	Cation exchange resins 1200H	84.04 mg/g	-	[20]
11	Cation exchange resins 1500H	188.67 mg/g	-	[20]
12	Cation exchange resins IRN97H	58.14 mg/g	-	[20]

Table 1. (*Continued*).

S. No	Adsorbent type	Q_{max} (mg/g)	Percent, %	Reference
13	Dried green alga U. Lactuca	8.91 mg/g	52.54	[21]
14	Activated carbon	93.92 mg/g	99.52	[21]
15	Activated carbon	28.019 mg/g	-	[22]
16	Electrochemical method	-	86.45	[23]
17	Amidoxime adsorb	31.68 mg/g	-	[24]

We conducted an investigation into the effect of adsorbent dosage, with the results presented in **Figures 3a** and **3c**. Upon increasing the adsorbent dose, the removal of Cr(VI) ions exhibited a sharp rise, increasing from 50% to 74.08% for Fe_2O_3/cellulose and from 41% to 78% for CuO_x-NPs when initial Cr(VI) ion concentrations were in the range of 1.25 mg/L. Further increases in adsorbent dose led to a gradual enhancement in removal efficiency, reaching 86.97% and 87.44% for Fe_2O_3/cellulose and CuO_x-NPs, respectively (**Figure 3c**). Conversely, when examining the adsorption capacity of Fe_2O_3/cellulose and CuO_x-NPs for an initial Cr(VI) ion concentration of 24 mg/L, it was observed that the adsorption capacity gradually decreased from 80 mg/g to 78 mg/g as the adsorbent dose increased. This phenomenon can be explained by the fact that the ratio of available binding sites to the amount of metal ions in the system affects the adsorbent's capacity for adsorption. At higher doses of Cr(VI) ions, the saturation of binding sites on the surface of CuO_x-NPs and Fe_2O_3/cellulose composites was not achieved, resulting in a reduced adsorption capacity per unit mass of CuO_x nanoparticles. Furthermore, the increased availability of surface area and open adsorption sites with higher adsorbent dosages contributed to the elevated removal of Cr(VI) ions. However, it should be noted that as equilibrium was approached, additional increases in adsorbent dosage resulted in only marginal improvements in Cr(VI) ion removal. Consequently, a dose of 1.25 g/L was selected for subsequent studies, as it balanced the desirable values of high removal efficiency and adsorption capacity per unit mass of Fe_2O_3/cellulose and CuO_x-NPs adsorbent [25,26]. In comparison **Table 1**, various adsorbents utilized for Cr(VI) adsorption, we examined the impact of varying Cr(VI) ion concentrations on the adsorption behavior of Fe_2O_3/cellulose and CuO_x nanoparticles (CuO_x-NPs), with the results shown in **Figure 3b**. It was observed that the highest removal efficiencies, reaching 90.04% and 94.08%, were achieved at a relatively low initial metal ion concentration of 5 mg/L. As the initial concentration of Cr(VI) ions was progressively increased from 5 to 50 mg/L, the removal efficiency exhibited a consistent decline, dropping to 69.16% and 62.5%. This phenomenon can be attributed to the availability of a greater number of active surface areas and binding sites on Fe_2O_3/Cellulose and CuO_x-NPs when exposed to lower Cr(VI) ion concentrations, resulting in optimal adsorption performance. Conversely, at higher initial concentrations of Cr(VI) ions, fewer sites were available for the acceptance of Cr(VI) ions on the synthesized materials, thereby leading to a decrease in the adsorption efficiency [27].

3.4. Influence of temperature on adsorption

A comprehensive investigation into the influence of temperature, spanning from

15 °C to 45 °C, on the adsorption behavior of Cr(VI) onto the surfaces of Fe_2O_3/cellulose and CuO_x nanoparticles (CuO_x-NPs), and the resultant data are visually shown in **Figure 4**. The findings unveiled a distinct temperature-dependent impact on the adsorption process. Specifically, an elevation in temperature within this specified range elicited divergent responses: a notable augmentation in the adsorption of Cr(VI) ions onto CuO_x-NPs, in stark contrast to a conspicuous reduction in adsorption observed for Fe_2O_3/cellulose composites. This intriguing phenomenon can be ascribed to the noteworthy reduction in solution viscosity with increasing temperature, a well-recognized phenomenon in the realm of chemical kinetics. Elevated temperatures serve as a catalyst, enhancing the diffusion rate of adsorbate molecules. This accelerated diffusion occurs both within the exterior boundary layer and, crucially, within the intricate network of pores intrinsic to the adsorbent particles. Consequently, the heightened thermal energy facilitates more efficient interaction between the Cr(VI) ions and the CuO_x-NPs, leading to an augmented adsorption capacity. In stark contrast, the adsorption performance of Cr(VI) onto Fe_2O_3/cellulose composites exhibits a counterintuitive decline with rising temperature. This paradoxical behavior can be attributed to complex interplays between temperature-induced changes in the physicochemical properties of the adsorbent and the nature of adsorbate interactions. These interactions influence the availability of active adsorption sites and, consequently, the overall adsorption efficiency [28,29].

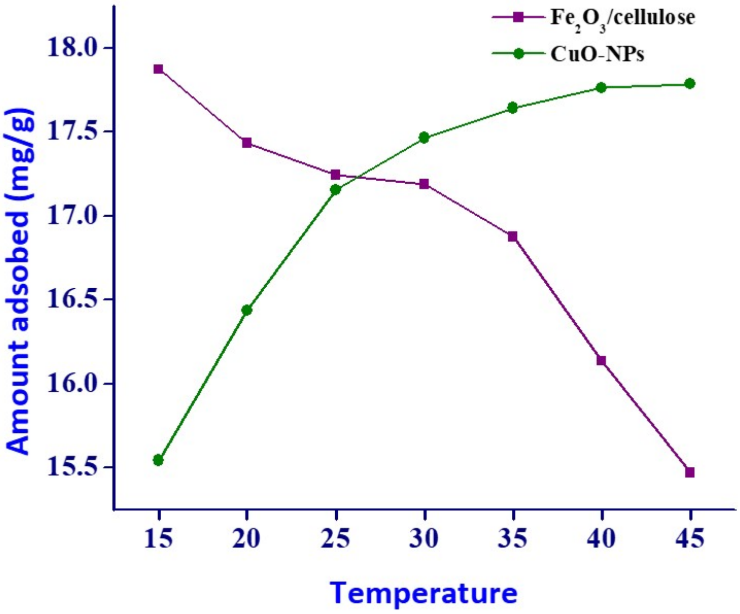

Figure 4. Effect of Temperature on Chromium adsorption utilizing Fe_2O_3/cellulose and CuO-NPs.

3.5. Kinetic study

Theoretical studies were conducted to study the nature of adsorption and establish potential adsorption mechanisms. To achieve this, well-known adsorption equations and models were utilized to analyze the acquired data. In the kinetic studies, common kinetic models/equations were applied to analyze the adsorption kinetics of the newly developed adsorbent.

3.5.1. Pseudo second order kinetic model

The model/equation is expressed as:

$$\frac{dq}{dt} = K_2(q_e - q_t)^2$$

The linear form of this model/equation is given as:

$$\frac{t}{q_t} = \frac{t}{q_e} - \frac{1}{K_2 q_e^2}$$

where q_e is the amount of sample adsorbed (mg/g) at equilibrium, qt is the amount of sample adsorbed (mg/g) at any given time (*t*) (min), and K_2 is the pseudo-second-order reaction rate constant for adsorption (g/mg.min). The constant K_2 = to calculate the initial adsorption rate (*h*) (mg/g.min), at $t \rightarrow 0$ as follows;

$$h = K_2 q_e^2$$

where K_2 is the pseudo-second-order reaction rate constant for adsorption (g/mg.min) and q_e is the amount of sample adsorbed (mg/g) at equilibrium. From the equilibrium time adsorption data, the time (*t*) (min) plotted with *t*/*qt* (**Figures 5a** and **5b**) with correlation co-efficient (R^2) of 0.9958 (slope = 1/qe 0.05418, CuO_x), plus R^2 = 0.9958 ($1/q_e$ = 0.05762, for Fe_2O_3/cellulose) and the pseudo-second-order-kinetic equation/model were constructed.

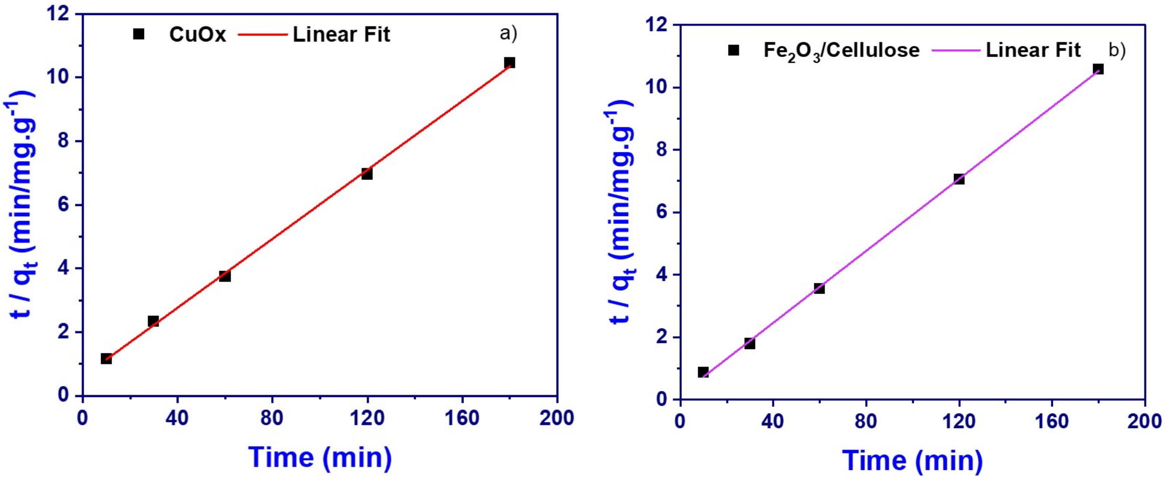

Figure 5. Pseudo second order kinetic model of **(a)** CuO_x; and **(b)** Fe_2O_3/cellulose.

3.5.2. Langmuir adsorption isotherm model

It is important to establish the most appropriate correlation for the equilibrium curves. An adsorption isotherm/model describes the relationship between the amount of adsorbate that is adsorbed on the adsorbent and the concentration of dissolved adsorbate in the liquid at equilibrium. Isotherm models such as those have been used to describe the equilibrium nature of adsorption; the Langmuir adsorption isotherm/model is the most frequently used model for the adsorption of an adsorbate from a liquid solution onto the adsorbent. This model is obtained under the ideal assumption of an adsorption surface. It is assumed that adsorbate occupied a site, and no further adsorption occurred. A saturated value is reached, and no further adsorption can take place. The Langmuir adsorption isotherm/model is used and is expressed by the following equation:

$$q_e = \frac{K_L C_e}{1 + a_L C_e}$$

In a linear form of this equation is given as;

$$\frac{C_e}{q_e} = \frac{1}{K_L} + \frac{a_L C_e}{K_L}$$

where C_e is the equilibrium concentration of sample (BPB) in the solution (mg/L), q_e is the amount of sample adsorbed (mg/g), K_L and a_L are the Langmuir adsorption isotherm/model constants and are related to the maximum adsorption capacity (L/g) and bonding strength (L/mg), respectively. The theoretical monolayer adsorption capacity (Q_o, mg/g) is numerically equal to K_L/a_L.

$$Q_o = \frac{K_L}{a_L}$$

The C_e (mg/L) was then plotted with C_e/q_e (**Figures 6a** and **6b**) with correlation co-efficient (R^2) of 0.9907 and the Langmuir adsorption isotherm/model was constructed. In the present study, it is highlighted that the adsorbent is favorable for the adsorption onto the newly developed adsorbent under the studied conditions.

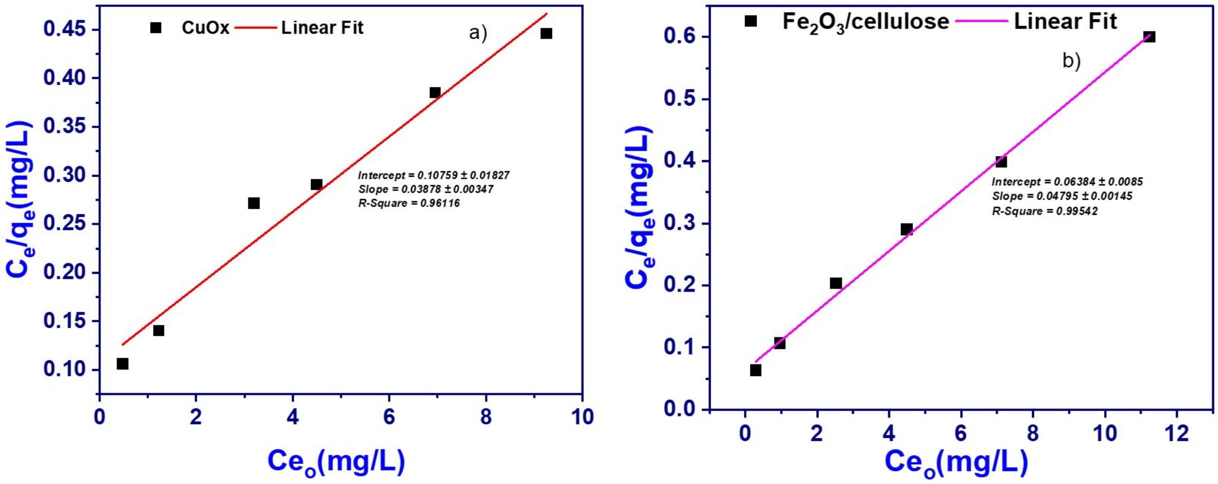

Figure 6. Langmuir adsorption isotherm/model of **(a)** CuO_x and **(b)** Fe_2O_3/cellulose.

3.6. Effectiveness of samples

In the pursuit of evaluating the effectiveness of removing Cr(VI) from authentic and synthetic wastewater samples, we employed Fe_2O_3/cellulose and CuO_x nanoparticles (CuO_x-NPs) under carefully optimized adsorption parameters, as illustrated in **Figure 7**. This comprehensive assessment encompassed the utilization of three distinct true water samples (comprising tap water, well water, and river water), an industrial effluent sample, and a synthetic wastewater sample. To commence the evaluation process, each of these samples underwent individual spiking with a Cr(VI) concentration of 25 mg/L. Following the completion of the adsorption procedure, we meticulously quantified the amount of adsorbed Cr. The results unveiled a noteworthy accomplishment in the removal of Cr(VI) ions, with removal percentages ranging from 53.52% to 70.97% for authentic water samples and 49.78% to 68.93% for wastewater samples, all facilitated by the utilization of the synthesized composites. These outcomes affirm the practical applicability of the synthesized materials in the purification of authentic water samples, wastewater, and industrial effluents.

Remarkably, it is worth noting that Fe_2O_3/cellulose outperformed CuO_x-NPs significantly in these diverse applications, underscoring its superior performance [29,30].

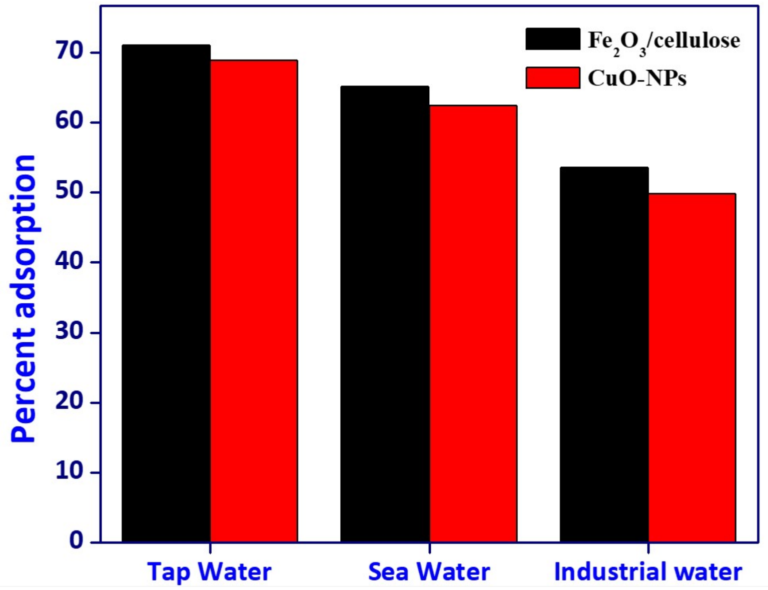

Figure 7. Adsorption of Cr (VI) ion using Fe_2O_3/cellulose and CuO- NPs in true samples.

4. Conclusions

In this study, cellulose-based ferric oxide (Fe_2O_3/cellulose) and copper oxide nanoparticles (CuO_x-NPs) were successfully synthesized using the co-precipitation approach. These newly synthesized nanoparticles were extensively characterized. The synthesized materials demonstrated promise for the removal of hazardous hexavalent chromium (Cr(VI)) ions from aqueous solutions. The investigation into the effect of pH on Cr(VI) adsorption revealed that the optimal pH for maximum adsorption was 2.0 and 4.0. The impact of adsorbent dosage indicated that an increase in dosage led to enhanced Cr(VI) ion removal, with saturation observed at higher doses. Furthermore, the influence of adsorbate concentration on adsorption performance demonstrated that lower initial Cr(VI) ion concentrations resulted in higher removal efficiencies. Thermal influence on adsorption was investigated, with CuO_x-NPs exhibiting increased adsorption at higher temperatures, attributed to enhanced diffusion rates. Conversely, Fe_2O_3/cellulose composites showed decreased adsorption at elevated temperatures, likely due to altered surface properties. The practical applicability of Fe_2O_3/cellulose and CuO_x-NPs was confirmed through successful Cr(VI) ion removal from real water samples, including tap water, well water, river water, and industrial effluent. These findings highlight the potential of these nanomaterials for efficient and sustainable heavy metal ion removal from aqueous environments, addressing environmental contamination concerns.

Author contributions: Literature, experimental investigation, SUK and BA; writing—review and editing, AH; supervision and project administration, AK. All authors have read and agreed to the published version of the manuscript.

Conflict of interest: The authors declare no conflicts of interest.

References

1. Gautam RK, Sharma SK, Mahiya S, et al. Contamination of Heavy Metals in Aquatic Media: Transport, Toxicity and Technologies for Remediation. In: Sharma S (editor). Heavy Metals in Water. Royal Society of Chemistry; 2014. pp. 1-24. doi: 10.1039/9781782620174-00001
2. Gupta A, Singh A, Mishra VK. Hexavalent Cr, Its Toxicity and Removal Strategy: Revealing PGPB Potential in Its Remediation. Water, Air, & Soil Pollution. 2023; 234(8). doi: 10.1007/s11270-023-06477-4
3. Ma T, Ding Y, Xu F, et al. Effects of Acute and Chronic Heavy Metal Chromium Stress on Heat Shock Protein Gene and Antioxidant Enzyme Activities of Orthetrum Albistylum Larvae. SSRN Journal. 2023.
4. Kurniawan TA, Othman MHD, Adam MR, et al. Chromium Removal from Aqueous Solution Using Natural Clinoptilolite. Water. 2023; 15(9): 1667. doi: 10.3390/w15091667
5. Ding ZJ, Liu Y, Weerasooriya R, et al. Electrochemical Determination of Chromium(VI) with Au/UiO-66 Modified Glassy Carbon and Screen-Printed Electrodes by Linear Sweep Voltammetry (LSV). Analytical Letters. 2023; 57(5): 753-771. doi: 10.1080/00032719.2023.2222425
6. Shrestha R, Ban S, Devkota S, et al. Technological trends in heavy metals removal from industrial wastewater: A review. Journal of Environmental Chemical Engineering. 2021; 9(4): 105688. doi: 10.1016/j.jece.2021.105688
7. Barakat MA. New trends in removing heavy metals from industrial wastewater. Arabian Journal of Chemistry. 2011; 4(4): 361-377. doi: 10.1016/j.arabjc.2010.07.019
8. Shaabani A, Nosrati H, Seyyedhamzeh M. Cellulose@Fe_2O_3 nanoparticle composites: magnetically recyclable nanocatalyst for the synthesis of 3-aminoimidazo[1,2-a]pyridines. Research on Chemical Intermediates. 2013; 41(6): 3719-3727. doi: 10.1007/s11164-013-1484-6
9. Luna IZ, Hilary LN, Chowdhury AMS, et al. Preparation and Characterization of Copper Oxide Nanoparticles Synthesized via Chemical Precipitation Method. OALib. 2015; 2(3): 1-8. doi: 10.4236/oalib.1101409
10. Nogueira AE, Giroto AS, Neto ABS, et al. CuO synthesized by solvothermal method as a high capacity adsorbent for hexavalent chromium. Colloids and Surfaces A: Physicochemical and Engineering Aspects. 2016; 498: 161-167. doi: 10.1016/j.colsurfa.2016.03.022
11. Haq A, Saeed M, Usman M, et al. A comparative sorption study of Cr^{3+} and Cr^{6+} using mango peels: kinetic, equilibrium and thermodynamic. Green Processing and Synthesis. 2019; 8(1): 337-347. doi: 10.1515/gps-2019-0001
12. Vu XH, Nguyen LH, Van HT, et al. Adsorption of Chromium(VI) onto Freshwater Snail Shell-Derived Biosorbent from Aqueous Solutions: Equilibrium, Kinetics, and Thermodynamics. Journal of Chemistry. 2019; 2019: 1-11. doi: 10.1155/2019/3038103
13. Tamjidi S, Esmaeili H. Chemically Modified CaO/Fe_3O_4 Nanocomposite by Sodium Dodecyl Sulfate for Cr(III) Removal from Water. Chemical Engineering & Technology. 2019; 42(3): 607-616. doi: 10.1002/ceat.201800488
14. Wang J, Cao R, He D, et al. Facile preparation of polyethyleneimine modified activated sludge-based adsorbent for hexavalent chromium removal from aqueous solution. Separation Science and Technology. 2020; 56(3): 498-506. doi: 10.1080/01496395.2020.1728324
15. Rengaraj S, Yeon KH, Moon SH. Removal of chromium from water and wastewater by ion exchange resins. Journal of Hazardous Materials. 2001; 87(1-3): 273-287. doi: 10.1016/S0304-3894(01)00291-6
16. Rana P, Mohan N, Rajagopal C. Electrochemical removal of chromium from wastewater by using carbon aerogel electrodes. Water Research. 2004; 38(12): 2811-2820. doi: 10.1016/j.watres.2004.02.029
17. Fahim N, Barsoum B, Eid A, et al. Removal of chromium(III) from tannery wastewater using activated carbon from sugar industrial waste. Journal of Hazardous Materials. 2006; 136(2): 303-309. doi: 10.1016/j.jhazmat.2005.12.014
18. Mella B, Glanert AC, Gutterres M. Removal of chromium from tanning wastewater and its reuse. Process Safety and Environmental Protection. 2015; 95: 195-201. doi: 10.1016/j.psep.2015.03.007
19. Sarin V, Pant K. Removal of chromium from industrial waste by using eucalyptus bark. Bioresource Technology. 2006; 97(1): 15-20. doi: 10.1016/j.biortech.2005.02.010

20. Rengaraj S, Joo CK, Kim Y, Yi J. Kinetics of removal of chromium from water and electronic process wastewater by ion exchange resins: 1200H, 1500H and IRN97H. Journal of Hazardous Materials. 2003; 102(2-3): 257-275. doi: 10.1016/S0304-3894(03)00209-7
21. El-Sikaily A, Nemr AE, Khaled A, et al. Removal of toxic chromium from wastewater using green alga Ulva lactuca and its activated carbon. Journal of Hazardous Materials. 2007; 148(1-2): 216-228. doi: 10.1016/j.jhazmat.2007.01.146
22. Acharya J, Sahu JN, Sahoo BK, et al. Removal of chromium(VI) from wastewater by activated carbon developed from Tamarind wood activated with zinc chloride. Chemical Engineering Journal. 2009; 150(1): 25-39. doi: 10.1016/j.cej.2008.11.035
23. Peng H, Leng Y, Guo J. Electrochemical Removal of Chromium (VI) from Wastewater. Applied Sciences. 2019; 9(6): 1156. doi: 10.3390/app9061156
24. Hayashi N, Chen J, Seko N. Nitrogen-containing fabric adsorbents prepared by radiation grafting for removal of chromium from wastewater. Polymers. 2018; 10(7): 744. doi: 10.3390/polym10070744
25. Kera NH, Bhaumik M, Pillay K, et al. Selective removal of toxic Cr(VI) from aqueous solution by adsorption combined with reduction at a magnetic nanocomposite surface. Journal of Colloid and Interface Science. 2017; 503: 214-228. doi: 10.1016/j.jcis.2017.05.018
26. Chen Y, Xu H, Wang S, et al. Removal of Cr(vi) from water using polypyrrole/attapulgite core–shell nanocomposites: equilibrium, thermodynamics and kinetics. RSC Advances. 2014; 4(34): 17805-17811. doi: 10.1039/c3ra47351a
27. Atieh MA, Bakather OY, Tawabini BS, et al. Removal of Chromium (III) from Water by Using Modified and Nonmodified Carbon Nanotubes. Journal of Nanomaterials. 2010; 2010: 1-9. doi: 10.1155/2010/232378
28. Ahmadi F, Esmaeili H. Chemically modified bentonite/Fe_3O_4 nanocomposite for Pb(II), Cd(II), and Ni(II) removal from synthetic wastewater. Desalination And Water Treatment. 2018; 110: 154-167. doi: 10.5004/dwt.2018.22228
29. Egodawatte S, Datt A, Burns EA, et al. Chemical Insight into the Adsorption of Chromium(III) on Iron Oxide/Mesoporous Silica Nanocomposites. Langmuir. 2015; 31(27): 7553-7562. doi: 10.1021/acs.langmuir.5b01483
30. Lingamdinne L, Kim IS, Ha JH, et al. Enhanced Adsorption Removal of Pb(II) and Cr(III) by Using Nickel Ferrite-Reduced Graphene Oxide Nanocomposite. Metals. 2017; 7(6): 225. doi: 10.3390/met7060225

Characterization and Application of Nanomaterials 2024, 7(1), 5756.
https://doi.org/10.24294/can.v7i1.5756

Article

Enhanced photocatalytic performance by ZnO/Graphene heterojunction grown on Ni foam for methylene blue removal

Lucas F. Melia[1], María V. Gallegos[2], Luciana Juncal[1], Marcos Meyer[1], Francisco J. Ibañez[3], Laura C. Damonte[1,*]

[1] Instituto de Física La Plata (IFLP), CONICET-UNLP, La Plata 1900, Argentina
[2] Centro de Investigación y Desarrollo en Ciencias Aplicadas (CINDECA), CONICET-UNLP-CIC, La Plata 1900, Argentina
[3] Instituto de Investigaciones Fisicoquímicas, Teóricas y Aplicadas (INIFTA), Universidad Nacional de La Plata-CONICET, La Plata 1900, Argentina
*** Corresponding author:** Laura C. Damonte, damonte@fisica.unlp.edu.ar

CITATION

Melia LF, Gallegos MV, Juncal L, et al. Enhanced photocatalytic performance by ZnO/Graphene heterojunction grown on Ni foam for methylene blue removal. Characterization and Application of Nanomaterials. 2024; 7(1): 5756. https://doi.org/10.24294/can.v7i1.5756

ARTICLE INFO

Received: 15 April 2024
Accepted: 30 April 2024
Available online: 29 May 2024

Abstract: ZnO nanostructures were obtained by electrodeposition on Ni foam, where graphene was previously grown by chemical vapor deposition (CVD). The resulting heterostructures were characterized by X-ray diffraction and SEM microscopy, and their potential application as a catalyst for the photodegradation of methylene blue (MB) was evaluated. The incorporation of graphene to the Ni substrate increases the amount of deposited ZnO at low potentials in comparison to bare Ni. SEM images show homogeneous growth of ZnO on Ni/G but not on bare Ni foam. A percent removal of almost 60% of MB was achieved by the Ni/G/ZnO sample, which represents a double quantity than the other catalysts proved in this work. The synergistic effects of ZnO-graphene heterojunctions play a key role in achieving better adsorption and photocatalytic performance. The results demonstrate the ease of depositing ZnO on seedless graphene by electrodeposition. The use of the film as a photocatalyst delivers interesting and competitive removal percentages for a potentially scalable degradation process enhanced by a non-toxic compound such as graphene.

Keywords: Ni foam; electrodeposition; zinc oxide; photocatalysis; graphene; methylene blue degradation

1. Introduction

It is known that water pollution is an environmental problem that worsens year after year. Human activities, such as industry and agricultural production, affect bodies of water and, consequently, human health [1]. It is believed that of all wastewaters generated by human activities, 80% are discharged without prior treatment. Poor-quality drinking water is a problem that is associated with 80% of childhood illnesses and 50% of child deaths worldwide [2]. Among water contaminants, organic dyes play a leading role: around 100,000 different types of dyes are produced annually, totaling more than 700,000 tons, with approximately 100 tons being dumped [3,4]. In addition to many of them being carcinogenic and dangerous for humans [5,6], they have good stability in environmental conditions [7] and cause, among other drawbacks, loss of transparency, reduction in the penetration of sunlight, retard biological activity of plants and animals, increase chemical oxygen demand (COD) and biochemical oxygen demand (BOD), etc. [8,9]. In this context, organic dyes contribute significantly to this environmental problem since they are one of the main sources of contamination of surface and groundwater [10]. One of the most commonly used dyes is methylene blue (MB). MB, from the thiazine class, is a heterocyclic aromatic compound; see **Figure**

1 [11]. This cationic dye is commonly used in the textile industry to dye wool, cotton, etc., where 15% is transferred to wastewater during this process as an industrial pollutant [12–14]. These dyes have also long been used in medicine and scientific purposes, such as in microscopy or as redox indicators [15]. Although this dye can be used as a drug against some diseases, such as malaria, it is also toxic to human health and the environment and can cause vomiting, nausea, irritation, and tachycardia, among other diseases, in humans. This pollutant can inhibit plant growth and reduce the pigment and protein content of algae [16–18]. For these reasons, the elimination of these pollutants from water is now one of the main areas of study [3].

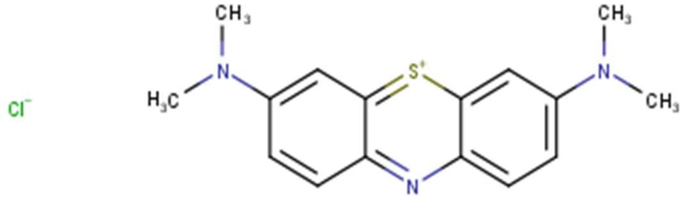

Figure 1. Schematic representation of methylene blue (MB) dye.

The removal mechanisms of MB and other contaminants from wastewater are frequently studied [19–21]. Photodegradation via photocatalysis using semiconductors is a preferred way to eliminate contaminants in various sources of water [22,23]. One of the main advantages of photocatalysis relies on the generation of non-harmful products, such as CO_2, H_2O, and inorganic salts, after activating the process with light [24,25]. Although there are various kinds of semiconductors that adapt well to these systems, including Fe_2O_3, CdS, and ZnS [3], TiO_2 and ZnO are the most used in photocatalysis applications [10]. Most likely due to their low toxicity, outstanding thermal and chemical stability, and relatively low cost [26]. In particular, ZnO presents higher percentages of contaminants degradation in water than TiO_2 [27], which could be due to the higher exciton binding energy and the higher electrical conductivity of ZnO compared to TiO_2, in addition to the ZnO band potentials (of valence and conduction) being lower than TiO_2 ones. This combination of properties allows an increase in the effectiveness of the degradation reactions [28,29]. In this context, the use of thinly supported ZnO films is most desired since it allows a very simple separation process, which consists of removing the catalyst from the solution and also facilitating the recycling of the catalyst. On the other hand, the use of ZnO powder involves separation by some subsequent process. In addition to this, it is known that the photodegradation efficiency increases as the specific surface increases [30]. This is why the use of porous supports, such as nickel foams, can obtain very high performance, comparable to powders.

ZnO thin films can be obtained through various methods, such as metal-organic chemical vapor deposition (CVD) [31,32], magnetron sputtering [33,34], molecular-beam epitaxy [35,36], sol-gel [37], spray pyrolysis [38,39] and electrodeposition [40–42]. What is interesting about the latter is the simple scalability, film control, and the possibility of depositing structures in many different shapes and sizes without using high temperatures or expensive equipment. Growth can be carried out through various solutions that use Zn^{2+} salts with different anions, whether chlorides, nitrates, or sulfates, as precursors [43–48]. By varying the type, concentration, or pH of these solutions, as well as the applied potential, the deposition time, or the current circulating in the cell, various types of ZnO films and morphologies can be obtained [49–54]. However, it is desirable to use low currents or voltages, low-concentrated salts with non-toxic precursors, and low times so that the process is profitable and easily scalable.

One of the ways to improve the properties of ZnO is to form heterostructures with graphene. CVD graphene presents outstanding properties such as transparency, flexibility, high carrier mobility, and mechanical stability [55–57]. When graphene is grown in 3D structures, the carbon atoms are exposed on the surface, resulting in a large surface area and a large number of active sites [58]. The three-dimensional ZnO-Graphene heterojunction provides synergetic properties and improves charge separation by ZnO followed by charge transport offered by highly conductive graphene, which dramatically reduces the probability of electron-hole recombination [59,60]. This happens because the work function of graphene (−4.5 eV) is lower than the conduction band of the semiconductor oxide (−4.1 eV), so the excited electrons in ZnO are transported toward graphene, which has a high carrier mobility, thus inhibiting recombination in ZnO and consequently increasing the photocatalysis degradation efficiency of MB [61]. Researchers have shown that the photocatalytic activity of ZnO improves whenever graphene is used as a co-catalyst [62]. In addition, graphene could extend the absorption range of ZnO to longer wavelengths further from the ultraviolet region [59]. These exceptional properties offered by the ZnO-Graphene heterojunction have been applied in various fields, including photocatalysis, photodetection, solar cells, etc.

In this work we propose the electrodeposition of ZnO on graphene already grown on a Ni foam by CVD to be used in photodegradation applications. This heterojunction is interesting both as an adsorbent material and for photocatalysis due to the high specific surface area provided by using Ni foam as a substrate, added to the improvement in conductivity and the decrease in electron/hole recombination provided by graphene.

2. Materials and methods

We proposed to grow ZnO nanostructures by electrodeposition on Ni foam, a low-cost and simple technique that had proved to be successful in obtaining ZnO films on different flat substrates like ITO and FTO [40–43].

2.1. Graphene growth in nickel foam

Nickel foam with 1.6 mm thickness and porosity of 87% was purchased from MTI Corp (Richmond, CA, USA). Graphene was grown on Ni foam by CVD method on Ni foam following the protocol described by Messina et al. [63]. Briefly, the bare Ni foam was sonicated in acetone for 20 min and placed in a quartz tube under a vacuum pressure of 8×10^{-5} torr. During the synthesis, a constant flow of H_2 was maintained at a rate of 75 mL min^{-1}. At 950 °C a flow of CH_4 was introduced at a rate of 35 mL min^{-1} for 5 min leading to the growth of graphene on the entire surface of Ni. Finally, the furnace was cooled down at a rate of 16 °C per minute until reaching room temperature.

2.2. Electrodeposited ZnO films

A thin layer of ZnO was grown on Ni with and without graphene by the electrodeposition technique using a Teq4 potentiostat from NanoTeq, Argentina. The aqueous solution was 0.01 mol/L $Zn(NO_3)_2$ (Sigma Aldrich, 98%) in 0.1 mol/L KCl (Anedra, 99.6%) and 0.1 mol/L KNO_3 (Anedra, 99.8%).

The electrolytic cell is a three-electrode setup where Ni foam, Pt wire, and Ag/AgCl electrodes immersed in 3.0 M KCl acted as working, counter, and reference electrodes, respectively. **Figure 2** shows a scheme of the cell. Before electrodeposition, the working electrode was washed with soapy water, sonicated in distilled water for 10 min, and then sonicated in isopropyl alcohol for 10 min. Electrodeposition was performed at constant temperature (70 ℃) and stirring (200 rpm) to ensure homogenous distribution. The applied voltage was −800 mV (chosen after performing cyclic Voltammetry on the studied system) for 60 min. The initial pH of the solution is 5.3. The samples obtained were called Ni/G (Ni foam + graphene), Ni/ZnO (ZnO on Ni foam), and Ni/G/ZnO (ZnO on Ni foam with graphene).

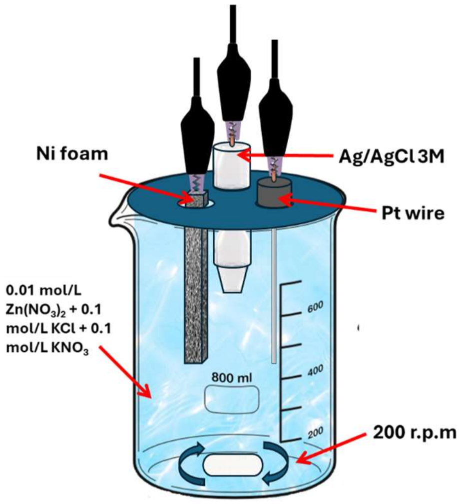

Figure 2. Scheme represents the three-electrode set-up under the parameters used in this work.

2.3. Sample characterization

Cyclic voltammetry and subsequent amperometry were performed using a Teq4 potentiostat from NanoTeq Co., Argentina. X-Ray Diffraction (XRD) patterns were acquired using a Philips PW1710, Panalytical X'Pert PRO diffractometer at 45 kV and 45 mA with monochromatized CuK_α radiation in the range of $20° \leq 2\theta \leq 40°$ with a step of 0.02 °/s and a grazing angle of 3°. Optical images were obtained through a Leica DM IL LED optical microscope. SEM images were obtained from an FEI Quanta 250 environmental scanning microscope (ESEM) at an operating voltage of 20 kV. The equipment has an X-ray detector, EDAX, through which the chemical composition was studied qualitatively using energy dispersive spectroscopy (EDS).

2.4. MB degradation

The photodegradation of MB was evaluated by immersing Ni, Ni/G, Ni/ZnO, and Ni/G/ZnO in 1.3 ppm methylene blue (MB) solution. The solution was kept in the dark for 15 min to reach adsorption equilibrium. Then, it was irradiated with an 8 W fluorescent lamp (BTE Lighting, Argentina) with a wavelength ranging from 250 to 600 nm. The UV lamp was kept on for 165 min and the experiment was carried out at room temperature. **Figure 3** shows the experimental set-up. At the indicated times, the sample was removed from the solution, and the absorbance of the remaining solution was measured using a Shimadzu UV-2600 spectrometer.

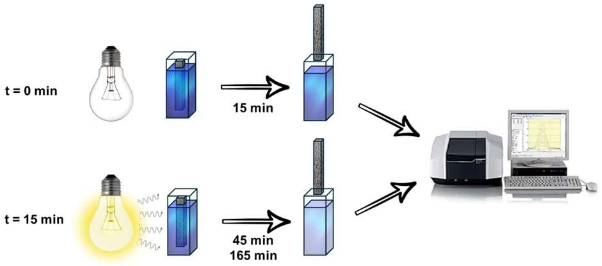

Figure 3. Scheme of the experimental set-up used to measure MB adsorption and degradation.

3. Results

In this section details of the electrodeposition method are presented along with the structural and morphological characterization of the obtained heterostructures. Also, the use of these samples on the MB removal is analyzed.

3.1. Cyclic voltammetry (CV) and amperometry

CVs were run from negative from 0 to −1.1 V and back to 0 V at 100 mV/s scan rate. **Figure 4** shows only the cathodic sweep that is of interest for the ZnO deposition. The CV reveals significant differences based on the electrode substrate. Our group successfully electrodeposited ZnO on different substrates, including ITO and FTO, by applying potentials between −700 mV and −1000 mV. We identified −800 mV as the optimal potential. Therefore, we applied −800 mV which resulted in a noticeable increase in the steep curve for Ni/G as compared to the naked Ni electrode shown in **Figure 4**. Due to the increase in slope observed in both cases, this potential was chosen and applied for 1 h. After amperometry, the Ni/G sample exhibited a white deposit to the naked eye, while no apparent change in color was observed for Ni foam.

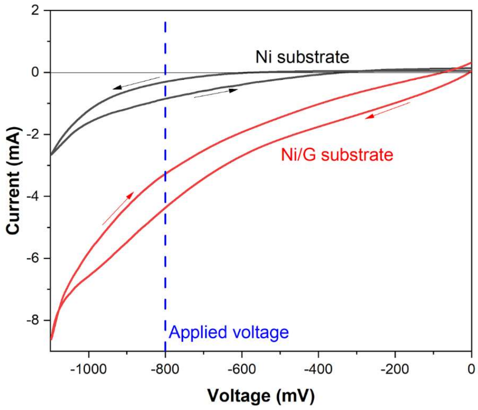

Figure 4. Cyclic Voltagrams corresponding to Ni (black) and Ni/G (red) electrodes.

3.2. X-Ray diffraction (XRD)

Figure 5 shows the diffractograms for Ni/ZnO and Ni/G/ZnO samples measured at angles between 20° and 40°, a region where the characteristic diffraction peaks of ZnO become more evident after smoothing the original signal using the Savitzky-Golay method. Amperometry was performed for 1 h on both samples. As it can be seen, no characteristic peak for ZnO was detected within the Ni/ZnO sample. This does not necessarily rule out the deposition of ZnO since there may be a low amount of mass that is below the limit of detection. On the other hand, for Ni/G/ZnO samples, three peaks clearly evolved, corresponding to (100), (002), and (101) crystallographic orientations that matched the peaks for ICSD no. 01-080-0074. This clearly confirms the successful deposition of the ZnO semiconductor onto the Ni/G sample. Furthermore, there is no evidence of preferential growth in the (002), as the intensity of this peak (at 34.335°) is not dominant. This is consistent with the literature, which has also shown predominant (101) peaks using electrodeposition and other techniques [30,64–66]. These results suggest that the as-deposited ZnO film does not display a nanocolumnar morphology [67]. Additionally, no other diffraction peaks are detected, as Ni exhibits diffraction peaks for 2θ > 40° [68]. The technique also allows us to confirm that no other crystalline material was deposited in large quantities, since the diffractograms do not present other peaks, nor amorphous ones, since no bands were observed at low angles.

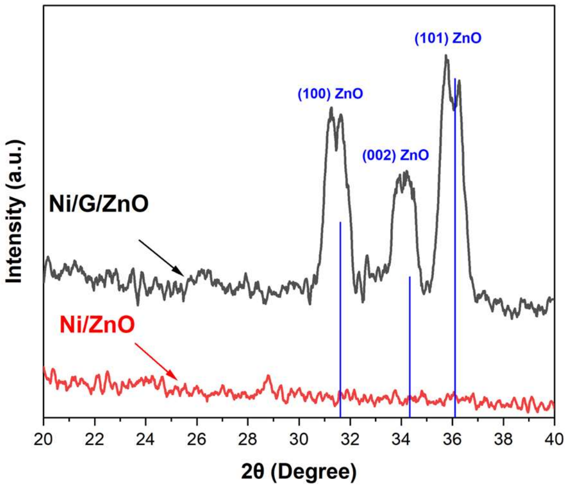

Figure 5. XRD Diffractogram comparing Ni/ZnO and Ni/G/ZnO samples. Blue lines that correspond to card no. 01-080-0074 are used as a comparison.

3.3. Optical microscopy

Figure 6A exhibits multiple pores within the naked Ni foam structure. No apparent changes were detected for graphene grown on Ni foam (not shown), most likely due to the poor resolution of the optical microscope. **Figures 6B** and **6C** clearly exhibits the as-deposited ZnO; however, the amount of deposit seems not to be uniform along the entire Ni/G/ZnO sample.

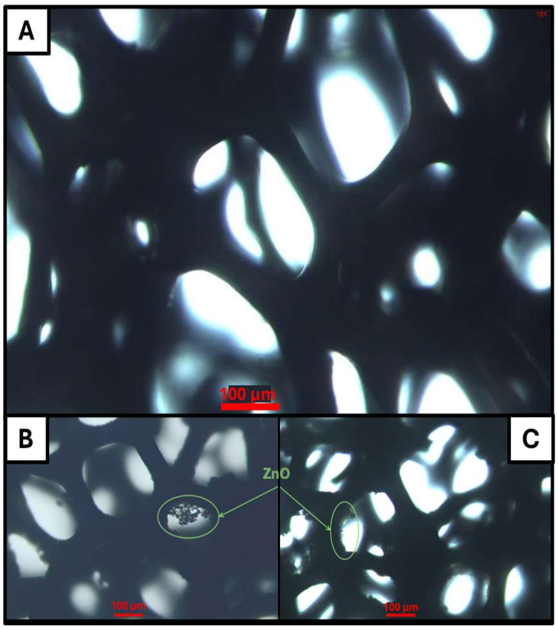

Figure 6. Optical images. **(A)** Ni foam; **(B)** Ni/G/ZnO sample; **(C)** Ni/G/ZnO sample.

3.4. SEM-EDS

Figure 7 shows SEM images for Ni (A), Ni/G (B), Ni/ZnO (C), and Ni/G/ZnO (D). Notable differences in the surfaces are observed between the electrodeposition of ZnO on bare Ni and on Ni/G using the same deposition parameters. **Figure 7B** clearly shows the growth of graphene on the surface of bare Ni. It can be seen there is a large amount of graphene in the center of the foam and that, close to the edge of the pores, that decreases. To confirm that it was a different material, it was analyzed with backscattered electrons, since in this type of image the contrast is based on the atomic number.

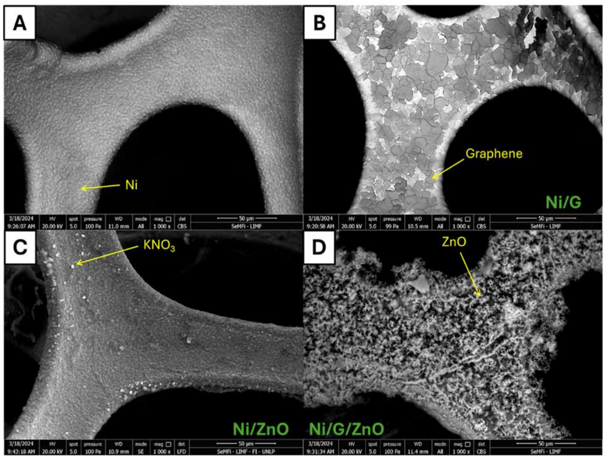

Figure 7. SEM images. **(A)** Ni; **(B)** Ni/G; **(C)** Ni/ZnO; **(D)** Ni/G/ZnO.

Figure 8 shows a SEM image of the Ni/G sample obtained by backscattered electrons. In these images the contrast is achieved with the difference in atomic number, which allows us to confirm that they are two different materials since the Ni substrate appears bright while the graphene deposit appears dark. This confirms that the CVD deposit was successful.

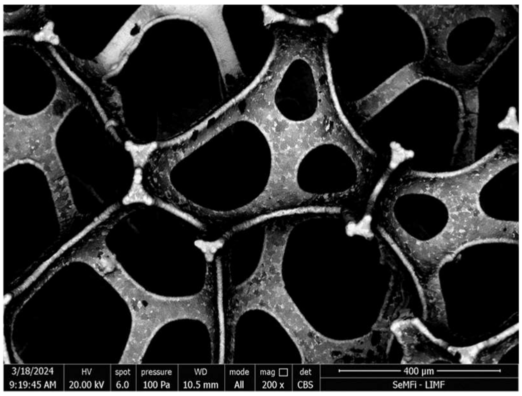

Figure 8. SEM image of the Ni/G sample obtained by backscattered electrons.

On the other hand, the Ni/ZnO sample does not present changes with respect to the Ni sample, except for the appearance of localized structures that are observed as white dots in **Figure 7C**. The amount of Zn provided by EDS in this sample is very low (about 3.5% by weight), consistent with a very low amount of ZnO deposited. As for other elements, the percentage by weight of O, K, N, and Cl revealed 40%, 25%, 13%, and 5% by weight, respectively. The presence of various elements, besides Zn, suggests the potential formation of KNO_3 and KCl crystals that arose during the drying-off process after electrodeposition.

Figure 7D shows the homogeneous growth of ZnO on the Ni/G substrate. EDS measured at various points in the sample indicated 27% and 31% by weight of Zn and O, respectively. In addition, a similar amount of C (31% by weight) was detected, consistent with the growth of graphene. This confirms the successful deposition of ZnO and indicates that graphene remains even after the voltage application in the synthesis. **Figure 9** shows the Ni/G/ZnO sample with a higher magnification, where an increase in the exposed surface can be seen due to the irregularity of the deposit. This type of morphology is comparable to those reported in the literature, despite using a different ZnO deposition technique [64,65]. Finally, **Figure 10** shows a color map obtained by EDS, which shows the location of the evaluated elements. It is confirmed that ZnO is deposited throughout the foam, unlike graphene, which is mostly located in the center of it.

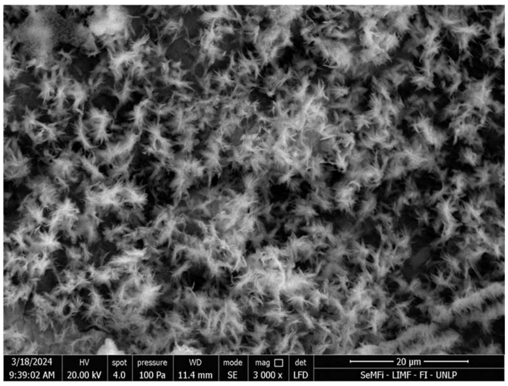

Figure 9. SEM image of the Ni/G/ZnO sample at higher magnification, showing the uniformity of the deposit.

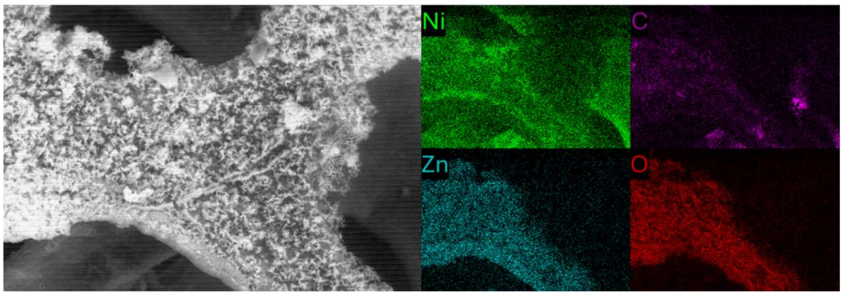

Figure 10. EDS color map showing the location of Ni, C, Zn, and O elements within the Ni/G/ZnO sample.

3.5. Removal of MB from a solution

An absorption spectrum was initially obtained after immersing the samples in 1.3 ppm MB solution for 15 min under dark conditions. In this way, the percentage of MB adsorption in the first min of the experiment was obtained. Then, the lamp was turned on and absorbance measured at 45 and 165 min. To calculate the percentage removal of MB in the solution, we choose to measure the area under the curve for the absorption band located at 662 nm. Finally, Equation (1) was applied to obtain the MB removal percentages:

$$\text{MB Removal [\%]} = (1 - A_t/A_0)\ 100 \qquad (1)$$

where A_t is the absorption measured at a certain time t and A_0 is the initial absorbance. **Figure 11** shows the absorbance spectra for each sample measured at the indicated times.

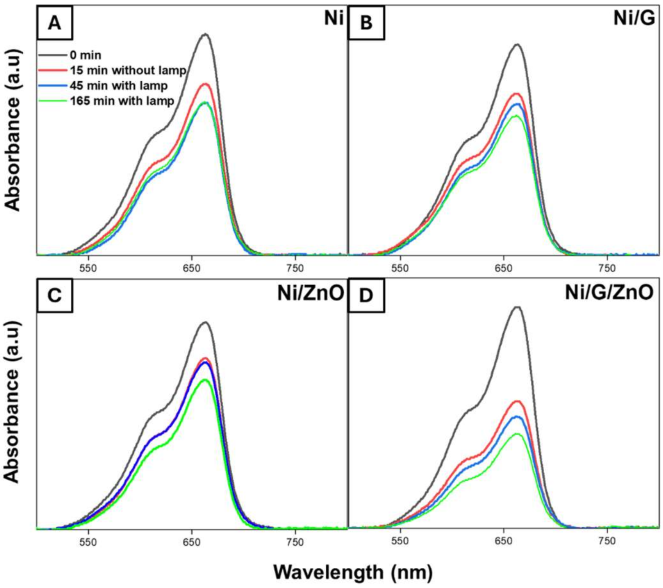

Figure 11. Absorbance spectra of the samples measured at different times: under dark (black curve), after 15 min exposure to light (red curve), after 45 min (blue curve) and 165 min (green curve). **(A)** Ni; **(B)** Ni/G; **(C)** Ni/ZnO; **(D)** Ni/G/ZnO.

Table 1 shows the MB removal percentages for each sample for two different periods of time: while the light was off, that is, the black and red curves indicated in **Figure 11**, and then once the light was turned on, that is, between the red and green curves of the same figure. It is clear that the Ni/G/ZnO sample exhibits a higher removal percentage than the other samples (almost double) in both time periods, thus improving both adsorption and degradation of the contaminant. The Ni foam and Ni/G foam are characterized by their abundance of microscopic-sized pores, which provide a large surface area leading to high contaminants adsorption capacity. The significant enhancement in adsorption observed in the samples with G/ZnO can be attributed to two concurrent factors. Firstly, the morphology of the deposited ZnO increases the contact surface, thereby facilitating increased adsorption. This fact is corroborated by SEM images **(Figures 7** and **9)**, where the nanostructured feature of ZnO is clearly appreciated. Secondly, the pH of the MB solution is 6, which results in the formation of $Zn(OH)^+$ on the ZnO surface. In contrast, the functional groups of MB carry a negative charge ($-SO3^-$). This allows the formation of an ionic bond that increases the adsorption capacity [69].

Figure 12 shows percentages of MB removal from the solution achieved for each sample after irradiation with UV light, represented by the black and green curves in **Figure 11**. Numerous studies [18,70,71] have corroborated that ZnO serves as a photocatalyst in this reaction. It is particularly noteworthy that the sample composed of Ni/G/ZnO exhibits the greatest efficiency, achieving about 60% removal of MB from the solution.

Table 1. MB removal percentages from the solution for each sample before and after light irradiation.

Sample	MB removal without light [%]	MB removal with light [%]
Ni	24	10
Ni/G	20	14
Ni/ZnO	20	14
Ni/G/ZnO	41	28

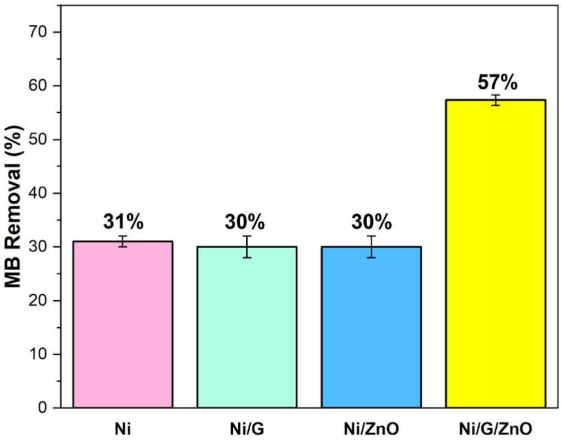

Figure 12. Percent removal of MB achieved by the different samples.

4. Discussion

This work reports on the growth of ZnO on Ni and Ni/G foams by electrodeposition and its possible application in the removal of dyes in water bodies. In the case of bare Ni foam, ZnO deposition is evidenced by the presence of Zn in EDS analysis, although ZnO growth could not be observed by XRD. On the other hand, when the Ni/G foam is used as a substrate, a large amount of ZnO deposition is observed by both techniques used. Unlike the work of Fei et al. [30], here, the growth of ZnO was achieved in a single step, without the need of adding seeds and performing heat treatments. This behavior could be due to the presence of defects and wrinkles in the graphene, which act as nucleation sites for ZnO. Then growth occurs in all directions.

It is worth highlighting that our starting solution has a low concentration of precursors compared to the growth solution used by Lv et al. [64]. The salt that contains the Zn^{2+}, $Zn(NO_3)_2$, has a concentration 20 times lower, while the supporting electrolyte KCl has a concentration 48 times lower. This makes our process more affordable and accessible. Furthermore, the application of a potential difference of −800 mV in our synthesis results in a more efficient and less demanding method in terms of equipment compared to the use of −10 V in the aforementioned study.

Regarding the incorporation of graphene, two benefits were found: in addition to allowing nucleation at lower applied voltages, it increases the percentage of MB removal from the solution (57%). In this context, it is interesting to note that graphene is an organic, non-toxic, and inexpensive material. The results obtained in this work are close to those obtained by various authors who grow ZnO on different substrates [3,72]. Fei et al. [30] do photocatalysis and photoelectrocatalysis using the Ni/ZnO and Ni/ZnO/MoS_2 heterojunction. The results obtained with both techniques with the Ni/ZnO electrode are less efficient than our findings doing photocatalysis with the Ni/G/ZnO heterostructure. However, Fei and co-workers achieved higher removal when using the Ni/ZnO/MoS_2 heterostructure, although it should be noted that graphene is a less toxic and cheaper compound.

On the other hand, Kulis-Kapuscinska et al. [10] have studied the photodegradation of MB by growing ZnO films by sputtering on Si(100) with a subsequent thermal treatment and have managed to remove 64% of MB from the solution in 540 min. That is, with a more complicated growth method they have achieved a result similar to that obtained in this work with a substantial difference in time: their experiment lasts 9 h while ours lasts 3 h, reducing the cost involved in maintaining the light on. This result is very important from the point of view that the degradation rate is usually a limiting factor for the selection of the photocatalyst. This could be due, in addition to the graphene, to the chosen substrate, since the Ni foam, being so porous, has a large active surface.

The improvements occur mainly due to the use of a nickel foam that increases the active surface compared to other flat substrates [30], added to the incorporation of graphene, which inhibits the recombination of electrons and holes according to the mechanism that can be seen in **Figure 13**. The conduction band of ZnO (−4.05 eV vs. vacuum) is aligned with the graphene in such a way that the electron excited in the semiconductor can be transferred to the graphene (also taking advantage of the high electron mobility), separating the charges and reducing, thus way, recombination. Then, the electron and the hole interact with the water in the solution: the molecular oxygen is reduced, generating the superoxide anion O_2^- and the water is oxidized to obtain hydroxyl radicals (OH*), which finally degrade the MB, and CO_2 and H_2O are obtained as products of this [59,62,73].

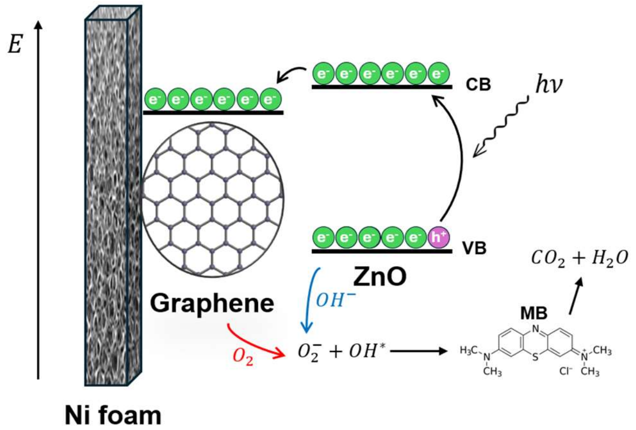

Figure 13. Scheme of the process with the ZnO and graphene bands.

5. Conclusion

In this study, ZnO was successfully electrodeposited on Ni/G foam substrates to obtain new materials with high specific surface area. Large amounts of ZnO were observed on Ni/G due to the presence of graphene, whose defects acted as nucleation sites. SEM images confirmed a homogeneous distribution of ZnO nanorods along the substrate. Instead, scarce deposition was observed for the bare Ni foam. The combined presence of ZnO and graphene increased the MB removal capacity, giving around 60% higher than what is achieved with the other heterostructures. The percentage improvement in terms of adsorption is due to the ionic bond that occurs between the ZnO surface and the negatively charged functional groups of the MB, while in photocatalysis it is probably due to a decrease in electron/hole recombination that leads to better charge separation.

Furthermore, the electrodeposition technique is a highly scalable method, so the synergistic effects of G/ZnO heterojunctions on a porous substrate become an interesting alternative for outperforming in areas of water cleaning and environmental remediation.

This study highlights the importance of the efficient synthesis of ZnO on Ni/G substrates via electrodeposition, not only for its applications in environmental remediation but also for its contribution to the development of sustainable practices within the framework of green chemistry.

Author contributions: Conceptualization, LCD; methodology, LCD, LFM, MVG; validation, LCD, MVG and LFM; formal analysis, LFM and LJ; investigation, LFM; resources, LCD, FJI and MM; data curation, LFM, MVG and LJ; writing—original draft preparation, LCD and LFM; writing—review and editing, LCD, FJI, LFM and MVG; visualization, LFM; supervision, LCD and FJI; project administration, LCD and MM; funding acquisition, LCD and FJI. All authors have read and agreed to the published version of the manuscript.

Funding: This research was funded by CONICET, grant numbers PIP0901 and PIP 0001 and UNLP grant numbers 11X933 and X-887.

Acknowledgments: LFM, MVG, LJ, MM, FJI and LCD are members of CONICET, Argentina. The authors acknowledge Sebastian Rabal, technical personnel of

CONICET, for technical assistance in the electrodeposition method. The authors also acknowledge the members of the Sensors and Electrocatalysis research group at INIFTA, for the growth of CVD graphene.

Conflict of interest: The authors declare no conflict of interest.

References

1. Xu X, Yang H, Li C. Theoretical Model and Actual Characteristics of Air Pollution Affecting Health Cost: A Review. International Journal of Environmental Research and Public Health. 2022; 19(6): 3532. doi: 10.3390/ijerph19063532
2. Lin L, Yang H, Xu X. Effects of Water Pollution on Human Health and Disease Heterogeneity: A Review. Frontiers in Environmental Science. 2022; 10. doi: 10.3389/fenvs.2022.880246
3. Lanjwani MF, Tuzen M, Khuhawar MY, et al. Trends in photocatalytic degradation of organic dye pollutants using nanoparticles: A review. Inorganic Chemistry Communications. 2024; 159: 111613. doi: 10.1016/j.inoche.2023.111613
4. Saleh TA. Advanced Nanomaterials for Water Engineering, Treatment, and Hydraulics. IGI Global; 2017.
5. Gupta VK, Mohan D, Suhas, et al. Removal of 2-Aminophenol Using Novel Adsorbents. Industrial & Engineering Chemistry Research. 2006; 45(3): 1113-1122. doi: 10.1021/ie051075k
6. Saleh TA. Mercury sorption by silica/carbon nanotubes and silica/activated carbon: a comparison study. Journal of Water Supply: Research and Technology - Aqua. 2015; 64(8): 892-903. doi: 10.2166/aqua.2015.050
7. Bin-Dahman OA, Saleh TA. Synthesis of polyamide grafted on biosupport as polymeric adsorbents for the removal of dye and metal ions. Biomass Conversion and Biorefinery. 2022; 14(2): 2439-2452. doi: 10.1007/s13399-022-02382-8
8. Crini G. Non-conventional low-cost adsorbents for dye removal: A review. Bioresource Technology. 2006; 97(9): 1061-1085. doi: 10.1016/j.biortech.2005.05.001
9. Lellis B, Fávaro-Polonio CZ, Pamphile JA, et al. Effects of textile dyes on health and the environment and bioremediation potential of living organisms. Biotechnology Research and Innovation. 2019; 3(2): 275-290. doi: 10.1016/j.biori.2019.09.001
10. Kulis-Kapuscinska A, Kwoka M, Borysiewicz MA, et al. Photocatalytic degradation of methylene blue at nanostructured ZnO thin films. Nanotechnology. 2023; 34(15): 155702. doi: 10.1088/1361-6528/aca910
11. Begum R, Najeeb J, Sattar A, et al. Chemical reduction of methylene blue in the presence of nanocatalysts: a critical review. Reviews in Chemical Engineering. 2019; 36(6): 749-770. doi: 10.1515/revce-2018-0047
12. American Association of Textile Chemists and Colorists. Color technology in the textile industry, 2nd ed. Amer Assn of Textile; 1997.
13. Varjani S, Rakholiya P, Shindhal T, et al. Trends in dye industry effluent treatment and recovery of value added products. Journal of Water Process Engineering. 2021; 39: 101734. doi: 10.1016/j.jwpe.2020.101734
14. Senobari S, Nezamzadeh-Ejhieh A. A comprehensive study on the enhanced photocatalytic activity of CuO-NiO nanoparticles: Designing the experiments. Journal of Molecular Liquids. 2018; 261: 208-217. doi: 10.1016/j.molliq.2018.04.028
15. Yazdani O, Irandoust M, Ghasemi JB, et al. Thermodynamic study of the dimerization equilibrium of methylene blue, methylene green and thiazole orange at various surfactant concentrations and different ionic strengths and in mixed solvents by spectral titration and chemometric analysis. Dyes and Pigments. 2012; 92(3): 1031-1041. doi: 10.1016/j.dyepig.2011.07.006
16. Pereira AGB, Rodrigues FHA, Paulino AT, et al. Recent advances on composite hydrogels designed for the remediation of dye-contaminated water and wastewater: A review. Journal of Cleaner Production. 2021; 284: 124703. doi: 10.1016/j.jclepro.2020.124703
17. Muzammal S, Ahmad A, Sheraz M, et al. Polymer-supported nanomaterials for photodegradation: Unraveling the methylene blue menace. Energy Conversion and Management: X. 2024; 22: 100547. doi: 10.1016/j.ecmx.2024.100547
18. Khan I, Saeed K, Zekker I, et al. Review on Methylene Blue: Its Properties, Uses, Toxicity and Photodegradation. Water. 2022; 14(2): 242. doi: 10.3390/w14020242
19. Radoor S, Karayil J, Jayakumar A, et al. Efficient removal of dyes, heavy metals and oil-water from wastewater using electrospun nanofiber membranes: A review. Journal of Water Process Engineering. 2024; 59: 104983. doi: 10.1016/j.jwpe.2024.104983
20. Rafatullah Mohd, Sulaiman O, Hashim R, et al. Adsorption of methylene blue on low-cost adsorbents: A review. Journal of

Hazardous Materials. 2010; 177(1-3): 70-80. doi: 10.1016/j.jhazmat.2009.12.047

21. Yaseen M, Khan A, Humayun M, et al. Fabrication and characterization of CuO–SiO_2/PVA polymer nanocomposite for effective wastewater treatment and prospective biological applications. Green Chemistry Letters and Reviews. 2024; 17(1). doi: 10.1080/17518253.2024.2321251
22. Buthiyappan A, Abdul Aziz AR, Wan Daud WMA. Recent advances and prospects of catalytic advanced oxidation process in treating textile effluents. Reviews in Chemical Engineering. 2016; 32(1): 1-47. doi: 10.1515/revce-2015-0034
23. Chan SHS, Yeong Wu T, Juan JC, et al. Recent developments of metal oxide semiconductors as photocatalysts in advanced oxidation processes (AOPs) for treatment of dye waste-water. Journal of Chemical Technology & Biotechnology. 2011; 86(9): 1130-1158. doi: 10.1002/jctb.2636
24. Herrmann JM. Heterogeneous photocatalysis: fundamentals and applications to the removal of various types of aqueous pollutants. Catalysis Today. 1999; 53: 115-29.
25. Lee YY, Moon JH, Choi YS, et al. Visible-Light Driven Photocatalytic Degradation of Organic Dyes over Ordered Mesoporous CdxZn1–xS Materials. The Journal of Physical Chemistry C. 2017; 121(9): 5137-5144. doi: 10.1021/acs.jpcc.7b00038
26. Saleh TA. Nanocomposite of carbon nanotubes/silica nanoparticles and their use for adsorption of Pb(II): from surface properties to sorption mechanism. Desalination and Water Treatment. 2015; 57(23): 10730-10744. doi: 10.1080/19443994.2015.1036784
27. Ravishankar TN, Manjunatha K, Ramakrishnappa T, et al. Comparison of the photocatalytic degradation of trypan blue by undoped and silver-doped zinc oxide nanoparticles. Materials Science in Semiconductor Processing. 2014; 26: 7-17. doi: 10.1016/j.mssp.2014.03.027
28. Jasso-Salcedo AB, Palestino G, Escobar-Barrios VA. Effect of Ag, pH, and time on the preparation of Ag-functionalized zinc oxide nanoagglomerates as photocatalysts. Journal of Catalysis. 2014; 318: 170-178. doi: 10.1016/j.jcat.2014.06.008
29. Wang Y, Wang Q, Zhan X, et al. Visible light driven type II heterostructures and their enhanced photocatalysis properties: a review. Nanoscale. 2013; 5(18): 8326. doi: 10.1039/c3nr01577g
30. Fei W, Li H, Li N, et al. Facile fabrication of ZnO/MoS_2 p-n junctions on Ni foam for efficient degradation of organic pollutants through photoelectrocatalytic process. Solar Energy. 2020; 199: 164-172. doi: 10.1016/j.solener.2020.02.037
31. Mustajab MA, Winata T, Arifin P. Lithium doping effect on microstructural and electrical properties of zinc oxide thin film grown by metal-organic chemical vapor deposition. Journal of Physics: Conference Series. 2022; 2243(1): 012054. doi: 10.1088/1742-6596/2243/1/012054
32. Bui QC, Ardila G, Roussel H, et al. Tuneable polarity and enhanced piezoelectric response of ZnO thin films grown by metal–organic chemical vapour deposition through the flow rate adjustment. Materials Advances. 2022; 3(1): 498-513. doi: 10.1039/d1ma00921d
33. Imran M, Ahmad R, Afzal N, et al. Copper ion implantation effects in ZnO film deposited on flexible polymer by DC magnetron sputtering. Vacuum. 2019; 165: 72-80. doi: 10.1016/j.vacuum.2019.04.010
34. Ghalmi L, Bensmaine S, Merzouk CEH. Structural Characterization of ZnO Thin Films Deposited onto Silicon Substrates using Cathodic Magnetron Sputtering. Journal of Renewable Energies. 2023; 26(1). doi: 10.54966/jreen.v26i1.1116
35. Mathew JA, Tsiumra V, Sajkowski JM, et al. Photoluminescence of Europium in ZnO and ZnMgO thin films grown by Molecular Beam Epitaxy. Journal of Luminescence. 2022; 251: 119167. doi: 10.1016/j.jlumin.2022.119167
36. Kennedy OW, Coke ML, White ER, et al. MBE growth and morphology control of ZnO nanobelts with polar axis perpendicular to growth direction. Materials Letters. 2018; 212: 51-53. doi: 10.1016/j.matlet.2017.10.017
37. Chander Joshi B, Chaudhri AK. Sol–Gel-Derived Cu-Doped ZnO Thin Films for Optoelectronic Applications. ACS Omega. 2022; 7(25): 21877-21881. doi: 10.1021/acsomega.2c02040
38. Rabeel M, Javed S, Khan R, et al. Controlling the Wettability of ZnO Thin Films by Spray Pyrolysis for Photocatalytic Applications. Materials. 2022; 15(9): 3364. doi: 10.3390/ma15093364
39. Badawi A, Althobaiti MG, Ali EE, et al. A comparative study of the structural and optical properties of transition metals (M = Fe, Co, Mn, Ni) doped ZnO films deposited by spray-pyrolysis technique for optoelectronic applications. Optical Materials. 2022; 124: 112055. doi: 10.1016/j.optmat.2022.112055
40. Donderis V, Orozco J, Cembrero J, et al. Doped Nanostructured Zinc Oxide Films Grown by Electrodeposition. Journal of Nanoscience and Nanotechnology. 2010; 10(2): 1387-1392. doi: 10.1166/jnn.2010.1869
41. Lghazi Y, Bahar J, Youbi B, et al. Nucleation/Growth and Optical Proprieties of Co-doped ZnO Electrodeposited on ITO

Substrate. Biointerface Research in Applied Chemistry. 2021; 12(5): 6776-6787. doi: 10.33263/briac125.67766787

42. Reyes Tolosa MD, Alajami M, Montero Reguera AE, et al. Influence of seed layer thickness on properties of electrodeposited ZnO nanostructured films. SN Applied Sciences. 2019; 1(10). doi: 10.1007/s42452-019-1293-7
43. Nedzinskas R, Suchodolskis A, Trinkler L, et al. Optical characterization of high-quality ZnO (0002) / Cu (111) epilayers grown by electrodeposition. Optical Materials. 2023; 138: 113650. doi: 10.1016/j.optmat.2023.113650
44. Chatterjee S, Kar AK. Precursor concentration induced nanostructural evolution of electrodeposited ZnO thin films and its effect on their optical and photocatalytic properties. Journal of Materials Science: Materials in Electronics. 2021; 33(11): 8970-8986. doi: 10.1007/s10854-021-07010-1
45. Lim HC, Park E, Shin I, et al. Electrodeposition of Zinc Oxide Nanowires as a Counter Electrode in Electrochromic Devices. Bulletin of the Korean Chemical Society. 2020; 41(3): 358-361. doi: 10.1002/bkcs.11953
46. Kim H, Moon JY, Lee HS. Effect of $ZnCl_2$ concentration on the growth of ZnO by electrochemical deposition. Current Applied Physics. 2012; 12: S35-S38. doi: 10.1016/j.cap.2012.05.036
47. Haga H, Jinnai M, Ogawa S, et al. Rapid fabrication of ZnO film by electrochemical deposition method from aqueous solution. Electrical Engineering in Japan. 2021; 214(2). doi: 10.1002/eej.23320
48. Yamabi S, Imai H. Growth conditions for wurtzite zinc oxide films in aqueous solutions. Journal of Materials Chemistry. 2002; 12(12): 3773-3778. doi: 10.1039/b205384e
49. Londhe PU, Chaure NB. Effect of pH on the properties of electrochemically prepared ZnO thin films. Materials Science in Semiconductor Processing. 2017; 60: 5-15. doi: 10.1016/j.mssp.2016.12.005
50. Xu L, Guo Y, Liao Q, et al. Morphological Control of ZnO Nanostructures by Electrodeposition. The Journal of Physical Chemistry B. 2005; 109(28): 13519-13522. doi: 10.1021/jp051007b
51. El-Shamy A, Elsayed E, Eessaa A, et al. Fabrication, characterization and monitoring the propagation of nanocrystalline zno thin film on ito substrate using electrodeposition technique. Egyptian Journal of Chemistry. 2022. doi: 10.21608/ejchem.2022.126134.5595
52. Liu WL, Chang YC, Hsieh SH, Chen WJ. Effects of Anions in Electrodeposition Baths on Morphologies of Zinc Oxide Thin Films. International Journal of Electrochemical Science. 2013; 8: 983-90.
53. Ghannam H, Bazin C, Chahboun A, et al. Control of the growth of electrodeposited zinc oxide on FTO glass. CrystEngComm. 2018; 20(41): 6618-6628. doi: 10.1039/c8ce01223g
54. Cembrero J, Busquets-Mataix D. ZnO crystals obtained by electrodeposition: Statistical analysis of most important process variables. Thin Solid Films. 2009; 517(9): 2859-2864. doi: 10.1016/j.tsf.2008.10.069
55. Urade AR, Lahiri I, Suresh KS. Graphene Properties, Synthesis and Applications: A Review. JOM. 2022; 75(3): 614-630. doi: 10.1007/s11837-022-05505-8
56. Jain P, Rajput RS, Kumar S, et al. Recent Advances in Graphene-Enabled Materials for Photovoltaic Applications: A Comprehensive Review. ACS Omega. 2024; 9(11): 12403-12425. doi: 10.1021/acsomega.3c07994
57. Yang H, Li J, Yu D, et al. Seed/Catalyst Free Growth and Self-Powered Photoresponse of Vertically Aligned ZnO Nanorods on Reduced Graphene Oxide Nanosheets. Crystal Growth & Design. 2016; 16(9): 4831-4838. doi: 10.1021/acs.cgd.6b00034
58. Messina MM, Picone AL, dos Santos Claro PC, et al. Graphene Grown on Ni Foam: Molecular Sensing, Graphene-Enhanced Raman Scattering, and Galvanic Exchange for Surface-Enhanced Raman Scattering Applications. The Journal of Physical Chemistry C. 2018; 122(16): 9152-9161. doi: 10.1021/acs.jpcc.7b12021
59. Gao C, Zhong K, Fang X, et al. Brief Review of Photocatalysis and Photoresponse Properties of ZnO–Graphene Nanocomposites. Energies. 2021; 14(19): 6403. doi: 10.3390/en14196403
60. Singh P, Shandilya P, Raizada P, et al. Review on various strategies for enhancing photocatalytic activity of graphene based nanocomposites for water purification. Arabian Journal of Chemistry. 2020; 13(1): 3498-3520. doi: 10.1016/j.arabjc.2018.12.001
61. Yoo DH, Cuong TV, Luan VH, et al. Photocatalytic Performance of a Ag/ZnO/CCG Multidimensional Heterostructure Prepared by a Solution-Based Method. The Journal of Physical Chemistry C. 2012; 116(12): 7180-7184. doi: 10.1021/jp210216w
62. Cai R, Wu J gen, Sun L, et al. 3D graphene/ZnO composite with enhanced photocatalytic activity. Materials & Design. 2016; 90: 839-844. doi: 10.1016/j.matdes.2015.11.020
63. Messina MM, Coustet ME, Ubogui J, et al. Simultaneous Detection and Photocatalysis Performed on a 3D Graphene/ZnO Hybrid Platform. Langmuir. 2020; 36(9): 2231-2239. doi: 10.1021/acs.langmuir.9b03502

64. Lv S, Geng P, Wang H, et al. In Situ Construction of ZnO/Ni_2S_3 Composite on Ni Foam by Combing Potentiostatic Deposition with Cyclic Voltammetric Electrodeposition. Micromachines. 2021; 12(7): 829. doi: 10.3390/mi12070829
65. Zhong Y, Yang S, Fang Y, et al. In situ constructing Ni foam supported ZnO-CdS nanorod arrays for enhanced photocatalytic and photoelectrochemical activity. Journal of Alloys and Compounds. 2021; 868: 159187. doi: 10.1016/j.jallcom.2021.159187
66. Miao F, Wu W, Miao R, et al. Graphene/nano-ZnO hybrid materials modify Ni-foam for high-performance electrochemical glucose sensors. Ionics. 2018; 24(12): 4005-4014. doi: 10.1007/s11581-018-2539-x
67. Abbas SI, Alattar AM, Al-Azawy AA. Enhanced ultraviolet photodetector based on Al-doped ZnO thin films prepared by spray pyrolysis method. Journal of Optics. 2023; 53(1): 396-403. doi: 10.1007/s12596-023-01164-3
68. Bidault F, Brett DJL, Middleton PH, et al. A new application for nickel foam in alkaline fuel cells. International Journal of Hydrogen Energy. 2009; 34(16): 6799-6808. doi: 10.1016/j.ijhydene.2009.06.035
69. Zhang F, Lan J, Yang Y, et al. Adsorption behavior and mechanism of methyl blue on zinc oxide nanoparticles. Journal of Nanoparticle Research. 2013; 15(11). doi: 10.1007/s11051-013-2034-2
70. He X, Yang Y, Li Y, et al. Effects of structure and surface properties on the performance of ZnO towards photocatalytic degradation of methylene blue. Applied Surface Science. 2022; 599: 153898. doi: 10.1016/j.apsusc.2022.153898
71. Waghchaure RH, Adole VA, Jagdale BS. Photocatalytic degradation of methylene blue, rhodamine B, methyl orange and Eriochrome black T dyes by modified ZnO nanocatalysts: A concise review. Inorganic Chemistry Communications. 2022; 143: 109764. doi: 10.1016/j.inoche.2022.109764
72. Prerna, Agarwal H, Goyal D. Photocatalytic degradation of textile dyes using phycosynthesised ZnO nanoparticles. Inorganic Chemistry Communications. 2022; 142: 109676. doi: 10.1016/j.inoche.2022.109676
73. Saleh TA, Gondal MA, Drmosh QA. Preparation of a MWCNT/ZnO nanocomposite and its photocatalytic activity for the removal of cyanide from water using a laser. Nanotechnology. 2010; 21(49): 495705. doi: 10.1088/0957-4484/21/49/495705

EnPress Publisher

Characterization and Application of Nanomaterials 2024, 7(1), 5523.
https://doi.org/10.24294/can.v7i1.5523

Article

Photocatalytic degradation properties

Aiza Maqbool

Department of Physics, University of Agriculture Faisalabad, Faisalabad 38040, Pakistan; aizamaqbool12@gmail.com

CITATION

Maqbool A. Photocatalytic degradation properties. Characterization and Application of Nanomaterials. 2024; 7(1): 5523. https://doi.org/10.24294/can.v7i1.5523

ARTICLE INFO

Received: 28 March 2024
Accepted: 23 April 2024
Available online: 31 May 2024

Abstract: Photocatalysis, an innovative technology, holds promise for addressing industrial pollution issues across aqueous solutions, surfaces, and gaseous effluents. The efficiency of photodegradation is notably influenced by light intensity and duration, underscoring the importance of optimizing these parameters. Furthermore, temperature and pH have a significant impact on pollutant speciation, surface chemistry, and reaction kinetics; therefore, process optimization must consider these factors. Photocatalytic degradation is an effective method for treating water in environmental remediation, providing a flexible and eco-friendly way to eliminate organic contaminants from wastewater. Selectivity in photocatalytic degradation is achieved by a multidisciplinary approach that includes reaction optimization, catalyst design, and profound awareness of chemical processes. To create efficient and environmentally responsible methods for pollution removal and environmental remediation, researchers are working to improve these components.

Keywords: catalyst dosage; pollutant degradation; environmental remediation; catalytic activity; reaction kinetics; water treatment; catalyst optimization; sustainable chemistry; environmental impact assessment

Introduction

Photocatalytic degradation refers to a process in which a substance is broken down into smaller, less harmful compounds under the influence of light and a photocatalyst. This phenomenon is often employed in environmental and industrial applications for the removal or transformation of pollutants, contaminants, or other undesirable substances. Here are some key aspects of photocatalytic degradation properties:

1. Photocatalyst

The photocatalyst is a material that facilitates the degradation process when exposed to light. The novel oxidation process known as photocatalysis works by using sunlight to cause electron-hole pairs to form on a photocatalyst's surface. An enhancement in this field is represented by composite photocatalysts, which improve doping, coupling, and sensitization of individual photocatalysts like ZnO, AgO_2, and TiO_2. These developments could lead to more innovative uses of environmental therapy [1]. Titanium dioxide (TiO_2) and zinc oxide (ZnO) are commonly used photocatalysts due to their stability, efficiency, and non-toxic nature. They are suitable for photocatalytic applications due to their broad bandgap, especially when subjected to ultraviolet (UV) light [2].

2. Light source

Typically, photocatalytic reactions require ultraviolet light to activate the catalyst.

However, advancements in photocatalytic materials and technologies have expanded the range of light sources to include visible light, making the process more practical and applicable in various settings. Photocatalysts produce electron-hole pairs when exposed to UV light, which excites electrons from the valence band to the conduction band. The breakdown of organic contaminants or the creation of beneficial compounds can result from these charge carriers engaging in redox reactions with adsorbed species on the oxide's surface [3]. Electrons in the valence band may be induced to move to the conduction band, forming a hole in the valence band, when a material absorbs photons with energy equal to or greater than the bandgap energy. The generation of superoxide radicals (O2•−) is triggered by interactions between electrons in the conduction band and oxygen molecules on the crystal surface [4]. Concurrently, water molecules on the crystal surface may interact with positively charged holes in the valence band, resulting in oxidation processes that generate hydroxyl radicals (·OH) [5]. **Figure 1** shows the process of photocatalytic water splitting [6]. These reactive oxygen species (ROS), which break down dye molecules and other organic pollutants, are essential to the photooxidation process. Some instances of ROS include superoxide and hydroxyl radicals [7].

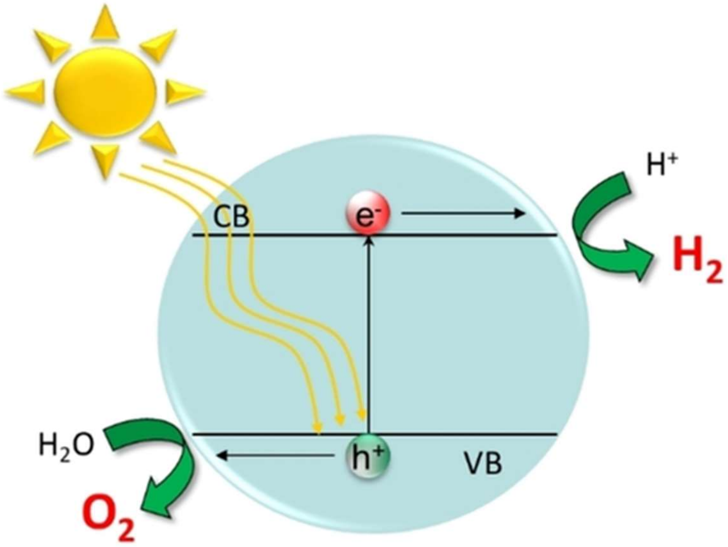

Figure 2. Process of Photocatalytic water splitting.

3. Substrate

The substance targeted for degradation is referred to as the substrate. Photocatalytic degradation is effective for various pollutants, including organic compounds, dyes, pesticides, and even some inorganic contaminants. TiO_2 [8], Ag, and ZnO [9] nanoparticles are the most commonly used substrates in the photocatalytic degradation of dyes in water and are effective due to their antimicrobial properties, UV radiation blocking capabilities, and photocatalytic characteristics [9]. These nanoparticles are commonly employed in the textile industry for various purposes such as self-cleaning, UV protection, and antibacterial properties. By harnessing their photocatalytic abilities, these nanoparticles facilitate the degradation of dyes present in water, thus aiding in water purification processes [1,2]. This multifunctional approach not only removes dyes but also provides additional benefits such as microbial control and UV protection, making it a versatile solution for water treatment and environmental remediation [10]. Heterogeneous photocatalysis has undergone a significant change in the last ten years, especially in the application of titania in its anatase form [1,2]. The majority of the applications for this photocatalyst were moderate oxidation processes in gaseous or liquid organic phases. But in more recent times, there has been a shift towards using it for the complete oxidation and breakdown of different organic chemicals and contaminants, especially in situations with humid air or water [1,2,11].

Reaction Mechanism: The photocatalytic degradation process involves the generation of ROS on the surface of the photocatalyst when exposed to light. These ROS, such as hydroxyl radicals (•OH), superoxide radicals ($O_2^{\bullet -}$), and others, then react with the substrate molecules, leading to their degradation into simpler and less harmful byproducts. The production of OH° radicals resulting from the presence of water has been ascribed to this alteration in photocatalytic behavior. This process's mechanism is based on the interaction of titania with water, which produces OH• radicals. These radicals are essential for promoting the complete oxidation and destruction of organic molecules and environmental contaminants. For instance, water molecules react with e^--hole pairs on the TiO_2 surface and generate radicals. These highly reactive species are the cause of photocatalytic degradation of organic molecules [12] through Equations (1)–(4):

$$\mathrm{TiO_2} + \mathrm{hv} \rightarrow \mathrm{TiO_2}(\mathrm{e^-} + \mathrm{h^+}) \text{ (Electron-Hole pair generation)} \quad (1)$$

$$\mathrm{TiO_2}(\mathrm{e^-}) + \mathrm{O_2} \rightarrow \mathrm{O_2^{\cdot -}} \text{ (Superoxide radical Anion)} \quad (2)$$

$$\mathrm{TiO_2}(\mathrm{h^+}) + \mathrm{H_2O} \rightarrow \mathrm{OH} \text{ (Hydroxyl radical)} \quad (3)$$

$$\mathrm{TiO_2}(\mathrm{e^-} + \mathrm{h^+}) + \text{Organic pollutant} \rightarrow \text{Degraded product} \quad (4)$$

4. Factors influencing efficiency

4.1. Catalyst surface area

A larger surface area provides more active sites for the photocatalytic reaction. Surface area can be increased by different strategies like coating, treating plasma, heating or cooling, and changing the shapes (thin films, cylindrical, etc.). Using ionic liquids for surface modification offers dual advantages as both a supply and an agent for enhancing the photocatalytic properties of materials. Through the introduction of external elements or functional groups onto the surface of photocatalysts, such as nitrogen or sulfur in bismuth oxyhalides, additional active sites can be created, impacting the material's electrical properties positively.

When a semiconductor material is illuminated, positive charges (h^+) are produced that combine with OH-anions to produce hydroxyl radicals. When water and oxygen are available, these radicals are crucial for the oxidation of organic materials [13]. Therefore, increasing the coating surface area helps to increase the photocatalytic activity of the coating. The increased specific surface area boosts the film's hydroxyl group concentration. When a semiconductor is exposed to light in the context of heterogeneous photocatalysis, electron-hole pairs (e and h^+) are produced. Hydroxyl radicals are produced when the negatively charged OH ions and positively charged holes (h^+) interact. The hydroxyl radicals generated at the photocatalyst's surface function as oxidizing agents, which ultimately increase the efficiency of the photocatalytic activity [14]. Additionally, the incorporation of organic groups facilitates improved charge carrier separation and enhanced adsorption of contaminants, thereby increasing surface area and photocatalytic efficiency. This surface modification process aims to capture photogenerated electrons, thus inhibiting the recombination of electron-hole pairs generated during photoinduction. Ultimately, the utilization of ionic liquids as a means of surface modification presents a versatile approach to optimize photocatalytic performance, leveraging their unique properties to enhance material functionality and effectiveness in environmental remediation and other applications [15].

4.2. Light intensity and duration

The duration and intensity of light are important factors in photodegradation, especially in photocatalysis, where light is utilized to start chemical reactions. Higher light intensity and longer exposure times generally enhance the degradation process. Through photocatalysis, a substance is activated by light, speeding up chemical reactions without permanently altering the catalyst's chemical composition. In contrast, conventional thermal catalysts require heat to activate them. The activation mode is the primary difference: photosensitive catalysts are activated by light, whereas thermal catalysts are activated by heat [16]. The rate of photodegradation is directly impacted by the light source intensity. Since more photons are available to activate the photocatalyst and produce reactive species, higher light intensities usually lead to faster degradation rates. Beyond a certain optimal intensity, nevertheless, additional increases might not appreciably speed up the rate of degradation. The optimal intensity varies based on the target pollutant and the particular photocatalyst. Another important consideration is the period spent in the light. Extended exposure periods typically result in higher deterioration rates because the photocatalyst absorbs more photons over time, producing a greater number of reactive species. Like light intensity, there might be an ideal time frame, though, after which the rate of degradation plateaus or increases just slightly.

Reaction kinetics principles lead to the link between light intensity, duration, and photodegradation rate. First-order kinetics, which states that the rate of reaction is proportional to the concentration of the pollutant and the concentration of the active species produced by the photocatalyst, is typically followed by the photodegradation process. The concentration of these active species is influenced by both the length and intensity of the light, which affects the overall response rate. Although photodegradation rates can be increased by longer exposure times and stronger light, there are realistic concerns about cost and energy efficiency. In large-scale applications, it might not be practical or cost-effective to use extremely high-intensity light sources or extended exposure times. To attain the intended degradation rate while consuming the least amount of energy, light intensity and duration must be optimized.

4.3. pH and temperature

The pH of the solution and the temperature can affect the rate of photocatalytic degradation. Advanced oxidation processes, or AOPs, are finding a broader application in environmental applications such as wastewater cleaning. These reactions are based on oxidation by reactive species and are usually catalyzed by photocatalysts like ZnO, TiO_2, CdS, Co_3O_4, or WO_3. These semiconductor photocatalysts undergo photoexcitation when they come into contact with an intense light source and an oxidizing agent such as air or oxygen, which produces reactive species [17]. The organic contaminants in the wastewater are then efficiently oxidized by these reactive species, leading to their elimination. The semiconductor used, the pH of the solution, and the light source intensity are some of the variables that affect the process efficiency [18]. The adsorption and interaction between the target pollutants and the photocatalyst are influenced by pH, which also changes their surface charges. The ideal pH range for many photocatalytic processes is one in which the photocatalyst surface charge and chemical makeup are most advantageous to the degradation process. Reduced efficiency may result from pH deviation because of variations in surface charge, surface chemistry, or pollutant speciation. The stability and solubility of the photocatalyst, which in turn impacts its duration and efficacy in the degradation process, can also be influenced by pH.

Temperature modifies the reaction kinetics, which affects how quickly photodegradation processes occur. Since more energy is available to activate surface reactions at higher temperatures, reactions often proceed more quickly. Nevertheless, overly high temperatures may cause the photocatalyst and the intended pollutants to thermally degrade, which would reduce the process' overall effectiveness. The ideal temperature range is frequently found through experimentation and can change based on the particular photocatalyst and contaminants present. Reaction kinetics may also be affected by temperature changes in the physical characteristics of the reaction environment, such as the viscosity and diffusion rates of reactants and products.

4.4. Catalyst dosage and Pollutant degradation

Catalyst dosage plays a crucial role in pollutant degradation efficiency. Ongoing research and literature reviews indicate that an appropriate catalyst dosage can significantly enhance degradation rates, leading to more effective pollutant removal. the need to strike a balance between increased catalyst dosage and economic feasibility. Excessive dosages may not proportionally improve degradation rates and can lead to diminishing returns in terms of cost-effectiveness. Photocatalysis using nanoparticles (NPs) is a promising method for dye removal from water due to their exceptional and highly tunable surface properties compared to bulk materials. NPs offer a wider scope in catalytic processes thanks to their unique surface characteristics, and they have higher diffusion rates coupled with lower reinforcing capabilities, all of which collectively enhance their catalytic performance [8,9,19,20]. Like the potential of rGO-250 as a robust photocatalyst for dye degradation, highlighting its adaptability and efficiency in well-defined circumstances that require pH, dye concentration, catalyst dosage, and recyclability into consideration. These results facilitate the creation of effective and long-lasting methods for environmental remediation that make use of cutting-edge substances like catalysts based on graphene [21].

5. Challenges

5.1. Selectivity

Ensuring that the photocatalytic process selectively targets the desired pollutants without causing unintended side reactions. The method of utilizing photocatalysts and light energy to decompose organic pollutants in wastewater or other environmental contaminants is known as photocatalytic degradation. Selectivity, or the photocatalyst's capacity to preferentially target and break down particular contaminants while mostly unaffected by other chemicals, is a crucial component of this process. Because it maximizes the effectiveness of pollution removal while minimizing the formation of hazardous byproducts, selective photocatalytic degradation is desired. Selectivity is attained via several factors: catalyst choice, reaction conditions, targeted modification, light source, and controlled reaction pathways.

Different photocatalysts exhibit varying affinities for different types of pollutants. By selecting a suitable photocatalyst based on the nature of the contaminants, researchers can enhance selectivity. Parameters such as pH, temperature, and the presence of co-catalysts or electron donors can influence the selectivity of the photocatalytic process. Optimizing these conditions can help tailor the degradation process toward specific pollutants. Surface modification of photocatalysts with specific functional groups or nanoparticles can enhance their affinity towards certain pollutants, thus improving selectivity. The wavelength and intensity of the light source used for photoexcitation can also influence selectivity. Tuning the light source to match the absorption spectrum of the target pollutant or photocatalyst can enhance the efficiency of degradation. Understanding the reaction pathways involved in photocatalytic degradation allows researchers to design strategies that promote the selective degradation of target pollutants while minimizing the formation of unwanted byproducts.

5.2. Catalyst recyclability

Strategies for reusing and recycling the photocatalyst to improve the economic and environmental sustainability of the process. The potential of catalyst recyclability is one of the major benefits of photocatalytic degradation. When subjected to light and an oxidizing agent, photocatalytic degradation is the process of breaking down organic contaminants in wastewater using catalysts, usually semiconductors such as TiO_2 [22], ZnO [23], CdS, Co_3O_4, or WO_3. By absorbing photons, these catalysts create electron-hole pairs, which when combined with oxygen and water, produce extremely reactive species like hydroxyl radicals. These free radicals can oxidize and break down organic contaminants into innocuous byproducts like water and CO_2. The catalyst may frequently be recovered and utilized again after the degrading process, which lowers operating costs and minimizes waste. To extract the catalyst from the wastewater that has been treated, a variety of techniques, including centrifugation and filtration, can be used. Furthermore, methods such as catalyst immobilization onto support materials can improve recyclability by limiting catalyst loss in the process. Overall, the combination of photocatalytic degradation and catalyst recyclability offers a promising approach for efficient and sustainable wastewater treatment, contributing to environmental protection and resource conservation.

5.3. Scale-up

Transitioning from laboratory-scale experiments to large-scale applications poses challenges in maintaining efficiency and cost-effectiveness. Many semiconductor materials have been investigated for photocatalytic water splitting since 1972. Their limited ability to absorb visible light has presented a significant obstacle, impeding their practicality for widespread use [24]. Significant progress has been achieved in the last few years in the identification and synthesis of semiconductor materials specifically designed for solar water splitting, especially in the visible light spectrum [25]. Scale-up in photocatalytic degradation involves transitioning laboratory-scale processes to larger industrial or municipal scales. This scaling-up process requires careful consideration of various factors to ensure efficient and effective operation:

Reactor Design: Designing reactors suitable for larger volumes while maintaining optimal contact between the photocatalyst and wastewater is crucial. Different reactor configurations, such as slurry reactors, fixed-bed reactors, or immobilized photocatalyst reactors, may be employed depending on the specific requirements.

Light Source: Ensuring adequate and uniform illumination across the entire reactor volume is essential. This may involve using powerful and efficient light sources, such as UV lamps or natural sunlight, along with appropriate light distribution mechanisms.

Catalyst Preparation: Developing scalable methods for preparing and immobilizing photocatalysts onto suitable supports or substrates is necessary. These methods should ensure consistent catalyst properties and performance at larger scales.

Mass Transfer: Optimizing the mass transfer of pollutants to the catalyst surface and products away from it is critical for efficient degradation. This may involve adjusting flow rates, agitation methods, or reactor geometries to minimize mass transfer limitations.

Operational Parameters: Identifying and optimizing operational parameters such as pH, temperature, catalyst loading, and residence time for larger-scale systems is essential to maximize degradation efficiency while minimizing operational costs.

Safety and Environmental Considerations: Ensuring safety protocols are in place for handling potentially hazardous materials and byproducts and assessing any potential environmental impacts of the scaled-up process.

Overall, successful scale-up of photocatalytic degradation processes requires interdisciplinary collaboration between scientists, engineers, and stakeholders to address technical, economic, and regulatory challenges while realizing the full potential of this environmentally friendly wastewater treatment technology.

Conflict of interest: The author declares no conflict of interest.

Abbreviations

TiO_2	Titanium dioxide
ZnO	Zinc oxide
UV	Ultraviolet
$O_2^{\bullet-}$	Superoxide radicals
$\cdot OH$	Hydroxyl radicals
ROS	Reactive oxygen species
CO_2	Carbon dioxide
e^+	Electron
h^+	Hole
Ag	Silver
AOPs	Advanced oxidation processes
CdS	Cadmium sulfide
WO_3	Tungsten oxide
Co_3O_4	Cobalt oxide
H_2O	Water
rGO	Graphene oxide

References

1. Maqbool A, Shukrullah S, Kashif F, et al. Photocatalytic response of plasma functionalized and sonochemically TiO2/BiOBr coated fabrics for self-cleaning application. AIP Advances. 2023; 13(12). doi: 10.1063/5.0182513
2. Kashif Z, Naz MY, Maqbool A, et al. Study of dual Z-scheme photocatalytic response of TiO2/Ag/ZnO coating on plasma-modified cotton fabric for self-cleaning application. AIP Advances. 2024; 14(1). doi: 10.1063/5.0187410
3. Nam Y, Lim JH, Ko KC, et al. Photocatalytic activity of TiO_2 nanoparticles: a theoretical aspect. Journal of Materials Chemistry A. 2019; 7(23): 13833-13859. doi: 10.1039/c9ta03385h
4. Karunakaran C, Abiramasundari G, Gomathisankar P, et al. Preparation and characterization of ZnO–TiO_2 nanocomposite for photocatalytic disinfection of bacteria and detoxification of cyanide under visible light. Materials Research Bulletin. 2011; 46(10): 1586-1592. doi: 10.1016/j.materresbull.2011.06.019
5. Verbič A, Gorjanc M, Simončič B. Zinc Oxide for Functional Textile Coatings: Recent Advances. Coatings. 2019; 9(9): 550. doi: 10.3390/coatings9090550
6. Marschall R. 50 Years of Materials Research for Photocatalytic Water Splitting. European Journal of Inorganic Chemistry. 2021; 2021(25): 2435-2441. doi: 10.1002/ejic.202100264
7. Rashid MM, Simončič B, Tomšič B. Recent advances in TiO_2-functionalized textile surfaces. Surfaces and Interfaces. 2021; 22: 100890. doi: 10.1016/j.surfin.2020.100890
8. Lin Z, Jiang X, Xu W, et al. The effects of water, substrate, and intermediate adsorption on the photocatalytic decomposition of air pollutants over nano-TiO_2 photocatalysts. Physical Chemistry Chemical Physics. 2024; 26(2): 662-678. doi: 10.1039/d3cp04350a
9. Lanjwani MF, Tuzen M, Khuhawar MY, et al. Trends in photocatalytic degradation of organic dye pollutants using nanoparticles: A review. Inorganic Chemistry Communications. 2024; 159: 111613. doi: 10.1016/j.inoche.2023.111613
10. Ansari M, Sajjadi SA, Sahebian S, et al. Photocatalytic and Antibacterial Activity of Silver/Titanium Dioxide/Zinc Oxide Nanoparticles Coated on Cotton Fabrics. ChemistrySelect. 2020; 5(27): 8370-8378. doi: 10.1002/slct.202001655
11. Herrmann JM, Guillard C. Photocatalytic degradation of pesticides in agricultural used waters. Comptes Rendus de l'Académie des Sciences-Series IIC-Chemistry. 2000; 3(6): 417-422. doi: 10.1016/S1387-1609(00)01137-3
12. Yang H, Yang B, Chen W, et al. Preparation and Photocatalytic Activities of TiO_2-Based Composite Catalysts. Catalysts. 2022; 12(10): 1263. doi: 10.3390/catal12101263

13. Page K. Photocatalytic Thin Films: Their Characterisation and Antimicrobial Properties [PhD thesis]. UCL (University College London); 2009.
14. Chan CC, Chang CC, Hsu WC, et al. Photocatalytic activities of Pd-loaded mesoporous TiO_2 thin films. Chemical Engineering Journal. 2009; 152(2-3): 492-497. doi: 10.1016/j.cej.2009.05.012
15. Wang Y, Deng K, Zhang L. Visible Light Photocatalysis of BiOI and Its Photocatalytic Activity Enhancement by in Situ Ionic Liquid Modification. The Journal of Physical Chemistry C. 2011; 115(29): 14300-14308. doi: 10.1021/jp2042069
16. Sadeghfar F, Zalipour Z, Taghizadeh M, et al. Photodegradation processes. In: Ghaedi M (editor). Interface Science and Technology. Academic Press; 2021. Volume 32. pp. 55-124. doi: 10.1016/b978-0-12-818806-4.00013-9
17. Sandhu N, Sandhu N, Kumar C, et al. Critical Review on Titania-Based Nanoparticles: Synthesis, Characterization, and Application as a Photocatalyst. Chemistry Africa. 2024; 7(4): 1-20. doi:10.1007/s42250-023-00875-1
18. Alkaim AF, Aljeboree AM, Alrazaq NA, et al. Effect of pH on Adsorption and Photocatalytic Degradation Efficiency of Different Catalysts on Removal of Methylene Blue. Asian Journal of Chemistry. 2014; 26(24): 8445-8448. doi: 10.14233/ajchem.2014.17908
19. Sudapalli AM, Shimpi NG. Tetragonal SnO_2 Nanoparticles: An Efficient Photocatalyst for the Degradation of Hazardous Ionic Dyes. ChemistrySelect. 2023; 8(1). doi: 10.1002/slct.202203310
20. Shakil AR, Begum ML, Shaikh MAA,et al. Jute Fiber Reinforced Hydrogel Composite for Removal of Methylene Blue Dye from Water. Dhaka University Journal of Science. 2022; 70(2): 59-64. doi: 10.3329/dujs.v70i2.62608
21. Shabil Sha M, Anwar H, Musthafa FN, et al. Photocatalytic degradation of organic dyes using reduced graphene oxide (rGO). Scientific Reports. 2024; 14(1). doi: 10.1038/s41598-024-53626-8
22. Yusuff AS, Popoola LT, Gbadamosi AO, et al. Coal fly ash-supported ZnO-promoted TiO_2 towards UV photocatalytic degradation of anthraquinone dye: Parametric optimization, kinetics and mechanism studies. Materials Today Communications. 2024; 38: 107999. doi: 10.1016/j.mtcomm.2023.107999
23. Gong H, Geng C, Wang R, et al. Shell-Fe/ZnO: A recyclable catalyst with Fe-doped ZnO shell structure for photocatalytic oxidative degradation of tetracycline hydrochloride. Applied Surface Science. 2024; 655: 159653. doi: 10.1016/j.apsusc.2024.159653
24. Miseki Y, Kato H, Kudo A. Water Splitting into H_2 and O_2 over $Ba_5Nb_4O_{15}$ Photocatalysts with Layered Perovskite Structure Prepared by Polymerizable Complex Method. Chemistry Letters. 2006; 35(9): 1052-1053. doi: 10.1246/cl.2006.1052
25. Sivula K, van de Krol R. Semiconducting materials for photoelectrochemical energy conversion. Nature Reviews Materials. 2016; 1(2). doi: 10.1038/natrevmats.2015.10

Characterization and Application of Nanomaterials 2024, 7(1), 4306.
https://doi.org/10.24294/can.v7i1.4306

Review

Application of nanotechnology in periodontal therapy: Narrative review

Svitlana Boitsaniuk[1], **Mariana Levkiv**[1,*], **Orest Kochan**[2,3]

[1] Department of Dental Therapy, Dean of Dental Faculty, I. Horbachevsky Ternopil National Medical University, 46000 Ternopil, Ukraine
[2] School of Computer Science, Hubei University of Technology, Wuhan 430068, China
[3] Department of Measuring Information Technologies, Institute of Computer Technologies, Automation and Metrology, Lviv Polytechnic National University, 79013 L'viv, Ukraine
*** Corresponding author:** Mariana Levkiv, levkiv@tdmu.edu.ua

CITATION

Boitsaniuk S, Levkiv M, Kochan O. Application of nanotechnology in periodontal therapy: Narrative review. Characterization and Application of Nanomaterials. 2024; 7(1): 4306.
https://doi.org/10.24294/can.v7i1.4306

ARTICLE INFO

Received: 19 January 2024
Accepted: 20 February 2024
Available online: 11 April 2024

Abstract: The potential of nanotechnology to improve human health, optimize natural resource utilization, and reduce environmental pollution is remarkable. With the ever-growing advancement in dentistry, one of the breakthroughs is using nanotechnology. Nanotechnology in periodontics has touched every aspect of treatment modality, from non-surgical therapy to implant procedures, including regenerative procedures. Understanding their mechanism plays a pivotal role in more efficient usage of nanotechnology, better treatment procedures, and eventually better outcomes. In this paper, we review the application of nanotechnology in periodontal therapy. We performed the search for papers in Scopus using the key words and phrases as follows: "nanodentistry"; "dentistry and nanotechnology"; "dentistry and nanoparticles"; "dentistry and nanomedicine"; "dentistry and nanorobots". There were found 530 papers in total. Some papers belonged to two and more categories. It is revealed that the number of papers versus year does not follow any specific pattern, but the cumulative amount of papers versus year is fitted with the exponential regression. There were also selected papers using certain inclusion/exclusion criteria. Only the selected papers were analyzed. Nanomedicine is subjected to intensive studies nowadays. There are some promising results that will likely be implemented into praxis soon in the fields of medical diagnostics and clinical therapeutics. The appearance of nanotechnology can have a considerable impact on the treatment of periodontal diseases.

Keywords: nano dentistry; nanoparticle; nanotechnology; periodontal tissue; periodontal disease; treatment options

1. Introduction

Modern materials science is developing at a very fast pace. This development is felt in almost all areas of science and technology. New materials for sensors [1,2] and medical applications [3,4] evolve. Novel materials create excellent opportunities for researchers and engineers to solve long lasting problems. On the other hand, the conservative fields suffer from stagnation for many decades because the existing materials are prone to degradation [5], while new materials have not achieved the required level of performance yet. So to solve the problem of materials, a quite complex design of sensors and measurement systems is required [6,7]. Another topical direction of studies is the internet of things [8,9], which also has medical applications [9]. In this paper, we focus our attention only on nanomaterials for dentistry.

The field of dentistry is closely connected to materials and often requires the development of new therapeutic materials, along with the necessary equipment, instruments, and treatment techniques. Developing new materials and technologies can solve issues in traditional dental care [10]. Conventional dental treatment can often be uncomfortable, painful, and anxiety-inducing for patients due to invasive procedures such as carious cavity preparation, filling, and tooth extraction. Nano dentistry presents a promising alternative to these procedures by utilizing nanosized materials, tissue engineering, and dental nanorobots to diagnose, treat, and prevent oral and dental diseases. Patients may experience discomfort and hypersensitivity to dentine during recovery from procedures like root scaling, planning, and curettage of periodontal pockets. However, nanorobotics aims to overcome the drawbacks of conventional medical techniques. For instance, inserting medicaments into periodontal pockets and then protecting them with periodontal dressing may cause discomfort for a patient during eating or communicating, and it can also disrupt the mouth's esthetic appearance. Additionally, medicaments may seep out of the pocket. To combat these issues, nanoparticles can be carriers for targeted drug delivery.

Nanotechnology is the field of science and technology that involves manipulating materials at the scale of nanometers. The term 'nano' comes from the Greek 'Nanos,' which means 'dwarf'. Nobel Prize-winning physicist Richard Feynman introduced the concept of nanotechnology in a 1959 lecture titled "There is a Plenty of Room at the Bottom." He ended the lecture by concluding, "This is a development which I think cannot be avoided" [11–13]. In 1974, Norio Taniguchi coined the term 'nanotechnology' to refer to the ability to precisely engineer materials with the dimension of nanometers. Dogra et al. [14] and Hamissi et al. [15] first introduced the field of «nanomedicine». At the molecular level, nanostructures and nanodevices are used to observe, control, and treat biological systems within the human body [16,17]. It improved materials' mechanical and physical properties and introduced new diagnostic modalities and nanodelivery systems, revolutionizing the medical and dental fields [18]. The increasing interest in using nanotechnology in dentistry has led to the emergence of a new field called 'nano dentistry' [19,20]. Nano dentistry can be approached from two different perspectives. One is called the "Bottom-up approach," where atomic elements are combined to build particles. The other approach is the "Top-Down approach," which involves using equipment to create a mechanical nanoscale [21–23]. Nanotechnology has a wide range of applications for preventing, diagnosing, and treating oral diseases.

Periodontitis and gingivitis are prevalent periodontal diseases affecting millions of people worldwide [24]. Conventional treatment methods for these diseases involve mechanical debridement, antimicrobial agents, and surgery. However, the emergence of nanotechnology has opened up new possibilities in treating periodontal diseases. Periodontics has been used to develop novel drug delivery systems, such as nanofibers and nanoparticles, which can penetrate deep into the periodontal tissues and release drugs over an extended period. Moreover, nanotechnology has also been utilized to develop antimicrobial agents, which can effectively eliminate periodontal pathogens while minimizing toxicity and side effects. For example, silver nanoparticles have shown promising results in inhibiting the growth of periodontal pathogens, such as *Porphyromonas gingivalis* and *Aggregatibacter actinomycetemcomitans*. In addition, nanotechnology has been applied in developing tissue engineering and regenerative medicine techniques, which aim to restore damaged or lost periodontal tissues. Nanofibrous scaffolds and nanoparticles have been used to promote cell adhesion, proliferation, and differentiation, forming new periodontal tissues. Integrating nanotechnology in the treatment modalities for periodontal diseases represents a significant advancement of periodontics and has a wide range of use (**Figure 1**). It offers new avenues for managing and preventing periodontal diseases, improving oral health outcomes that improve patients' quality of life.

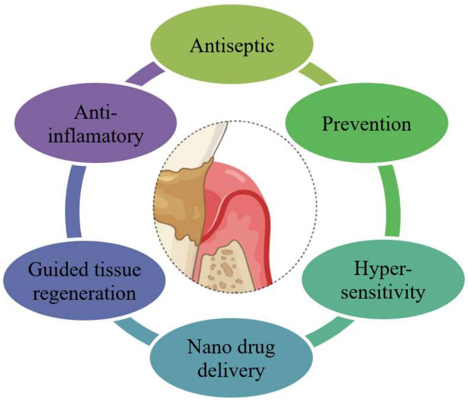

Figure 1. Areas of applications of nanotechnology in periodontics.

This review article aims to provide recent updates on nanotechnology-based approaches for periodontal disease therapy. Additionally, the present review will help the reader understand nanoscience and its benefits and limitations by addressing its ethical, social, and health implications.

2. The technique of data preparation

For this paper, we chose the form of narrative review [25]. For this narrative review, the search was performed within the Scopus database to identify the number of papers found for the keywords and phrases such as "nanodentistry"; "dentistry and nanotechnology"; "dentistry and nanoparticles"; "dentistry and nanomedicine"; "dentistry and nanorobots". The search considered works published in Scopus till 5th of November 2023 (included). Only relevant literature in English from the electronic search was selected for the present review. The nanoparticles had to be used in periodontics.

The found papers were subjected to the inclusion and exclusion criteria. The inclusion criteria are as follows: i) use of nanoparticles in periodontics; ii) full text journal articles written in English; iii) books and book chapters written in English; iv) scientific works published in 2013 and later (older works are mentioned only in the Introduction chapter).

The exclusion criteria are as follows: i) case reports (clinical trials); ii) conference papers; iii) materials published earlier than 2013; iv) randomized controlled studies; v) editorials; vi) errata. The search was carried out in Scopus, using the keywords and phrases "nanodentistry", "dentistry and nanotechnology", "dentistry and nanoparticles", "dentistry and nanomedicine", "dentistry and nanorobots".

In total, 530 records were found.

1) We excluded the types of papers that fit the exclusion criteria.
2) The first and second co-authors analyzed the remaining records for compliance with the inclusion and exclusion criteria. Some points were clarified with additional hand searching, in particular the peculiarities of the use of triclosan,

bone grafting, and data about periodontal disease. There were 27 additional records identified from the hand search.

3) All selected records were distributed among all authors for reading of the full text articles and preparation of the manuscript. The procedure is generalized in **Figure 2** in the PRISMA flowchart.

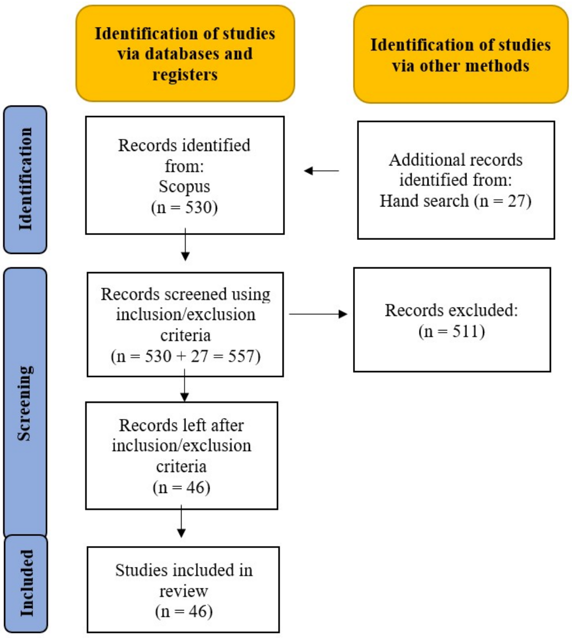

Figure 2. PRISMA (Preferred reporting items for systematic reviews and meta-analyses) flow diagram of inclusion/exclusion criteria.

3. Results

The results of the search are summarized in **Table 1** and explained in details below this table.

Table 1. Results of the search.

	Nano-dentistry	Dentistry and nanotechnology	Dentistry and nanoparticles	Dentistry and nanomedicine	Dentistry and nanorobots	Total (along row)
Nanodentistry	53	18	8	18	2	99
Dentistry and nanotechnology	18	148	19	15	0	200
Dentistry and nanoparticles	8	19	169	4	0	200
Dentistry and nanomedicine	18	15	4	75	0	112
Dentistry and nanorobots	2	0	0	0	1	3

The first column contains key words as well as the first row. The numbers on intersections of rows and columns indicate the number of papers belonging to both key words. The intersection of the key word along the row and column indicates the number of papers that belong exclusively to this particular key word. The table is symmetric, i.e., the number of papers on the intersection of a certain row and a certain column is the same as the number of papers on the intersection of a certain column and row with the same key words. The column entitled "Total (along row)" indicates the amount of papers that belong solely to a certain key word and in combination with other key words. Since the table is symmetric, the total amount of papers in each column equals to that of each row. The last row, “Total papers” indicates the total amount of papers.

Numerical analysis of publication in a certain field can be interesting and useful. It can reveal some patterns of development, ties to other fields, and trends of development [19,26].

The total list of unique papers contains 530 ones. This number can also be found when we add the numbers on intersections of a row and a column with the same key word, i.e., along the diagonal. These include 6 editorials, 7 conference papers, 103 book chapters, 222 journal articles, 187 reviews, and 5 other articles (errata, notes, etc.).

The distribution of papers by year and cumulative amount of papers by year are given in **Table 2**.

Table 2. The amount of paper year by year and cumulative amount of papers by year.

Year	Papers by year	Cumulative number of papers
2000	2	2
2006	1	3
2007	1	4
2009	2	6
2010	3	9
2011	14	23
2012	9	32
2013	8	40
2014	9	49
2015	14	63
2016	10	73
2017	9	82
2018	16	98
2019	17	115
2020	56	171
2021	76	247
2022	117	364
2023	166	530

The cumulative amount of papers by year can be expressed with the formula [27].

$$N(X \leq x) = \sum_{(x_i \leq x)} n(x_i) \tag{1}$$

where $N(X \leq x)$ is the cumulative amount of papers for a certain year x; $n(x_i)$ is the amount of papers for i-th year.

These data are also given in **Figure 3**. The left-hand side Y-axis is for the blue curve, which shows the amount of papers each year. The right-hand side Y-axis is for the orange curve, which shows the cumulative distribution of papers, i.e., the sum of papers for this particular year and all years prior to this one.

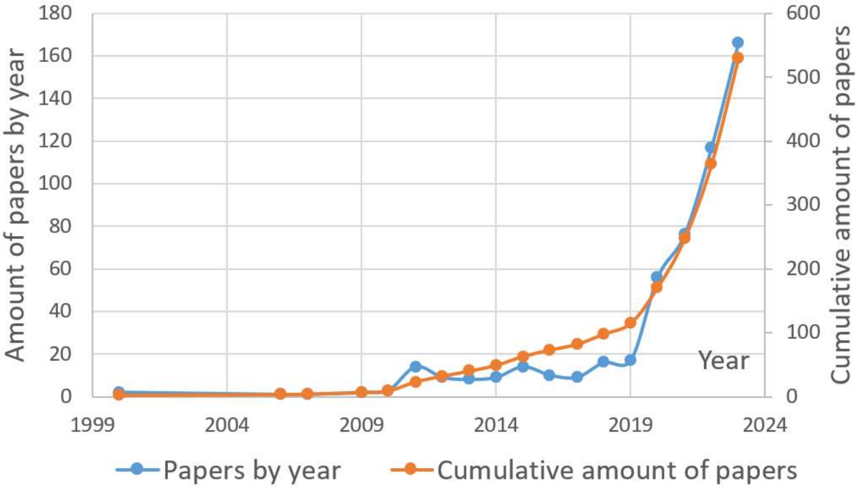

Figure 3. The amount of paper versus year (left hand side axis Y) and cumulative amount of papers (right hand side axis Y).

As can be seen from **Figure 2,** the number of papers published within 2020–2023 has sharply increased. This rise agrees with the prediction made in the study by Kochan [19]. However, it seems to us as a new trend, so it is impossible to fit any curve to describe the data and make any prediction for the field's future development.

We try to fit the curve to data. There are several tools, such as regression analysis [28] and neural networks [29,30] to solve such a task. However, according to Spiegelhalter [31], it is preferable to use regressions in relatively simple tasks like this. We applied this approach in the study by Kochan [19], and we will follow it in this paper too.

We failed to fit the curve to the amount of paper versus year because there is no such a typical equation [28] to fit the amount of papers by year.

However, we can fit the cumulative amount of papers. To do it, we need to preprocess the data. First of all, we eliminate the data prior to 2006 to avoid gaps in the independent variable (year). Then, to simplify the coefficients, we subtract 2000 from each year (i.e., we use only two last digits to denote a year), and plug is in Equation (2). From **Figure 3**, we assume the data can be fitted with the model as follows:

$$Cumulative\ Amount\ of\ Papers = a_0 \cdot a_1^{year} \quad (2)$$

To estimate the unknown coefficients a_0 and a_1 we log both sides, so the linear model is as follows:

$$Log(Cumulative\ Amount\ of\ Papers) = log(a_0) + year \cdot log(a_1) \quad (3)$$

Equation (3) is the simple linear regression [27,28]. Having applied the conventional procedure of the least squares we got coefficients of Equation (3). The distribution of residuals is given in **Figure 4**.

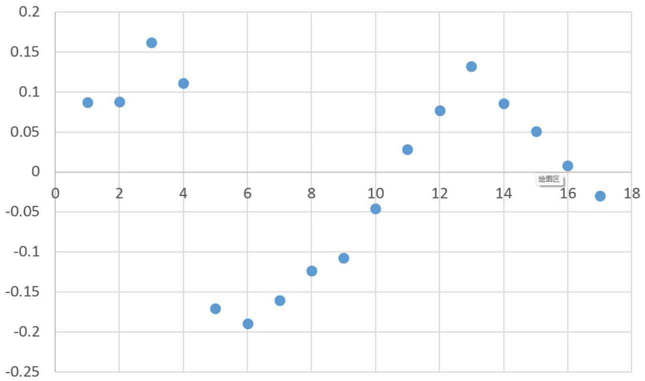

Figure 4. The distribution of residuals for linearized Equation (3).

We use the coefficients of the linearized model to compute the coefficients of Equation (2) according to the procedure described in the study by Mendenhall et al. [28]. We plug numerical values of coefficients in Equation (2) to get the formula that can be used for calculating the cumulative amount of papers:

$$Cumulative\ Amount\ of\ Papers = 0{,}649 \cdot 1{,}334^{year} \tag{4}$$

The coefficient of determination is 0.97, which means the model explains the variation of 97% of the data. According to DeCoursey [27] and Mendenhall et al. [28], in a fully valid linear model, residuals have to be distributed randomly. This was the case in the study by Kochan et al. [19]. However, **Figure 4** shows some pattern in distribution, so the model can be used with some care; that is why we do not use it for forecasting, unlike Kochan et al. [19], despite a very high value of the coefficient of determination. However, the forecast can be made according to the technique given in the study by Hu et al. [9].

4. Discussion

4.1. Properties of nanomaterials

Nanotechnology refers to the science and art of engineering materials on a scale of less than 100 nanometers [29–31]. The term “nanotechnology” was initially coined by Norio Taniguchi, a professor at Tokyo Science University, in 1974. According to scientific research, nanotechnology involves processing materials by manipulating them at the level of individual atoms or molecules [32]. Materials with components measuring less than 100 nanometers in at least one dimension are called nanomaterials. This includes synthetic or natural materials such as clusters of atoms, grains less than 100 nanometers in size, fibers with a diameter of less than 100 nanometers, films less than 100 nanometers in thickness, nanoholes, and composites that are a combination of these [33,34].

Unique physical and chemical properties are possessed by materials on the nanoscale, commonly referred to as nanomaterials. Nanostructures, another name for nanomaterials, can be classified based on their dimension. Zero-dimensional nanostructures are known as nanoparticles, while nanowires and nanorods are considered one-dimensional nanostructures. Two-dimensional nanostructures are referred to as thin films. All of these structures meet the definition of a nanomaterial or nanostructure, being smaller than 100 nm in at least one dimension (**Figure 5**) [35].

The characteristics of the material have been enhanced, resulting in improved toughness, stiffness, and transparency, as well as increased resistance to scratches, abrasions, solvents, and heat. Furthermore, nanoparticles possess distinctive attributes that distinguish them from other particles, such as varied chemical, optical, magnetic, and electro-optical properties, which are not found in bulk species or individual molecules [35].

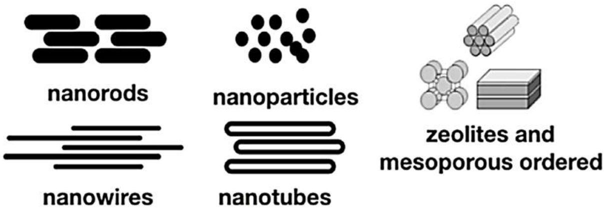

Figure 5. Representation of the structure of nanomaterials that are highly beneficial for medical purposes.

The shape of nanoparticles and their size distribution vary depending on the method of synthesis used. Both top-down and bottom-up approaches can be utilized in the creation of nanoparticles. The synthesis methods for nanoparticles depend on the material classification of the particle, such as metal, ceramic, or polymer.

Silver nanoparticles are commonly used in dental materials because of their ability to destroy microbes. Metal complexes are typically reduced in dilute solutions under carefully controlled reduction reaction conditions to create metal colloidal dispersions containing metallic nanoparticles [36]. Drug delivery often employs polymer nanoparticles, such as nanospheres and nanocapsules, which often contain active pharmaceutical ingredients within each particle or have macromolecular substances adsorbed on their surface. Polymerization-based methods like emulsion polymerization, dispersion polymerization, interfacial complexation, and polymer participation methods such as single/double emulsion, solvent displacement, or salting out can be used to prepare polymer nanoparticles. Drugs can be incorporated either during nanoparticle preparation or after [37]. Typical polymers for polymer nanoparticles include chitosan, polyacrylamide, polyacrylate, and polyesters. Biodegradable polymer nanoparticles are often employed to release drugs from nanoparticles into the human body. Polymer nanoparticles can be used as a drug delivery mechanism, which offers many benefits over traditional drug applications. These benefits include the ability to target specific tissues and cells through ligand specificity, efficient absorption of polymer nanoparticles into cells, lower doses of drugs required for treatment, reduced toxic effects, sustained release of drugs at the target site, and improved therapeutic potential [38]. The fusion of nanotechnology in the treatment modalities for periodontal diseases can be considered one of the breakthroughs in periodontics.

4.2. Periodontal diseases

Periodontal disease, which is a major dental illness, affects millions of people across the globe. The disease is one of the significant public health problems in many countries [39,40], as it possesses the criteria such as being widespread and having severe consequences on individuals, communities, and health services in terms of social, psychological, and economic aspects [41,42].

Inflammation and damage to the supportive tissues surrounding the teeth, including the periodontal ligament, alveolar bone, cementum, and gum, often occur due to the invasion of anaerobic Gram-negative bacteria (**Figure 6**). This condition is commonly known as periodontal disease [43]. The cause of periodontal disease is the imbalance between the colonization of bacterial pathogens and the host's immune response toward infection [44,45].

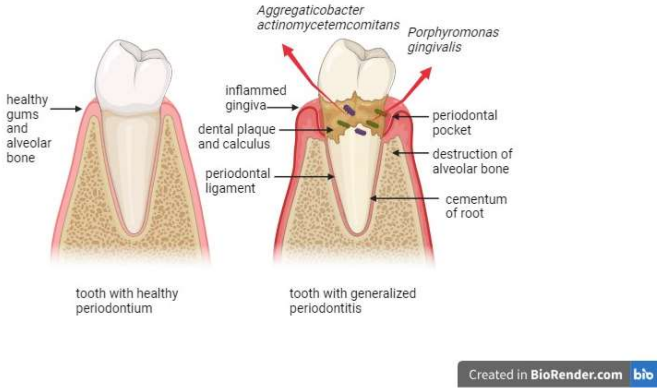

Figure 6. Schematic representation of healthy periodontal tissues and generalized periodontitis.

Periodontal treatment aims to address infections and restore the function and structure of periodontal tissues, including cementum, periodontal ligament (PDL) fibres, and bone. However, it is still difficult to fully recover these three tissue types and re-establish the strong attachment of PDL fibres to the new cementum and alveolar bone [46,47].

Recent developments in nano-materials and nano-technology have created promising possibilities for the efficient management of periodontitis. Various newer techniques, such as the use of bio-adhesive polymers to achieve extended drug release, enhancing intrapocket drug penetration, improving mechanical features through chemical cross-linkers, and the potential of loading multiple drugs in a single delivery system, offer several significant advantages. These benefits pave the way for further research opportunities in advancing dental therapeutics through the development of drug delivery systems [48–51].

4.3. Applications of nanotechnology in periodontics

Antiseptic treatment of periodontal diseases involves using disinfectants, which can contain irritating compounds and cannot be applied to soft tissues like mucosa. An exciting alternative to these strong disinfectants is the development of Ozone water. Unlike other disinfectants, Ozone water does not damage skin cells, and repeated use does not result in skin roughness or oral mucosa irritation. After use, ozone decomposes to oxygen and leaves no harmful residues. Additionally, ozone nanobubble water, which has been stable for over six months in storage in an electrolyte solution, has been created [52].

Nanotechnology in periodontics has touched every aspect of treatment modality, from non-surgical therapy to implant procedures, including regenerative procedures (**Table 3**).

Table 3. Overview of advancements in nanomaterial, and nanotechnology in periodontics.

Active ingredient/brand name	Properties and advantages	Reference/year
Ozone water	Ozone water is an exciting alternative to strong disinfectants (i.e. Alcohol, povidone iodine) used in antiseptic treatment of periodontal diseases. It can be used on soft tissues like mucosa and does not contain irritating compounds.	[52]/2017 year
Antimicrobial and antibiofilm activity of curcumin-silver nanoparticles	Curcumin-silver exhibited excellent antibacterial activity against both Gram-positive and Gram-negative bacteria and were less toxic to human keratinocytes. Cur-AgNPs were effective in inhibiting biofilm formation and exhibited anti-inflammatory effects on human macrophages.	[53]/2018 year
Triclosan	It is a noncationic antimicrobial agent that has been proven efficacious against several plaque forming bacteria.	[54]/2020 year [55]/2021 year
Tetracycline microspheres	Tetracycline Microspheres(TM) were more effective in treating chronic periodontitis through clinical parameters and microbiological analysis. Additionally, TM had a superior method of local drug in terms of usage and application.	[56]/2017 year
Minocycline Microspheres, Arestin®	The microspheres are combined with the person's saliva as they are dispensed. This mixture transforms into a semi-solid gel that fills the small crevices of the gum pocket and tooth. The microsphere gel compound can move around the mouth after inoculation, better coating the infected area. The microspheres slowly dissolve over three weeks to a month, releasing minocycline. This allows the drug to target the biofilms around the area and directly attack these species.	[57]/2023 year
Harungana madagascariensis (Hypericaceae)	H. madagascariensis, a plant found in tropical Africa and Madagascar, has medicinal properties that have been traditionally used to cure diseases. It has antibacterial potential against both sensitive and MDR bacteria. Its anthranoids constituents show promise in developing herbal medicine and pharmaceuticals to combat bacterial drug resistance.	[58]/2023 year
Tricalcium phosphate scaffolds for bone regeneration/Vitosso (Orthovita, Inc., USA) HA+tricalcium phosphate	Biomaterials made of ceramics, such as CaP, are excellent choices for restoring lost function and hard-tissue engineering. The minerals in them are comparable to those found in bones, and they have the ability to induce the growth and specialization of cells.Additionally, their relatively low degradation rate can facilitate prolonged guided tissue remodeling and structural support.	[59]/2017 year
Nano-Hydroxyapatite for Bone Tissue Engineering, Nano crystalline particles of HA Ostims commercially available in a syringe as a ready-to-use paste (Heraeus Kutzer, Hanau, Germany)	HAp can promote new bone ingrowth through osteoconduction mechanism without causing any local or systemic toxicity, inflammation or foreign body response. Nanocrystaline hydroxyapatite (nHA) is a drug delivery carrier that can be used instead of HA ceramics. The reason for this is that it has a reactive surface area that is quite high, nanoscale porosity, and it is capable of in vivo degradability	[60]/2019 year
Chitosan Nanohydrogel as a Bone Regenerative Material	It has the potential to act as a scaffold material that can enhance the differentiation of osteoprogenitor cells, chitosan hydrogel in combination with a bone graft showed superior bone regenerative potential and could prove to be an excellent candidate for bone regeneration.	[61]/2021 year
Chitosan hydrogels for drug delivery	The study tested a prototype toothpaste containing $CaCl_2$/chitosan microspheres for remineralization of human tooth enamels. The toothpaste was found to be effective in increasing calcium contents and Ca/P weight ratios in treated enamels, resulting in larger remineralization bands compared to the negative control group.	[62]/2018 year
Micro-nanorobots	Dental nanorobots can quickly relieve dentine hypersensitivity by closing specific dentinal tubes. Dentifrobots can prevent cavities by targeting harmful bacteria and allowing good bacteria to thrive. Utilizing micro/nanorobots, stem cells have been transported to a damaged area for the purpose of restoring tissue. These uses exemplify that micro/nanorobots could act as foundations for cell-based therapy and regenerative medicine. This has the potential to be particularly advantageous during the later phases of life, as organs and systems may begin to deteriorate.	[63]/2023 year [64]/2018 year

Understanding their mechanism plays a pivotal role in more efficient usage of nanotechnology, better treatment procedures, and eventually better outcomes. Effectively treating periodontal disease involves utilizing NPs that can eradicate pathogenic bacteria, as bacterial colonization is among the initial stages that cause this condition. According to available reports, combining azithromycin and clarithromycin with silver nanoparticles (AgNPs) has been found to have a synergistic antimicrobial effect against microorganisms that cause periodontal disease [53, 65]. In another study, produced glutathione-capped bimetallic NPs with great antibacterial potential against the anaerobic oral pathogen *Porphyromonas gingivalis* was suggested [53]. Curcumin-silver nanoparticles (Cur-AgNPs) exhibited excellent antibacterial activity against both Gram-positive and Gram-negative bacteria and were less toxic to human keratinocytes [66]. Moreover, Cur-AgNPs exhibited anti-inflammatory effects on human macrophages by reducing the secretion of pro-inflammatory cytokines IL-6 and TNF-α compared to chemically synthesized AgNPs. Implants can be coated with titanium oxide nanotubes and infused with silver nanoparticles to help prevent infections and prolong the lifespan of the implants [67].

4.4. Dentinal hypersensitivity

Dentin hypersensitivity is an area where dental nanorobots may find their use. Dentin hypersensitivity is a condition that occurs when changes in pressure are transmitted through the surface of the tooth, affecting the pulp [68].

The density of dentinal tubules on hypersensitive teeth is eight times higher than on non-sensitive teeth. Additionally, the diameter of these tubules is twice as large. It is possible to use dental nanorobots to occlude these tubules within a few minutes. This procedure offers patients a fast and permanent solution to their hypersensitivity [69]. The dentinal tubules are reached by tiny nanorobots that move towards the pulp while being directed by chemical gradients and temperature changes, all controlled by a nanocomputer. These nanorobots can get the pulp within 100 s, providing quick relief from sensitivity [63,70].

4.5. Drug delivery

In periodontal treatments, local drug delivery is necessary for reliable outcomes. Drug delivery systems based on triclosan-incorporated nanoparticles have been developed. Triclosan-loaded nanoparticles have been produced by emulsification-diffusion to obtain a novel delivery system for the treatment of periodontal disease. In this research article [54], the authors investigated the properties of triclosan (TCS), a hydrophobic antibacterial agent with broad-spectrum activity. To improve its antimicrobial and bacteriostatic effects, a novel amphiphilic copolymer containing tertiary amine groups, called monomethyl ether poly (ethylene glycol)-b-poly{α-[4-(diethylamino)methyl-1,2,3-triazol]-caprolactone-co-caprolactone} (mPEG-PDCL), was synthesized and designed. This copolymer was used to create micelles that served as carriers for TCS. Micelles released the cargo faster in acidic environments and demonstrated excellent antimicrobial ability against *S. aureus* and *E. coli.* Significant regeneration of the lost bone was revealed for the nanogels-treated group as per another study [55] based on morphometric findings. The developed nano-gel system, loaded with antimicrobial TCS and anti-inflammatory FLB (flurbiprofen-loaded nanogels), showed a superior healing effect in treating periodontitis based on the overall results.

The use of microspheres containing tetracycline is presently being evaluated for treating periodontal pockets. Based on the study by Kumar et al. [56], it was concluded with the help of clinical parameters and microbiological analysis that Tetracycline Microspheres (TM) were more efficient than commercially available Tetracycline Fibers (TF) (Periodontal Plus AB) in the treatment of chronic periodontitis. Also, TM had a better mode of local drug delivery in comparison to TF for both dentists and patients in terms of usage and application.

Arestin is a famous brand of antibiotic minocycline that is claimed to aid in regaining at least 1 mm of gingival reattachment height. This treatment does not require bandages or stitches and is bio-adhesive and bioresorbable, which means that it will not leak or fall out and does not need to be removed by the dentist or hygienist in a follow-up visit. When combined with deep cleaning, using Arestin to treat periodontal disease can help keep gum pockets below the threshold for surgical intervention. Moreover, the application of Arestin is comfortable and does not require anaesthesia. Clinical trials have demonstrated that a single dose of microspheres introduced into an infected gum pocket can be released for over three weeks, compared to minocycline oral capsules, commonly prescribed for 15 days [57]. Arestin® doses, which contain minocycline hydrochloride impregnated within a polymer, are delivered in 1 mg increments into the gum pocket, allowing the minocycline to be released slowly over three weeks to a month.

Although several chemical agents are available commercially, the search for alternatives persists, and traditional medicinal plants are considered a viable option, as they contain natural phytochemicals that could serve as substitutes.

An African plant called Harungana madagascariensis (Hypericaceae) possesses antimicrobial properties and contains various antimicrobial components. The leaves were subjected to successive Soxhlet solvent extractions to prepare an ethyl acetate extract, which was then tested against several oral pathogens. The extract killed all oral bacteria tested, including Actinomyces, Fusobacterium, Lactobacillus, Prevotella, Propionibacterium, and Streptococcus species. However, the activity of poly(d,l-lactide-co-glycolide) nanoparticles containing the extract was enhanced. The authors suggested that the polymer's bioadhesive properties might have led to the extract being in contact with the bacteria for prolonged periods [58].

4.6. Bone regeneration

Bone loss is a significant hallmark of periodontitis. Losing bone support causes tooth movement and dislocation, ultimately resulting in tooth loss [71]. Biologic or synthetic biomaterial intended for human implantation to restore bone health, preserve bone structure, or fill bone loss is considered a bone substitute [72]. Bone grafts can be conveniently divided into four groups:

- The patient himself (autogenous grafts)—"gold standard" for bone replacement [73];

- Different donors from the same species (allogeneic grafts), including freeze-dried bone allografts and demineralized freeze-dried bone allografts [74];
- Donors from different species (xenogeneic grafts), for example, Bio-Oss [75];
- Synthetically created materials (alloplastics), for example, tricalcium phosphates [59], a calcium-layered polymer of polymethyl methacrylate and hydroxyethyl methacrylate [76], bioactive glass [77], and hydroxyapatite (HA) [78].

Hydroxyapatite (HAp) is the primary mineral constituent of vertebrate bones and teeth. Hydroxyapatite (HAp) powder has been used for biomedical applications such as bone implant substitutes, scaffolds for complex tissue engineering, or superficial coating of implants due to a great chemical similarity with biologically calcified tissues. Synthetic HAp has been of interest for decades due to its excellent biocompatibility, affinity to biopolymers, and high osteogenic potential. It has been well documented that HAp can promote new bone in growth through osteoconduction without causing local or systemic toxicity, inflammation, or a foreign body response [79]. Among the various HAp structures, nanosized HAp, also known as HAp nanoparticles, with appropriate stoichiometry, morphology, and purity, have stimulated great interest in basic scientific research and various biomedical applications.

Nanosized HAp, which has a grain size less than 100 nm in at least one direction, has high surface activity and an ultrafine structure, similar to the mineral found in hard tissues. In recent years, bioceramics and biocomposites based on nanosized HAp have been the most promising materials for a variety of biomedical applications. Nanocrystaline hydroxyapatite (nHA) is a drug delivery carrier that can be used instead of HA ceramics. The reason for this is that it has a reactive surface area that is quite high, nanoscale porosity, and it is capable of in vivo degradability. Numerous techniques have been created for linking nHA with a broad range of antibiotics, especially tetracyclines, gentamicin, and vancomycin. The effectiveness of the delivery mechanism relies on the interplay of antibiotics with the surface of nHA, the scaffold's porosity, the capacity of antibiotic loading on the nHA nanoparticles, and the gradual release of antibiotics in the defect [60]. Apart from its therapeutic activity, nHA also acts as a bioactive matrix for newly formed bone, which may be improved with metal (Zn^{2+} and Sr^{2+}) and carbonate substitution (CO_3^{2-}) in the apatite structure. Methods for the preparation of HAp nanoparticles are given in **Figure 7** [80].

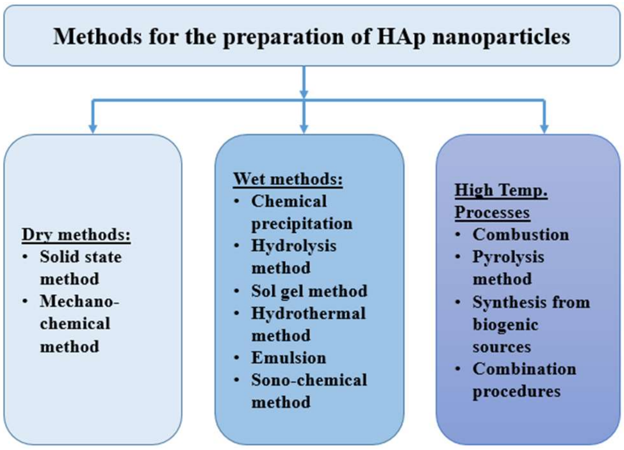

Figure 7. Methods for the preparation of HAp nanoparticles.

Various techniques have been developed to enhance the osteogenesis process, including bone grafts [81], scaffolds [82], stem cells [83], and growth factors [84]. All of these techniques have significant clinical drawbacks. Autologous grafts are limited in availability, growth factors are often unstable, and biomaterials have a high failure rate. Consequently, there is a great need for treatments that are highly effective and efficient in order to pave the way for periodontal tissue renewal. Designing scaffolds that imitate the intricate shape and organization of periodontal tissues is a significant challenge in regenerative periodontology.

Ceramics and polymers are the most commonly used materials for restoring and replacing lost oral tissues in periodontal regeneration. Ceramic biomaterials, such as calcium phosphate (CaP), calcium sulfate (CS), and bioactive glass (BG), are highly suitable for the construction of complex tissues. They can effectively restore lost function due to their similar composition to bone minerals, ability to stimulate cell proliferation and differentiation, and relatively low degradation rate. The latter is particularly beneficial for promoting long-term guided tissue remodelling and structural support. Nevertheless, these materials' brittleness and low ductility should be considered. Polymers, such as polylactic acid (PLA), polyglycolic acid (PGA), the copolymer poly (lactic-co-glycolic acid), and PCL, are highly adjustable and can be mass-produced [59].

Although many options are available, achieving complete regeneration is still challenging. Therefore, there is a focus on utilizing natural materials to overcome the limitations of synthetic ones. Chitosan is a naturally occurring biopolymer that is abundant [85]. It has the potential to act as a scaffold material that can enhance the differentiation of osteoprogenitor cells, which in turn promotes bone regeneration [86]. The study's outcome showed that chitosan significantly improved clinical and radiological parameters [61]. When bone grafts were mixed with chitosan gel and used to treat defects, it substantially reduced probing depth, improved clinical attachment loss, and achieved significant defect resolution at six months [87].

4.7. Prevention

Delivery of nanorobotic dentifrice is possible through toothpaste or mouthwash, allowing it to patrol all surfaces above and below the gum line. It can metabolize trapped organic matter into harmless, odorless vapors while performing continuous calculus debridement [88].

Mouthwash or toothpaste can release tiny robots called dentifrice nanorobots (or dentifrobots) onto the surfaces of teeth. These robots, which can be as small as 1–10 microns, move quickly (at a rate of 1–10 microns/second) and can clean up organic residues on both the supragingival and subgingival surfaces of teeth. By doing so, they can continuously prevent the buildup of calculus. Dentifrobots are designed to be safe for humans; they are deactivated when swallowed. Additionally, if they are correctly configured, dentifrobots can detect and eliminate harmful bacteria that may be present in dental plaque [64].

In scientific research [62], we tested a prototype toothpaste containing $CaCl_2$/chitosan microspheres for remineralization of human tooth enamels. The toothpaste was found to be effective in increasing calcium contents and Ca/P weight ratios in treated enamels, resulting in larger remineralization bands compared to the negative control group.

Antimicrobial peptides can be immobilized on the surface of medical devices and instruments to provide them with antimicrobial properties [89].

4.8. Challenges faced by nano dentistry

The healthcare industry is set to undergo a significant transformation through the utilization of nanotechnology, which provides new possibilities for disease diagnosis and prevention, drug delivery, and gene therapy. Despite the groundbreaking methods and equipment introduced by nanotechnology in the dental field, certain apprehensions must be addressed (**Table 4**). These include cost-effective mass production of nanorobots, ethical dilemmas and human safety, biocompatibility issues, and the necessity for precision positioning and technical expertise in nanotechnology [90–94].

Table 4. Problems and challenges of nanotechnology.

Area	Problems and challenges
Engineering	Feasibility of mass production technique Assembly lines for mass production Precise monitoring and control of production processes Metrological service of measuring instruments
Biological	Development of biofriendly nanomaterial Development of safe materials for human beings Biocompatibility the human body
Social	Ethics Public opinion and acceptance Regulation and human safety Affordability Accessibility

5. Conclusion

The field of nanotechnology is relatively new and holds immense potential for advancements. There are numerous paths for its development and progress. It is a rapidly growing area with the potential to produce advanced clinical tools and devices for oral healthcare.

The future of periodontics looks incomplete without incorporating nanotechnology in routine periodontal therapy, be it surgical or non-surgical; however, it will take extensive research to develop nanoscale biomaterials, which can be safely instilled in the human body. Nanotechnology promises to play an essential role in minimizing patient discomfort and, at the same time, maximizing the effects of a particular periodontal therapy.

Numerous nanomedicine approaches are being pursued today, and their successful development will likely occur very soon. These approaches are already close enough to the realization that their subsequent incorporation into valuable medical diagnostics or clinical therapeutics is almost inevitable. The fusion of nanotechnology in the treatment modalities for periodontal diseases is one of the breakthroughs in periodontics.

Conflict of interest: The authors declare no conflict of interest.

References

1. Krolczyk G, Legutko S, Gajek M. Predicting the surface roughness in the dry machining of duplex stainless steel (DSS). Metalurgija. 2013; 52(2): 259-62.
2. Anatychuk L, Kochan O, Pasechnikova N, et al. Thermoelectric medical device for measuring heat flux from ocular surface. In: Proceedings of the 2021 13th International Conference on Measurement; 17-19 May 2021; Bratislava, Slovakia. pp. 178-181. doi: 10.23919/Measurement52780.2021.9446775
3. Pieniak D, Niewczas AM, Pikuła K, et al. Effect of Hydrothermal Factors on the Microhardness of Bulk-Fill and Nanohybrid Composites. Materials. 2023; 16(5): 2130. doi: 10.3390/ma16052130
4. Pirmoradian M, Hooshmand T, Jafari-Semnani S, et al. Degree of conversion and microhardness of bulk-fill dental composites polymerized by LED and QTH light curing units. Journal of Oral Biosciences. 2020; 62(1): 107-113. doi: 10.1016/j.job.2019.12.004
5. Jun S, Kochan OV, Jotsov VS. Methods of Reducing the Effect of the Acquired Thermoelectric Inhomogeneity of Thermocouples on Temperature Measurement Error. Measurement Techniques. 2015; 58(3): 327-331. doi: 10.1007/s11018-015-0709-z
6. Kochan O, Kochan R, Bojko O, et al. Temperature Measurement System Based on Thermocouple with Controlled Temperature Field. In: Proceedings of the 2007 4th IEEE Workshop on Intelligent Data Acquisition and Advanced Computing Systems: Technology and Applications; 6-8 September 2007; Dortmund, Germany. pp. 47-50. doi: 10.1109/idaacs.2007.4488370
7. Vasylkiv N, Kochan O, Kochan R, et al. The control system of the profile of temperature field. In: Proceedings of the 2009 IEEE International Workshop on Intelligent Data Acquisition and Advanced Computing Systems: Technology and Applications; 21-23 September 2009; Rende, Italy. pp. 201-206. doi: 10.1109/idaacs.2009.5342994
8. Hu Z, Bodyanskiy YV, Kulishova NYe, et al. A Multidimensional Extended Neo-Fuzzy Neuron for Facial Expression Recognition. International Journal of Intelligent Systems and Applications. 2017; 9(9): 29-36. doi: 10.5815/ijisa.2017.09.04
9. Hu Z, Tereikovskyi I, et al. Procedure for Processing Biometric Parameters Based on Wavelet Transformations. International Journal of Modern Education and Computer Science. 2021; 13(2): 11-22. doi: 10.5815/ijmecs.2021.02.02
10. Dobrzański L, Dobrzański L, Dobrzańska-Danikiewicz A, et al. The Concept of Sustainable Development of Modern Dentistry. Processes. 2020; 8(12): 1605. doi: 10.3390/pr8121605
11. Ng XW, Mundargi RC, Venkatraman SS. Nanomedicine: size-related drug delivery applications, including periodontics and endodontics. In: Kishen A (editor). Nanotechnology in Endodontics: Current and Potential Clinical Applications. Springer; 2015. pp. 71-95. doi: 10.1007/978-3-319-13575-5_5
12. Ozak ST, Ozkan P. Nanotechnology and dentistry. European Journal of Dentistry. 2013; 7(01): 145-51.
13. Mantri SS, Mantri SP. The nano era in dentistry. Journal of Natural Science, Biology, and Medicine. 2013; 4(1): 39. doi: 10.4103%2F0976-9668.107258
14. Dogra S, Gupta A, Goyal V, et al. Recent trends, therapeutic applications, and future trends of nanomaterials in dentistry. In: Kanchi S, Sharma D (editors). Nanomaterials in Diagnostic Tools and Devices. Elsevier; 2020. pp. 257-292. doi: 10.1016/b978-0-12-817923-9.00010-9
15. Hamissi H, Hamissi Z, Hamissi ZH. Nanotechnology in dental practice: current achievement and prospects. Acta Medica Mediterranea. 2016; 32: 1441-8.
16. Freitas RA. Molecular robots and other high-tech possibilities. The Journal of the American Dental Association. 2000; 131: 1559-1565. doi: 10.14219/jada.archive.2000
17. Thoutam LR, Tayal S, Ajayan J, et al. Emerging Materials. Springer Nature Singapore; 2022. doi: 10.1007/978-981-19-1312-9
18. Nahar L, Sarker SD. Nanotechnology and oral health. In: Talukdar AD, Sarker SD, Patra JK (editors). Advances in Nanotechnology-Based Drug Delivery Systems. Elsevier; 2022. pp. 155-176. doi: 10.1016/b978-0-323-88450-1.00014-4

19. Kochan O, Boitsaniuk S, Levkiv M, et al. Emergence of Nano-Dentistry as a Reality of Contemporary Dentistry. Applied Sciences. 2022; 12(4): 2008. doi: 10.3390/app12042008
20. Althahban S, Alomari AS, El-Din M. Sallam H, Jazaa Y. An investigation of wear, mechanical, and water sorption/solubility behaviors of a commercial restorative composite containing nano-additives. Journal of Materials Research and Technology. 2023; 23: 491-502. doi: 10.1016/j.jmrt.2023.01.025
21. Aminu N, Chan SY, Toh SM. Roles of nanotechnological approaches in periodontal disease therapy. Journal of Applied Pharmaceutical Science. 2017; 7(7): 234-42. doi: 10.7324/JAPS.2017.70735
22. Verma S, Chevvuri R, Sharma H. Nanotechnology in dentistry: unleashing the hidden gems. Journal of Indian Society of Periodontology. 2018; 22(3): 196. doi: 10.4103/jisp.jisp_35_18
23. Sinha N, Kulshreshtha NM, Dixit M, et al. Nanodentistry: novel approaches. In: Ecaterina Andronescu and Alexandru Mihai Grumezescu (editors). Nanostructures for Oral Medicine. Elsevier; 2017. pp. 751-776. doi: 10.1016/b978-0-323-47720-8.00025-0
24. Denefil O, Chorniy S, Boitsaniuk S, et al. Analysis of microbiocenosis of a gingival sulcus and periodontal pockets of patients with periodontal diseases associated with systemic pathology. Exploration of Medicine. Published online December 11, 2023: 942-955. doi: 10.37349/emed.2023.00186
25. Gurevitch J, Koricheva J, Nakagawa S, et al. Meta-analysis and the science of research synthesis. Nature. 2018; 555(7695): 175-182. doi: 10.1038/nature25753
26. Dagli N, Patel B, Dagli R, et al. Bibliometric analysis and visualization of research on nanotechnology in dentistry from 1999 to 2022. Journal of Applied Pharmaceutical Science. 2023; 13(9): 58-66. doi: 10.7324/japs.2023.146431
27. DeCoursey W. Statistics and Probability for Engineering Applications. Elsevier; 2003.
28. Mendenhall W, Sincich T, Boudreau NS. A Second Course in Statistics: Regression Analysis. Prentice Hall; 2003.
29. Sun L, Qin H, Przystupa K, et al. Individualized Short-Term Electric Load Forecasting Using Data-Driven Meta-Heuristic Method Based on LSTM Network. Sensors. 2022; 22(20): 7900. doi: 10.3390/s22207900
30. Chen X, Przystupa K, Ye Z, et al. Forecasting short-term electric load using extreme learning machine with improved tree seed algorithm based on Lévy flight. Eksploatacja i Niezawodność - Maintenance and Reliability. 2022; 24(1): 153-162. doi: 10.17531/ein.2022.1.17
31. Spiegelhalter D. The Art of Statistics: Learning from Data. Penguin UK; 2019.
32. Luby Š. Nanoscience - from manipulation of atoms to human needs. European Pharmaceutical Journal. 2021; 68(1): 84-88. doi: 10.2478/afpuc-2021-0005
33. Malik S, Muhammad K, Waheed Y. Emerging Applications of Nanotechnology in Healthcare and Medicine. Molecules. 2023; 28(18): 6624. doi: 10.3390/molecules28186624
34. Guo T, Yang M, Wang D, et al. Antibiofilm and mechanical properties of silver nanowire-modified glass ionomer cement. Journal of Dentistry. 2023; 135: 104569. doi: 10.1016/j.jdent.2023.104569
35. Bonilla-Represa V, Abalos-Labruzzi C, Herrera-Martinez M, et al. Nanomaterials in Dentistry: State of the Art and Future Challenges. Nanomaterials. 2020; 10(9): 1770. doi: 10.3390/nano10091770
36. Beyene HD, Werkneh AA, Bezabh HK, et al. Synthesis paradigm and applications of silver nanoparticles (AgNPs), a review. Sustainable Materials and Technologies. 2017; 13: 18-23. doi: 10.1016/j.susmat.2017.08.001
37. Jandt KD, Watts DC. Nanotechnology in dentistry: Present and future perspectives on dental nanomaterials. Dental Materials. 2020; 36(11): 1365-1378. doi: 10.1016/j.dental.2020.08.006
38. Rokaya D, Srimaneepong V, Sapkota J, et al. Polymeric materials and films in dentistry: An overview. Journal of Advanced Research. 2018; 14: 25-34. doi: 10.1016/j.jare.2018.05.001
39. Aizenbud I, Wilensky A, Almoznino G. Periodontal Disease and Its Association with Metabolic Syndrome—A Comprehensive Review. International Journal of Molecular Sciences. 2023; 24(16): 13011. doi: 10.3390/ijms241613011
40. Alsalleeh F, Alhadlaq AS, Althumiri NA, et al. Public Awareness of the Association between Periodontal Disease and Systemic Disease. Healthcare. 2022; 11(1): 88. doi: 10.3390/healthcare11010088
41. Pyo J, Lee M, Ock M, et al. Quality of Life and Health in Patients with Chronic Periodontitis: A Qualitative Study. International Journal of Environmental Research and Public Health. 2020; 17(13): 4895. doi: 10.3390/ijerph17134895
42. Foong LK, Foroughi MM, Mirhosseini AF, et al. Applications of nano-materials in diverse dentistry regimes. RSC Advances. 2020; 10(26): 15430-15460. doi: 10.1039/d0ra00762e

43. Ji S, Choi YS, Choi Y. Bacterial invasion and persistence: critical events in the pathogenesis of periodontitis? Journal of Periodontal Research. 2014; 50(5): 570-585. doi: 10.1111/jre.12248
44. Coppola N, Cantile T, Adamo D, et al. Supportive care and antiviral treatments in primary herpetic gingivostomatitis: a systematic review. Clinical Oral Investigations. 2023; 27(11): 6333-6344. doi: 10.1007/s00784-023-05250-5
45. Suárez LJ, Garzón H, Arboleda S, et al. Oral Dysbiosis and Autoimmunity: From Local Periodontal Responses to an Imbalanced Systemic Immunity. A Review. Frontiers in Immunology. 2020; 11. doi: 10.3389/fimmu.2020.591255
46. Iviglia G, Kargozar S, Baino F. Biomaterials, Current Strategies, and Novel Nano-Technological Approaches for Periodontal Regeneration. Journal of Functional Biomaterials. 2019; 10(1): 3. doi: 10.3390/jfb10010003
47. Santonocito S, Ferlito S, Polizzi A, et al. Therapeutic and Metagenomic Potential of the Biomolecular Therapies against Periodontitis and the Oral Microbiome: Current Evidence and Future Perspectives. International Journal of Molecular Sciences. 2022; 23(22): 13708. doi: 10.3390/ijms232213708
48. Chi M, Qi M, A L, et al. Novel Bioactive and Therapeutic Dental Polymeric Materials to Inhibit Periodontal Pathogens and Biofilms. International Journal of Molecular Sciences. 2019; 20(2): 278. doi: 10.3390/ijms20020278
49. Liang J, Peng X, Zhou X, et al. Emerging Applications of Drug Delivery Systems in Oral Infectious Diseases Prevention and Treatment. Molecules. 2020; 25(3): 516. doi: 10.3390/molecules25030516
50. Makvandi P, Josic U, Delfi M, et al. Drug Delivery (Nano)Platforms for Oral and Dental Applications: Tissue Regeneration, Infection Control, and Cancer Management. Advanced Science. 2021; 8(8). doi: 10.1002/advs.202004014
51. Hanafy N, Leporatti S, El-Kemary M. Mucoadhesive Hydrogel Nanoparticles as Smart Biomedical Drug Delivery System. Applied Sciences. 2019; 9(5): 825. doi: 10.3390/app9050825
52. Seki M, Ishikawa T, Terada H, Nashimoto M. Microbicidal Effects of Stored Aqueous Ozone Solution Generated by Nano-bubble Technology. Vivo. 2017; 31(4): 579-583. doi: 10.21873/invivo.11097
53. Jaiswal S, Mishra P. Antimicrobial and antibiofilm activity of curcumin-silver nanoparticles with improved stability and selective toxicity to bacteria over mammalian cells. Medical Microbiology and Immunology. 2017; 207(1): 39-53. doi: 10.1007/s00430-017-0525-y
54. Lei D, Wang Q, Kong Y, et al. Triclosan-loaded pH-responsive copolymer to target bacteria and to have long bacteriostatic efficacy. European Journal of Pharmaceutical Sciences. 2020; 148: 105320. doi: 10.1016/j.ejps.2020.105320
55. Aminu N, Yam MF, Chan SY, et al. The evaluation of healing effect of triclosan and flurbiprofen-loaded nanogels in experimental periodontitis in rats by morphometric analysis. The Saudi Dental Journal. 2021; 33(7): 554-559. doi: 10.1016/j.sdentj.2020.08.0
56. Kumar M, Sharma M, Govila V, et al. A Comparative Evaluation of Tetracycline Containing Microspheres and Commercially Available Tetracycline Fibers to Evaluate Their Efficacy in Periodontal Pocket Therapy—A Clinical and Microbiological Study. Global Journal for Research Analysis. 2017; 6(8): 65-67.
57. Plemmons D, Sneed K, Pathak Y. Nano therapy Spotlight: Arestin™ Minocycline Microspheres. Chemical & Pharmaceutical Research. 2023; 5(1). doi: 10.33425/2689-1050.1046
58. Kuete V, Seukep AJ. Harungana madagascariensis as a source of antibacterial agents. In: Advances in Botanical Research. Academic Press; 2023.
59. Carter SSD, Costa PF, Vaquette C, et al. Additive Biomanufacturing: An Advanced Approach for Periodontal Tissue Regeneration. Annals of Biomedical Engineering. 2016; 45(1): 12-22. doi: 10.1007/s10439-016-1687-2
60. Calasans-Maia MD, Barboza Junior CAB, Soriano-Souza CA, et al. Microspheres of alginate encapsulated minocycline-loaded nanocrystalline carbonated hydroxyapatite: therapeutic potential and effects on bone regeneration. International Journal of Nanomedicine. 2019; 14: 4559-4571. doi: 10.2147/IJN.S201631
61. Meenakshi SS, Sankari M. Effectiveness of Chitosan Nanohydrogel as a Bone Regenerative Material in Intrabony Defects in Patients with Chronic Periodontitis: A Randomized Clinical Trial. Journal of Advanced Oral Research. 2021; 12(2): 222-228. doi: 10.1177/2320206821998574
62. Wu L, Li F, Morrow BR, Jiang S, et al. A novel antimicrobial and remineralizing toothpaste containing CaCl2/chitosan microspheres. American Journal of Dentistry. 2018; 31(3): 149.
63. Thomas S, Baiju RM (editors). Nanomaterials in Dental Medicine. Springer Nature Singapore; 2023. doi: 10.1007/978-981-19-8718-2
64. Bordoloi P, Shahira S, Ramesh A, Thomas B. Nanorobotic wonders: A revolutionary era in periodontics. Indian Journal of Multidisciplinary Dentistry. 2018; 8: 101-5. doi: 10.4103/ijmd.ijmd_29_18

65. Zong TX, Silveira AP, Morais JAV, et al. Recent Advances in Antimicrobial Nano-Drug Delivery Systems. Nanomaterials. 2022; 12(11): 1855. doi: 10.3390/nano12111855
66. Loza K, Heggen M, Epple M. Synthesis, Structure, Properties, and Applications of Bimetallic Nanoparticles of Noble Metals. Advanced Functional Materials. 2020; 30(21). doi: 10.1002/adfm.201909260
67. Nandi SK, Shivaram A, Bose S, et al. Silver nanoparticle deposited implants to treat osteomyelitis. Journal of Biomedical Materials Research Part B: Applied Biomaterials. 2017; 106(3): 1073-1083. doi: 10.1002/jbm.b.33910
68. Chornij N, Boitsaniuk S, Stechyshyn I, et al. Prevention and methods of correction of hyperesthesia of dental hard tissues of teeth. Pharmacologyonline. 2021; 2: 1436-42.
69. Singh AV, Ansari MHD, Laux P, et al. Micro-nanorobots: important considerations when developing novel drug delivery platforms. Expert Opinion on Drug Delivery. 2019; 16(11): 1259-1275. doi: 10.1080/17425247.2019.1676228
70. Arjmand T, Legallais M, Nguyen TTT, et al. Functional Devices from Bottom-Up Silicon Nanowires: A Review. Nanomaterials. 2022; 12(7): 1043. doi: 10.3390/nano12071043
71. Zhu L, Zhou C, Chen S, et al. Osteoporosis and Alveolar Bone Health in Periodontitis Niche: A Predisposing Factors-Centered Review. Cells. 2022; 11(21): 3380. doi: 10.3390/cells11213380
72. Kim HW, Kim YJ. Effect of silicon or cerium doping on the anti-inflammatory activity of biphasic calcium phosphate scaffolds for bone regeneration. Progress in Biomaterials. 2022; 11(4): 421-430. doi: 10.1007/s40204-022-00206-6
73. Santonocito S, Ferlito S, Polizzi A, et al. Impact exerted by scaffolds and biomaterials in periodontal bone and tissue regeneration engineering: new challenges and perspectives for disease treatment. Exploration of Medicine. 2023; 4: 215-234. doi: 10.37349/emed.2023.00135
74. Grassi FR, Grassi R, Vivarelli L, et al. Design Techniques to Optimize the Scaffold Performance: Freeze-dried Bone Custom-made Allografts for Maxillary Alveolar Horizontal Ridge Augmentation. Materials. 2020; 13(6): 1393. doi: 10.3390/ma13061393
75. Francisco I, Basílio Â, Ribeiro MP, et al. Three-Dimensional Impression of Biomaterials for Alveolar Graft: Scoping Review. Journal of Functional Biomaterials. 2023; 14(2): 76. doi: 10.3390/jfb14020076
76. Rajula MP, Narayanan V, Venkatasubbu GD, et al. Synthesis and Characterization of Naringin Functionalized Nano-Hydroxyapatite for Bone Tissue Engineering. Journal of Pharmacy and Bioallied Sciences. 2023;15(Suppl 1): S372-S376. doi: 10.4103/jpbs.jpbs_626_22
77. Liu J, Ruan J, Weir MD, et al. Periodontal Bone-Ligament-Cementum Regeneration via Scaffolds and Stem Cells. Cells. 2019; 8(6): 537. doi: 10.3390/cells8060537
78. Mohd N, Razali M, Ghazali MJ, et al. 3D-Printed Hydroxyapatite and Tricalcium Phosphates-Based Scaffolds for Alveolar Bone Regeneration in Animal Models: A Scoping Review. Materials. 2022; 15(7): 2621. doi: 10.3390/ma15072621
79. Gavinho SR, Pádua AS, Holz LIV, et al. Bioactive Glasses Containing Strontium or Magnesium Ions to Enhance the Biological Response in Bone Regeneration. Nanomaterials. 2023; 13(19): 2717. doi: 10.3390/nano13192717
80. Sadat-Shojai M, Khorasani MT, Dinpanah-Khoshdargi E, et al. Synthesis methods for nanosized hydroxyapatite with diverse structures. Acta Biomaterialia. 2013; 9(8): 7591-7621. doi: 10.1016/j.actbio.2013.04.012
81. Alqahtani AM. Guided Tissue and Bone Regeneration Membranes: A Review of Biomaterials and Techniques for Periodontal Treatments. Polymers. 2023; 15(16): 3355. doi: 10.3390/polym15163355
82. Creste CFZ, Orsi PR, Landim-Alvarenga FC, et al. Highly Effective Fibrin Biopolymer Scaffold for Stem Cells Upgrading Bone Regeneration. Materials. 2020; 13(12): 2747. doi: 10.3390/ma13122747
83. Mansoor A, Khurshid Z, Khan MT, et al. Medical and Dental Applications of Titania Nanoparticles: An Overview. Nanomaterials. 2022; 12(20): 3670. doi: 10.3390/nano12203670
84. Subramani K, Ahmed W. Emerging Nanotechnologies in Dentistry. William Andrew; 2017.
85. Harugade A, Sherje AP, Pethe A. Chitosan: A review on properties, biological activities and recent progress in biomedical applications. Reactive and Functional Polymers. 2023; 191: 105634. doi: 10.1016/j.reactfunctpolym.2023.105634
86. Gaihre B, Lecka-Czernik B, Jayasuriya AC. Injectable nanosilica-chitosan microparticles for bone regeneration applications. Journal of Biomaterials Applications. 2017; 32(6): 813-825. doi: 10.1177/0885328217741523
87. Iglesias N, Galbis E, Valencia C, et al. Biodegradable double cross-linked chitosan hydrogels for drug delivery: Impact of chemistry on rheological and pharmacological performance. International Journal of Biological Macromolecules. 2020; 165: 2205-2218. doi: 10.1016/j.ijbiomac.2020.10.006

88. Mitthra S, Karthick A, Anuradha B, et al. Nanorobots - A Small Wonder. Biosciences, Biotechnology Research Asia. 2016; 13(4): 2131-2134. doi: 10.13005/bbra/2374
89. Comune M, Rai A, Palma P, et al. Antimicrobial and pro-angiogenic properties of soluble and nanoparticle-immobilized LL37 peptides. Biomaterials Science. 2021; 9(24): 8153-8159. doi: 10.1039/d1bm01034d
90. Hasan DM, Abbas MJ, Al-Ghurabi BH. Impact of indium oxide nanoparticles mouth wash in prevention of human dental enamel caries (in vitro study). Medical Journal of Babylon. 2023; 20(2): 322-31. doi: 10.4103/MJBL.MJBL_345_22
91. Gumber HK, Louyakis AS, Sarma T, et al. Effect of a Stannous Fluoride Dentifrice on Biofilm Composition, Gene Expression and Biomechanical Properties. Microorganisms. 2022; 10(9): 1691. doi: 10.3390/microorganisms10091691
92. Giri G, Maddahi Y, Zareinia K. A Brief Review on Challenges in Design and Development of Nanorobots for Medical Applications. Applied Sciences. 2021; 11(21): 10385. doi: 10.3390/app112110385
93. Glowacka-Sobotta A, Ziental D, Czarczynska-Goslinska B, et al. Nanotechnology for Dentistry: Prospects and Applications. Nanomaterials. 2023; 13(14): 2130. doi: 10.3390/nano13142130
94. Malik S, Niazi M, Khan M, et al. Cytotoxicity Study of Gold Nanoparticle Synthesis Using Aloe vera, Honey, and Gymnema sylvestre Leaf Extract. ACS Omega. 2023; 8(7): 6325-6336. doi: 10.1021/acsomega.2c06491

Characterization and Application of Nanomaterials 2024, 7(1), 4654.
https://doi.org/10.24294/can.v7i1.4654

Review

Carbon nanomaterial-based electrochemical sensor in biomedical application, a comprehensive study

Srabani Majumdar[1], Razu Shahazi[1], Amirul Islam Saddam[1], Mohammed Muzibur Rahman[2,3], Md. Mahmud Alam[1,2,*], Ajoy Kumer[4], Giti Paimard[5]

[1] Department of Chemical Engineering, Z. H. Sikder University of Science and Technology (ZHSUST), Shariatpur 8024, Bangladesh
[2] Center of Excellence for Advanced Materials Research (CEAMR), King Abdulaziz University, Jeddah 21589, Saudi Arabia
[3] Chemistry Department, Faculty of Science, King Abdulaziz University, Jeddah 21589, Saudi Arabia
[4] Department of Chemistry, College of Arts and Sciences, IUBAT-International University of Business Agriculture and Technology, Dhaka 1230, Bangladesh
[5] Laboratory of Nanoscale Biosensing and Bioimaging (NBAB), School of Ophthalmology and Optometry, School of Biomedical Engineering, State Key Laboratory of Ophthalmology Optometry, and Vision Science, Wenzhou Medical University, Wenzhou 325027, China
*** Corresponding author:** Md. Mahmud Alam, alam-mahmud@hotmail.com, mmalam@zhsust.ac.bd

CITATION

Majumdar S, Shahazi R, Saddam AI, et al. Carbon nanomaterial-based electrochemical sensor in biomedical application, a comprehensive study. Characterization and Application of Nanomaterials. 2024; 7(1): 4654. https://doi.org/10.24294/can.v7i1.4654

ARTICLE INFO

Received: 15 February 2024
Accepted: 12 March 2024
Available online: 12 April 2024

Abstract: Recently, carbon nanocomposites have garnered a lot of curiosity because of their distinctive characteristics and extensive variety of possible possibilities. Among all of these applications, the development of sensors with electrochemical properties based on carbon nanocomposites for use in biomedicine has shown as an area with potential. These sensors are suitable for an assortment of biomedical applications, such as prescribing medications, disease diagnostics, and biomarker detection. They have many benefits, including outstanding sensitivity, selectivity, and low limitations on detection. This comprehensive review aims to provide an in-depth analysis of the recent advancements in carbon nanocomposites-based electrochemical sensors for biomedical applications. The different types of carbon nanomaterials used in sensor fabrication, their synthesis methods, and the functionalization techniques employed to enhance their sensing properties have been discussed. Furthermore, we enumerate the numerous biological and biomedical uses of electrochemical sensors based on carbon nanocomposites, among them their employment in illness diagnosis, physiological parameter monitoring, and biomolecule detection. The challenges and prospects of these sensors in biomedical applications are also discussed. Overall, this review highlights the tremendous potential of carbon nanomaterial-based electrochemical sensors in revolutionizing biomedical research and clinical diagnostics.

Keywords: carbon nanocomposites; sensitivity; selectivity; low detection limits; detecting biomolecules; monitoring physiological parameters; diagnosing diseases; electrochemical sensors

1. Introduction

Because electrochemical sensors can identify and measure the different biochemicals present in human fluid, they are essential in biomedical applications. It provides excellent sensitivity and selectivity for identifying target analytes and can quickly and precisely identify certain compounds or biomarkers in complex biological samples. Because of this, electrochemical sensors' sensitivity and selectivity make them useful instruments for monitoring and diagnosing diseases early on [1–5]. As known, the electrochemical sensors provide rapid analysis, delivering real-time results within minutes or seconds, which is essential in critical medical situations for timely diagnosis and treatment decisions [6–8]. Thus, it eliminates the step of sending samples to a clinical laboratory and deletes the late medical interventions. In addition, electrochemical sensors are often cost-effective compared to traditional laboratory-based analytical techniques, making them accessible in resource-limited settings [9,10].

Multiplexed analysis can be made possible by designing the electrochemical sensors to detect numerous analytes at once. This is another potential feature. This function is very helpful for biomarker profiling, as the combination of several biomarkers can yield more thorough diagnostic data [11,12]. In terms of long-term monitoring, the electrochemical sensors can be integrated into implantable or wearable devices for long-term monitoring of physiological parameters or drug delivery. This allows continuous monitoring of patient health and therapeutic efficacy over extended periods, providing valuable insights for personalized medicine and treatment optimization [13,14]. Thus, electrochemical sensors have diverse applications in biomedicine, including disease diagnosis, drug discovery, monitoring of therapeutic interventions, environmental monitoring, and biosecurity. Their versatility allows them to be adapted for various biomedical needs.

In short, electrochemical sensors offer high sensitivity, selectivity, rapid analysis, and versatility, making them indispensable tools in biomedical applications. They have the potential to revolutionize medical diagnostics, patient monitoring, and personalized medicine by providing accurate, real-time, and cost-effective solutions.

2. Instrumentation of electrochemical sensors

Electrochemical sensors are widely used for detecting and quantifying various analytes in fields such as environmental monitoring, healthcare, and industrial processes. The instrumentation of electrochemical sensors typically involves several key components and techniques. The basic setup of an electrochemical sensor consists of an electrochemical cell. This cell typically includes an electrode system, which consists of a working electrode, a reference electrode, and a counter electrode. The analyte of interest interacts with the working electrode surface, leading to an electrochemical reaction. To control and measure the electrical potential or current during electrochemical measurements, a potentiostat or galvanostat is used. These instruments provide a stable potential or current to the working electrode and maintain it at the desired value throughout the experiment. Potentiostats are commonly used for most electrochemical measurements. The reference electrode is a stable electrode with a known and constant potential. It provides a reference point for measuring the potential at the working electrode. Common reference electrodes include silver/silver chloride (Ag/AgCl) and saturated calomel electrode (SCE). The counter electrode completes the electrical circuit in the electrochemical cell. It compensates for the current flowing through the working electrode during the electrochemical reaction. Common counter electrodes are made of materials such as platinum, graphite, or gold. The electrochemical signal generated at the working electrode is typically small and requires amplification and conditioning for accurate measurement. Signal amplifiers and filters are used to enhance the signal-to-noise ratio and remove unwanted noise or interference. A data acquisition system is used to collect and process the output from the electrochemical sensor. It typically includes analog-to-digital converters (ADCs) to convert the analog electrochemical signal into a digital format, which can be further processed and analyzed by a computer or microcontroller. Electrochemical sensors often require calibration to establish a relationship between the measured signal and the analyte concentration. Calibration involves measuring the sensor response with known concentrations of the analyte and creating a calibration curve. Standardization ensures the accuracy and reliability of the sensor measurements by using certified reference materials. In recent years, there has been a trend toward miniaturizing electrochemical sensors and integrating them with portable or wearable devices. This allows for on-site and real-time monitoring of analytes in various applications, including point-of-care diagnostics and environmental sensing. In **Figure 1**, the instrumentation of an electrochemical sensor is illustrated.

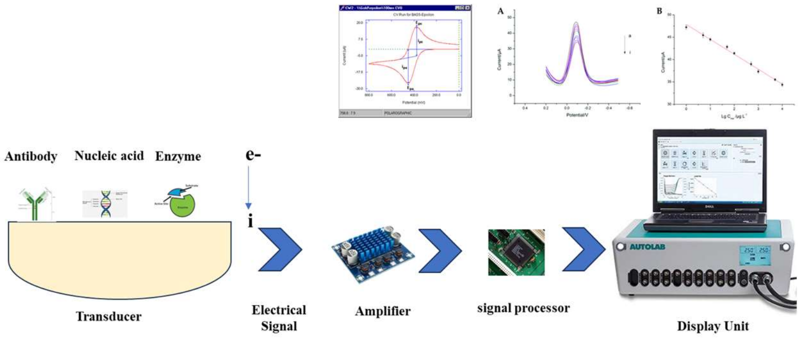

Figure 1. Instrumentation of electrochemical sensor.

3. Reagent and biomolecules for electrochemical sensing

Electrochemical sensors utilize specific reagents and biomolecules to facilitate the detection and quantification of analytes. The choice of reagents and biomolecules depends on the nature of the analyte and the sensing mechanism employed. Enzymes are widely used in electrochemical sensors due to their high catalytic activity and specificity. They can be immobilized on the electrode surface or incorporated into the sensor matrix. Examples include glucose oxidase for glucose sensing, lactate oxidase for lactate sensing, and cholinesterase for acetylcholine sensing [15–17]. Antibodies or antibody fragments (e.g., monoclonal antibodies) are used in immunosensors for the detection of specific antigens or biomarkers. The antibodies are immobilized on the electrode surface or on nanoparticles that are subsequently captured by the electrode. This allows for highly specific recognition and measurement of target analytes [18,19]. Besides this, DNA or RNA probes are employed in nucleic acid sensors for the detection of specific DNA sequences or RNA molecules. Probes can be designed to hybridize with the target sequence, leading to changes in the electrochemical signal. Various strategies, such as hybridization chain reaction (HCR) or strand displacement amplification (SDA), can be used to enhance the sensitivity of nucleic acid sensors [20,21]. Moreover, Redox mediators are small molecules that facilitate the transfer of electrons between the electrode and the analyte, enhancing the electrochemical signal. Examples include ferrocene derivatives, methylene blue, and quinones. Redox mediators can be incorporated into the sensor system to mediate the electrochemical reaction and amplify the signal [22,23]. Reducing or oxidizing agents can be added to the sensor system to modulate the electrochemical reaction or enhance the signal. For example, in amperometric glucose sensors, a reducing agent (e.g., ascorbic acid) can be added to minimize interference from other electroactive species [24,25]. In addition, electrochemical sensors often require buffer solutions to maintain a stable pH and optimize the electrochemical reactions. Common buffer systems include phosphate-buffered saline (PBS), Tris-HCl, or acetate buffers. The buffer composition and pH are chosen based on the requirements of the specific electrochemical reaction and the stability of the biomolecules involved [26,27].

4. Role of carbon nanomaterials in electrochemical sensor development

The creation of electrochemical sensors greatly benefits from the use of carbon nanomaterials. Its remarkable mechanical, chemical, and electrical characteristics make it an excellent choice for applications involving electrochemical sensing. Due to its huge reactive surface area and strong electrical conductivity, it can move electrons efficiently and has increased sensitivity. The performance of conventional electrodes can be enhanced by using carbon nanomaterials as modifiers or by directly integrating them into the electrode structure [28,29]. Besides this, it can serve as excellent support for electro-catalysts in electrochemical sensors. The high surface area and good mechanical stability of carbon nanomaterials enhance the catalyst's activity and stability, leading to improved sensor performance [30,31]. In addition, carbon nanomaterials can act as electrochemical sensing platforms themselves. Carbon nanomaterials can be utilized to amplify the electrochemical signals generated during electrochemical sensing processes. A schematic setup of an electrochemical sensor is demonstrated in **Figure 2**.

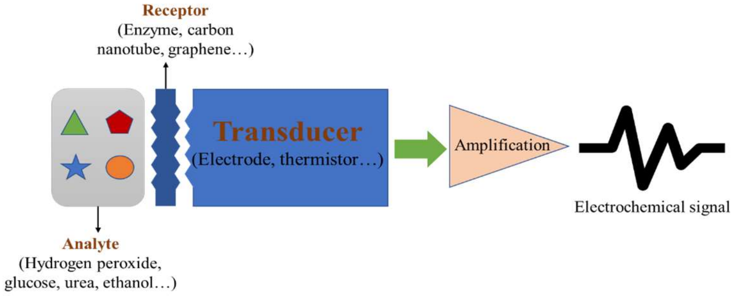

Figure 2. Schematic diagram of an electrochemical sensor.

Thus, this signal amplification approach improves the electrochemical sensor's sensitivity, enabling the detection of trace analytes [32,33]. On the other hand, the carbon nanomaterials can be tailored to exhibit selective interactions with target analytes, enabling the development of highly specific electrochemical sensors. Functionalization of the carbon nanomaterial surface with specific receptors, such as antibodies, enzymes, or molecular imprints, allows for the selective recognition and detection of target molecules in complex samples [34,35]. Therefore, carbon nanomaterials have revolutionized the field of electrochemical sensing by providing enhanced sensitivity, excellent electrical conductivity, versatile functionalization, stability, and integration capabilities. Ongoing research continues to explore new synthesis and functionalization techniques, as well as innovative sensor designs, to further optimize the properties of carbon nanomaterials and expand their applications in various fields, including environmental monitoring, healthcare diagnostics, and food safety.

5. Types of carbon nanomaterials

There are several types of carbon nanomaterials, each with unique structures and properties.

5.1. Carbon nanotubes (CNTs)

Carbon nanotubes are cylindrical structures made of rolled-up graphene sheets. They can be classified as single-walled (SWCNTs) or multi-walled (MWCNTs) depending on the number of graphene layers. CNTs possess excellent mechanical strength, high electrical conductivity, and large surface area. Various types of carbon nanotubes are illustrated in **Figure 3**. They are widely used in various applications as electronics, energy storage, and composite materials.

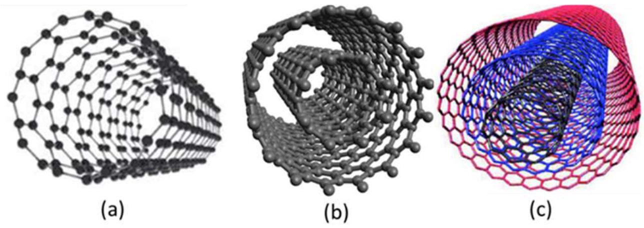

Figure 3. Structure. **(a)** single-walled carbon nanotube (SWCNT); **(b)** double-walled carbon nanotube (DWCNT); **(c)** multi-walled carbon nanotube (MWCNT).

Thus, carbon nanotubes can serve as excellent transducers in electrochemical sensors due to their unique electrical properties. When CNTs are functionalized or modified with specific biomolecules or receptors, they can selectively recognize and bind to target analytes, such as disease-specific biomarkers or molecules indicative of a particular disease [36–38]. Thus, the unique properties of carbon nanotubes, including their high sensitivity, excellent electrical conductivity, electrochemical activity, and compatibility with functionalization and integration, make them highly valuable for electrochemical sensing applications. Ongoing research aims to further optimize the properties of CNTs, explore new synthesis and functionalization techniques, and develop innovative sensor designs for enhanced performance and broader application domains.

5.2. Graphene

A further important aspect of the carbon nanomaterial family is graphene, which is a substance made up of just a single layer of carbon atoms organized in a two-dimensional in nature honeycomb lattice. The structure of graphene is shown in **Figure 4**. It is a highly conductive, flexible, and incredibly thin material. Because of its remarkable mechanical, electrical, and thermal features, ranging graphene receives application throughout a variety of fields, including medicinal devices, electronics, sensors, and energy storage. To achieve high selectivity and specificity towards the target biomarker, graphene-based electrochemical sensors can be functionalized with particular receptors, such as antibodies, aptamers, or molecularly imprinted polymers. Functionalization lowers false-positive or false-negative readings by enabling the sensor to distinguish between the target biomarker and other interfering species present in the sample. Graphene, like carbon nanotubes, can be used in sensor arrays to allow for the simultaneous multiplexed detection of several biomarkers. An array of graphene-based sensors can be functionalized with distinct receptors for various biomarkers, enabling simultaneous analysis and thorough illness diagnosis [39–42]. The application of graphene in electrochemical sensing has shown great promise, and ongoing research aims to further optimize its properties, explore new fabrication techniques, and develop innovative sensor designs. Graphene-based electrochemical sensors have the potential to revolutionize fields such as environmental monitoring, healthcare diagnostics, food safety, and many other areas where sensitive and selective detection of analytes is crucial.

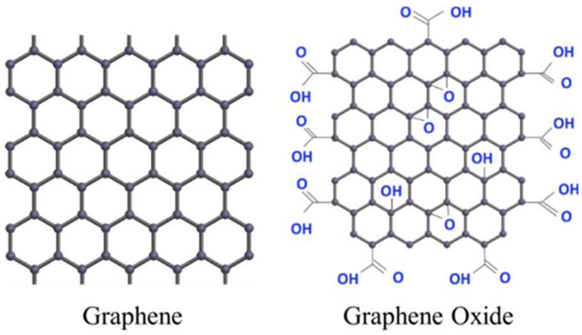

Figure 4. Structure of graphene and graphene oxide.

5.3. Graphene oxide (GO)

Graphene oxide is derived from graphene by introducing oxygen-containing functional groups. The structure of graphene oxide is shown in **Figure 4**. GO exhibits good dispersibility in water and other solvents, making it easier to process and functionalize. It is used in various fields, including sensors, membranes, drug delivery systems, and composites [43,44]. Thus, the application of graphene oxide in electrochemical sensors has shown great promise in various fields, including environmental monitoring, healthcare diagnostics, and food safety. Ongoing research is focused on further optimizing the properties of GO-based sensors [45,46] and exploring new applications in areas such as energy storage, wearable devices, and point-of-care diagnostics.

5.4. Carbon nanofibers (CNFs)

Carbon nanofibers are elongated structures composed of graphene sheets stacked together in a fibrous form. The structure of carbon nanofiber is illustrated in **Figure 5**. They can be produced through various methods, including chemical vapor deposition and electrospinning. CNFs possess high mechanical strength, electrical conductivity, and thermal stability. They find applications in composite materials, energy storage, and sensors. Therefore, carbon nanofibers offer a range of advantages for electrochemical sensing applications, including high surface area, excellent conductivity, versatile functionalization, and compatibility with other materials

[47,78]. Ongoing research aims to further optimize the properties of CNFs, explore new synthesis techniques, and develop innovative sensor designs for various analytical applications.

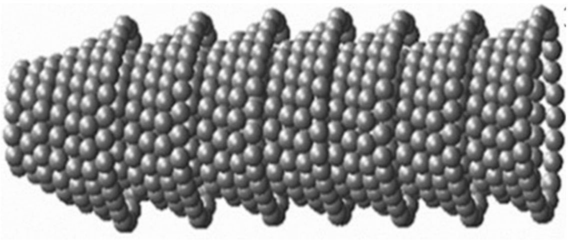

Figure 5. Structure of carbon nanofiber.

5.5. Fullerenes

Fullerenes are closed-cage carbon molecules with a hollow spherical or ellipsoidal structure. The most well-known fullerene is C60, also called buckminsterfullerene or Buckyball. Fullerenes exhibit unique electronic and optical properties and have applications in electronics, photovoltaics, and biomedical research. Thus, fullerene, specifically C60 (buckminsterfullerene), has shown promising potential for various electrochemical sensor applications. While fullerene-based sensors are not as extensively studied as other carbon nanomaterials like graphene or carbon nanotubes, they offer unique properties that make them attractive for certain sensing applications. Here are some potential applications of C60 as an electrochemical sensor [49–51]. While the use of C60 as an electrochemical sensor is still an active area of research, its unique properties, including redox activity, electron transfer kinetics, stability, and the ability to detect reactive species, make it an intriguing material for certain sensing applications. Further research and development are needed to explore and optimize the potential of C60-based electrochemical sensors and to understand their performance characteristics in various sensing scenarios. The larger C70 molecule, similar to C60, belongs to the fullerene family. It resembles the ellipsoidal cage structure of a rugby ball. The structures of C70 and C60 fullerene are shown in **Figure 6b,c**. A fullerene C70 cube is used for sensing volatile aromatic solvent vapors [52,53].

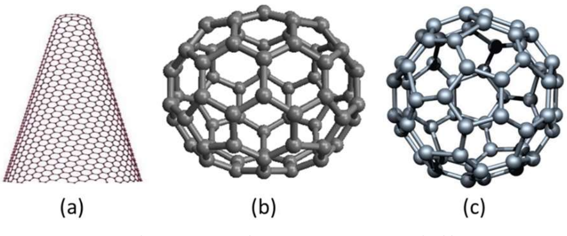

Figure 6. Structure. **(a)** carbon nanohorn; **(b)** C70 fullerene; **(c)** C60 fullerene.

5.6. Carbon dots

Carbon dots are small carbon nanoparticles with sizes typically less than 10 nanometers. They exhibit strong fluorescence properties and can be easily functionalized. As illustrated in **Figure 7**, CDs are comprised of graphene quantum dots, carbon quantum dots, carbon nanodots, and carbonized polymer dots. These dots are categorized based on the particular characteristics of their carbon core structure, surface groups, and properties [54].

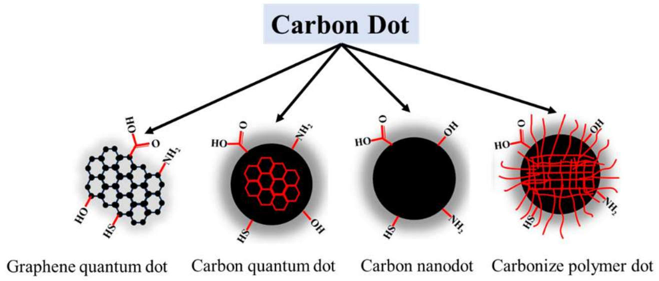

Figure 7. Classification of carbon dots.

Carbon dots find applications in bioimaging, optoelectronics, and sensing. Therefore, carbon dots as electrochemical sensors are an active area of research, with ongoing efforts focused on optimizing their properties, exploring new synthesis techniques, and developing innovative sensing strategies. The unique characteristics of CDs, including their electrochemical activity, high surface area, sensitivity, and versatility, make them attractive for a wide range of electrochemical sensing applications [55–57].

5.7. Carbon nanohorns

Carbon nanohorns (CNHs) are unique carbon nanostructures that have gained significant attention in various fields, including electrochemical sensor applications. CNHs are three-dimensional, hollow, horn-shaped carbon nanoparticles with a high surface area and unique electronic properties. The structure of carbon nanohorn is shown in **Figure 6a**. These properties make them promising candidates for sensor development, particularly in electrochemical sensing [58,59]. Ongoing research and development in this field aim to further optimize the performance of CNH-based sensors and explore new applications in sensing and detection.

6. Carbon nanomaterial-based electrochemical sensors

Due to its special qualities, which include strong electrical conductivity, a huge surface area, and exceptional chemical stability, carbon nanomaterials have demonstrated significant potential in the field of electrochemical sensors, as was previously mentioned. Their ability to efficiently transport electrons and offer a large surface area for analyte adsorption makes them excellent choices for sensing applications. A summary of the electrochemical sensors that have been developed utilizing various carbon nanomaterials is presented in **Table 1**. Applications for carbon nanomaterial-based electrochemical sensors are numerous and include food safety, industrial process control, healthcare diagnostics, and environmental monitoring [60,61]. Target analytes can be detected swiftly, cautiously, and exquisitely attributable to the distinctive characteristics of carbon nanomaterials. The goal of ongoing research is to further improve the performance of these sensors by the integration of cutting-edge signal transduction techniques, the optimization of carbon nanomaterial manufacturing, and the investigation of novel functionalization procedures.

Table 1. Carbon nanomaterials based modified electrochemical sensors [62].

Modified electrode	Drug	Method	Linear range	Limit of detection
MWNT-COOH/GCE	6-mercaptopurine	Amperometry	-	-
MWNT-COOH/GCE	6-mercaptopurine	Amperometry	0.4–100 µM	0.2 µM
SWNT-DCP/GCE	Epirubicin	Linear sweep voltammetry	0.05–50 µM	0.02 µM
CNT-CTAB/GCE	Daunorubicin	Cyclic voltammetry	20–500 nM	10 nM
MWCNT/GCE	Enrofloxacin Ciprofloxacin	Linear sweep voltammetry	2.0–780.0 µM	0.5 µM
MWCNT/GCE	Ciprofloxacin	Linear sweep voltammetry	40–1000 µM	6.0 µM
MWCNT/GCE	Gatifloxacin	Differential pulse voltammetry	21.3–1700 uM	4.5 nM
Ag NPs/MWCNTs-COOH/GCE	Adriamycin	Differential pulse voltammetry	8.2–19 nM	1.7 nM
Cyclodextrin-Gr NS/GCE	Doxorubicin Methotrexate	Differential pulse voltammetry	10 nM–0.2 µM	0.1 nM
MWCNTs/CPE	6-Mercaptopurine	Linear sweep voltammetry	0.5–900 µM	0.1 µM
O-MWNTs/GCE	Methotrexate	Differential pulse voltammetry	0.1–8.0 µM	0.015 µM
Q-MWNTs/GCE	Methotrexate	Amperometry	0.01–20 mg/L	0.2 µM/L
dsDNA-modified PPyMWCNTs/PGE	6-Mercaptopurine	Differential pulse voltammetry	0.2–100 µM	0.08 µM
CQDs/GCE	Etoposide	Differential pulse voltammetry	0.02–10.0 µM	0.005 µM
GQD/GCE	Doxorubicin hydrochloride	Differential pulse voltammetry	0.018–3.600 µM	0.016 µM
GQD/GCE	Doxorubicin hydrochloride	Differential pulse voltammetry	0.018–3.60 µM	0.016 µM
MWCNT/GCE	6-Mercaptopurine	Linear sweep voltammetry	0.5–3.0 µM	8.41 nM
MWCNT/Pt E	Doxorubicin	Cyclic voltammetry	0.2–4.0 µM/mL	0.002 µM/mL
DNA/SWCNTs/PPy/PGE	Ciprofloxacin	Differential pulse voltammetry	0.008–30.0 µM	4 nM
CB/B-CD/SPE	Flutamide	Differential pulse voltammetry	0.05–158.3 µM	0.016 µM
MWCNTs/GCE	Dacarbazine	Differential pulse voltammetry	0.4–2500 nM	0.12 nM
MWCNT-PUFIX/HF-PGE	Capecitabine Erlotinib	Differential pulse voltammetry	7.70–142.00 µM	0.11 µM
N-rGO-CS/Au	Doxorubicin	Differential pulse voltammetry	0.010–15 µM	10 nM
CNPs/N/GCE	Azathioprine	Cyclic voltammetry	0.2–50 µM	80 µM
NDG/CS/GCE	Azathioprine	Cyclic voltammetry	0.2–100 µM	65 µM

7. Working principles of electrochemical sensors

The cornerstone for the functioning of electrochemical sensors is the principle of converting an electrical signal from a chemical signal, such as the presence or concentration of an analyte. Usually, they are made up of an electrode/electrolyte system that aids in the electrochemical reactions necessary for sensing. These comprise the general working principles of electrochemical sensors; however, they might differ based on the particular design and configuration as:

7.1. Potentiometric sensors

Potentiometric sensors measure the potential difference (voltage) between two or more electrodes in an electrochemical cell. The potential difference is related to the concentration of the analyte under investigation. These sensors typically employ ion-selective electrodes (ISEs), such as pH electrodes or ion-specific electrodes, that selectively respond to specific ions in the solution. The potential difference generated by the ISE is measured and correlated with the analyte concentration using a calibration curve.

7.2. Amperometric sensors

Amperometric sensors detect the current generated by an electrochemical reaction at an electrode surface. The current is proportional to the concentration of the analyte. These sensors usually consist of a working electrode, a reference electrode, and sometimes a counter electrode. The working electrode is typically modified with a catalyst or specific molecules that facilitate the electrochemical reaction of the analyte. When the analyte comes into contact with the working electrode, it undergoes an oxidation or reduction reaction, resulting in the generation of a current that is measured and correlated with the analyte concentration.

7.3. Voltammetric sensors

Voltammetric sensors involve the measurement of the current as a function of the applied potential (voltage) at an electrode. These sensors utilize techniques such as cyclic voltammetry, differential pulse voltammetry, or square wave voltammetry. The potential is scanned over a specific range, and the resulting current response provides information about the analyte concentration. Voltammetric sensors are commonly used for the detection of redox-active species or for studying the electrochemical behavior of analytes.

7.4. Impedimetric sensors

Impedimetric sensors track variations in the electrode-electrolyte interface's impedance, or frequency-dependent resistance, in response to analyte interaction. Usually, these sensors use highly surface-aread electrodes or certain surface treatments to increase sensitivity. The electrical characteristics of the electrode-electrolyte interface, such as capacitance or charge transfer resistance, change in the presence of the analyte and are measured in order to ascertain the analyte concentration.

8. Fabrication methods of electrochemical sensor

The fabrication of electrochemical sensors involves several key steps, including the selection of materials, electrode preparation, immobilization of sensing elements, and assembly of the sensor. Here is a general overview of the fabrication process:

8.1. Material selection

The first step is to select suitable materials for the sensor components. This includes choosing appropriate electrode materials, such as metals (e.g., gold, platinum), carbon-based materials (e.g., graphite, carbon nanotubes), or conductive polymers. The selection depends on factors such as the target analyte, desired sensitivity, and compatibility with the chosen fabrication techniques.

8.2. Electrode preparation

The electrodes can be prepared through various techniques, such as physical deposition, screen printing, or lithography. For example, metal electrodes can be fabricated by depositing a thin layer of the metal onto a substrate using techniques like sputtering or evaporation. Carbon-based electrodes can be prepared by screen printing a carbon ink onto a substrate or by directly growing carbon nanomaterials on the electrode surface.

8.3. Surface modification

Surface modification is often performed to enhance the sensitivity and selectivity of the sensor. This can involve functionalizing the electrode surface with specific molecules or nanoparticles. Functionalization can be achieved through self-assembled monolayers (SAMs), electrodeposition, or chemical modification techniques. The functionalized surface allows for the immobilization of sensing elements or recognition elements that interact with the target analyte. The surface of nanotubes can be functionalized in different ways as illustrated in **Figure 8**.

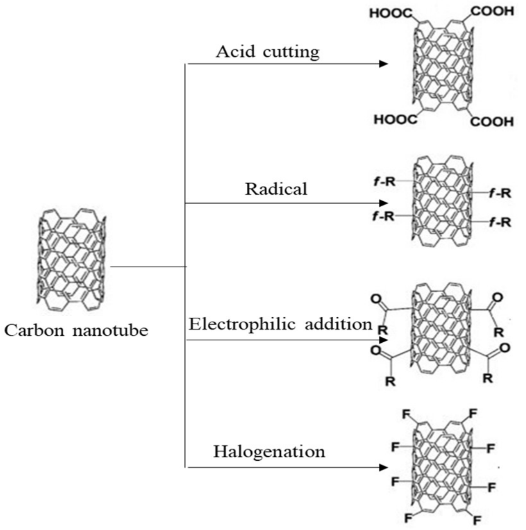

Figure 8. Surface functionalization of carbon nanotubes.

8.4. Immobilization of sensing elements

Sensing elements, such as enzymes, antibodies, or DNA probes, are immobilized onto the electrode surface to enable the selective detection of the target analyte. Immobilization techniques can include physical adsorption, covalent attachment, or entrapment within a polymer matrix. The immobilization method should ensure the stability and activity of the sensing element while allowing for efficient analyte interaction.

8.5. Sensor assembly

Once the electrode and sensing elements are prepared, the sensor is assembled. This typically involves placing the prepared electrode into a suitable housing or cell that allows for the introduction of the analyte and the connection to measurement equipment. The assembly can include additional components, such as reference electrodes or counter electrodes, depending on the sensor design.

8.6. Sensor characterization and testing

After fabrication, the sensor needs to be characterized and tested to evaluate its performance. This includes calibrating the sensor response, determining the detection limit, assessing the selectivity, and evaluating the stability and reproducibility of the sensor. Various electrochemical techniques, such as cyclic voltammetry or amperometry, are commonly used for characterization and testing.

9. Biomedical applications of electrochemical sensor

Electrochemical sensors have found numerous applications in the field of biomedicine due to their ability to provide sensitive and selective detection of various biomolecules and analytes. Here are some key biomedical applications of electrochemical sensors:

9.1. Detection of biomolecules

The detection of biomolecules, such as proteins, DNA, and other analytes, is frequently accomplished through the use of electrochemical sensors. Thus, there are electrochemical sensors that can identify DNA using a variety of approaches, such as amplification and DNA hybridization. The particular binding between a DNA probe that has been mounted on the sensor surface and its complementary target DNA sequence is what drives DNA hybridization-based sensors. A change in the electrochemical signal, such as a change in voltage or current, is caused by the hybridization event and can be monitored to determine whether the target DNA is present or concentrated [48–50]. Additionally, it could detect proteins using a variety of methods, including immunosorbent assays involving enzymes (ELISAs) and antibody-based tests. Target proteins in the sample attach to particular antibodies that have been permanently selected on the sensor surface in antibody-based sensors. Protein identification is made conceivable by the binding event, which causes a modification in the electrochemical signal. Enzyme-labeled antibodies that react with the target protein to produce an electrochemical signal are used in ELISA-based electrochemical sensors [63–66]. In addition, enzymatic activity, which is frequently employed to quantify the presence of particular biomolecules, can be detected by electrochemical sensors. Immobilized enzymes that have been immobilized that catalyze particular reactions with the target analyte are used in enzyme-based sensors. An electrochemical signal, such as a shift in potential or current, has been generated by the enzymatic process and can be evaluated for determining the quantity of the target biomolecule [67–69]. Aptamers, which are short single-stranded DNA or RNA molecules, can bind to target molecules with high specificity. Electrochemical sensors can be functionalized with aptamers, allowing for the selective detection of various analytes, including small molecules, proteins, and toxins. The binding of the target analyte to the aptamer leads to changes in the electrochemical signal, enabling sensitive and specific detection [70–72]. In addition, electrochemical sensors can be integrated with nucleic acid amplification techniques, such as polymerase chain reaction (PCR) or loop-mediated isothermal amplification (LAMP), to enhance the sensitivity of DNA or RNA detection [73–75]. These amplification techniques produce multiple copies of the target nucleic acid sequence, which can be detected by the electrochemical sensor.

9.2. Disease diagnosis

In the detection and monitoring of cancer, infectious diseases, and other medical disorders, electrochemical sensors have demonstrated considerable promise in the field of disease diagnostics. It may be useful in the early identification and treatment of cancer. Prostate-specific antigen (PSA) for prostate cancer and carcinoembryonic antigen (CEA) for colorectal cancer are two examples of specific biomarkers that they can identify. Electrochemical sensors can provide important information for cancer screening, diagnosis, and treatment response monitoring by detecting the concentration of these biomarkers in patient samples [76–78]. Besides this, electrochemical sensors are also employed for the rapid and sensitive detection of infectious agents, including bacteria, viruses, and parasites. By targeting specific nucleic acid sequences or antigens associated with the pathogens, electrochemical sensors can identify infections such as HIV, hepatitis, malaria, and respiratory infections. These sensors offer the potential for point-of-care testing, enabling early diagnosis and timely treatment [79–81]. In addition, electrochemical sensors are commonly used for continuous glucose monitoring in diabetes management. By measuring glucose levels in body fluids, such as blood or interstitial fluid, electrochemical sensors provide real-time information about glucose concentration. This helps individuals with diabetes to monitor and manage their blood sugar levels, ensuring proper insulin administration and dietary adjustments [82,83]. It is also employed for the detection of cardiac biomarkers, such as troponin, creatine kinase-MB (CK-MB), and brain natriuretic peptide (BNP). These biomarkers are indicative of heart damage or dysfunction and are used in the diagnosis of acute myocardial infarction (heart attack), heart failure, and other cardiac conditions [83–86]. Thus, electrochemical sensors can provide rapid and sensitive measurements of these biomarkers, aiding in early diagnosis and risk assessment. Moreover, electrochemical sensors can be used for genetic disease screening, such as detecting mutations or variations in specific genes associated with inherited disorders. By incorporating DNA probes or aptamers specific to the target genetic sequence, electrochemical sensors can identify genetic mutations and variations linked to diseases like cystic fibrosis, sickle cell anemia, and genetic predisposition to certain cancers [87–88]. Again more, electrochemical sensors have applications in the diagnosis and monitoring of neurological disorders. They can measure neurotransmitters, such as dopamine and serotonin, in the central nervous system, providing insights into conditions like Parkinson’s disease, depression, and schizophrenia. It can also detect biomarkers associated with neurodegenerative diseases, such as Alzheimer’s and Huntington’s diseases [89–91].

9.3. Electrochemical biosensing in drug delivery

The use of biosensors in drug delivery systems to track and regulate different medication administration parameters is known as “biosensing in drug delivery”. Medication delivery can be tailored and optimized with the help of biosensors, which can offer real-time data on medication release, drug concentration, physiological parameters, and patient reaction. Drug release from delivery methods like implants, patches, or nanoparticles can be tracked using biosensors. Biosensors ensure the intended therapeutic impact by providing feedback on the release profile through the incorporation of sensing devices that react to changes in medication concentration or release kinetics. The drug delivery mechanism can be improved or the dosage can be changed with the use of this information [92,93]. Drug monitoring, Biosensors can measure drug concentrations in biological fluids, such as blood or interstitial fluid, enabling the monitoring of drug levels in real-time. This information helps in maintaining therapeutic drug concentrations within the desired range, ensuring efficacy while minimizing side effects or toxicity [94–96]. Besides this, biosensors can be designed to detect specific drugs or drug classes using various sensing mechanisms, including enzymatic reactions, immunoassays, or affinity-based interactions. Moreover, it can be integrated into drug delivery systems to monitor relevant physiological parameters. For example, biosensors can measure parameters such as pH, temperature, oxygen levels, or biomarkers indicative of disease progression or treatment response. This information can be used to optimize drug delivery parameters or trigger drug release in response to specific physiological cues. In addition, biosensors can be coupled with drug delivery systems to create closed-loop or feedback control systems. Biosensors continuously monitor drug concentrations or physiological parameters and provide feedback to control drug delivery rates or adjust dosing algorithms in real-time. This enables personalized and adaptive drug delivery, ensuring optimal therapeutic outcomes [97,98].

10. Challenges and future perspectives of electrochemical sensors

Because of their special qualities and possible uses, carbon-based electrochemical sensors—such as carbon nanotubes (CNTs) and graphene—have drawn a lot of interest. But they also have to deal with some difficulties. Because of their high electrical conductivity and huge surface area, carbon-based sensors frequently show great sensitivity. However, achieving consistent and reproducible sensor performance can be challenging due to variations in material properties and fabrication techniques. Future research aims to optimize sensor performance by developing standardized fabrication processes, improving material quality, and enhancing the understanding of surface interactions and electrochemical properties. Selectivity is a crucial aspect of sensor performance, as it determines the ability to distinguish the target analyte from interfering species. Thus, carbon-based sensors may suffer from non-specific adsorption or interference from other components present in complex samples. Future efforts focus on surface functionalization, selective modification, and integration with specific recognition elements (e.g., antibodies or aptamers) to enhance selectivity and mitigate interference effects.

Long-term stability is a challenge for carbon-based sensors, as they can be susceptible to fouling, surface contamination, or material degradation over time. Researchers are exploring surface modification techniques, protective coatings, and encapsulation strategies to improve the stability and longevity of carbon-based sensors, especially in harsh or dynamic environments. Scalability of carbon-based sensors for mass production is an important consideration for their practical applications. Challenges exist in translating lab-scale fabrication techniques to scalable manufacturing processes while maintaining sensor performance and consistency. Future research aims to develop cost-effective and scalable manufacturing methods for carbon-based sensors, including roll-to-roll printing, solution processing, and other high-throughput techniques. Integration of carbon-based sensors into compact, portable devices or wearable systems is a key area of development. Miniaturization of these sensors requires addressing challenges related to electronics integration, power management, and device packaging. Future perspectives involve advancements in flexible electronics, wireless communication, and microfabrication techniques to enable the seamless integration of carbon-based sensors into various form factors.

Carbon-based sensors have the potential for multifunctionality and multimodal sensing by combining their electrochemical properties with other sensing modalities, such as optical or mechanical sensing. Integrating multiple sensing mechanisms can provide complementary information and enhance overall sensor performance. Future research focuses on developing hybrid sensor platforms that combine carbon-based materials with other functional materials or transduction principles for multimodal sensing capabilities. As with any technology, environmental considerations are important for carbon-based electrochemical sensors. Efforts are being made to develop eco-friendly and sustainable fabrication processes, minimize the use of hazardous materials, and explore recycling or disposal strategies for sensor devices.

11. Conclusion

In conclusion, carbon-based electrochemical sensors offer unique properties and tremendous potential for various applications. These sensors exhibit high sensitivity, a large surface area, excellent electrical conductivity, and can be functionalized to enhance selectivity. However, they also face challenges such as achieving consistent and reproducible sensor performance, addressing selectivity and interference issues, ensuring stability and longevity, enabling scalable manufacturing, facilitating integration and miniaturization, and considering environmental sustainability. Despite these challenges, ongoing research and technological advancements are paving the way for the future of carbon-based electrochemical sensors. Efforts are focused on optimizing sensor performance through standardized fabrication processes, improving material quality, and understanding surface interactions. Selectivity is being enhanced through surface functionalization, selective modification, and integration with recognition elements. Stability and longevity are being improved through surface modification techniques and protective coatings. Scalable manufacturing methods are being developed to enable mass production, and integration into compact, portable devices and wearable systems is being pursued. Multifunctionality and multimodal sensing capabilities are being explored by combining carbon-based materials with other sensing modalities. Additionally, environmental considerations, such as eco-friendly fabrication processes and recycling strategies, are being addressed.

Conflict of interest: The authors declare no conflict of interest.

References

1. Lu H, He B, Gao B. Emerging electrochemical sensors for life healthcare. Engineered Regeneration. 2021; 2: 175-181. doi: 10.1016/j.engreg.2021.12.002
2. Sinha K, Uddin Z, Kawsar HI, et al. Analyzing chronic disease biomarkers using electrochemical sensors and artificial neural networks. TrAC Trends in Analytical Chemistry. 2023; 158: 116861. doi: 10.1016/j.trac.2022.116861
3. Taniselass S, Arshad MKM, Gopinath SCB. Graphene-based electrochemical biosensors for monitoring noncommunicable disease biomarkers. Biosensors and Bioelectronics. 2019; 130: 276-292. doi: 10.1016/j.bios.2019.01.047
4. Haque S, Yasir M, Ciocan S, et al. Enzymatic Fuel Cells and Biosensors. In: Ghangrekar MM, Duteanu NM, Surampalli RY, Zhang TC (editors). Microbial Electrochemical Technologies. Wiley‐VCH GmbH; 2023. pp. 467-494. doi: 10.1002/9783527839001.ch19
5. Haque S, Nasar A, Duteanu N, et al. Carbon based-nanomaterials used in biofuel cells – A review. Fuel. 2023; 331: 125634. doi: 10.1016/j.fuel.2022.125634
6. Simoska O, Stevenson KJ. Electrochemical sensors for rapid diagnosis of pathogens in real time. The Analyst. 2019; 144(22): 6461-6478. doi: 10.1039/c9an01747j
7. Min J, Sempionatto JR, Teymourian H, et al. Wearable electrochemical biosensors in North America. Biosensors and Bioelectronics. 2021; 172: 112750. doi: 10.1016/j.bios.2020.112750
8. Campuzano S, Barderas R, Moreno-Casbas MT, et al. Pursuing precision in medicine and nutrition: the rise of electrochemical biosensing at the molecular level. Analytical and Bioanalytical Chemistry. 2023; 416(9): 2151-2172. doi: 10.1007/s00216-023-04805-5
9. Umapathi R, Ghoreishian SM, Rani GM, et al. Review—Emerging Trends in the Development of Electrochemical Devices for the On-Site Detection of Food Contaminants. ECS Sensors Plus. 2022; 1(4): 044601. doi: 10.1149/2754-2726/ac9d4a
10. Zhang W, Wang R, Luo F, et al. Miniaturized electrochemical sensors and their point-of-care applications. Chinese Chemical Letters. 2020; 31(3): 589-600. doi: 10.1016/j.cclet.2019.09.022
11. Pakchin PS, Nakhjavani SA, Saber R, et al. Recent advances in simultaneous electrochemical multi-analyte sensing platforms. TrAC Trends in Analytical Chemistry. 2017; 92: 32-41. doi: 10.1016/j.trac.2017.04.010
12. Zhu C, Yang G, Li H, et al. Electrochemical Sensors and Biosensors Based on Nanomaterials and Nanostructures. Analytical Chemistry. 2014; 87(1): 230-249. doi: 10.1021/ac5039863
13. Teymourian H, Parrilla M, Sempionatto JR, et al. Wearable Electrochemical Sensors for the Monitoring and Screening of Drugs. ACS Sensors. 2020; 5(9): 2679-2700. doi: 10.1021/acssensors.0c01318
14. Lu T, Ji S, Jin W, et al. Biocompatible and Long-Term Monitoring Strategies of Wearable, Ingestible and Implantable Biosensors: Reform the Next Generation Healthcare. Sensors. 2023; 23(6): 2991. doi: 10.3390/s23062991
15. Rossi LM, Quach AD, Rosenzweig Z. Glucose oxidase? magnetite nanoparticle bioconjugate for glucose sensing. Analytical and Bioanalytical Chemistry. 2004; 380(4): 606-613. doi: 10.1007/s00216-004-2770-3
16. Madden J, Vaughan E, Thompson M, et al. Electrochemical sensor for enzymatic lactate detection based on laser-scribed graphitic carbon modified with platinum, chitosan and lactate oxidase. Talanta. 2022; 246: 123492. doi: 10.1016/j.talanta.2022.123492
17. Singh AP, Balayan S, Hooda V, et al. Nano-interface driven electrochemical sensor for pesticides detection based on the acetylcholinesterase enzyme inhibition. International Journal of Biological Macromolecules. 2020; 164: 3943-3952. doi: 10.1016/j.ijbiomac.2020.08.215
18. Teeparuksapun K, Hedström M, Mattiasson B. A Sensitive Capacitive Biosensor for Protein a Detection Using Human IgG Immobilized on an Electrode Using Layer-by-Layer Applied Gold Nanoparticles. Sensors. 2021; 22(1): 99. doi: 10.3390/s22010099
19. Razzino CA, Serafín V, Gamella M, et al. An electrochemical immunosensor using gold nanoparticles-PAMAM-nanostructured screen-printed carbon electrodes for tau protein determination in plasma and brain tissues from Alzheimer patients. Biosensors and Bioelectronics. 2020; 163: 112238. doi: 10.1016/j.bios.2020.112238
20. Wu Y, Arroyo-Currás N. Advances in nucleic acid architectures for electrochemical sensing. Current Opinion in Electrochemistry. 2021; 27: 100695. doi: 10.1016/j.coelec.2021.100695
21. Wang DX, Wang J, Wang YX, et al. DNA nanostructure-based nucleic acid probes: construction and biological applications. Chemical Science. 2021; 12(22): 7602-7622. doi: 10.1039/d1sc00587a

22. Gao X, Dong S, Fu L, et al. Use of Triangular Silver Nanoplates as Low Potential Redox Mediators for Electrochemical Sensing. Analytical Chemistry. 2021; 93(6): 3295-3300. doi: 10.1021/acs.analchem.0c05342
23. Mayall RM, Marenco AJ, Kilgore M, et al. Ultrasensitive Detection of Surface-Confined Redox Molecules by Mediation-Based Amplification. ChemElectroChem. 2021; 8(10): 1873-1880. doi: 10.1002/celc.202100369
24. Nishitani S, Sakata T. Enhancement of Signal-to-Noise Ratio for Serotonin Detection with Well-Designed Nanofilter-Coated Potentiometric Electrochemical Biosensor. ACS Applied Materials & Interfaces. 2020; 12(13): 14761-14769. doi: 10.1021/acsami.9b19309
25. Hassan MH, Vyas C, Grieve B, et al. Recent Advances in Enzymatic and Non-Enzymatic Electrochemical Glucose Sensing. Sensors. 2021; 21(14): 4672. doi: 10.3390/s21144672
26. Manjakkal L, Szwagierczak D, Dahiya R. Metal oxides based electrochemical pH sensors: Current progress and future perspectives. Progress in Materials Science. 2020; 109: 100635. doi: 10.1016/j.pmatsci.2019.100635
27. Beaver K, Dantanarayana A, Minteer SD. Materials Approaches for Improving Electrochemical Sensor Performance. The Journal of Physical Chemistry B. 2021; 125(43): 11820-11834. doi: 10.1021/acs.jpcb.1c07063
28. Porto LS, Silva DN, de Oliveira AEF, et al. Carbon nanomaterials: synthesis and applications to development of electrochemical sensors in determination of drugs and compounds of clinical interest. Reviews in Analytical Chemistry. 2020; 38(3). doi: 10.1515/revac-2019-0017
29. Asadian E, Ghalkhani M, Shahrokhian S. Electrochemical sensing based on carbon nanoparticles: A review. Sensors and Actuators B: Chemical. 2019; 293: 183-209. doi: 10.1016/j.snb.2019.04.075
30. Cho IH, Kim DH, Park S. Electrochemical biosensors: perspective on functional nanomaterials for on-site analysis. Biomaterials Research. 2020; 24(1). doi: 10.1186/s40824-019-0181-y
31. Yan Y, Miao J, Yang Z, et al. Carbon nanotube catalysts: recent advances in synthesis, characterization and applications. Chemical Society Reviews. 2015; 44(10): 3295-3346. doi: 10.1039/c4cs00492b
32. Zhou C, Zou H, Sun C, et al. Recent advances in biosensors for antibiotic detection: Selectivity and signal amplification with nanomaterials. Food Chemistry. 2021; 361: 130109. doi: 10.1016/j.foodchem.2021.130109
33. Cho IH, Lee J, Kim J, et al. Current Technologies of Electrochemical Immunosensors: Perspective on Signal Amplification. Sensors. 2018; 18(2): 207. doi: 10.3390/s18010207
34. Zamora-Gálvez A, Morales-Narváez E, Mayorga-Martinez CC, et al. Nanomaterials connected to antibodies and molecularly imprinted polymers as bio/receptors for bio/sensor applications. Applied Materials Today. 2017; 9: 387-401. doi: 10.1016/j.apmt.2017.09.006
35. Mahmoudpour M, Ezzati Nazhad Dolatabadi J, Torbati M, et al. Nanomaterials and new biorecognition molecules based surface plasmon resonance biosensors for mycotoxin detection. Biosensors and Bioelectronics. 2019; 143: 111603. doi: 10.1016/j.bios.2019.111603
36. Pasinszki T, Krebsz M, Tung TT, et al. Carbon Nanomaterial Based Biosensors for Non-Invasive Detection of Cancer and Disease Biomarkers for Clinical Diagnosis. Sensors. 2017; 17(8): 1919. doi: 10.3390/s17081919
37. Fahmy HM, Abu Serea ES, Salah-Eldin RE, et al. Recent Progress in Graphene- and Related Carbon-Nanomaterial-based Electrochemical Biosensors for Early Disease Detection. ACS Biomaterials Science & Engineering. 2022; 8(3): 964-1000. doi: 10.1021/acsbiomaterials.1c00710
38. Pineda S, Han Z, Ostrikov K. Plasma-Enabled Carbon Nanostructures for Early Diagnosis of Neurodegenerative Diseases. Materials. 2014; 7(7): 4896-4929. doi: 10.3390/ma7074896
39. Gan T, Hu, S. Electrochemical sensors based on graphene materials. Microchimica Acta. 2011; 175: 1–19. doi: 10.1007/s00604-011-0639-7S
40. Li SJ, Xing Y, Wang GF. A graphene-based electrochemical sensor for sensitive and selective determination of hydroquinone. Microchimica Acta. 2011; 176(1-2): 163-168. doi: 10.1007/s00604-011-0709-x
41. Terse-Thakoor T, Badhulika S, Mulchandani A. Graphene based biosensors for healthcare. Journal of Materials Research. 2017; 32(15): 2905-2929. doi: 10.1557/jmr.2017.175
42. Coroş M, Pruneanu S, Stefan-van Staden RI. Review—Recent Progress in the Graphene-Based Electrochemical Sensors and Biosensors. Journal of The Electrochemical Society. 2019; 167(3): 037528. doi: 10.1149/2.0282003jes
43. Ahmad H, Fan M, Hui D. Graphene oxide incorporated functional materials: A review. Composites Part B: Engineering. 2018; 145: 270-280. doi: 10.1016/j.compositesb.2018.02.006

44. Hayyan M, Abo-Hamad A, AlSaadi MA, et al. Functionalization of graphene using deep eutectic solvents. Nanoscale Research Letters. 2015; 10(1). doi: 10.1186/s11671-015-1004-2
45. Li J, Kuang D, Feng Y, et al. A graphene oxide-based electrochemical sensor for sensitive determination of 4-nitrophenol. Journal of Hazardous Materials. 2012; 201-202: 250-259. doi: 10.1016/j.jhazmat.2011.11.076
46. Qian L, Thiruppathi AR, Elmahdy R, et al. Graphene-Oxide-Based Electrochemical Sensors for the Sensitive Detection of Pharmaceutical Drug Naproxen. Sensors. 2020; 20(5): 1252. doi: 10.3390/s20051252
47. Zhang L, Yin M, Wei X, et al. Recent advances in morphology, aperture control, functional control and electrochemical sensors applications of carbon nanofibers. Analytical Biochemistry. 2022; 656: 114882. doi: 10.1016/j.ab.2022.114882
48. Jahromi Z, Mirzaei E, Savardashtaki A, et al. A rapid and selective electrochemical sensor based on electrospun carbon nanofibers for tramadol detection. Microchemical Journal. 2020; 157: 104942. doi: 10.1016/j.microc.2020.104942
49. Kurbanoglu S, Cevher SC, Toppare L, et al. Electrochemical biosensor based on three components random conjugated polymer with fullerene (C60). Bioelectrochemistry. 2022; 147: 108219. doi: 10.1016/j.bioelechem.2022.108219
50. Paukov M, Kramberger C, Begichev I, et al. Functionalized Fullerenes and Their Applications in Electrochemistry, Solar Cells, and Nanoelectronics. Materials. 2023; 16(3): 1276. doi: 10.3390/ma16031276
51. Gakhar T, Rosenwaks Y, Hazra A. Fullerene (C60) functionalized TiO_2 nanotubes for conductometric sensing of formaldehyde. Sensors and Actuators B: Chemical. 2022; 364: 131892. doi: 10.1016/j.snb.2022.131892
52. Bai J, Sun C, Jiang X. Carbon dots-decorated multiwalled carbon nanotubes nanocomposites as a high-performance electrochemical sensor for detection of H_2O_2 in living cells. Analytical and Bioanalytical Chemistry. 2016; 408(17): 4705-4714. doi: 10.1007/s00216-016-9554-4
53. Lin X, Xiong M, Zhang J, et al. Carbon dots based on natural resources: Synthesis and applications in sensors. Microchemical Journal. 2021; 160: 105604. doi: 10.1016/j.microc.2020.105604
54. Xu D, Lin Q, Chang H. Recent Advances and Sensing Applications of Carbon Dots. Small Methods. 2019; 4(4). doi: 10.1002/smtd.201900387
55. Carli S, Lambertini L, Zucchini E, et al. Single walled carbon nanohorns composite for neural sensing and stimulation. Sensors and Actuators B: Chemical. 2018; 271: 280-288. doi: 10.1016/j.snb.2018.05.083
56. Zhang R, Fu K, Zou F, et al. Highly sensitive electrochemical sensor based on Pt nanoparticles/carbon nanohorns for simultaneous determination of morphine and MDMA in biological samples. Electrochimica Acta. 2021; 370: 137803. doi: 10.1016/j.electacta.2021.137803
57. Qureshi A, Kang WP, Davidson JL, et al. Review on carbon-derived, solid-state, micro and nano sensors for electrochemical sensing applications. Diamond and Related Materials. 2009; 18(12): 1401-1420. doi: 10.1016/j.diamond.2009.09.008
58. Yang Y, Yang X, Yang Y, et al. Aptamer-functionalized carbon nanomaterials electrochemical sensors for detecting cancer relevant biomolecules. Carbon. 2018; 129: 380-395. doi: 10.1016/j.carbon.2017.12.013
59. Lv MM, Fan SF, Wang QL, et al. An enzyme-free electrochemical sandwich DNA assay based on the use of hybridization chain reaction and gold nanoparticles: application to the determination of the DNA of Helicobacter pylori. Microchimica Acta. 2019; 187(1). doi: 10.1007/s00604-019-3999-z
60. Santhanam M, Algov I, Alfonta L. DNA/RNA Electrochemical Biosensing Devices a Future Replacement of PCR Methods for a Fast Epidemic Containment. Sensors. 2020; 20(16): 4648. doi: 10.3390/s20164648
61. Zhang L, Su W, Liu S, et al. Recent Progresses in Electrochemical DNA Biosensors for MicroRNA Detection. Phenomics. 2022; 2(1): 18-32. doi: 10.1007/s43657-021-00032-z
62. Mazouz Z, Mokni M, Fourati N, et al. Computational approach and electrochemical measurements for protein detection with MIP-based sensor. Biosensors and Bioelectronics. 2020; 151: 111978. doi: 10.1016/j.bios.2019.111978
63. Vanova V, Mitrevska K, Milosavljevic V, et al. Peptide-based electrochemical biosensors utilized for protein detection. Biosensors and Bioelectronics. 2021; 180: 113087. doi: 10.1016/j.bios.2021.113087
64. Yakoh A, Pimpitak U, Rengpipat S, et al. Paper-based electrochemical biosensor for diagnosing COVID-19: Detection of SARS-CoV-2 antibodies and antigen. Biosensors and Bioelectronics. 2021; 176: 112912. doi: 10.1016/j.bios.2020.112912
65. Ranallo S, Bracaglia S, Sorrentino D, et al. Synthetic Antigen-Conjugated DNA Systems for Antibody Detection and Characterization. ACS Sensors. 2023; 8(7): 2415-2426. doi: 10.1021/acssensors.3c00564
66. Coronado-Apodaca KG, González-Meza GM, Aguayo-Acosta A, et al. Immobilized Enzyme-based Novel Biosensing System for Recognition of Toxic Elements in the Aqueous Environment. Topics in Catalysis. 2023; 66(9-12): 606-624. doi: 10.1007/s11244-023-01786-8

67. Bucur B, Purcarea C, Andreescu S, et al. Addressing the Selectivity of Enzyme Biosensors: Solutions and Perspectives. Sensors. 2021; 21(9): 3038. doi: 10.3390/s21093038
68. Cavalcante FTT, de A. Falcão IR, da S. Souza JE, et al. Designing of Nanomaterials-Based Enzymatic Biosensors: Synthesis, Properties, and Applications. Electrochem. 2021; 2(1): 149-184. doi: 10.3390/electrochem2010012
69. Ziółkowski R, Jarczewska M, Górski Ł, et al. From Small Molecules toward Whole Cells Detection: Application of Electrochemical Aptasensors in Modern Medical Diagnostics. Sensors. 2021; 21(3): 724. doi: 10.3390/s21030724
70. Onaş AM, Dascălu C, Raicopol MD, et al. Critical Design Factors for Electrochemical Aptasensors Based on Target-Induced Conformational Changes: The Case of Small-Molecule Targets. Biosensors. 2022; 12(10): 816. doi: 10.3390/bios12100816
71. Mahmoudpour M, Karimzadeh Z, Ebrahimi G, et al. Synergizing Functional Nanomaterials with Aptamers Based on Electrochemical Strategies for Pesticide Detection: Current Status and Perspectives. Critical Reviews in Analytical Chemistry. 2021; 52(8): 1818-1845. doi: 10.1080/10408347.2021.1919987
72. Wang Z, Li P, Cui L, et al. Integration of nanomaterials with nucleic acid amplification approaches for biosensing. TrAC Trends in Analytical Chemistry. 2020; 129: 115959. doi: 10.1016/j.trac.2020.115959
73. Chen Y, Qian C, Liu C, et al. Nucleic acid amplification free biosensors for pathogen detection. Biosensors and Bioelectronics. 2020; 153: 112049. doi: 10.1016/j.bios.2020.112049
74. Wang Z yue, Li P, Cui L, et al. Integration of nanomaterials with nucleic acid amplification approaches for biosensing. TrAC Trends in Analytical Chemistry. 2020; 129: 115959. doi: 10.1016/j.trac.2020.115959
75. Bertok T, Bertokova A, Hroncekova S, et al. Novel Prostate Cancer Biomarkers: Aetiology, Clinical Performance and Sensing Applications. Chemosensors. 2021; 9(8): 205. doi: 10.3390/chemosensors9080205
76. Zhang W, Xiao G, Chen J, et al. Electrochemical biosensors for measurement of colorectal cancer biomarkers. Analytical and Bioanalytical Chemistry. 2021; 413(9): 2407-2428. doi: 10.1007/s00216-021-03197-8
77. Dowlatshahi S, Abdekhodaie MJ. Electrochemical prostate-specific antigen biosensors based on electroconductive nanomaterials and polymers. Clinica Chimica Acta. 2021; 516: 111-135. doi: 10.1016/j.cca.2021.01.018
78. Menon S, Mathew MR, Sam S, et al. Recent advances and challenges in electrochemical biosensors for emerging and re-emerging infectious diseases. Journal of Electroanalytical Chemistry. 2020; 878: 114596. doi: 10.1016/j.jelechem.2020.114596
79. Brazaca LC, dos Santos PL, de Oliveira PR, et al. Biosensing strategies for the electrochemical detection of viruses and viral diseases – A review. Analytica Chimica Acta. 2021; 1159: 338384. doi: 10.1016/j.aca.2021.338384
80. Cesewski E, Johnson BN. Electrochemical biosensors for pathogen detection. Biosensors and Bioelectronics. 2020; 159: 112214. doi: 10.1016/j.bios.2020.112214
81. Karyakin AA. Glucose biosensors for clinical and personal use. Electrochemistry Communications. 2021; 125: 106973. doi: 10.1016/j.elecom.2021.106973
82. Lipińska W, Grochowska K, Siuzdak K. Enzyme Immobilization on Gold Nanoparticles for Electrochemical Glucose Biosensors. Nanomaterials. 2021; 11(5): 1156. doi: 10.3390/nano11051156
83. Shinde R, Juwarwala I, Modi V, et al. Chandarana C. Utility of cardiac biomarkers and biosensors for diagnosis of acute myocardial infarction. Global Translational Medicine. 2023; 2(2): 0403. doi: 10.36922/gtm.0403
84. Zhong S, Chen L, Shi X, et al. Recent advances in electrochemical aptasensors for detecting cardiac biomarkers: A review. Microchemical Journal. 2023; 193: 109063. doi: 10.1016/j.microc.2023.109063
85. Kazemi Asl S, Rahimzadegan M. Recent Advances in the Fabrication of Nano-aptasensors for the Detection of Troponin as a Main Biomarker of Acute Myocardial Infarction. Critical Reviews in Analytical Chemistry. 2021; 53(3): 594-613. doi: 10.1080/10408347.2021.1967721
86. Aljabali AA, Obeid MA, Amawi HA, et al. Application of Nanomaterials in the Diagnosis and Treatment of Genetic Disorders. In: Applications of Nanomaterials in Human Health. Springer; 2020.
87. Jiang H, Xi H, Juhas M, et al. Biosensors for Point Mutation Detection. Frontiers in Bioengineering and Biotechnology. 2021; 9. doi: 10.3389/fbioe.2021.797831
88. Song Z, Zhou Y, Han X, et al. Recent advances in enzymeless-based electrochemical sensors to diagnose neurodegenerative diseases. Journal of Materials Chemistry B. 2021; 9(5): 1175-1188. doi: 10.1039/d0tb02745f
89. Karaboğa MNS, Sezgintürk MK. Biosensor approaches on the diagnosis of neurodegenerative diseases: Sensing the past to the future. Journal of Pharmaceutical and Biomedical Analysis. 2022; 209: 114479. doi: 10.1016/j.jpba.2021.114479

90. Brazaca LC, Sampaio I, Zucolotto V, et al. Applications of biosensors in Alzheimer's disease diagnosis. Talanta. 2020; 210: 120644. doi: 10.1016/j.talanta.2019.120644
91. Jampilek J, Kralova K. Advances in Drug Delivery Nanosystems Using Graphene-Based Materials and Carbon Nanotubes. Materials. 2021; 14(5): 1059. doi: 10.3390/ma14051059
92. Castro KPR, Colombo RNP, Iost RM, et al. Low-dimensionality carbon-based biosensors: the new era of emerging technologies in bioanalytical chemistry. Analytical and Bioanalytical Chemistry. 2023; 415(18): 3879-3895. doi: 10.1007/s00216-023-04578-x
93. Hassanpour S, Behnam B, Baradaran B, et al. Carbon based nanomaterials for the detection of narrow therapeutic index pharmaceuticals. Talanta. 2021; 221: 121610. doi: 10.1016/j.talanta.2020.121610
94. Qian L, Durairaj S, Prins S, et al. Nanomaterial-based electrochemical sensors and biosensors for the detection of pharmaceutical compounds. Biosensors and Bioelectronics. 2021; 175: 112836. doi: 10.1016/j.bios.2020.112836
95. Fu E, Khederlou K, Lefevre N, et al. Progress on Electrochemical Sensing of Pharmaceutical Drugs in Complex Biofluids. Chemosensors. 2023; 11(8): 467. doi: 10.3390/chemosensors11080467
96. Manikkath J, Subramony JA. Toward closed-loop drug delivery: Integrating wearable technologies with transdermal drug delivery systems. Advanced Drug Delivery Reviews. 2021; 179: 113997. doi: 10.1016/j.addr.2021.113997
97. Bhave G, Chen JC, Singer A, et al. Distributed sensor and actuator networks for closed-loop bioelectronic medicine. Materials Today. 2021; 46: 125-135. doi: 10.1016/j.mattod.2020.12.020
98. Cicha I, Priefer R, Severino P, et al. Biosensor-Integrated Drug Delivery Systems as New Materials for Biomedical Applications. Biomolecules. 2022; 12(9): 1198. doi: 10.3390/biom12091198

Characterization and Application of Nanomaterials 2024, 7(1), 4581.
https://doi.org/10.24294/can.v7i1.4581

Review

Graphene in gas separation membranes—State-of-the-art and potential spoors

Ayesha Kausar[1,2,*], **Ishaq Ahmad**[1,2]

[1] NPU-NCP Joint International Research Center on Advanced Nanomaterials and Defects Engineering, Northwestern Polytechnical University, Xi'an 710072, China

[2] UNESCO-UNISA Africa Chair in Nanosciences/Nanotechnology, iThemba LABS, Somerset West 7129, South Africa

*** Corresponding author:** Ayesha Kausar, dr.ayeshakausar@yahoo.com

CITATION

Kausar A, Ahmad I. Graphene in gas separation membranes—State-of-the-art and potential spoors. Characterization and Application of Nanomaterials. 2024; 7(1): 4581. https://doi.org/10.24294/can.v7i1.4581

ARTICLE INFO

Received: 7 February 2024
Accepted: 27 February 2024
Available online: 9 April 2024

Abstract: Graphene and derivatives have been frequently used to form advanced nanocomposites. A very significant utilization of polymer/graphene nanocomposite was found in the membrane sector. The up-to-date overview essentially highlights the design, features, and advanced functions of graphene nanocomposite membranes towards gas separations. In this concern, pristine thin layer graphene as well as graphene nanocomposites with poly(dimethyl siloxane), polysulfone, poly(methyl methacrylate), polyimide, and other matrices have been perceived as gas separation membranes. In these membranes, the graphene dispersion and interaction with polymers through applying the appropriate processing techniques have led to optimum porosity, pore sizes, and pore distribution, i.e., suitable for selective separation of gaseous molecules. Consequently, the graphene-derived nanocomposites brought about numerous revolutions in high-performance gas separation membranes. The structural diversity of polymer/graphene nanocomposites has facilitated the membrane selective separation, permeation, and barrier processes, especially in the separation of desired gaseous molecules, ions, and contaminants. Future research on the innovative nanoporous graphene-based membrane can overcome design/performance-related challenging factors for technical utilizations.

Keywords: graphene; polymer; nanocomposite; membrane; gas separation; selectivity; permeation

1. Introduction

For environmental remediation purposes, membrane technology has been widely adopted, especially for the separation of desired or toxic gaseous species [1]. Among membranes, polymeric membranes have durability, long functioning, and efficient performance, so they have achieved significance for separation applications. The graphene-filled nanocomposite membranes possess superior characteristics for technical fields such as gaseous, water molecules, and chemical separations [2]. The subsequent membranes were formed for large-scale gas separation, water decontamination, fuel cells, and several other applied fields [3,4]. Primarily, the graphene-derived nanocomposite membranes have been developed with torturing pathways in the matrices to promote gaseous, water molecules, ions, or diffusion of other species [5]. Consistent graphene dispersion in the membranes was found to improve the targeted impurities and toxic molecules from the medium of interest [6,7]. The membrane processes studied for these nanocomposites include ultrafiltration, microfiltration, nanofiltration, and reverse osmosis [8–10]. The resultant membranes were competently applied for eliminating the pollutants [11]. The graphene-reinforced membranes revealed superior structural benefits than the pristine polymer designs due to facile manufacturing and performance advantages [12]. Research developments have reported technical growth of these membranes for numerous sectors [13].

In the polymeric membranes, graphene, graphene oxide, and other modified graphene forms have been applied [14]. It is worth mentioning that the thin layer of neat graphene nanosheet has been designed for selective permeation of gaseous molecules [15]. In polymeric matrices, graphene has revealed fine reinforcement effects relative to other carbon nanofillers (fullerene, carbon nanotube, etc.) [16]. Including multilayered graphene or graphene oxide in the polymer membranes has been known to form two-dimensional nanochannels for the selective permeation and barrier effects of gaseous molecules [17]. Efficient and facile processing technologies have been applied, such as solution casting, doctors blading technique, in situ method, phase inversion, infiltration, lift-off/float-on, etching, etc. [18,19]. Mostly, thermoplastic matrices have been examined to form graphene-derived nanocomposites and membranes for gas separation [20–22]. The pore sizes and graphene dispersion patterns directly affect the gaseous molecular permeability and diffusivity features of these membranes [23–25]. Consequently, graphene scattering and layering in matrices have been known to develop percolation trails for the diffusing gaseous molecule [26]. However, fine graphene dispersion, optimization of pore sizes, and processing conditions have yet to be attained towards high-performance commercial-scale gas separation membranes. Applications of gas separation membranes for gaseous pollutants and desired molecules were found in the fields of fuel cells, gas sensors, chemical industries, etc. [27,28].

This review basically focuses on the design, development, and aspects of graphene-derived nanocomposite membranes for selective gas permeation applications. Fine graphene dispersion, interface effects, and optimum pore formation in the membranes have broadened the potential of the gas partition membranes. This overview is groundbreaking to portray the methodical progressions of graphene resultant membranes for gas separation. For the separation of gaseous species from mixtures, various polymer matrices have been filled with the graphene nanofillers to form the selectively permeable membranes. To the best of knowledge, this state-of-the-art review is innovative to depict the advancements in gas separation membranes, including the membrane designs, physical properties, and effect of graphene inclusion on the gas transportation features. This manuscript has been found indispensable for the future advances of gas separation graphene nanocomposite membranes, and so it can be a helpful guide for the interested field researchers.

2. Graphene

A two-dimensional nanosheet like carbon nanostructure is referred to as graphene [29]. It is constituted of sp^2 hybridized carbon atoms, discovered in 2004 [30]. Graphene was synthesized using numerous strategies like mechanical or liquid exfoliation of graphite, chemical vapor deposition, laser technique, plasma practice, and chemical synthesis methods [31–33]. Graphene is a thin, layered, transparent nanostructure [34]. Graphene has high electron mobilization of around 200,000 $cm^2V^{-1}s^{-1}$ and high thermal conductivity of 3000–5000 W/mK [35]. Excellent mechanical properties of graphene include a high Young's modulus of 1 TPa and a strength of >200 times that of steel [36]. Graphene nanosheets have a wrinkling effect due to the van der Waals interactions [37]. To enhance the dispersion effects and final features, graphene nanosheets have been functionalized to introduce various surface functionalities such as hydroxyl, carbonyl, carboxylic, epoxide, etc. [38]. The properties of graphene have been synergistically combined with other nanomaterials to form the nanocomposites. Graphene-based nanocomposites revealed numerous superior electrical, mechanical, thermal, and physical features [39–41]. Consequently, the graphene-derived nanomaterials have been applied in wide-ranging technological structures and applications like electronics, sensors, actuators, energy devices, including fuel cells, batteries, membranes, engineering structures, and biomedical advanced devices [42].

3. Graphene and nanocomposites in gas separation

Graphene-based nanoporous membranes have been applied for gas molecule transport [43–45]. The ultrathin graphene nanosheets have been designed for gas separation [46–48]. Lee et al. [49] studied the selective separation of carbon dioxide CO_2 molecules from CO_2/CH_4, CO_2/O_2, and CO_2/N_2 gas mixtures. Graphene nanosheets have affinity for CO_2 molecules, and pores in graphene nanosheets were suitable for the passage [50–52]. Among the gas mixtures, a high gas flux was observed for CO_2/O_2 at 0.43 [53]. Jiang et al. [54] used first principles density functional theory to examine the permeability and selectivity of nanoporous graphene nanosheets. **Figure 1** shows graphene nanosheet with hydrogen-passivated pore. The nanopore width was 0.02 Å according to electron density isosurface isovalue. The snapshot of gas molecules passing is given in **Figure 2**.

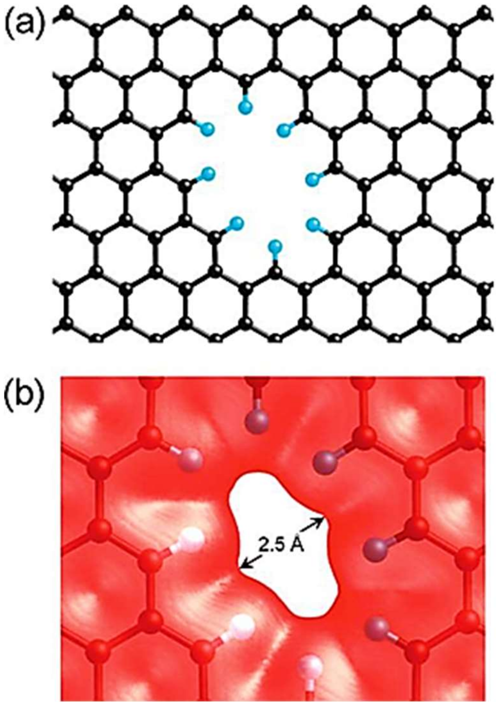

Figure 1. (a) An all-hydrogen passivated pore in graphene; **(b)** pore electron-density isosurface Isovalue is at 0.02 e/Å3 [54]. Reproduced with permission from ACS.

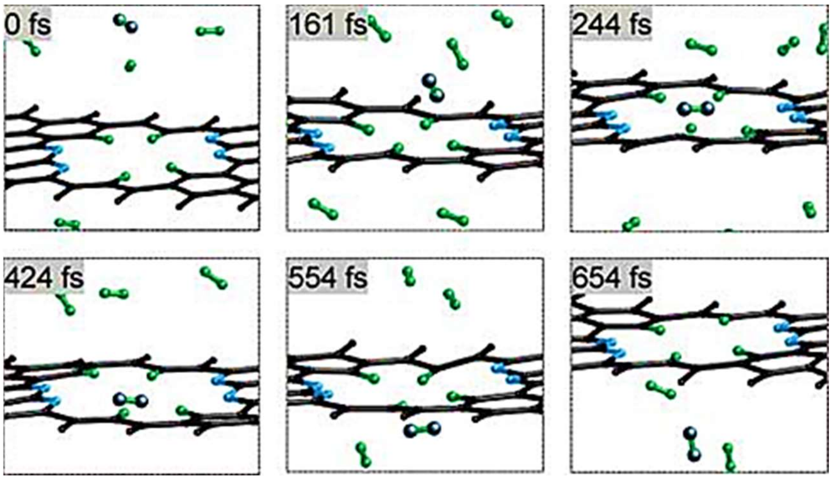

Figure 2. Molecular dynamics simulations of H_2 diffusing through nitrogen functional pore (600 K) [54]. Reproduced with permission from ACS.

According to geometry optimization studies, H_2 molecules entered through pores at 244 fs, and molecules stayed there for 180 fs. Then molecules diffuse out through pores at 424 fs. High H_2/CH_4 permselectivity was observed, as per first principles molecular dynamics simulation studies on porous graphene. It has been observed that hydrogen atoms on graphene nanopores decreased the pore width to 2.5 Å, while the pore length remained the same as 3.8 Å (**Figure 3**). Consequently, the interaction energy of incoming molecules with graphene nanosheets and diffusion barriers affected molecular adsorption or transportation. The resulting van der Waals density functional barrier for H_2 and CH_4 was observed as 0.22 and 1.60 eV, respectively.

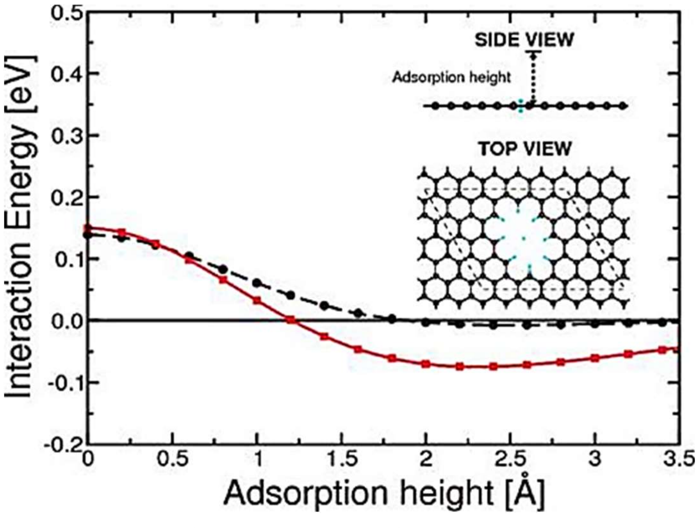

Figure 3. Interaction energy between H_2 vs. adsorption height. Inset: adsorption height and orientation of H_2. Red squares/solid lines = vdW-DF; black circle/dashed lines = PBE [54]. Reproduced with permission from ACS.

The graphene membranes having porous nanostructures were designed and studied aiming for gas separation [55–57]. Graphene and graphene oxide membranes were designed with fine pores for molecular sieving purposes. Koenig and colleagues [58] deposited the single-layered graphene on a silicon oxide substrate. The graphene layer was studied for the permeation of gas molecules. The etching process was applied for the separation of the membrane from the substrate. The pristine graphene nanosheet is not permeable to gas molecules; however, the etched graphene membrane had a porous nanostructure for gas molecule passage. Consequently, the etched graphene nanosheet was permeable to H_2 and CO_2 gas molecules [59–61]. Li and researchers [62] designed the ultrathin porous graphene oxide membranes with pore sizes of −0.34 nm to 1 nm. The membranes were studied for permeability and selectivity properties of CO_2, H_2, N_2, and gases. The H_2/CO_2 selectivity of 3400 and H_2/N_2 of 900 were observed [63,64]. Smaller gas molecules revealed facile permeation relative to the larger molecules through the porous membranes [65–67].

For gas separation applications, poly(methyl methacrylate) was applied for effective membrane thermoplastic material [68–70]. For the formation of polymer/graphene nanocomposite membranes, facile methods have been used [71,72]. Most commonly, the solution casting procedure has been applied [73]. In this method, the polymer is dissolved in an appropriate solvent. The nanoparticles of interest are also dispersed in a solvent. Afterwards, both the dispersions are mixed to yield a consistent phase. The mixed solution is spread on an open surface to evaporate the solvent. The phase inversion method has also been used for the fabrication of graphene-filled nanocomposite membranes [74]. In this procedure, polymer is transformed from the liquid to solid phase. During this process, controlled solution evaporation and immersion precipitation are involved. Additionally, interfacial polymerization has been used for the formation of graphene nanocomposite membranes [75]. Interfacial polymerization consists of various steps such as oil phase formation, emulsification, and finally solvent evaporation. All the membrane formation methods have capabilities for fine dispersion of graphene nanofiller in the polymeric matrices.

Baldanza and co-workers [76] developed the graphene-filled poly(methyl methacrylate) nanocomposite membranes by applying the wet deposition process. Here, the ‘lift-off/float-on’ method was used for obtaining membrane [77–79]. For the preparation of fine graphene nanosheets, the chemical vapor deposition practice was used. **Figure 4** illustrates the lift-off/float-on procedure for the membrane formation. The poly(methyl methacrylate)/graphene nanocomposite membrane with 0.06% loading had a thickness of 550 nm. According to the scanning electron microscopy images, graphene nanosheets were found to be sequentially layered in the polymeric membranes. According to permeability coefficients of humidified or pure O_2 and CO_2 measured for varying R.H. levels for poly(methyl methacrylate) and poly(methyl methacrylate)/graphene, the resultant membranes own a lower permeability coefficient of 1.30×10^{-17} and 0.21×10^{-17} $mol \cdot m \cdot m^{-2} \cdot Pa^{-1} \cdot s^{-1}$, respectively, for CO_2 and O_2, than the unfilled polymeric membrane (**Figure 5** and **Table 1**). The reduced permeability values of gases were attributed to the formation of better dispersion and the development of more twisted gas diffusion paths for gas molecule permeation [80]. Nevertheless, few studies have reported the poly(methyl methacrylate) and graphene nanocomposite-based gas separation systems, and more concentrated future research efforts may lead to the formation of high-performance selective gas permeation membranes.

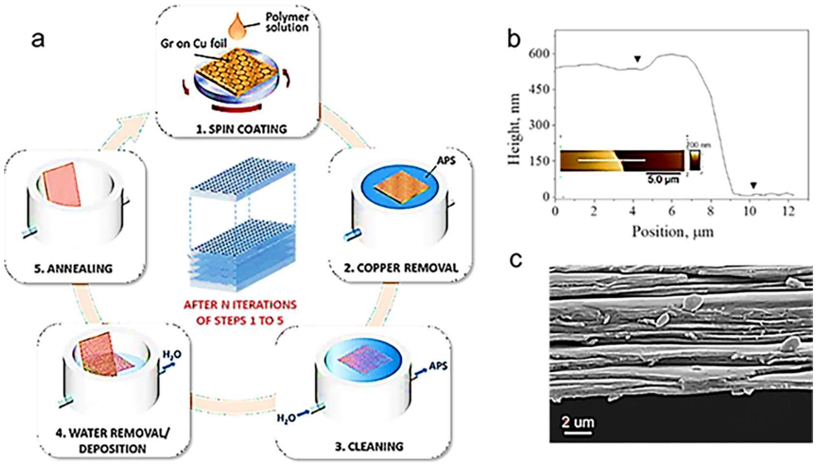

Figure 4. **(a)** 'Lift-off/float-on' and wet depositions adopted to produce poly(methyl methacrylate); **(b)** thickness of single nanocomposite layer on Si wafer (inset: cross-section AFM); **(c)** SEM cross-section plane of nanolaminate [76]. Reproduced with permission from MDPI.

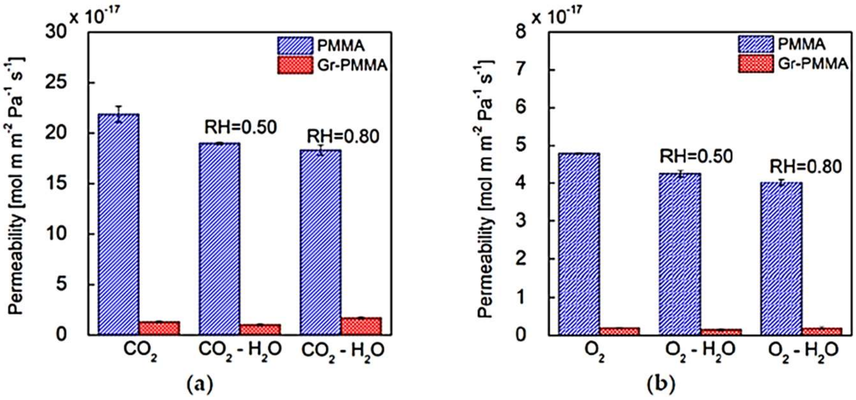

Figure 5. Gas permeability coefficients (25 °C), PMMA (blue bars) and Gr-PMMA (red bars): **(a)** CO_2 and humidified CO_2; **(b)** O_2 and humidified O_2 [76]. Reproduced with permission from MDPI.

Table 1. Permeability coefficients of CO_2 or O_2 through PMMA nanocomposite [76]. Reproduced with permission from MDPI.

Nanolaminate/Permeating Gas	P [$mol\cdot m\cdot m^{-2}\cdot Pa^{-1}\cdot s^{-1}$]	P [Barrer]
PMMA/CO_2	21.9 (± 0.8) × 10^{-17}	6.5 (± 0.2) × 10^{-1}
Gr-PMMA/CO_2	1.30 (± 0.1) × 10^{-17}	0.39 (± 0.03) × 10^{-1}
PMMA/O_2	4.79 (± 0.01) × 10^{-17}	1.434 (± 0.003) × 10^{-1}
Gr-PMMA/O_2	0.21 (± 0.01) × 10^{-17}	0.063 (± 0.003) × 10^{-1}

Poly(dimethyl siloxane) was investigated towards essential material aiming membrane formation [81–83]. The separation processes of carbon dioxide and other toxic gases have been studied using the poly(dimethyl siloxane) membranes. Here, membrane thickness has been found to affect the gas permeability and separation properties [84]. To enhance the membrane features, nanofillers have been reinforced in the matrices for fine performance. Ha and co-workers [85] reported on the graphene oxide-filled poly(dimethyl siloxane) membranes through solution processing. The kinetic diameters of CO_2, O_2, N_2, and CH_4 gases (in the range of 0.16 to 0.50 Å) affected the selectivity and permeability performance according to membrane porosity and microstructures. The membrane permeability was observed up to 99.9% by including 8 wt.% graphene oxide. Moreover, selectivity properties of the CO_2/CH_4, CO_2/O_2, and CO_2/N_2 have been observed. The gas transportation features were found to be reliant on the fine nanoparticle scattering in the polymer matrix. The microstructure and matrix-nanofiller interactions were also observed to be linked with the nanofiller alignment and scattering in the matrix for the formation of gas transportation pathways. Koolivand and researchers [86] fabricated the poly(dimethyl siloxane) and graphene oxide-derived membranes. Facile Hummer's method was used to form graphene oxide [87]. For these membranes, the combination of solution and ultrasonication processing methods have been applied. Adding 5 wt.% graphene oxide loading, CO_2 permeability and CO_2/CH_4 selectivity of 29% and 112%, respectively, were observed. Berean et al. [88] opted for solution processing and ultrasonication for the formation of poly(dimethyl siloxane)/graphene nanocomposite membranes. Due to the interactions, graphene dispersion and matrix-nanofiller interactions have been perceived. **Figure 6** shows a change in the permeability behavior of the membranes with graphene loading. The membrane permeability was about 60% enhanced with the nanofiller loading for CO_2, N_2, Ar, and CH_4 gases. Among these, CO_2 had greater permeation with the 0.5 wt.% graphene than other gases showing permeation at 0.25 wt.%. The greater permeation of CO_2 at higher nanofiller contents was observed due to its fine affinity towards graphene nanosheets.

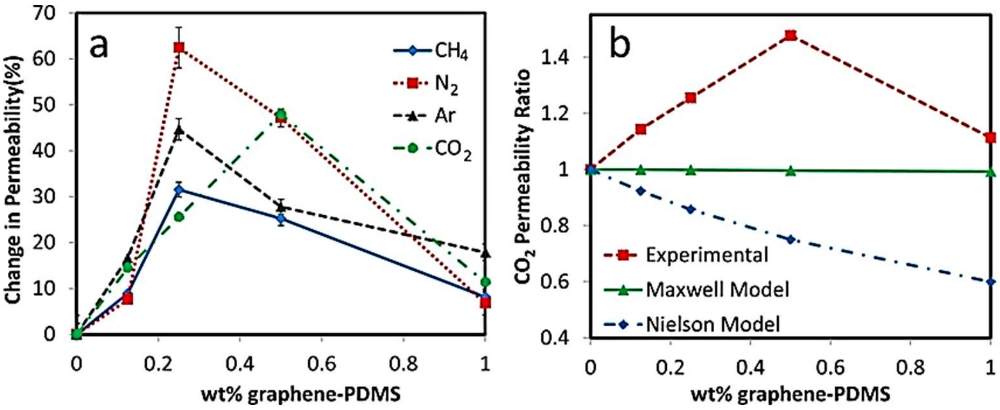

Figure 6. (a) change in permeability for gas species with graphene concentration; **(b)** experimental data, Maxwell model & Nielson model for CO_2 permeation (0.25 wt.% nanocomposite) [88]. Reproduced with permission from ACS.

Figure 7 depicts the formation and behavior of diffusion pathways in poly(dimethyl siloxane) and graphene-reinforced poly(dimethyl siloxane) nanocomposites. Aligned graphene nanosheets developed layered nanostructures with voids in the matrix. The formation of continuous gas diffusion trails was responsible for the passivation of the gaseous molecules through the matrix. Gas permeability of N_2, CO_2, Ar, and CH_4 was enhanced up to 60% with just 0.2 wt.% graphene contents. Consequently, neat poly(dimethyl siloxane) had CO_2/CH_4 selectivity of 3.6, which was increased up to 4.2 in the poly(dimethyl siloxane)/graphene membrane.

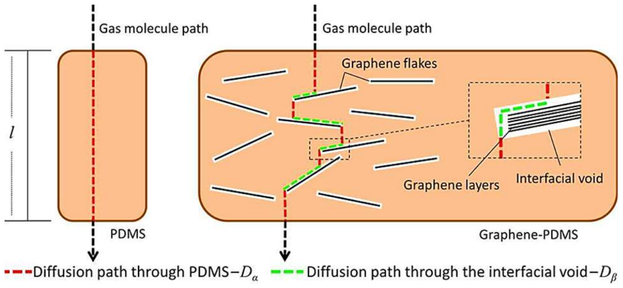

Figure 7. Diffusion paths for PDMS and PDMS/graphene nanocomposites, path length = l; diffusion path (Dα) = red; diffusion path through interfacial void (Dβ) = green [88]. Reproduced with permission from ACS.

Polysulfone has been used as a popular matrix for membrane formation and also for the gas separation application [89–91]. In this context, the mixed matrix membranes of polysulfone have been reported [92–94]. The resulting polysulfone membranes have been observed to be functional for toxic gas separation such as carbon dioxide, nitrogen, and sulfur oxides [95]. Zahri and co-workers [96] reported on polysulfone and graphene oxide-based membranes through the dry wet phase inversion process. The polysulfone-based nanocomposite membranes revealed high CO_2 permeability of 64–87 GPU. In addition, with the nanofiller loading, CO_2/CH_4 selectivity was increased in the range of 19–25. The fine selectivity of the nanocomposite membranes was credited to the dispersal patterns in the polymer matrix [97]. Sainath and co-worker [98] designed the mixed matrix gas separation polysulfone/graphene oxide nanocomposite membrane for gas separation using the solution method. As compared to a pristine polysulfone membrane, the graphene oxide-filled system revealed >3 times higher selectivity for CO_2/CH_4. Fine selectivity was attributed to the homogeneous dispersion and formation of efficient diffusion trails in the matrix. Zhu and co-workers [99] opted for the vacuum infiltration process to form graphene oxide-filled nanocomposite membranes of the phosphotungstic acid-grafted polyphenylsulfone-pyridine matrix. Transmission electron micrographs of polyphenylsulfone-pyridine, phosphotungstic acid, and graphene oxide-based systems are given in **Figure 8**. The nanofiller was observed to be homogeneously dispersed in the polymer matrix.

With the increasing nanofiller concentrations, fine nanoparticle distribution was observed in the matrix. In addition, with increasing nanoparticle loading, pore diameter as well as porosity have been found to enhance. It has been observed that the grafting of polymer matrix was also effective to disperse the nanofiller particles in the matrix. Henceforth, polysulfone and derivative-based membranes with graphene or graphene oxide have been developed with superior morphology, gas separation, selectivity, and permeation performance.

Some membrane systems based on polyimide and graphene have been reported for efficient gas separation [100–102]. An attempt by Melicchio and colleagues [103] used the knife casting method to form graphene oxide-filled Matrimid® 5218 polyimide-derived membranes. The membranes were studied for the permeability and selectivity of H_2 and CO_2 gases. H_2/CO_2 selectivity was found as 3.5, while the permeability of H_2 and CO_2 gases was 8–28 Barrer. The nanocomposite membrane permeability and selectivity were found to rely on the nanofiller contents and dispersion in the polymer matrix.

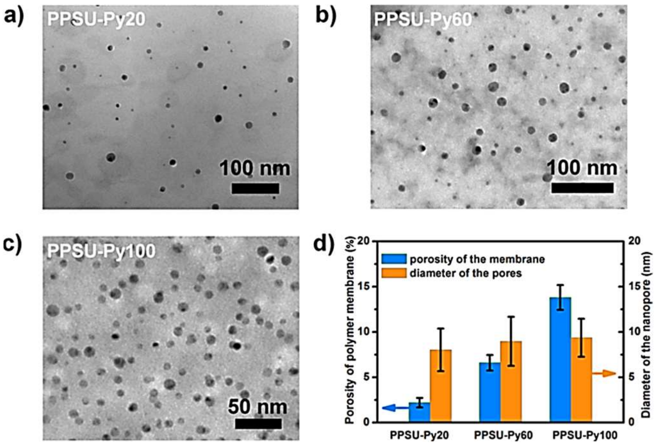

Figure 8. Transmission electron microscopy images with different pyridine moiety proportions in PPSU-Pyx (polyphenylsulfone-pyridine) **(a)** 20%; **(b)** 60%; **(c)** 100%; **(d)** porosity and diameter of membranes [99]. Reproduced with permission from ACS.

For membrane application, poly(1-trimethylsilyl-1-propyne) matrix material has been found useful [104–106]. Albertoa and co-workers [107] formed graphene-reinforced poly(1-trimethylsilyl-1-propyne for CO_2 separation. Accordingly, the CO_2 permeability of poly(1-trimethylsilyl-1-propyne)/graphene nanocomposite membrane was 3.5×10^3 Barrer, i.e., 39% lower than the neat polymer membrane. For poly(1-trimethylsilyl-1-propyne), graphene oxide has been rarely used as a nanofiller. Olivieri et al. [108] designed the graphene oxide-filled poly(1-trimethylsilyl-1-propyne) using solvent technique with chloroform. For the membranes, the CO_2, N_2, and CH_4 gases had diffusion coefficients of 25%, 14%, and 9%, respectively. The membrane systems based on poly(2,6-dimethyl-1,4-phenylene oxide) have also been researched [109–111]. Rea and colleagues [112] developed 0.3–15 wt.% graphene-filled poly(2,6-dimethyl-1,4-phenylene oxide) membranes. According to scanning electron micrographs, the matrix-nanofiller interfaces have been observed with the nanofiller flakes dispersed in the membrane matrix (**Figure 9**). The membrane permeability was studied at 35 and 65 °C (**Figure 10**).

For He, CO_2 and N_2, the membrane permeability was found to slightly decrease with the nanofiller loading levels. The decreasing permeability was attributed to the increased nanofiller dispersion and membrane selectivity towards these gases. The dispersed graphene nanoplatelets were supposed to develop percolation pathways for the diffusion of gaseous species. **Table 2** shows the permeability behavior of the membranes with different nanofiller loadings at 35 and 65 °C. In this way, efficient graphene-filled nanocomposite membranes have been designed for the selective gas separation or permeation properties [113–115]. The selective permeability of the membranes was found to depend upon nanofiller scattering plus alignment in the matrix [116,117]. Future studies on advanced graphene nanocomposite membranes may lead to better gas molecule separation from mixtures of gases.

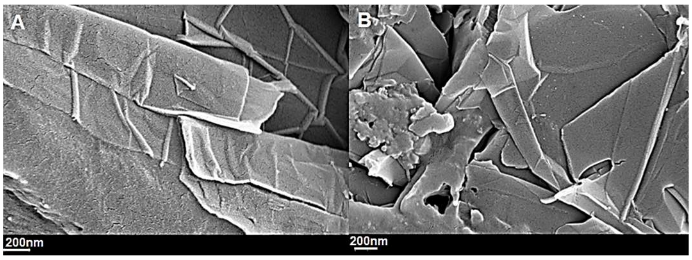

Figure 9. SEM images of membranes. **(A)** PPO/0.3 wt.% graphene; **(B)** PPO/1 wt.% graphene [112]. SEM=scanning electron microscopy; PPO = poly(1-trimethylsilyl-1-propyne). Reproduced with permission from MDPI.

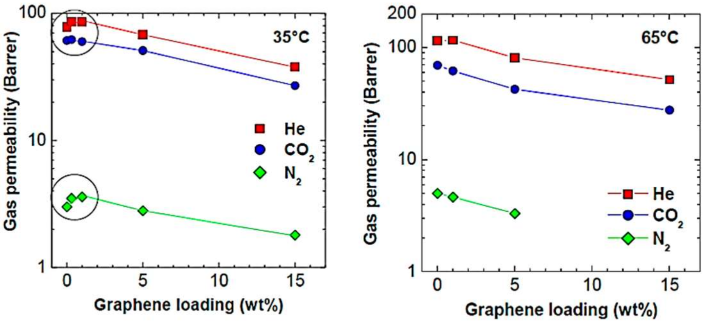

Figure 10. Gas permeability. **(a)** 35 °C; **(b)** 65 °C; and after graphene addition (as a function of graphene loading in poly(1-trimethylsilyl-1-propyne) matrix [112]. Reproduced with permission from MDPI.

Table 2. Permeability of the various gases in PPO and nanocomposite membranes [112]. PPO = poly(1-trimethylsilyl-1-propyne). Reproduced with permission from MDPI.

Permeability at 35 °C, Barrer	**PPO**	**PPO/0.3 wt.% graphene**	**PPO/1 wt.% graphene**	**PPO/5 wt.% graphene**	**PPO/15 wt.% graphene**
He	78 ± 3.8	86 ± 4.2	86 ± 4.1	68 ± 2.0	38 ± 3.2
N_2	3.0 ± 0.2	3.5 ± 0.2	3.6 ± 0.2	2.8 ± 0.1	1.8 ± 0.2
CO_2	61 ± 2.0	62 ± 2.9	60 ± 2.9	51 ± 1.5	27 ± 2.3
Permeability at 65 °C, Barrer	PPO	PPO/0.3 wt.% graphene	PPO/1 wt.% graphene	PPO/5 wt.% graphene	PPO/15 wt.% graphene
He	114 ± 5.0	-	116 ± 6.7	81.0 ± 2.4	51.6 ± 4.4
N_2	5.00 ± 0.4	-	4.64 ± 0.3	3.31 ± 0.1	-
CO_2	69.3 ± 2	-	61.9 ± 3.6	42.3 ± 1.2	27.6 ± 2.4

4. Prospects, challenges and gaps

In the formation and application of graphene nanocomposites as high-performance membrane materials, numerous challenges have been faced during the field research efforts. Generally speaking, not much effort has been observed for various categories of polymer/graphene nanocomposite membranes such as poly(dimethyl sulfoxide)/graphene, polysulfone/graphene, poly(methyl methacrylate)/graphene, polyimide/graphene, polyamide/graphene, etc. The experimental designs of the polymer/graphene nanocomposite membranes have been reported using the matrices, graphene nanofillers, processing techniques (solution, phase inversion, infiltration, etc.), and related preparation parameters.

Table 3 outlines the experimental design of the gas separation nanocomposite membranes used in important studies. Adding graphene in polymer matrices affected the membrane morphology, physical properties, permeability, selectivity, and separation properties. Polysulfone-based nanocomposite membranes have efficient CO_2/CH_4 selectivity of 45%–74%. For gas separation membranes of poly(dimethyl siloxane) nanocomposites, N_2, CO_2, and other gases permeability was observed >99.9%. Similarly, higher selectivity values for gases like CO_2/CH_4 have been observed. Hence, there is huge scope for fabrication and investigations on graphene-based air/water purification membranes.

Development and investigation of more designs definitely can lead to better analysis of optimum fabrication, selectivity, permeation, and gas separation performance, along with better understandings on the structure-property relationship and mechanism of innovative graphene membranes [118]. Major challenges hindering the gas separation membrane performance have been observed as graphene dispersion depending upon nanofiller contents, functionality, matrix nanofiller interactions, and interface formation [7]. The formation of interweaving pathways due to graphene dispersion in the polymer matrices has directly influenced the gas transportation properties. Controlled pore sizes, shapes, and distribution in the matrices have also been found indispensable to promote the gas membrane performance. Important solutions to the nanofiller dispersion have been proposed depending upon the graphene modification as well as by applying appropriate processing techniques and steps with the optimized conditions [119]. Further challenges have been observed regarding the fabrication of graphene-based membranes on a large scale and subsequent commercialization. Here, the appropriate fabrication techniques and processing parameters need to be implemented for the massive production of graphene nanocomposite membranes. In this case, the development of nanofibrous polymer/graphene membranes must be developed with a high surface area and well-dispersed nanoparticles for separating the desired gaseous molecules [120]. By controlling and overcoming all the above-mentioned graphene and graphene nanocomposite membrane design and processing challenges leading to the fine microstructure, robustness, permeability, selectivity, and barrier characteristics [121]. Briefly speaking, further research on the mentioned line may lead to the proposition of high-tech future gas transportation membranes for commercial purposes.

Table 3. Significant features of polymer/graphene nanocomposite membranes for gas separation.

Polymer	Nanofiller	Fabrication way	Physicochemical properties	Membrane properties	References
Polymer	Graphene or graphene oxide	Solution casting	Ion-molecule interaction; 1.8–20 nm thickness	H_2/N_2 selectivity 900; H_2/CO_2 selectivity 3400; pore size 0.34 nm	[62]
Poly(dimethyl siloxane)	Graphene oxide	Solution casting	Matrix-nanofiller interactions; interaction between graphene oxide and polymer	8 wt.% nanofiller; H_2, O_2, N_2, CH_4 and CO_2 permeability 99.9%	[85]
Poly(dimethyl siloxane)	Graphene oxide	Solution/ultrasonication methods; tetrahydrofuran solvent	Interfacial interactions between functional groups of graphene oxide and polymer; density 1.09–1.12; Thickness 1.9–2.8 nm	5 wt.% nanofiller; CO_2/CH_4 selectivity 112%; CO_2 permeability 29%.	[86]

Table 3. (*Continued*).

Polymer	**Nanofiller**	**Fabrication way**	**Physicochemical properties**	**Membrane properties**	**References**
Poly(dimethyl siloxane)	Graphene	Solution casting; p-xylene solvent	π-π interactions in matrix-nanofiller	0.2 wt.% nanofiller; N_2, CO_2, Ar, and CH_4 permeation 60%; CO_2/CH_4 selectivity 4.2	[88]
Polysulfone	Graphene	Phase inversion; hollow fiber mixed matrix membrane	Nanosize synthesized graphene; Interfacial interaction between graphene and polymer matrix	CO_2/N_2 selectivity 158%; CO_2/CH_4 selectivity 74%	[97]
Polysulfone	Graphene oxide	Solution route; N-Methyl-2-pyrrolidone solvent	Physical interaction between oxygenated functional groups of graphene oxide and polymer; Interactions between functional groups of nanocomposites and gas molecules	CO_2/CH_4 selectivity 45	[98]
Polyphenylsulfone-pyridine	Graphene oxide	Vacuum infiltration technique	Wettability and surface charge response to pH; acidic pH = 3 form hydrophilic state contact angle 63.3°; alkaline pH = 11 form hydrophobic state contact angle 106.5°; charge-density-tunable nanoporous; power of ≈ 0.76 W m^{-2}	Dispersion; morphology	[99]
Poly(1-trimethylsilyl-1-propyne)	Graphene oxide	Solution casting; chloroform solvent	Anchoring of graphene oxide nanosheets lowers membrane flexibility; less free volume; covalent cross-linking of polymer	1 wt.% graphene; diffusion coefficients CO_2 (25%); N_2 (14); CH_4 (9%)	[108]
Poly(1-trimethylsilyl-1-propyne)	Graphene	Solution route	Interaction between filler andpolymer matrix; 0.93–1.36 MPa; 38–44 MPa	0.05 wt.% nanofiller; CO_2 permeability 3.5 × 10^3 Barrer	[107]
Poly(2,6-dimethyl-1,4-phenylene oxide)	Graphene	Solution route	Void formation at interface; glassy polymer filled with graphene; graphene inclusion for physical constraint to relaxation of polymer chains	0.3–15 wt.% nanofiller reduced permeability	[112]

The research progress on the polymer/graphene nanocomposite membranes has led to several advances in the kinds, design, and applications to overcome the crucial foremost problems in this field. These separation membranes have been used for the efficient removal of gaseous pollutants with optimally high flux and permeation. For this purpose, microstructure and mechanical features like strength and flexibility have been considered important. For the enhancements in these properties, nanoparticle dispersion has been found significant for the matrix-nanofiller interactions to advance the ultimate membrane characters. In this context, compatibility of graphene nanoparticles with matrices must be enhanced for better miscibility and reinforcing effects. The pore shape, size, and distribution in the matrices have been found to affect the membrane selectivity/permeability features. The most important challenges of graphene-based gas separation membranes include graphene nanosheet aggregation, phase separation, and uncontrolled and undefined fabrication parameters. Such undefined conditions may lead to the different pore shapes, sizes, and random distribution in the matrices. The membranes with various pore sizes and shapes may cause major hinderances towards the separation of particular gaseous molecules of specific types. The random pore distribution in membranes also affects the strength, durability, and life of the membranes. In addition, poor membrane performance may result in restricted cyclic uses. Consequently, the uncontrolled membrane features may cause poor barrier effects and selective molecular transportation. Hence, perfect membrane design features need to be identified before commercial-scale production of these membranes. Investigations on the membrane separation mechanisms may be used to overcome the barrier, molecular selective diffusion, and performance challenges. In addition, advanced and facile fabrication methods need to be designed to form efficient membranes with controlled pore dimensions and essential features. Future research to resolve the stated challenging directions can be beneficial for the formation of high-performance gas separation membranes.

5. Conclusions

In this state-of-the-art review article, the design, physical properties, and gas partition features have been scrutinized for important graphene and nanocomposite-based membranes. Consequently, graphene has been filled in various polymeric matrices to form the efficient gas separation membranes. These membranes have been studied for the selective separation or permeation of various toxic or desired gas molecules such as O_2, N_2, CO_2, CH_4, etc. from the gas mixtures. Consequently, the membrane performance has been analyzed based on the microstructure, pore size, pore distribution, and specific tests related to the separation or permeation of the gaseous molecules. It has been observed that by varying the nanofiller contents and nanofiller functionalities, as well as polymer type and fabrication methods, the resulting membrane performance has been rehabilitated. In addition, the graphene alignment and dispersion pattern in the polymer matrices resulted in advanced membrane performance with optimum porosity and tortuous pathway formation for the passage of gas molecules. In the future, well-organized graphene-based membranes need to be designed by overcoming the dispersion and processing challenges behind the development of high-performance systems.

Conflict of interest: The authors declare no conflict of interest.

References

1. Bellucci S. Decontamination of surface water from organic pollutants using graphene membranes. Characterization and Application of Nanomaterials. 2023; 6(1): 2033. doi: 10.24294/can.v6i1.2033
2. Kausar A. Nanoporous graphene in polymeric nanocomposite membranes for gas separation and water purification—standings and headways. Journal of Macromolecular Science, Part A. 2023; 60(2): 81-91. doi: 10.1080/10601325.2023.2177170
3. Kausar A. Poly(methyl methacrylate) nanocomposite reinforced with graphene, graphene oxide, and graphite: a review. Polymer-Plastics Technology and Materials. 2019; 58(8): 821-842. doi: 10.1080/25740881.2018.1563112
4. Kausar A. Applications of polymer/graphene nanocomposite membranes: A review. Materials Research Innovations. 2018; 23(5): 276-287. doi: 10.1080/14328917.2018.1456636
5. Kumar SR, Wang JJ, Wu YS, et al. Synergistic role of graphene oxide-magnetite nanofillers contribution on ionic conductivity and permeability for polybenzimidazole membrane electrolytes. Journal of Power Sources. 2020; 445: 227293. doi: 10.1016/j.jpowsour.2019.227293

6. Anegbe B, Ifijen IH, Maliki M, et al. Graphene oxide synthesis and applications in emerging contaminant removal: a comprehensive review. Environmental Sciences Europe. 2024; 36(1). doi: 10.1186/s12302-023-00814-4
7. Li Y, Lin Z, He X. New nonporous fillers-based hybrid membranes for gas separations and water treatment process. In: Basile A, Favvas EP (editors). Current Trends and Future Developments on (Bio-) Membranes. Elsevier; 2024. pp. 53-105. doi: 10.1016/b978-0-323-99311-1.00002-7
8. Gupta S, Singh A, Sharma T, et al. Applications of ultrafiltration, nanofiltration, and reverse osmosis in pharmaceutical wastewater treatment. In: Shah MP, Rodriguez-Couto S (editors). Development in Wastewater Treatment Research and Processes. Elsevier; 2024. pp. 33-49. doi: 10.1016/b978-0-323-99278-7.00017-1
9. Jalali SHS. Investigation of nanofiltration systems efficiency for removal of chromium and copper from groundwater resources. Environmental Quality Management. 2024. doi: 10.1002/tqem.22178
10. Ribeiro Pinela S, Larasati A, Meulepas RJW, et al. Ultrafiltration (UF) and biological oxygen-dosed activated carbon (BODAC) filtration to prevent fouling of reversed osmosis (RO) membranes: A mass balance analysis. Journal of Water Process Engineering. 2024; 57: 104648. doi: 10.1016/j.jwpe.2023.104648
11. Rana K, Kaur H, Singh N, et al. Graphene-based materials: Unravelling its impact in wastewater treatment for sustainable environments. Next Materials. 2024; 3: 100107. doi: 10.1016/j.nxmate.2024.100107
12. Nwosu CN, Iliut M, Vijayaraghavan A. Graphene and water-based elastomer nanocomposites – a review. Nanoscale. 2021; 13(21): 9505-9540. doi: 10.1039/d1nr01324f
13. Lawal AT. Recent progress in graphene based polymer nanocomposites. Cogent Chemistry. 2020; 6(1): 1833476. doi: 10.1080/23312009.2020.1833476
14. Kausar A, Ahmad I, Lam TD. High-tech graphene oxide reinforced conducting matrix nanocomposites—Current status and progress. Characterization and Application of Nanomaterials. 2023; 6(1). doi: 10.24294/can.v6i1.2637
15. Rehman F, Memon FH, Ali A, et al. Recent progress on fabrication methods of graphene-based membranes for water purification, gas separation, and energy sustainability. Reviews in Inorganic Chemistry. 2022; 43(1): 13-31. doi: 10.1515/revic-2022-0001
16. Javed RMN, Al-Othman A, Tawalbeh M, Olabi AG. Recent developments in graphene and graphene oxide materials for polymer electrolyte membrane fuel cells applications. Renewable and Sustainable Energy Reviews. 2022; 168: 112836.
17. Favre E. Membrane Separation Processes and Post-Combustion Carbon Capture: State of the Art and Prospects. Membranes. 2022; 12(9): 884. doi: 10.3390/membranes12090884
18. Lee J, Park CY, Kong CI, et al. Ultrathin Water-Cast Polymer Membranes for Hydrogen Purification. ACS Applied Materials & Interfaces. 2022; 14(5): 7292-7300. doi: 10.1021/acsami.1c21780
19. He X, Ou D, Wu S, et al. A mini review on factors affecting network in thermally enhanced polymer composites: filler content, shape, size, and tailoring methods. Advanced Composites and Hybrid Materials. 2021; 5(1): 21-38. doi: 10.1007/s42114-021-00321-1
20. Bera B, Dey A. The use of polymer-graphene composites as membrane. Polymer Nanocomposites Containing Graphene. Published online 2022: 557-588. doi: 10.1016/b978-0-12-821639-2.00024-0
21. Katia Cecilia de SF, Gustavo Feliciano de JB, André Santarosa F. Graphene Membranes: From Reverse Osmosis to Gas Separation. International Journal of Membrane Science and Technology. 2021; 8(2): 1-27. doi: 10.15379/2410-1869.2021.08.02.01
22. Bhandari S, Rahaman M. Thermal properties of polymer-graphene composites. In: Rahaman M, Nayak L, Hussein IA, Das NC (editors). Polymer Nanocomposites Containing Graphene. Elsevier; 2022. pp. 163-181. doi: 10.1016/b978-0-12-821639-2.00014-8
23. Alen SK, Nam S, Dastgheib SA. Recent Advances in Graphene Oxide Membranes for Gas Separation Applications. International Journal of Molecular Sciences. 2019; 20(22): 5609. doi: 10.3390/ijms20225609
24. Hegab HM, Kallem P, Pandey RP, et al. Mechanistic insights into the selective mass-transport and fabrication of holey graphene-based membranes for water purification applications. Chemical Engineering Journal. 2022; 431: 134248. doi: 10.1016/j.cej.2021.134248
25. Castro-Muñoz R, Cruz-Cruz A, Alfaro-Sommers Y, et al. Reviewing the recent developments of using graphene-based nanosized materials in membrane separations. Critical Reviews in Environmental Science and Technology. 2021; 52(19): 3415-3452. doi: 10.1080/10643389.2021.1918509

26. Fatemi SM, Fatemi SJ, Abbasi Z. Gas separation using graphene nanosheet: insights from theory and simulation. Journal of Molecular Modeling. 2020; 26(11). doi: 10.1007/s00894-020-04581-4
27. Liu M, Cen R, Zhao J, et al. Selective gradient separation of aminophenol isomers by cucurbit[6]uril. Separation and Purification Technology. 2023; 304: 122342. doi: 10.1016/j.seppur.2022.122342
28. Bahri M, Gebre SH, Elaguech MA, et al. Recent advances in chemical vapour deposition techniques for graphene-based nanoarchitectures: From synthesis to contemporary applications. Coordination Chemistry Reviews. 2023; 475: 214910. doi: 10.1016/j.ccr.2022.214910
29. You X, Zhang Q, Yang J, et al. Review on 3D-printed graphene-reinforced composites for structural applications. Composites Part A: Applied Science and Manufacturing. 2023; 167: 107420. doi: 10.1016/j.compositesa.2022.107420
30. Berger C, Song Z, Li X, et al. Electronic Confinement and Coherence in Patterned Epitaxial Graphene. Science. 2006; 312(5777): 1191-1196. doi: 10.1126/science.1125925
31. Li M, Yin B, Gao C, et al. Graphene: Preparation, tailoring, and modification. In: Book Graphene: Preparation, Tailoring, and Modification. Wiley Online Library; 2023.
32. Sumdani MG, Islam MR, Yahaya ANA, et al. Recent advances of the graphite exfoliation processes and structural modification of graphene: a review. Journal of Nanoparticle Research. 2021; 23(11). doi: 10.1007/s11051-021-05371-6
33. Urade AR, Lahiri I, Suresh KS. Graphene Properties, Synthesis and Applications: A Review. JOM. 2022; 75(3): 614-630. doi: 10.1007/s11837-022-05505-8
34. Narayanam PK, Botcha VD, Ghosh M, et al. Growth and photocatalytic behavior of transparent reduced GO–ZnO nanocomposite sheets. Nanotechnology. 2019; 30(48): 485601. doi: 10.1088/1361-6528/ab3ced
35. Shen X, Zeng X, Dang C. Graphene Composites. In: Celasco E, Chaika AN, Stauber T, et al. (editors). Handbook of Graphene. Scrivener Publishing LLC; 2019. pp. 1-25. doi: 10.1002/9781119468455.ch53
36. Zandiatashbar A, Lee GH, An SJ, et al. Effect of defects on the intrinsic strength and stiffness of graphene. Nature Communications. 2014; 5(1). doi: 10.1038/ncomms4186
37. Zhou Q, Xia G, Du M, et al. Scotch-tape-like exfoliation effect of graphene quantum dots for efficient preparation of graphene nanosheets in water. Applied Surface Science. 2019; 483: 52-59. doi: 10.1016/j.apsusc.2019.03.290
38. Lee H, Lee KS. Interlayer distance controlled graphene, supercapacitor and method of producing the same. In: Book Interlayer Distance Controlled Graphene, Supercapacitor and Method of producing the Same. Google Patents; 2019.
39. Ibrahim A, Klopocinska A, Horvat K, et al. Graphene-Based Nanocomposites: Synthesis, Mechanical Properties, and Characterizations. Polymers. 2021; 13(17): 2869. doi: 10.3390/polym13172869
40. Shahryari Z, Yeganeh M, Gheisari K, et al. A brief review of the graphene oxide-based polymer nanocomposite coatings: preparation, characterization, and properties. Journal of Coatings Technology and Research. 2021; 18(4): 945-969. doi: 10.1007/s11998-021-00488-8
41. Smaisim GF, Abed AM, Al-Madhhachi H, et al. Graphene-Based Important Carbon Structures and Nanomaterials for Energy Storage Applications as Chemical Capacitors and Supercapacitor Electrodes: a Review. BioNanoScience. 2022; 13(1): 219-248. doi: 10.1007/s12668-022-01048-z
42. Worku AK, Ayele DW. Recent Advances of Graphene-Based Materials for Emerging Technologies. Results in Chemistry; 2023.
43. Szomek M, Moesgaard L, Reinholdt P, et al. Membrane organization and intracellular transport of a fluorescent analogue of 27-hydroxycholesterol. Chemistry and Physics of Lipids. 2020; 233: 105004. doi: 10.1016/j.chemphyslip.2020.105004
44. Li Z, Zhang J, Zhang N, et al. Tunable nano-wrinked channels of reduced graphene oxide membranes for molecular sieving gas separation. Carbon. 2024; 216: 118524. doi: 10.1016/j.carbon.2023.118524
45. Castro-Muñoz R, Agrawal KV, Lai Z, et al. Towards large-scale application of nanoporous materials in membranes for separation of energy-relevant gas mixtures. Separation and Purification Technology. 2023; 308: 122919. doi: 10.1016/j.seppur.2022.122919
46. Elzubair A, Uchôa LR, Da Silva MHP. Production and Characterization of Graphene Oxide/Polymer Support Composite Membranes for Water Desalination and Purification. Desalination and Water Treatment; 2024.
47. Nidamanuri N, Li Y, Li Q, Dong M. Graphene and graphene oxide-based membranes for gas separation. Engineered Science. 2020; 9(9): 3-16.

48. Sainath K, Modi A, Bellare J. CO_2/CH_4 mixed gas separation using graphene oxide nanosheets embedded hollow fiber membranes: Evaluating effect of filler concentration on performance. Chemical Engineering Journal Advances. 2021; 5: 100074. doi: 10.1016/j.ceja.2020.100074
49. Lee J, Aluru NR. Water-solubility-driven separation of gases using graphene membrane. Journal of Membrane Science. 2013; 428: 546-553. doi: 10.1016/j.memsci.2012.11.006
50. Liu N, Cheng J, Hou W, et al. Unsaturated Zn–N2–O active sites derived from hydroxyl in graphene oxide and zinc atoms in core shell ZIF-8@ZIF-67 nanocomposites enhanced CO_2 adsorption capacity. Microporous and Mesoporous Materials. 2021; 312: 110786. doi: 10.1016/j.micromeso.2020.110786
51. Szczęśniak B, Choma J. Graphene-containing microporous composites for selective CO_2 adsorption. Microporous and Mesoporous Materials. 2020; 292: 109761. doi: 10.1016/j.micromeso.2019.109761
52. Zhang X, Liu H, Shi Y, et al. Boosting CO_2 Conversion with Terminal Alkynes by Molecular Architecture of Graphene Oxide-Supported Ag Nanoparticles. Matter. 2020; 3(2): 558-570. doi: 10.1016/j.matt.2020.07.022
53. Miricioiu MG, Iacob C, Nechifor G, et al. High Selective Mixed Membranes Based on Mesoporous MCM-41 and MCM-41-NH2 Particles in a Polysulfone Matrix. Frontiers in Chemistry. 2019; 7. doi: 10.3389/fchem.2019.00332
54. Jiang D, Cooper VR, Dai S. Porous Graphene as the Ultimate Membrane for Gas Separation. Nano Letters. 2009; 9(12): 4019-4024. doi: 10.1021/nl9021946
55. Du Y, Huang L, Wang Y, et al. Recent developments in graphene-based polymer composite membranes: Preparation, mass transfer mechanism, and applications. Journal of Applied Polymer Science. 2019; 136(28). doi: 10.1002/app.47761
56. Cheng Y, Pu Y, Zhao D. Two-Dimensional Membranes: New Paradigms for High-Performance Separation Membranes. Chemistry – An Asian Journal. 2020; 15(15): 2241-2270. doi: 10.1002/asia.202000013
57. Li M, Wang F, Guo Z. The fabrication and application of triphase reaction interface based on superwettability for improved reaction efficiency. Journal of Materials Chemistry A. 2024.
58. Koenig SP, Wang L, Pellegrino J, et al. Selective molecular sieving through porous graphene. Nature Nanotechnology. 2012; 7(11): 728-732. doi: 10.1038/nnano.2012.162
59. Huang L, Jia W, Lin H. Etching and acidifying graphene oxide membranes to increase gas permeance while retaining molecular sieving ability. AIChE Journal. 2020; 66(12). doi: 10.1002/aic.17022
60. Singh S, Varghese AM, Reinalda D, et al. Graphene - based membranes for carbon dioxide separation. Journal of CO_2 Utilization. 2021; 49: 101544. doi: 10.1016/j.jcou.2021.101544
61. Hu L, Bui VT, Esmaeili N, et al. Nanoengineering membrane surfaces: A new paradigm for efficient CO_2 capture. Carbon Capture Science & Technology. 2024; 10: 100150. doi: 10.1016/j.ccst.2023.100150
62. Li H, Song Z, Zhang X, et al. Ultrathin, Molecular-Sieving Graphene Oxide Membranes for Selective Hydrogen Separation. Science. 2013; 342(6154): 95-98. doi: 10.1126/science.1236686
63. Dong G, Hou J, Wang J, et al. Enhanced CO_2/N_2 separation by porous reduced graphene oxide/Pebax mixed matrix membranes. Journal of Membrane Science. 2016; 520: 860-868. doi: 10.1016/j.memsci.2016.08.059
64. Ibrahim AFM, Banihashemi F, Lin YS. Graphene oxide membranes with narrow inter-sheet galleries for enhanced hydrogen separation. Chemical Communications. 2019; 55(21): 3077-3080. doi: 10.1039/c8cc10283j
65. Yang Y, Bolling L, Priolo MA, et al. Super Gas Barrier and Selectivity of Graphene Oxide-Polymer Multilayer Thin Films. Advanced Materials. 2012; 25(4): 503-508. doi: 10.1002/adma.201202951
66. Chuah CY, Lee J, Song J, et al. Carbon Molecular Sieve Membranes Comprising Graphene Oxides and Porous Carbon for CO2/N2 Separation. Membranes. 2021; 11(4): 284. doi: 10.3390/membranes11040284
67. Lee SE, Jang J, Kim J, et al. Tunable sieving of small gas molecules using horizontal graphene oxide membrane. Journal of Membrane Science. 2020; 610: 118178. doi: 10.1016/j.memsci.2020.118178
68. Xu S, Li H, Xiao L, et al. Quantitative Determination of Poly (methyl Methacrylate) Micro/Nanoplastics by Cooling-Assisted Solid-Phase Microextraction Coupled to Gas Chromatography–Mass Spectrometry: Theoretical and Experimental Insights. Analytical Chemistry. 2024.
69. Brito dos Santos F, Perez ID, McMichael PS, et al. Synthesis of a Novel Cellulose Nanofiber-Based Composite Hydrogel with Poly(methyl methacrylate-co-methacrylic Acid) for Effective Water Removal from Liquid Fuels. Industrial & Engineering Chemistry Research. 2024; 63(5): 2210-2222. doi: 10.1021/acs.iecr.3c02019

70. Bahrami A, Raisi A. Polyurethane-Based Blend Membrane Containing Polycarbonate for Gas Separation: Compatibility Analysis, Microstructure Evaluation, and CO_2 Separation Performance. Industrial & Engineering Chemistry Research. 2024; 63(2): 1080-1099. doi: 10.1021/acs.iecr.3c03251
71. Ajaj Y, AL-Salman HNK, Hussein AM, et al. Effect and investigating of graphene nanoparticles on mechanical, physical properties of polylactic acid polymer. Case Studies in Chemical and Environmental Engineering. 2024; 9: 100612. doi: 10.1016/j.cscee.2024.100612
72. Khan I, Khan I, Saeed K, et al. Polymer nanocomposites: an overview. In: Ali N, Bila M, Khan A, et al. (editors). Smart Polymer Nanocomposites. Elsevier; 2023. pp. 167-184. doi: 10.1016/b978-0-323-91611-0.00017-7
73. Sin C, Baranovskii ES. Hölder continuity of solutions for unsteady generalized Navier–Stokes equations with p(x,t)-power law in 2D. Journal of Mathematical Analysis and Applications. 2023; 517(2): 126632. doi: 10.1016/j.jmaa.2022.126632
74. Ray M, Verma A, Maiti A, et al. Nano-Engineered Polymer Matrix-Based Composites. In: Verma RK, Kesarwani S, Xu J, Davim JP (editors). Polymer Nanocomposites: Fabrication to Applications. CRC Press; 2023. pp. 21-39. doi: 10.1201/9781003343912-2
75. Wang Y, Nie W, Wang L, et al. Understanding the graphene-polymer interfacial mechanical behavior via coarse-grained modeling. Computational Materials Science. 2023; 222: 112109. doi: 10.1016/j.commatsci.2023.112109
76. Baldanza A, Pastore Carbone MG, Brondi C, et al. Chemical Vapour Deposition Graphene–PMMA Nanolaminates for Flexible Gas Barrier. Membranes. 2022; 12(6): 611. doi: 10.3390/membranes12060611
77. Francis J, Ramesh A, Suchand Sangeeth CS. Self-Assembled Monolayer-Based Molecular Electronic Devices. Nanoelectronics Devices: Design, Materials, and Applications (Part I). In: Rawat G, Yadav AB (editors). Bentham Science Publishers; 2023. pp. 33-77. doi: 10.2174/9789815136623123010005
78. Naik SG, Rabinal MK. Liquid free float metal contacts to form multiple molecular junctions. Materials Science in Semiconductor Processing. 2023; 156: 107270. doi: 10.1016/j.mssp.2022.107270
79. Herrer L, Martín S, Cea P. Nanofabrication Techniques in Large-Area Molecular Electronic Devices. Applied Sciences. 2020; 10(17): 6064. doi: 10.3390/app10176064
80. Agrawal KV, Benck JD, Yuan Z, et al. Fabrication, Pressure Testing, and Nanopore Formation of Single-Layer Graphene Membranes. The Journal of Physical Chemistry C. 2017; 121(26): 14312-14321. doi: 10.1021/acs.jpcc.7b01796
81. Liu J, Pan Y, Xu J, et al. Introducing amphipathic copolymer into intermediate layer to fabricate ultra-thin Pebax composite membrane for efficient CO_2 capture. Journal of Membrane Science. 2023; 667: 121183. doi: 10.1016/j.memsci.2022.121183
82. Gonçalves BJA, de Souza Figueiredo KC. Mixed matrix membranes of polydimethylsiloxane with activated carbon for ABE separation. Journal of Applied Polymer Science. 2024.
83. Junaidi A, Zulfiani U, Khomariyah S, et al. Utilization of polyphenylene sulfide as an organic additive to enhance gas separation performance in polysulfone membranes. RSC Advances. 2024; 14(4): 2311-2319. doi: 10.1039/d3ra06136a
84. Zhang W, Shi Y, Wang B, et al. High-strength electrospun polydimethylsiloxane/polytetrafluoroethylene hybrid membranes with stable and controllable coral-like structures. Composites Part A: Applied Science and Manufacturing. 2023; 164: 107316. doi: 10.1016/j.compositesa.2022.107316
85. Ha H, Park J, Ando S, et al. Gas permeation and selectivity of poly(dimethylsiloxane)/graphene oxide composite elastomer membranes. Journal of Membrane Science. 2016; 518: 131-140. doi: 10.1016/j.memsci.2016.06.028
86. Koolivand H, Sharif A, Chehrazi E, et al. Mixed-matrix membranes comprising graphene-oxide nanosheets for CO_2/CH_4 separation: A comparison between glassy and rubbery polymer matrices. Polymer Science, Series A. 2016; 58(5): 801-809. doi: 10.1134/s0965545x16050084
87. Zhang Q, Yang Y, Fan H, et al. Synthesis of graphene oxide using boric acid in hummers method. Colloids and Surfaces A: Physicochemical and Engineering Aspects. 2022; 652: 129802. doi: 10.1016/j.colsurfa.2022.129802
88. Berean KJ, Ou JZ, Nour M, et al. Enhanced Gas Permeation through Graphene Nanocomposites. The Journal of Physical Chemistry C. 2015; 119(24): 13700-13712. doi: 10.1021/acs.jpcc.5b02995
89. Vinodh R, Atchudan R, Kim HJ, et al. Recent Advancements in Polysulfone Based Membranes for Fuel Cell (PEMFCs, DMFCs and AMFCs) Applications: A Critical Review. Polymers. 2022; 14(2): 300. doi: 10.3390/polym14020300
90. Ali ME, Shahat A, Ayoub TI, Kamel RM. Fabrication of high flux polysulfone/mesoporous silica nanocomposite ultrafiltration membranes for industrial wastewater treatment. Biointerface Research in Applied Chemistry. 2022; 12: 7556-7572.

91. Sherugar P, Déon S, Nagaraja KK, et al. Tailoring the structure of polysulfone nanocomposite membranes by incorporating iron oxide doped aluminium oxide for excellent separation performance and antifouling property. Environmental Science: Water Research & Technology. 2022; 8(5): 1059-1077. doi: 10.1039/d1ew00936b
92. Costa Flores M, Figueiredo KC de S. Asymmetric oxygen-functionalized carbon nanotubes dispersed in polysulfone for CO_2 separation. Journal of Applied Polymer Science. 2022; 140(2). doi: 10.1002/app.53303
93. Jaid GM, AbdulRazak AA, Meskher H, et al. Metal-organic frameworks (MOFs), covalent organic frameworks (COFs), and hydrogen-bonded organic frameworks (HOFs) in mixed matrix membranes. Materials Today Sustainability. 2024; 25: 100672. doi: 10.1016/j.mtsust.2024.100672
94. Hashemi T, Mehrnia MR, Pourafshari Chenar M. Morphological effects of spherical SiO_2 and hexagonal mesoporous MCM-41 nanoparticles in polyacrylonitrile mixed matrix membranes on the biofouling mitigation in short-term filtration. Journal of Applied Polymer Science. 2023; 141(3). doi: 10.1002/app.54830
95. Said N, Mansur S, Zainol Abidin MN, Ismail AF. Fabrication and characterization of polysulfone/iron oxide nanoparticle mixed matrix hollow fiber membranes for hemodialysis: Effect of dope extrusion rate and air gap. Journal of Membrane Science and Research. 2023; 9(1).
96. Zahri K, Goh PS, Ismail AF. The incorporation of graphene oxide into polysulfone mixed matrix membrane for CO_2/CH_4 separation. IOP Conference Series: Earth and Environmental Science. 2016; 36: 012007. doi: 10.1088/1755-1315/36/1/012007
97. Zahri K, Wong KC, Goh PS, et al. Graphene oxide/polysulfone hollow fiber mixed matrix membranes for gas separation. RSC Advances. 2016; 6(92): 89130-89139. doi: 10.1039/c6ra16820e
98. Sainath K, Modi A, Bellare J. In-situ growth of zeolitic imidazolate framework-67 nanoparticles on polysulfone/graphene oxide hollow fiber membranes enhance CO_2/CH_4 separation. Journal of Membrane Science. 2020; 614: 118506. doi: 10.1016/j.memsci.2020.118506
99. Zhu X, Zhou Y, Hao J, et al. A Charge-Density-Tunable Three/Two-Dimensional Polymer/Graphene Oxide Heterogeneous Nanoporous Membrane for Ion Transport. ACS Nano. 2017; 11(11): 10816-10824. doi: 10.1021/acsnano.7b03576
100. Zhu S, Bi X, Shi Y, et al. Thin Films Based on Polyimide/Metal–Organic Framework Nanoparticle Composite Membranes with Substantially Improved Stability for CO_2/CH_4 Separation. ACS Applied Nano Materials. 2022; 5(7): 8997-9007. doi: 10.1021/acsanm.2c01248
101. Esmaielzadeh S, Ahmadizadegan H. Gas permeation, thermal, morphology and mechanical properties of polyimide/clay nanocomposites: Effect of organically modified montmorillonite. Journal of Thermoplastic Composite Materials. 2023; 37(1): 363-386. doi: 10.1177/08927057231176421
102. Mehrabi M, Vatanpour V. Polyimide-based separation membranes for liquid separation: A review on fabrication techniques, applications, and future perspectives. Materials Today Chemistry. 2024; 35: 101895. doi: 10.1016/j.mtchem.2024.101895
103. Melicchio A, Favvas EP. Preparation and characterization of graphene oxide as a candidate filler material for the preparation of mixed matrix polyimide membranes. Surface and Coatings Technology. 2018; 349: 1058-1068. doi: 10.1016/j.surfcoat.2018.06.082
104. Shishatskiy S, Makrushin V, Levin I, et al. Effect of Immobilization of Phenolic Antioxidant on Thermo-Oxidative Stability and Aging of Poly(1-trimethylsilyl-1-propyne) in View of Membrane Application. Polymers. 2022; 14(3): 462. doi: 10.3390/polym14030462
105. Seiiedhoseiny M, Ghasemzadeh K, Basile A. Membrane technology in integrated gasification combined cycles. In: Basile A, Lipnizki F, Rahimpour MR, Piemonte V (editors). Current Trends and Future Developments on (Bio-) Membranes. Elsevier; 2024. pp. 743-763. doi: 10.1016/b978-0-323-90258-8.00032-8
106. Santoro S, Tufa RA, Curcio E. Pervaporation and membrane contactors. In: Basile A, Lipnizki F, Rahimpour MR, Piemonte V (editors). Current Trends and Future Developments on (Bio-) Membranes. Elsevier; 2024. pp. 765-788. doi: 10.1016/b978-0-323-90258-8.00019-5
107. Alberto M, Bhavsar R, Luque-Alled JM, et al. Impeded physical aging in PIM-1 membranes containing graphene-like fillers. Journal of Membrane Science. 2018; 563: 513-520. doi: 10.1016/j.memsci.2018.06.026
108. Olivieri L, Ligi S, De Angelis MG, et al. Effect of Graphene and Graphene Oxide Nanoplatelets on the Gas Permselectivity and Aging Behavior of Poly(trimethylsilyl propyne) (PTMSP). Industrial & Engineering Chemistry Research. 2015; 54(44): 11199-11211. doi: 10.1021/acs.iecr.5b03251

109. Zhang D, Xu S, Wan R, et al. Functionalized graphene oxide cross-linked poly(2,6-dimethyl-1,4-phenylene oxide)-based anion exchange membranes with superior ionic conductivity. Journal of Power Sources. 2022; 517: 230720. doi: 10.1016/j.jpowsour.2021.230720
110. Chen J, Zhang M, Shen C, et al. Preparation and Characterization of Non-N-Bonded Side-Chain Anion Exchange Membranes Based on Poly(2,6-dimethyl-1,4-phenylene oxide). Industrial & Engineering Chemistry Research. 2022; 61(4): 1715-1724. doi: 10.1021/acs.iecr.1c04171
111. Chu X, Miao S, Zhou A, et al. A strategy to design quaternized poly(2,6-dimethyl-1,4-phenylene oxide) anion exchange membranes by atom transfer radical coupling. Journal of Membrane Science. 2022; 649: 120397. doi: 10.1016/j.memsci.2022.120397
112. Rea R, Ligi S, Christian M, et al. Permeability and Selectivity of PPO/Graphene Composites as Mixed Matrix Membranes for CO_2 Capture and Gas Separation. Polymers. 2018; 10(2): 129. doi: 10.3390/polym10020129
113. Theravalappil R, Rahaman M. Patents on graphene-based polymer composites and their applications. Polymer Nanocomposites Containing Graphene. Published online 2022: 615-638. doi: 10.1016/b978-0-12-821639-2.00018-5
114. Kausar A, Bocchetta P. Polymer/Graphene Nanocomposite Membranes: Status and Emerging Prospects. Journal of Composites Science. 2022; 6(3): 76. doi: 10.3390/jcs6030076
115. Penkova AV, Dmitrenko ME, Hafusa A, et al. Analytical applications of graphene oxide for membrane processes as separation and concentration methods. In: Hussain CM (editor). Comprehensive Analytical Chemistry. Elsevier; 2020. pp. 99-124. doi: 10.1016/bs.coac.2020.09.002
116. Zhu Z, Song M, Qu F, et al. Engineering Multinanochannel Polymer-Intercalated Graphene Oxide Membrane for Strict Volatile Sieving in Membrane Distillation. Environmental Science & Technology. 2024.
117. Lichaei MM, Thibault J. Mixed matrix membranes based on two-dimensional materials for efficient CO_2 separation: A comprehensive review. Process Safety and Environmental Protection. 2024; 183: 952-975. doi: 10.1016/j.psep.2024.01.069
118. Dischinger SM, Miller DJ, Vermaas DA, et al. Unifying the Conversation: Membrane Separation Performance in Energy, Water, and Industrial Applications. ACS ES&T Engineering. 2024; 4(2): 277-289. doi: 10.1021/acsestengg.3c00475
119. Ren Y, Xu Y. Recent advances in two-dimensional polymers: synthesis, assembly and energy-related applications. Chemical Society Reviews. 2024; 4.
120. Venmathi Maran BA, Jeyachandran S, Kimura M. A Review on the Electrospinning of Polymer Nanofibers and Its Biomedical Applications. Journal of Composites Science. 2024; 8(1): 32. doi: 10.3390/jcs8010032
121. Yang C, Gede M, Abdulhamid MA, et al. Solvent and material selection for greener membrane manufacturing. In: Basile A, Favvas EP (editors). Current Trends and Future Developments on (Bio-) Membranes. Elsevier; 2024. pp. 249-293. doi: 10.1016/b978-0-323-99311-1.00016-7

Characterization and Application of Nanomaterials 2024, 7(1), 4959.
https://doi.org/10.24294/can.v7i1.4959

Review

Polymeric Nanoparticles (PNPs) as drug delivery systems for SARS-CoV-2

Elizabeth Adu[†], Siddharth A. Patel[†], Arthur J. Catino, Riddhiman Medhi[*]

Department of Chemistry, University of Scranton, Scranton, PA 18510, United States
*** Corresponding author:** Riddhiman Medhi, riddhiman.medhi@scranton.edu
[†] The authors contributed equally to this research.

CITATION

Adu E, Patel SA, Catino AJ, Medhi R. Polymeric Nanoparticles (PNPs) as drug delivery systems for SARS-CoV-2. Characterization and Application of Nanomaterials. 2024; 7(1): 4959.
https://doi.org/10.24294/can.v7i1.4959

ARTICLE INFO

Received: 5 March 2024
Accepted: 9 April 2024
Available online: 30 May 2024

Abstract: Researchers from all over the world have been working tirelessly to combat the severe acute respiratory syndrome coronavirus 2 (SARS-CoV-2) COVID-19 pandemic since the World Health Organization (WHO) proclaimed it to be a pandemic in 2019. Expanding testing capacities, creating efficient medications, and creating safe and efficient COVID-19 (SARS CoV-2) vaccinations that provide the human body with long-lasting protection are a few tactics that need to be investigated. In clinical studies, drug delivery techniques, including nanoparticles, have been used since the early 1990s. Since then, as technology has advanced and the need for improved medication delivery has increased, the field of nanomedicine has recently seen significant development. PNPs, or polymeric nanoparticles, are solid particles or particulate dispersions that range in size from 10 to 1000 nm, and their ability to efficiently deliver therapeutics to specific targets makes them ideal drug carriers. This review article discusses the many polymeric nanoparticle (PNP) platforms developed to counteract the recent COVID-19 pandemic-related severe acute respiratory syndrome coronavirus (SARS-CoV-2). The primary subjects of this article are the size, shape, cytotoxicity, and release mechanism of each nanoparticle. The two kinds of preparation methods in the synthesis of polymeric nanoparticles have been discussed: the first group uses premade polymers, while the other group depends on the direct polymerization of monomers. A few of the PNPs that have been utilized to combat previous viral outbreaks against SARS-CoV-2 are also covered.

Keywords: SARS CoV-2; COVID-19; polymeric nanoparticle; drug delivery

1. Introduction

Nanotechnology is the study and creation of devices and structures at the nanoscale. Because of their ability to increase drug stability, prolong the therapeutic effect of the drug, decrease metabolism of the drug, and reduce cellular uptake, nanoparticles have been the subject of extensive research in the biomedical and biotechnological fields. This is especially true when it comes to drug delivery systems [1].

The rapid evolution of humanity has led to the development of technology that can help us overcome daily struggles. While some advances may not be essential for survival, others are crucial. One such necessary development is the field of vaccine development and delivery. For many years, humans have faced numerous infectious diseases, some of which have proven to be deadly on a global scale, such as the plague, cholera, and various types of coronaviruses. Throughout history, countless pandemics have been caused by viruses, including the Spanish flu.

(H1N1) in 1918 [2], Ebola in 1976, AIDS (HIV) in 1981, avian flu (H5N1) in 1996, SARS (SARSCoV) in 2002, MERS (MERS-CoV) in 2012, and COVID-19 (SARS-CoV-2) in 2019 [3,4]. These outbreaks have taught us valuable lessons about the importance of novel technologies for testing, tracing, and developing vaccines to effectively respond to pandemics in the future [5,6].

Respiratory tract infections are a major cause of disease and a significant public health concern globally. Lower respiratory tract infections (LRTI) and pneumonia have been reported to be responsible for over four million deaths each year, which is more than the combined deaths caused by HIV, malaria, and tuberculosis. Respiratory viruses are the cause of more than 80% of these infections [7]. An outbreak of the lung illness coronavirus disease 2019 (COVID-19) began in December 2019 in the Chinese city of Wuhan due to a new coronavirus known as severe acute respiratory syndrome coronavirus 2 (SARS-CoV-2) [8,9]. Fever, severe respiratory disease, pneumonia, and dyspnea are the main signs and symptoms of COVID-19 [10,11]. The morphology of SARS-CoV-2 is shown in **Figure 1**. We must prioritize the development of rapid diagnostic testing, drug repurposing, and biomarkers of disease severity, as well as new platforms for vaccine production [12,13].

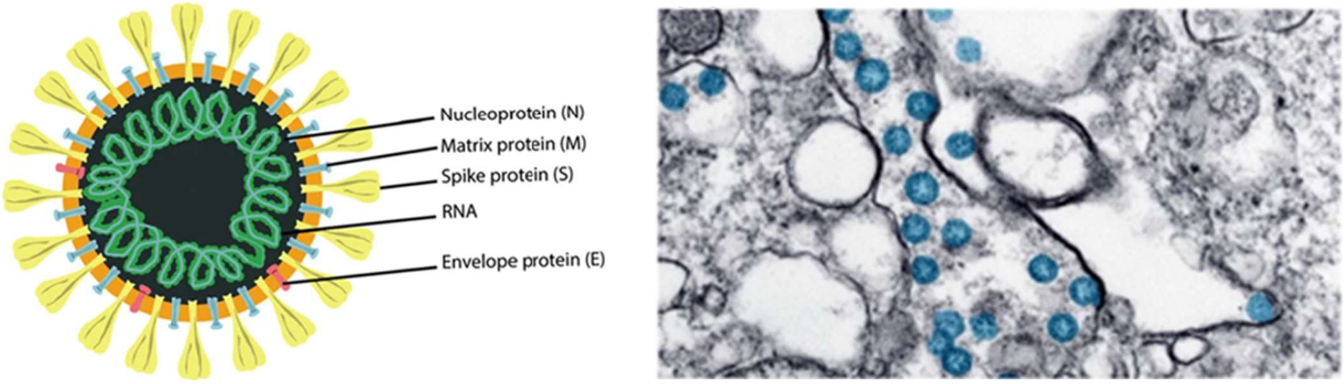

(a) **(b)**

Figure 1. SARS-CoV-2 morphology. **(a)** Representation of the viral structure is illustrated with its structural viral proteins; **(b)** Transmission electron microscope image of SARS-CoV-2 spherical viral particles in a cell. The virus is colorized in blue (adapted from the US Centers for Disease Control) permission from Udugama et al. [22].

One of the most crucial considerations in vaccine development is the availability of platforms that can deliver the vaccine to specific sites in the human body without interfering with other functions [14]. In recent decades, nanoparticles have been developed to address the limitations of free drug molecules and overcome biological barriers at both systemic and cellular levels [15]. This has resulted in the development of new therapeutics to treat a variety of diseases [16]. Various types of nanoparticles are currently in use for different applications [17], but this paper only focuses on Polymeric Nanoparticles (PNPs). PNPs are particles that range in size from 1 to 1000 nm [18] and can be loaded with active compounds that travel through our body to deliver the active compound to the targeted location [19]. PNPs can be divided into two categories: natural and synthetic. Both offer excellent medicinal applicability due to their non-toxicity and biodegradability [20]. PNPs can be modified to control drug release based on receptor proteins, temperature, and pH [21].

This review article discusses various PNPs platforms that have been developed to fight against the most recent pandemic, SARS-CoV-2. The article focuses on the polymeric material, size, design, cytotoxicity, and release mechanism of each NP. It also covers some of the NPs that have been used against other viral outbreaks but exhibit potential for use against SARS-CoV-2. Common polymers covered in this paper include poly (lactic-co-glycolic acid) (PLGA), poly (ethyleneglycol) (PEG), poly(N-isopropylacrylamide) (PNIPAM), and poly (3,4-ethylene dioxythiophene) (PEDOT).

2. Polymer Nanoparticles (PNPs)

The term “polymeric nanoparticle” refers to solid nanospheres or nanocapsules that either adsorb molecules on their surface or encapsulate them within a polymeric matrix, as shown in **Figure 2** [19,23,24]. Biodegradable polymeric nanoparticles are the most promising drug delivery strategy for pulmonary/respiratory applications [25,26]. PNPs can be used instead of liposomes. They have similar size and shape properties as liposomes but offer additional benefits such as improved stability in vitro and in vivo, high cargo capacity, and targeting. Their ability to efficiently deliver therapeutics to specific targets makes them ideal drug carriers [27]. A wide range of products and application fields, such as electronics, photonics, paints, adhesives, food technology, cosmetics, catalysis, analytical assays, sensors, purifications, and drug administration, have shown interest in polymer particles [28].

Various polymeric structures have been developed for vaccine delivery systems, including solid polymeric nanoparticles, micelles, nanogels, polymersomes, and core-shell nanoparticles [29]. Biocompatible and biodegradable lipids that remain solid at room temperature and body temperature make up solid lipid nanoparticles (SLNs), which are submicron-sized drug carriers [30]. For controlled and targeted delivery, solid lipid nanoparticles (SLNs) are becoming a more viable option than colloidal systems as carriers and amalgamate the benefits of various colloidal carriers, such as emulsions and liposomes, which are physiologically acceptable and can be expected to release drugs from the lipid matrix in a controlled manner, much like polymeric nanoparticles [31,32]. In recent years, the polymeric micelles (PM) system has garnered increasing scientific attention as an effective drug carrier due to its unique properties such as solubilization, selective targeting, inhibition of P-glycoprotein, altered drug internalization route, and subcellular localization [33,34]. Delivering drugs to their targets with micellar solutions of amphiphiles is an efficient method. Owing to the hydrophobic environment present in the core of micelles, drugs that are insoluble in water can be readily dissolved and subsequently transported to the desired locations [35]. Additionally, polymer chains that are cross-linked form three-dimensional networks known as nanogels [36,37]. To improve a wide range of therapies and diagnostic tests for various human diseases, nanogels are widely acknowledged as highly versatile drug delivery systems. Significant volumes of water or biological fluid can be absorbed by these hydrophilic cross-linked polymers that are three-dimensional [38]. A class of artificial vesicles called polymersomes (Ps) is created from synthetic amphiphilic block copolymers. Typical Ps are hollow spheres with a bi-layer membrane enclosing an aqueous solution within [39]. Additionally, Ps have many advantages over liposomes in the delivery of drugs because of their high levels of stability, control over their architecture, adaptability to surface modifications, and high drug loading efficiencies [40]. Understanding how core/shell particles form has been the subject of several studies, and creating core/shell particles as a practical way to encapsulate a wide range of materials, from organic molecules to biological macromolecules, has drawn a lot of attention [41]. Because bare nanoparticles are toxic, host tissues may be harmed or troubled. Core-shell nanoparticles exhibit better characteristics than bare nanoparticles, including reduced cytotoxicity, high dispersible nature biocompatibility, improved conjugation with drugs and biomolecules because of improved surface properties, and improved chemical and thermal stability [42,43].

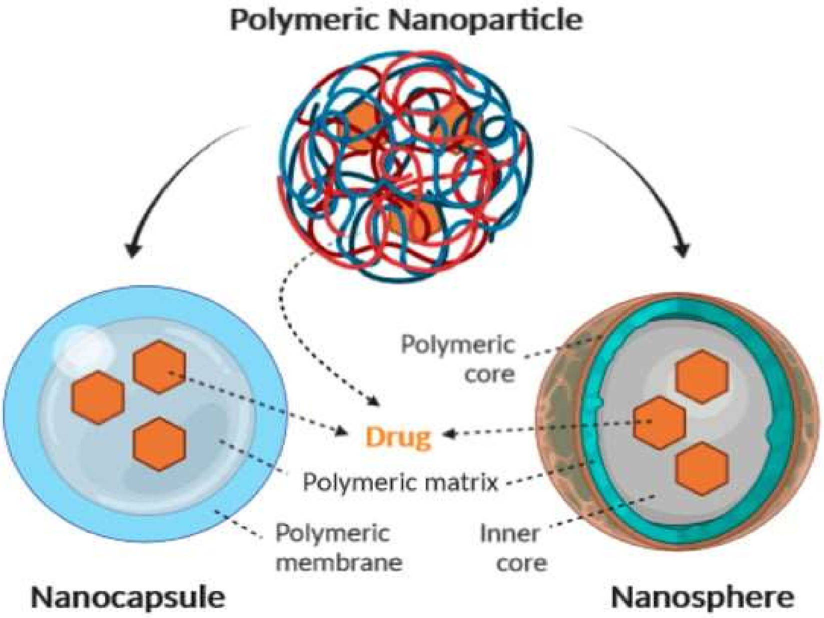

Figure 2. Schematic representation of the structure of nanocapsules and nanospheres. The arrow indicates the presence of drug or bioactive within the nanoparticles. Reproduced with permission from Zielińska et al. [19].

2.1. Synthesis of PNPs

PNPs are created using biodegradable polymers such as polyesters (such as poly(lactideco-glycolide) (PLGA) and poly-caprolactone (PCL), polyamides (such as gelatin and albumin), polyanhydrides, polyurethanes, and polyphosphazenes. These polymers are utilized to produce PNPs [2,44].

Several preparation techniques have been developed; these can be categorized into two groups: those that rely on the polymerization of monomers and those that utilize preformed polymers. These techniques can be further divided into two groups: one-step procedures where the formation of nanoparticles does not require emulsification and two-step procedures that involve the preparation of an emulsification system followed by the formation of nanoparticles in the second step of the process [20].

2.1.1. Emulsification/solvent diffusion (ESD)

This is an altered form of the solvent evaporation technique [45]. To maintain the initial thermodynamic equilibrium of both liquids, the encapsulating polymer is dissolved in a solvent that is partially soluble in water, such as propylene carbonate, and then saturated with water. When the organic solvent is partially miscible with water, it is necessary to dilute it with excess water to promote the diffusion of the solvent of the dispersed phase; in the opposite case, it is necessary to dilute it with another organic solvent to produce the precipitation of the polymer and the subsequent formation of nanoparticles. The solvent phase that is saturated with polymer and water is then emulsified in an aqueous solution that contains a stabilizer. This process causes the solvent to diffuse to the exterior phase and, depending on the oil-to-polymer ratio, forms nanospheres or nano capsules. Ultimately, the solvent is removed through either filtering or evaporation based on its boiling point. **Figure 3** illustrates the process. Various emulsion types can be employed, but oil/water emulsions are noteworthy due to their use of water as a nonsolvent. This reduces the need for recycling, facilitates the washing step, and minimizes agglomeration, all of which simplifies and enhances process economics [46].

Numerous benefits come with this method, including high encapsulation efficiency (usually >70%), simplicity, ease of scale-up, high batch-to-batch consistency, and narrow size distribution. It also doesn't require homogenization. The large amounts of water that must be removed from the suspension and the water-soluble medication that leaks into the saturated-aqueous exterior phase during emulsification, decreasing the effectiveness of encapsulation, are drawbacks [1,46]. Like a few others, this method works well for encasing lipophilic medications. The ESD method produced several drug-loaded nanoparticles, including meso-tetra (3-hydroxyphenyl) porphine (mTHPP)-loaded PLGA nanoparticles, polylactic acid (PLA) nanoparticles [47,48] loaded with plasmid deoxyribonucleic acid (DNA) [49], PLGA nanoparticles loaded with doxorubicin, PLA nanoparticles loaded with coumarin [46], indocyanine, cyclosporine (CyA)-laden gelatin, and sodium glycolate nanoparticles loaded with cyclosporin (Cy-A) [46,50].

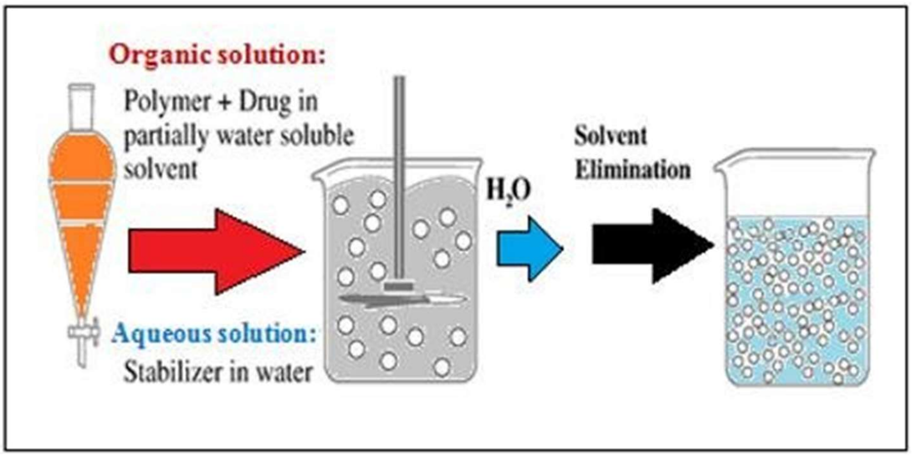

Figure 3. Schematic representation of the emulsification/solvent diffusion technique. Reproduced with permission from Nagavarma et al. [50].

2.1.2. Polymerization of monomers

The previously mentioned technique did not require any polymerization operations; instead, PNPs were produced from premade polymers. During the polymerization of monomers, appropriate polymer nanoparticles can be developed to achieve the required qualities for a certain application. The article discusses methods for producing PNPs by polymerizing monomers, with a primary focus on three main techniques: mini-, micro-, and emulsion polymerization [51]. Emulsion polymerization remains the most widely utilized and well-proven technique as of 2013. When an aqueous and an organic phase are mixed, spontaneous emulsification takes place in the production of nano-emulsions. Whereas the organic phase is a homogenous mixture of lipophilic surfactant, oil, and water-miscible solvent, the aqueous phase is composed of hydrophilic surfactant and water [52]. PNPs with very small droplets (50–100 nm) will form at the end of the reaction [53]. It is well known that this process raises costs and complicates purification since it needs a lot of surfactants or co-surfactants to create tiny NPs [54]. Thus, Nakabayashi and colleagues [55] used ‘acoustic emulsification,’ one of the effective methods for producing emulsions quickly and sustainably, to produce poly(methyl methacrylate) (PMMA) NPs with regulated size as shown in **Figure 4**. By employing consecutive ultrasonic irradiation, they created a new synthesis technique for size-controlled PNPs in surfactant-free environments [52]. In **Figure 4**, the original MMA solution in an aqueous solution mixture is shown (a) after 20 kHz for 8 min; (c) 20 kHz for 8 min → 500 kHz; (d) 20 kHz for 8 min → 500 kHz, 10 min → 1.6 MHz, 10 min; and (e) 20 kHz for 8 min → 500 kHz, 10 min → 1.6 MHz, 10 min → 2.4 MHz, 10 min.

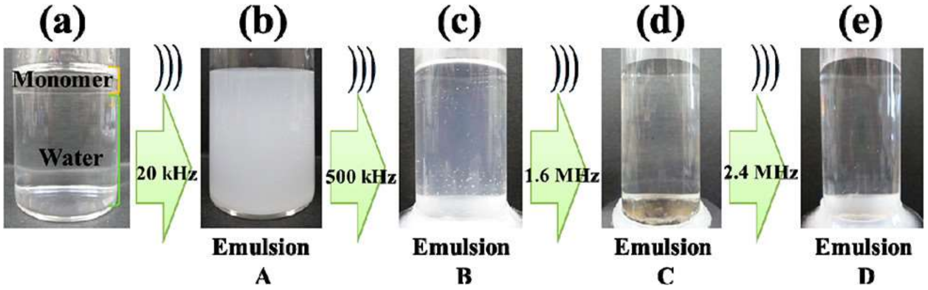

Figure 4. Photographic documentation of MMA in aqueous solution using tandem acoustic emulsification. Reproduced with permission from Nakabayashi et al. [55].

2.2. Characteristics of PNPs

In the fields of nanotechnology and nanomedicine, a wide range of nanomaterials are utilized to deliver drugs with various beneficial properties such as enhanced solubility, extended formulation action, different degrees of lipophilicity or hydrophilicity, and reduced toxicity. Nanoparticle drug delivery systems possess unique physicochemical characteristics including surface properties, shape, size (**Figure 5a**), treatment efficacy, drug release, and loading, among others. The surface properties of nanoparticles can significantly impact the biocompatibility, biodistribution, and pharmacokinetics of the drug molecules [26,56].

2.2.1. Infrared spectroscopy

Fourier transformed infrared spectroscopy (FTIR) is a spectroscopic technique based on the measurement of vibrational transitions between different excitation states of molecules [57]. Tulbah and Lee employed FTIR analysis to investigate potential peak shifts or modifications in the favipiravir solid lipid nanoparticles (FPV-SLN) formulation resulting from the usage of chemicals like Tween 80 and Compritol 888 in the nanoparticle manufacturing process. The FTIR of unprocessed favipiravir

(FPV), measured between 400 and 4000 cm^{-1}, is shown in **Figure 5c**. The C=O, C–F, and C–OH stretching were characterized by stretching peaks at 1659.17, 1259.51, and 1178.64 cm^{-1}, respectively [58].

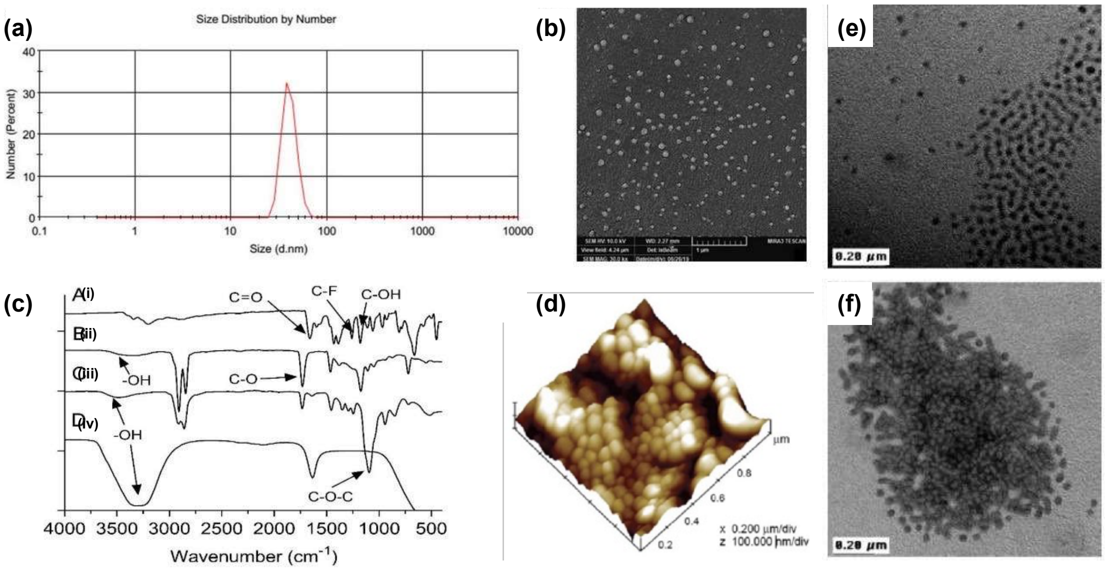

Figure 5. (a–b) Characterization of PLGA-PEG-PLGA NPs loaded with 5FU@Chrysin; **(c)** FTIR spectra of (i) Unprocessed (FPV); (ii) Compritol 888; (iii) Tween 80; and (iv) FPV-SLNs; **(d)** AFM analysis of PEG-g-PLA PNPs' surface morphology; **(e–f)** TEM photographs of bare and hydrogenated spherical PS/PBD core-shell NPs, respectively. Reproduced with permission from Mostafavi et al. [13], Khaledi et al. [59], Tulbah and Lee [58], and Wang et al. [60], respectively.

2.2.2. Scanning electron microscopy

Before being placed on a sample holder and coated with a conductive metal, such as gold, using a sputter coater, the nanoparticle solution needs to be dried out for SEM characterization. After that, a finely focused electron beam is utilized to scan the sample. The secondary electrons that are released from the sample surface provide information about their surface properties. The polymer may be harmed by the electron beam, and the nanoparticles need to be able to endure a vacuum. The SEM mean size and the dynamic light scattering mean size are similar [53]. **Figure 5a,b** shows the particle size distribution and SEM of the size and shape of PLGA-PEG-PLGA loaded with 5FU@Chrysin.

2.2.3. Atomic force microscopy

Atomic force microscopy (AFM) is an additional sophisticated microscopic method for characterizing nanoparticles. This is a novel method for imaging the particles' natural, unaltered form and surface characteristics. This method achieves a spatial resolution of up to 0.01 nm due to the force operating between the probing tip and the surface. It is not necessary for the samples to be conductive, and sample preparation is straightforward. As a result, it permits the examination of samples that are solvent- and hydrate-containing compounds [31,53]. It is used to calculate the force that exists between the sample's particle surface and the probing tip. The technique offers good resolution, easy sample preparation, and quick picture capture. AFM does not require a vacuum, nor does it require a conducting sample [30]. AFM analysis of PEG-g-PLA PNPs’ surface morphology with X-axis scale of 0.200 μm/div is shown in **Figure 5d**.

2.2.4. Transmission Electron Microscope (TEM)

Nanostructures are small, making it impossible to measure their physical properties with conventional methods, which makes them challenging to examine experimentally. Imaging, diffraction, and spectroscopic data of the specimen can be obtained using transmission electron microscopy techniques with an atomic or sub-nanometer spatial resolution, either concurrently or individually [61]. A microscopy method called TEM involves “transmitting” an electron beam through an extremely thin material. The electrons’ interaction effects with the sample produce a picture with a resolution of up to 0.08 nm [62]. **Figure 5e**,**f** show TEM of PS/PBD core-shell and hydrogenated PS/PBD nanoparticles.

3. PNPs for Antiviral Drug Delivery Systems

Across the world, there are thousands of committed drug delivery scientists who are working tirelessly to develop vaccines that are safer and more effective against the new variants of SARS-CoV-2. They are also focused on creating new carriers and drug delivery strategies to fight against any future viral pathogens that may emerge [63].

A well-designed delivery system can significantly improve the bioavailability of viral antigens by enhancing cellular uptake, providing metabolic stability, and targeting relevant tissues [64]. The efficacy of antiviral drugs can be enhanced using polymeric nanoparticles that facilitate prolonged drug release and target the virus. Ivermectin, a SARS-CoV-2 inhibitor, has been successfully administered utilizing PLGA-b-PEG-Mal polymeric nanoparticles [16].

One of the main elements influencing drug release is the molecular weight of the polymer. The polymer’s chain length can be determined by its molecular weight, where a higher molecular weight corresponds to a longer chain [65]. In addition, the hydrophilicity/lipophilicity of the polymer is reflected in the chain length. Longer chains have a higher lipophilicity and a slower rate of polymer breakdown. Therefore, the drug release kinetics and polymer breakdown rate can be adjusted by adjusting the molecular weight [65,66].

Physical stability, cellular absorption, biodistribution, and drug release are all strongly impacted by particle size, making it a crucial parameter. Nanoparticle performance often improves with decreasing particle size [65]. Some of the effects of nanoparticle grain size are:

- Decrease drug resistance [66].
- Enhance the rate of dissolution [67].
- Increase surface area [68].
- Enhance solubility [69]
- Enhance oral bioavailability [70].
- Decrease toxicity [71].
- Increase the stability of the drug and formulation [68].
- Increase drug-targeting ability [69].

3.1. PLGA

PLGA is a popular polymer used in the creation of micelles, which are used as drug delivery systems. One of the reasons for its widespread use is its high level of biocompatibility and biodegradability. The FDA approved its clinical use in 1989 [72].

In a recent study, researchers aimed to develop a biodegradable drug delivery system that targets specific receptor-binding sites for controlled drug release. They used the commonly used PNP, PLGA, and loaded it with oseltamivir phosphate (OP), a well-known antiviral drug [73]. The PLGA nanoparticles were modified to bind specifically to spike binding peptide-1 (SBP1) of SARS-CoV-2. The size of the OP-loaded NPs and the OP-loaded NPs targeted with SBP1 peptide were reported as 162.0 ± 11.0 and 226.9 ± 21.4 nm, respectively. The drug release study was conducted at a pH of 7.4 and a temperature of 37 °C, and it showed a long and effective release of OP. The release rate was fast for the first 30 days and then steady at about 72 days. There was no burst release of OP, indicating a successful development of the drug delivery system as indicated in **Figure 6** [74].

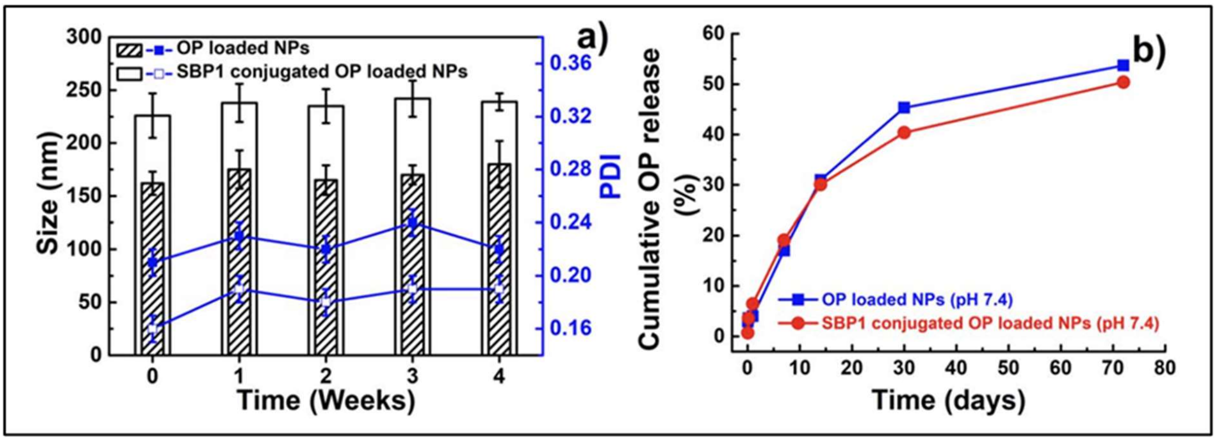

Figure 6. In-vitro stability evaluation and release profile of OP-loaded NPs. **(a)** Size stored at 5 °C for four weeks. **(b)** Release profile of the OP from the NPs targeted with SBP1 peptide or not. Reproduced with permission from Ucar et al. [74]

In another study, PLGA was utilized to administer Fingolimod (FTY720). The NPs were fabricated through a single emulsion solvent evaporation technique, resulting in a positively charged system with reported sizes of approximately 400 and 190 nm for empty NPs and FTY720-NP, respectively. The system demonstrated a notable drug entrapment rate of 90%, with drug release being contingent upon pH [75]. The study found that drug release required an acidic environment, which the developed NPs can access through caveolin-mediated endocytosis and micropinocytosis pathways. Once inside lysosomes, the required acidic environment becomes available to the NPs. The drug release rate at pH 5 was 10%, 80%, and 100% after 2, 8, and 24 h, respectively. However, at pH 7.4, a lower drug release rate of 10%, 10%, and 20% was observed for the same time spans as shown in **Figure 7**. The size of the system remained relatively unchanged over 90 days, and the use of NPs allowed for 70 times higher inhibition of viral infection compared to free drugs. Cytotoxicity studies on human and VeroCCL81 cell lines at 24, 48, and 72 h intervals showed that the

FTY720-NP system was less toxic than the free drug. Overall, the drug delivery system has great potential as it helps preserve the drug until it reaches a specific pH [59].

Similar works were done by Lui and colleagues in 2024 [3], and Struzek and Scherließ in 2023 reported on the preparation of ovalbumin (OVA)-loaded PLGA NP with a size of 700 nm for pulmonary delivery of antigens. They were successfully produced using several principles of quality by design [76]. Also in the work of Chandan and coworkers in 2010, porous PLA and PLGA nanoparticles were tested for pulmonary delivery of the hepatitis B vaccine [77]. Similar work was also done by Claudia and colleagues on the topic "Characterization of polymeric nanoparticles for intravenous delivery: Focus on stability" [78].

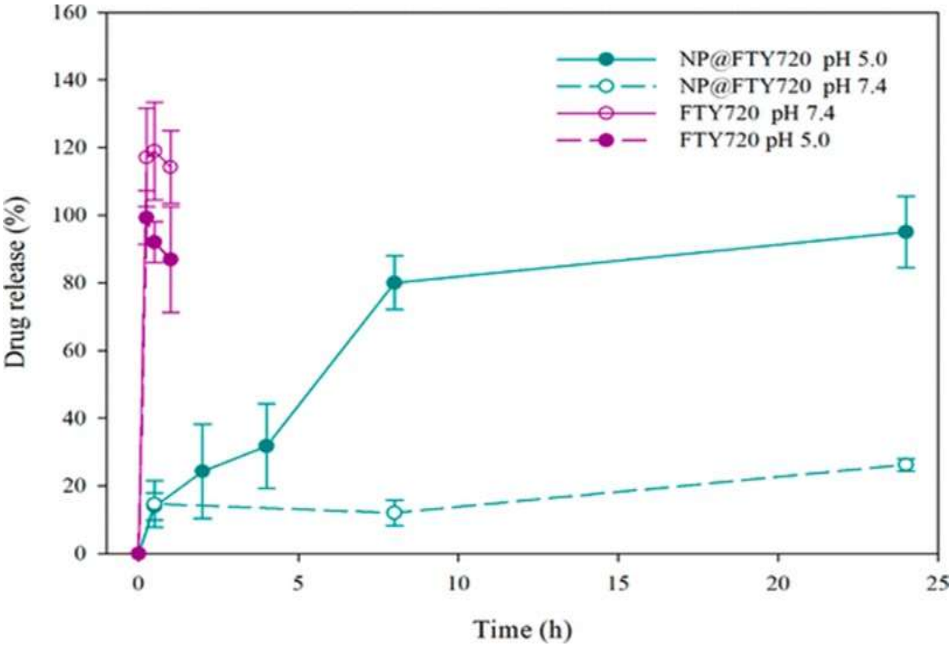

Figure 7. FTY720 release from the nanostructure system. FTY720 release profile from NP@FTY720 in a phosphate buffer with pH 7.4 and an acetate medium with pH 5.0. Data show the average of three independent measurements (n = 3) ± standard deviation (SD). Obtained from Mirinda et al. [75].

3.2. Poly (N-isopropyl acrylamide) (PNIPAM)

Xu and his colleagues developed a drug delivery system that releases drugs in response to specific temperatures. They loaded the FPV drug into silica nanocapsules (SNCs) and functionalized the NCs with block polymers [79,80]. The poly (N-isopropyl acrylamide)-block-poly (N, N-dimethylamino ethyl methacrylate) (PNIPAM-b-PDMAEMA)-modified SNCs were embedded in multilayer films to extend release time. The system can release as low as 50% of the drug over 80 days at 37 and 40 °C. A morphological stability study showed that the system was unharmed for 80 days, promising an effective drug release for a longer period as indicated in **Figure 8** [79]. **Figure 8c** shows the schematic representation of "on-demand" temperature-triggered film swelling and drug release from multilayer films.

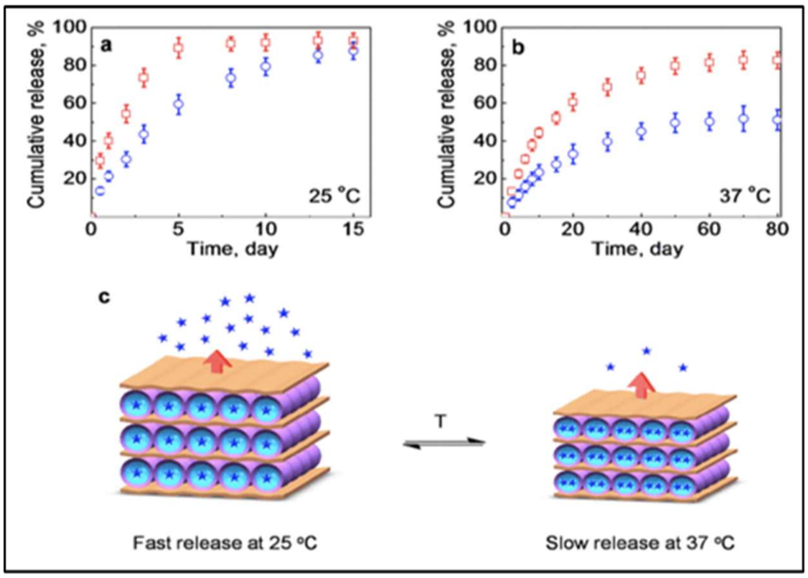

Figure 8. Release kinetics of FPV from [SNC-g-PNIPAM-b-PDMAEMA/PMAA]3 (squares) and [SNC-g-PNIPAM-b-Q100M/PMAA]3 (circles) films at **(a)** 25 and **(b)** 37 °C; **(c)** Schematic representation of mechanism. Reproduced with permission from Xu et al. [79].

In a study also conducted by Xu and colleagues, they coated silica nanocapsules (SNCs) with block polymers and loaded Molnupiravir into the system [81]. Molnupiravir is a drug that was approved for the treatment of SARS-CoV-2 from its early days. The block copolymer was quaternized to a certain degree to control the steric hindrance around the charged groups of the polymer blocks in the capsule. The entire SNC-Block polymer nanoparticle system was then embedded in well-defined films with polystyrene sulfonate (PSS) homopolymers by layer-by-layer self-assembly via electrostatic interaction. The polymer that the study group coated on SNCs was PNIPAM-bPDMAEMA, which is sensitive to temperature change. Therefore, the drug release was dependent on the temperature [81]. Speaking of how Molnupiravir operates, it introduces copying errors during viral RNA replication. The average thickness of various combinations of the system, namely [SNC-g-PNIPAM-b-PDMAEMA/PSS], [SNC-g-PNIPAM-b-Q20M/PSS], [SNC-g-PNIPAM-bQ40M/PSS], and [SNC-g-PNIPAM-b-Q100M/PSS] films, were reported as 125 ± 16, 135 ± 19, 170 ± 25, and 205 ± 28 nm, respectively, at 37 °C. The drug release was found to be around 81, 76, 62, and 45 % from [SNC-g-PNIPAM-b-PDMAEMA/PSS]3, [SNC-g-PNIPAM-b-Q20M/PSS]3, [SNC-g-PNIPAM-b-Q40M/PSS]3, and [SNC-g-PNIPAM-b-Q100M/PSS]3 films after 80 days, respectively [81] as shown in **Figure 9**. Like the previous study, the drug release was found to be faster as the temperature was decreased, and the reason behind this could be the temperature-induced hydration of PNIPAM moieties in LBL films, as per the researchers [81]. The transition of the delivery system in terms of its thickness was found to be reversible even after going through so many temperature-manipulating cycles, suggesting the system to be robust [81]. The overall design of this drug delivery system, where steric hindrance in the amino group of QPDMAEMA moieties was enhanced and the quaternization degree, the thickness of the film layer, and molecular diffusion distance were increased, allowed a reduction in the drug release from the nanoparticle system [81].

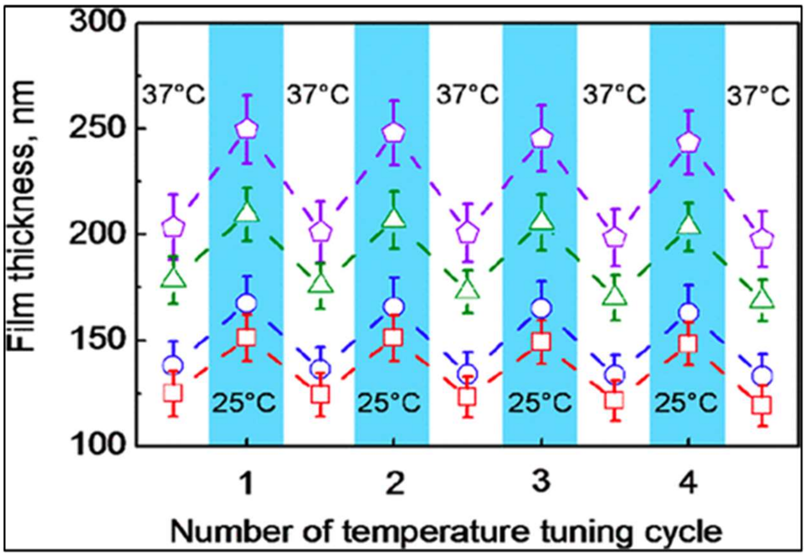

Figure 9. Reversible temperature-triggered swelling/deswelling of [SNC-g-PNIPAM-b-PDMAEMA/PSS]3 (squares), [SNC-g-PNIPAM-b-Q20M/PSS]3 (circles), [SNC-g-PNIPAM-bQ40M/PSS]3 (triangles), and [SNC-g-PNIPAM-b-Q100M/PSS]3 (pentagons) films at 25 and 37 °C, respectively. Reproduced with permission from Xu et al. [81].

3.3. PEG/PLGA-b PEG

Moving on, the next system was developed using PLGA-b-PEG-Mal nanoparticles in which the Ivermectin drug (IVM) was loaded, and this can be delivered orally [82]. The reported size of nanoparticles was 70-80 nm with a 20% feed capability of IVM [82]. The goal of the researchers was to develop a system that can decrease the expression of viral spike protein present on SARS-CoV-2 as well as down-regulate its receptor protein (ACE2), and therefore they attached an Fc immunoglobulin fragment forming T-Fc-IVM-NPs (IgG Fc antibody-treated IVM-NPs) [82]. The mechanism of action of this NP system has been reported by the researchers in the paper, but for now, it is important to know that the results of western blotting showed a significantly lower spike protein and ACE2 in the HEK293T and HELA cells when T-Fc-IVM-NPs were administered, but not by free IVM [82]. The cytotoxic results reported suggest that the free IVM decreases basal and maximum [82] respiration and severely impacts ATP production inside the mitochondria of cells; however, no such side effects were observed when NT-IVM-NP (not treated IVM-NPs) and T-Fc-IVM-NP were administered to the cells [82]. This result shows a great possibility of decreasing the spread of any virus from the SARS family, including SARS-CoV-2, as the system targets the spike proteins present on the surface of each member of this family [82].

Up next, we found another study that used Ivermectin (IVM), which was loaded in synthetic nanoparticles: Poly (L-lactide-co-glycolide)-block-poly (ethylene glycol)-amide (PLGA-b-PEG-NH2); PLGA-b-PEG-Mal.; Poly (L-lactide-co-glycolide)-block-poly (ethylene glycol)-hydroxide (PLGA-b-PEG-OH), against Zika virus [16,83]. The goal of this group was to develop a platform that allows the delivery of IVM at a higher concentration without affecting other cellular functions inside our body. They created a system whose size was found to be 60 nm at IVM fed of 10%

and 140 nm at IVM fed of 50%; however, they also reported the NP system was only stable up to 30% fed [82]. They reported that the targeted T-Fc-IVM-NPs were successfully able to cross the intestinal epithelial barrier model and enter the bloodstream in comparison to non-targeted NT-OH-IVM-MPs. Specifically, 65% of injected targeted NP was distributed in the blood after 24 h, and the rest (24%) was still in different parts of the intestine [83]. A comparison study with free IVM showed that most of the drug was stuck in intestinal tissue, indicating that the NPs are needed to cross that intestinal barrier [83]. The study also reported that the free IVM was easily able to cross the placental membrane in comparison to that of T-Fc-IVM-NPs; however, the free IVM completely disrupts the cellular respirations of the cell that forms the placental barrier, but this is not the case for T-Fc-IVM-NPs [83]. The overall cytotoxic study showed that the toxicity of IVM is significantly reduced when loaded with polymeric NPs, as indicated in **Figures 10** and **11** [83]. Specifically, **Figures 10 A,B** show the western blot decreasing expression of ACE2 in A549 adenocarcinoma alveolar basal epithelial cells transfected with a plasmid expressing spike protein with the treatment of IVM, NT-IVM-NPs, or T-Fc-IVM-, while **Figure 10C** shows the ACE2 expression in HeLa malignant epithelial cells. Immunofluorescence staining in **Figure 10D** confirms the same trend in A549 cells. Additionally, the researchers also reported that T-FC-IVM-NP can reduce NS1 protein, suggesting its usage could be beneficial against the ZIKA virus and other viral infections [83]. Taking their word as it is, one can tweak this NP system to target the spike proteins present in SARS-CoV-2.

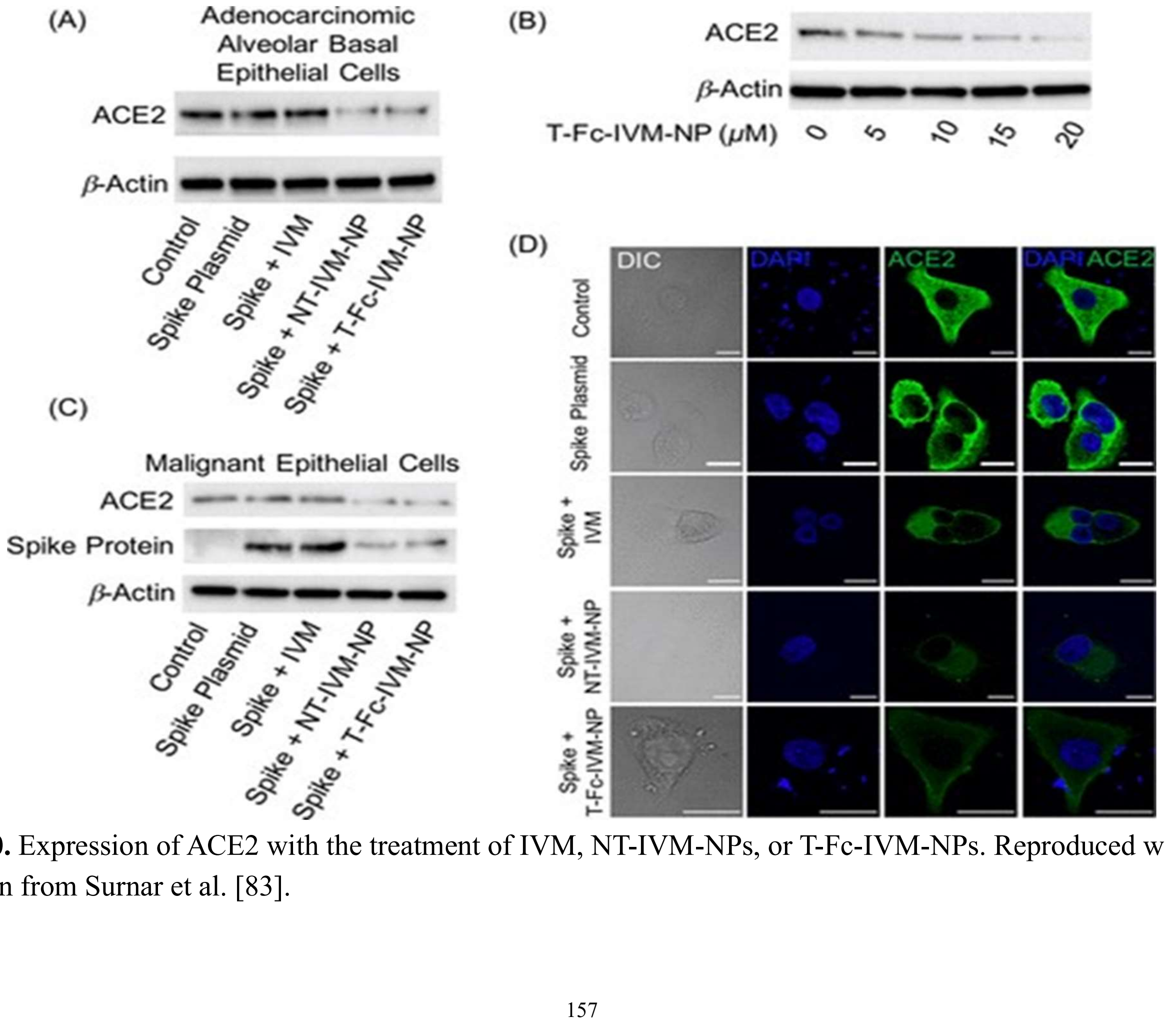

Figure 10. Expression of ACE2 with the treatment of IVM, NT-IVM-NPs, or T-Fc-IVM-NPs. Reproduced with permission from Surnar et al. [83].

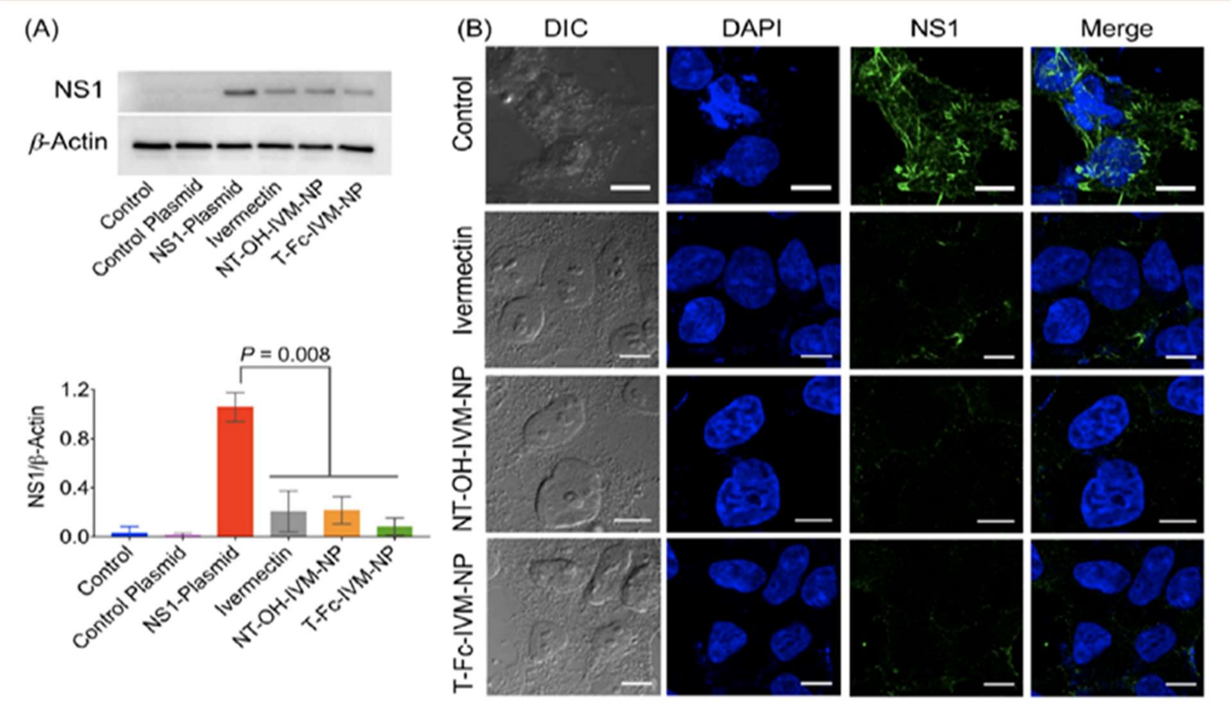

Figure 11. NS1 expression level in HEK293T cells after treatment with NPs by (A) Western blotting and (B) immunofluorescence. Cells were treated with IVM, NT-OH-IVM-NP, or T-Fc-IVM-NP at a concentration of 10 µM concerning IVM for 6 h—scale bar: 10 µM. Reproduced with permission from Surnar et al. [83].

3.4. PEDOT

We found a new study that used a unique system that responds to electricity. The researchers used curcumin (CUR), an antiviral and anticancer drug, and combined it with electrospun poly(ε-caprolactone) (PCL) microfibers (MFs) loaded with poly (3,4-ethylene dioxythiophene) nanoparticles (PEDOT NPs). The PEDOT NPs, which are polymeric nanoparticles, have a diameter of 99 ± 21 nm and are located inside the PCL MFs [84]. The study reported that when external stimuli were applied after embedding PEDOT NPs in the electro-fiber, the release of CUR was promoted [84]. Although the release of CUR by simple diffusion was very low, a linear increase in drug release was observed with the increased number of potential pulses. Notably, this increase in the release was not observed when PEDOT was excluded from the system, indicating that their presence is crucial for responding to electrical stimuli in the form of potential pulses in a PBS + Tween 20 electrolyte medium, mimicking a physiological environment. The study found that the specific increases with the number of pulses for PCL/PEDOT/CUR MFs were 8.1% ± 4.3%, 18.4% ± 7.2%, and 30.2% ± 10.2% after 1, 3, and 5 potential pulses, respectively [84]. The increase is based on the voltametric response of PEDOT NPs, which results in volume variations and structural changes [84]. The drug system's cytotoxic study revealed that cell growth decreases only when PEDOT is not used, indicating that the presence of PEDOT also reduces the toxicity of CUR, as shown in **Figure 12** [84]. In conclusion, this study shows the potential for using PCL/PEDOT/CUR MFs to control drug release in response to electrical stimulation within our bodies, regardless of the virus we are dealing with.

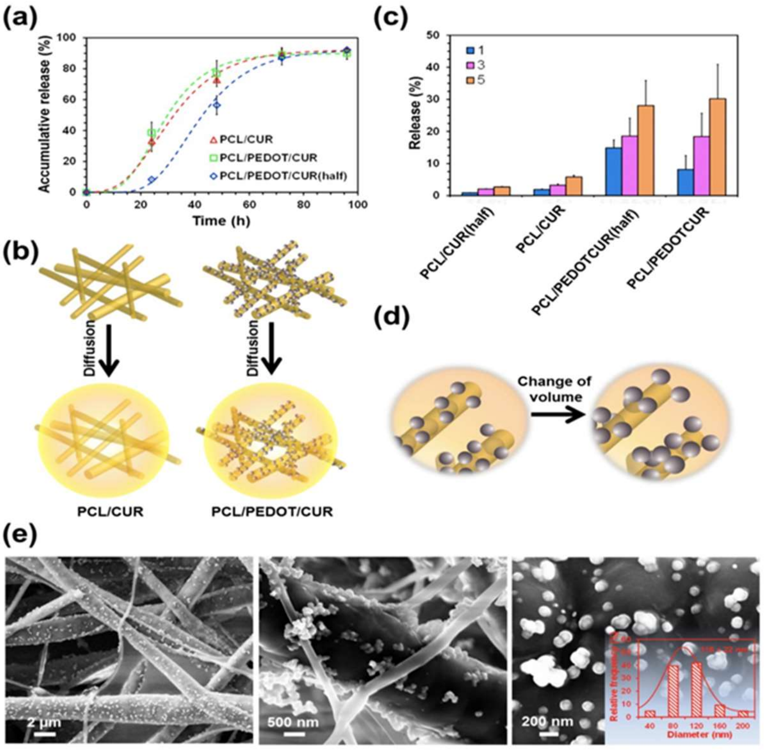

Figure 12. CUR release from PCL/CUR and PCL/PEDOT/CUR MFs. **(a,c)** CUR release profiles in PBS-EtOH, and after electrostimulation by applying 1, 3, and 5 consecutive potential pulses, respectively; **(b,d)** Scheme representing the diffusion mechanism for CUR release in the absence/presence of electrostimulation, respectively; **(e)** SEM micrographs of PCL/PEDOT/CUR fibers after electrostimulation. Reproduced with permission from Puiggali-Jou et al. [84].

4. Conclusion

According to the findings, the utilization of PNPs presents numerous therapeutic benefits in combating the SARS-CoV-2 virus. PNPs provide a means of effectively delivering drugs to targeted locations for a prolonged period, thereby saving considerable costs associated with repeated drug administration due to quick elimination from the body. **Table 1** shows a list of selected PNPs used for anti-viral drug delivery strategies.

Table 1. List of selected PNPs used for anti-viral drug delivery strategies.

Polymer	Conjugate	Properties	Application	Ref
PLGA	PLGA-b-PEG-NH_2 OVA-PLGA	water-insoluble, biocompatibility, and biodegradability	drug delivery of hydrophilic as well as hydrophobic actives, diabetic retinopathy, neovascular age-related macular degeneration (ocular neovascularization)	[76], [85–87]
PEDOT	PCL/PEDOT/CUR	electrical conductivity, electrochemical activity, thermoelectric behavior, and high specific capacitance.	facilitating cell spreading and enhancing cell proliferation	[84], [88–90]
PNIPAM	PNIPAM-b-PDMAEMA	temperature-triggered hydration−dehydration transition, high surface areas, and irregular structures	temperature-modulated drug delivery systems	[81], [91], [92]
PEG	T-Fc-IVM	biocompatibility, protein repellent ability,	immunodeficiency disease, bioconjugation, and drug delivery	[93], [94]

Table 1. (*Continued*).

Polymer	Conjugate	Properties	Application	Ref
Remdesivir	Remdesivir-GS-5734	the heterocyclic part analogous to adenine, allowing hydrogen bonding, contains C-nucleoside, the presence of a 1′-CN group, the ribosyl moiety ensuing inhibition of RNA (instead of DNA) synthesis, and the presence of a phosphoramidate group, contributing to its tissue targeting	Activity against Ebolavirus, Filo-, Pneumo and Paramyxoviruses	[95]
PCL	PEO-PCL	excellent biocompatibility, high hydrophobicity, and neutral biodegradation end products	used as emulsifying agents, solubilizing agents, surfactants, wetting agents, and treating HIV/AIDS	[96]
PVA	PVA-TPU-Ag	antibacterial and antiviral properties	wound dressings, medical device coatings, treatment of COVID-19	[97]
PLA	PLA-Ag	high mechanical strength, biocompatibility and non-toxicity	biomedical packaging, food packaging, and 3D printing technology.	[98]
PNIIPAM	PNIPAM	high stability, biocompatibility,	Treat HIV-1 infection	[99]

Additionally, various studies have shown that PNPs significantly reduce the cytotoxicity of many drugs on vital cells within the body. Given their biodegradability, PNPs are promising contenders for replacing current drug delivery systems with polymeric nanoparticle-based systems for COVID-19. Some PEG-based nanoparticle systems have already been applied in clinical trials for COVID-related treatment [100]. Additionally, PEG-PLGA systems have been widely applied in clinical trials for anti-cancer treatment [101,102] and hence one can expect these platforms to be approved for coronavirus-related trials as well in the near future. The number of nanoparticles in clinical approvals has gone up each year since 1992 and saw a total of 32 approvals in 2020, a part of which were for COVID-19 vaccines [103]. Further, the number of human clinical trials peaked in 2021 for various nanoparticle systems, which only provides a bright prospect for the upcoming future.

Acknowledgments: We thank the University of Scranton for generously supporting this research.

Conflict of interest: The authors declare no conflict of interest.

Abbreviations

AFM	atomic force microscopy
CUR	Curcumin
Cy-A	cyclosporin
DNA	deoxyribonucleic acid
ESD	emulsification/solvent diffusion
FTIR	Fourier transformed infrared spectroscopy
FPV	Favipiravir
FPV-SLN	favipiravir solid lipid nanoparticles
FTY720	Fingolimod
H_1N_1	Spanish flu, lower respiratory tract infections

IVM	Ivermectin drug
Mal	Maleimide
MFs	Microfibers
mTHPP	meso-tetra (3-hydroxyphenyl) porphine
NH_2	Amide
OP	oseltamivir phosphate
OVA	Ovalbumin
PBD	Polybutadiene
PCL	poly-caprolactone
PBS	polybutylene succinate
PEDOT	Poly (3,4-ethylene dioxythiophene)
PLA	polylactic acid
PLGA	Poly (lactic-co-glycolic acid)
PM	polymeric micelles
PMMA	Poly (methyl methacrylate)
PNIPAM-b-PDMAEMA	Poly (N-isopropyl acrylamide)-block-poly (N, N-dimethylamino ethyl methacrylate)
PNIPAM	Poly (N-isopropyl acrylamide)
PEG	Poly (ethylene glycol)
PNP	polymeric nanoparticle
PS	Polystyrene
Ps	Polymersomes
PSS	polystyrene sulfonate
SARS-CoV-2 COVID 19	Severe Acute Respiratory Syndrome Coronavirus 2
SBP1	spike binding peptide
SEM	scanning electron microscopy
SD	standard deviation
SLNs	solid lipid nanoparticles
SNCs	silica nanocapsules
TEM	transmission electron microscope
WHO	World Health Organization

References

1. Bohrey S, Chourasiya V, Pandey A. Polymeric nanoparticles containing diazepam: preparation, optimization, characterization, in-vitro drug release and release kinetic study. Nano Convergence. 2016; 3(1). doi: 10.1186/s40580-016-0061-2
2. Ftouh M, Kalboussi N, Abid N, et al. Contribution of Nanotechnologies to Vaccine Development and Drug Delivery against Respiratory Viruses. PPAR Research. 2021; 2021: 1-28. doi: 10.1155/2021/6741290
3. Liu S, Hu M, Liu X, et al. Nanoparticles and Antiviral Vaccines. Vaccines. 2023; 12(1): 30. doi: 10.3390/vaccines12010030
4. Ahmad MZ, Ahmad J, Aslam M, et al. Repurposed drug against COVID-19: nanomedicine as an approach for finding new hope in old medicines. Nano Express. 2021; 2(2): 022007. doi: 10.1088/2632-959x/abffed
5. Rastogi A, Singh A, Naik K, et al. A systemic review on liquid crystals, nanoformulations and its application for detection and treatment of SARS-CoV-2 (COVID-19). Journal of Molecular Liquids. 2022; 362: 119795. doi: 10.1016/j.molliq.2022.119795
6. Li M, Li Y, Li S, et al. The nano delivery systems and applications of mRNA. European Journal of Medicinal Chemistry. 2022; 227: 113910. doi: 10.1016/j.ejmech.2021.113910

7. Chan Y, Ng SW, Singh SK, et al. Revolutionizing polymer-based nanoparticle-linked vaccines for targeting respiratory viruses: A perspective. Life Sciences. 2021; 280: 119744. doi: 10.1016/j.lfs.2021.119744
8. Medhi R, Srinoi P, Ngo N, et al. Nanoparticle-Based Strategies to Combat COVID-19. ACS Applied Nano Materials. 2020; 3(9): 8557-8580. doi: 10.1021/acsanm.0c01978
9. Wrapp D, Wang N, Corbett KS, et al. Cryo-EM structure of the 2019-nCoV spike in the prefusion conformation. Science. 2020; 367(6483): 1260-1263. doi: 10.1126/science.abb2507
10. Chan JF, Yuan S, Kok KH, et al. A familial cluster of pneumonia associated with the 2019 novel coronavirus indicating person-to-person transmission: a study of a family cluster. Lancet. 2020; 395: 514-523. doi: 10.1016/S0140-6736(20)30154-9
11. Huang C, Wang Y, Li X, et al. Clinical features of patients infected with 2019 novel coronavirus in Wuhan, China. Lancet. 2020; 395: 497-506. doi: 10.1016/S0140-6736(20)30183-5
12. Piret J, Boivin G. Pandemics Throughout History. Frontiers in Microbiology. 2021; 11. doi: 10.3389/fmicb.2020.631736
13. Mostafavi E, Iravani S, Varma RS. Nanosponges: An overlooked promising strategy to combat SARS-CoV-2. Drug Discovery Today. 2022; 27(10): 103330. doi: 10.1016/j.drudis.2022.07.015
14. Li W, Meng J, Ma X, et al. Advanced materials for the delivery of vaccines for infectious diseases. Biosafety and Health. 2022; 4(2): 95-104. doi: 10.1016/j.bsheal.2022.03.002
15. Chintagunta AD, M SK, Nalluru S, et al. Nanotechnology: an emerging approach to combat COVID-19. Emergent Materials. 2021; 4(1): 119-130. doi: 10.1007/s42247-021-00178-6
16. Duan Y, Wang S, Zhang Q, et al. Nanoparticle approaches against SARS-CoV-2 infection. Current Opinion in Solid State and Materials Science. 2021; 25(6): 100964. doi: 10.1016/j.cossms.2021.100964
17. Bourguignon T, Godinez-Leon JA, Gref R. Nanosized Drug Delivery Systems to Fight Tuberculosis. Pharmaceutics. 2023; 15(2): 393. doi: 10.3390/pharmaceutics15020393
18. Tosi G, Costantino L, Ruozi B, et al. Polymeric nanoparticles for the drug delivery to the central nervous system. Expert Opinion on Drug Delivery. 2008; 5(2): 155-174. doi: 10.1517/17425247.5.2.155
19. Zielińska A, Carreiró F, Oliveira AM, et al. Polymeric Nanoparticles: Production, Characterization, Toxicology and Ecotoxicology. Molecules. 2020; 25(16): 3731. doi: 10.3390/molecules25163731
20. Crucho CIC, Barros MT. Polymeric nanoparticles: A study on the preparation variables and characterization methods. Materials Science and Engineering: C. 2017; 80: 771-784. doi: 10.1016/j.msec.2017.06.004
21. Abd Elkodous M, Olojede SO, Morsi M, et al. Nanomaterial-based drug delivery systems as promising carriers for patients with COVID-19. RSC Advances. 2021; 11(43): 26463-26480. doi: 10.1039/d1ra04835j
22. Udugama B, Kadhiresan P, Kozlowski HN, et al. Diagnosing COVID-19: The Disease and Tools for Detection. ACS Nano. 2020; 14(4): 3822-3835. doi: 10.1021/acsnano.0c02624
23. Bai X, Smith Z, Wang Y, et al. Sustained Drug Release from Smart Nanoparticles in Cancer Therapy: A Comprehensive Review. Micromachines. 2022; 13(10): 1623. doi: 10.3390/mi13101623
24. Mukherjee B, Bhattacharya A, Mukhopadhyay R, et al. Pathobiology of Parasitic Protozoa: Dynamics and Dimensions. Springer Nature Singapore; 2023. doi: 10.1007/978-981-19-8225-5
25. Patnaik A, Jena GK, Patra ChN. Recent Advancements and Patent Search on Polymeric Nanoparticles. BioNanoScience. 2023; 13(4): 1463-1469. doi: 10.1007/s12668-023-01220-z
26. Al-Nemrawi NK, Darweesh RS, Al-shriem LA, et al. Polymeric Nanoparticles for Inhaled Vaccines. Polymers. 2022; 14(20): 4450. doi: 10.3390/polym14204450
27. Sachan I. Investigating Current Delivery Vehicles for Efficient and Targeted Delivery of Therapeutic RNA and Future Perspectives. University of Nottingham; 2023.
28. Kempe H, Kempe M. Ouzo polymerization: A bottom-up green synthesis of polymer nanoparticles by free-radical polymerization of monomers spontaneously nucleated by the Ouzo effect; Application to molecular imprinting. Journal of Colloid and Interface Science. 2022; 616: 560-570. doi: 10.1016/j.jcis.2022.02.035
29. Wibowo D, Jorritsma SHT, Gonzaga ZJ, et al. Polymeric nanoparticle vaccines to combat emerging and pandemic threats. Biomaterials. 2021; 268: 120597. doi: 10.1016/j.biomaterials.2020.120597
30. S. Pragati, S. Kuldeep, S. Ashok, M. Satheesh. Solid Lipid Nanoparticles: A Promising Drug Delivery Technology. International Journal of Pharmaceutical Sciences and Nanotechnology. 2009; 2(2): 509-516. doi: 10.37285/ijpsn.2009.2.2.3

31. Manjunath K, Reddy JS, Venkateswarlu V. Solid lipid nanoparticles as drug delivery systems. Methods and Findings in Experimental and Clinical Pharmacology. 2005; 27(2): 127. doi: 10.1358/mf.2005.27.2.876286
32. Mohammadi-Samani S, Ghasemiyeh P. Solid lipid nanoparticles and nanostructured lipid carriers as novel drug delivery systems: applications, advantages and disadvantages. Research in Pharmaceutical Sciences. 2018; 13(4): 288. doi: 10.4103/1735-5362.235156
33. Gong J, Chen M, Zheng Y, et al. Polymeric micelles drug delivery system in oncology. Journal of Controlled Release. 2012; 159(3): 312-323. doi: 10.1016/j.jconrel.2011.12.012
34. Miyata K, Christie RJ, Kataoka K. Polymeric micelles for nano-scale drug delivery. Reactive and Functional Polymers. 2011; 71(3): 227-234. doi: 10.1016/j.reactfunctpolym.2010.10.009
35. Ahmad Z, Shah A, Siddiq M, et al. Polymeric micelles as drug delivery vehicles. RSC Advances. 2014; 4(33): 17028-17038. doi: 10.1039/c3ra47370h
36. Kousalová J, Etrych T. Polymeric Nanogels as Drug Delivery Systems. Physiological Research. 2018; 67(Suppl.2): S305-S317. doi: 10.33549/physiolres.933979
37. Sultana F, Manirujjaman M, Haque MdIU, et al. An Overview of Nanogel Drug Delivery System. Journal of Applied Pharmaceutical Science. 2013; 3 (8 Suppl 1): S95-S105. doi: 10.7324/japs.2013.38.s15
38. Manimaran V, Nivetha RP, Tamilanban T, et al. Nanogels as novel drug nanocarriers for CNS drug delivery. Frontiers in Molecular Biosciences. 2023; 10. doi: 10.3389/fmolb.2023.1232109
39. Lee JS, Feijen J. Polymersomes for drug delivery: Design, formation and characterization. Journal of Controlled Release. 2012; 161(2): 473-483. doi: 10.1016/j.jconrel.2011.10.005
40. Baghbanbashi M, Kakkar A. Polymersomes: Soft Nanoparticles from Miktoarm Stars for Applications in Drug Delivery. Molecular Pharmaceutics. 2022; 19(6): 1687-1703. doi: 10.1021/acs.molpharmaceut.1c00928
41. Oh KS, Lee KE, Han SS, et al. Formation of Core/Shell Nanoparticles with a Lipid Core and Their Application as a Drug Delivery System. Biomacromolecules. 2005; 6(2): 1062-1067. doi: 10.1021/bm049234r
42. Kumar R, Mondal K, Panda PK, et al. Core-shell nanostructures: perspectives towards drug delivery applications. Journal of Materials Chemistry B. 2020; 8(39): 8992-9027. doi: 10.1039/d0tb01559h
43. Deshpande S, Sharma S, Koul V, et al. Core-Shell Nanoparticles as an Efficient, Sustained, and Triggered Drug-Delivery System. ACS Omega. 2017; 2(10): 6455-6463. doi: 10.1021/acsomega.7b01016
44. Sezgin-Bayindir Z, Losada-Barreiro S, Bravo-Díaz C, et al. Nanotechnology-Based Drug Delivery to Improve the Therapeutic Benefits of NRF2 Modulators in Cancer Therapy. Antioxidants. 2021; 10(5): 685. doi: 10.3390/antiox10050685
45. Niwa T, Takeuchi H, Hino T, et al. Preparations of biodegradable nanospheres of water-soluble and insoluble drugs with D,L-lactide/glycolide copolymer by a novel spontaneous emulsification solvent diffusion method, and the drug release behavior. Journal of Controlled Release. 1993; 25: 89-98. doi: 10.1016/0168-3659(93)90097-O
46. Pinto Reis C, Neufeld RJ, Ribeiro, et al. Nanoencapsulation I. Methods for preparation of drug-loaded polymeric nanoparticles. Nanomedicine: Nanotechnology, Biology and Medicine. 2006; 2(1): 8-21. doi: 10.1016/j.nano.2005.12.003
47. Vargas A, Pegaz B, Debefve E, et al. Improved photodynamic activity of porphyrin loaded into nanoparticles: an in vivo evaluation using chick embryos. International Journal of Pharmaceutics. 2004; 286(1-2): 131-145. doi: 10.1016/j.ijpharm.2004.07.029
48. Konan YN, Gurney R, Allemann E. State of the art in the delivery of photosensitizers for photodynamic therapy. Journal of Photochemistry andPhotobiology B: Biology. 2002; 66: 89-106. doi: 10.1016/S1011-1344(01)00267-6
49. Perez C, Sanchez A, Putnam D, et al. Poly (lactic acid)-poly(ethylene glycol) nanoparticles as new carriers for the delivery of plasmid DNA. Journal of Control. 2001; 75: 211-224. doi: 10.1016/S0168-3659(01)00397-2
50. Nagavarma BVN, Yadav HKS, Ayaz A, et al. Different techniques for preparation of polymeric nanoparticles—A review. Asian J. Pharm. Asian Journal of Pharmaceutical and Clinical Research. 2012; 5(3): 16-23.
51. Rao JP, Geckeler KE. Polymer nanoparticles: Preparation techniques and size-control parameters. Progress in Polymer Science. 2011; 36(7): 887-913. doi: 10.1016/j.progpolymsci.2011.01.001
52. Mallakpour S, Behranvand V. Polymeric nanoparticles: Recent development in synthesis and application. Express Polymer Letters. 2016; 10(11): 895-913. doi: 10.3144/expresspolymlett.2016.84
53. Sundar S, Kundu J, Kundu SC. Biopolymeric nanoparticles. Science and Technology of Advanced Materials. 2010; 11(1): 014104. doi: 10.1088/1468-6996/11/1/014104

54. Zhang G, Niu A, Peng S, et al. Formation of Novel Polymeric Nanoparticles. Accounts of Chemical Research. 2001; 34(3): 249-256. doi: 10.1021/ar000011x
55. Nakabayashi K, Kojima M, Inagi S, et al. Size-Controlled Synthesis of Polymer Nanoparticles with Tandem Acoustic Emulsification Followed by Soap-Free Emulsion Polymerization. ACS Macro Letters. 2013; 2(6): 482-484. doi: 10.1021/mz4001817
56. Chowdhury NK, Deepika, Choudhury R, et al. Nanoparticles as an effective drug delivery system in COVID-19. Biomedicine & Pharmacotherapy. 2021; 143: 112162. doi: 10.1016/j.biopha.2021.112162
57. Fornaguera C, Solans C. Analytical Methods to Characterize and Purify Polymeric Nanoparticles. International Journal of Polymer Science. 2018; 2018: 1-10. doi: 10.1155/2018/6387826
58. Tulbah AS, Lee WH. Physicochemical Characteristics and In Vitro Toxicity/Anti-SARS-CoV-2 Activity of Favipiravir Solid Lipid Nanoparticles (SLNs). Pharmaceuticals. 2021; 14(10): 1059. doi: 10.3390/ph14101059
59. Khaledi S, Jafari S, Hamidi S, et al. Preparation and characterization of PLGA-PEG-PLGA polymeric nanoparticles for co-delivery of 5-Fluorouracil and Chrysin. Journal of Biomaterials Science, Polymer Edition. 2020; 31(9): 1107-1126. doi: 10.1080/09205063.2020.1743946
60. Wang X, Hall JE, Warren S, et al. Synthesis, Characterization, and Application of Novel Polymeric Nanoparticles. Macromolecules. 2007; 40(3): 499-508. doi: 10.1021/ma0613739
61. Bhatia S. Natural Polymer Drug Delivery Systems—Nanoparticles, Plants, and Algae. Springer International Publishing; 2016.
62. Alipour A, Zarinabadi S, Azimi A, et al. Adsorptive removal of Pb(II) ions from aqueous solutions by thiourea-functionalized magnetic ZnO/nanocellulose composite: Optimization by response surface methodology (RSM). International Journal of Biological Macromolecules. 2020; 151: 124-135. doi: 10.1016/j.ijbiomac.2020.02.109
63. Labouta HI, Langer R, Cullis PR, et al. Role of drug delivery technologies in the success of COVID-19 vaccines: a perspective. Drug Delivery and Translational Research. 2022; 12(11): 2581-2588. doi: 10.1007/s13346-022-01146-1
64. Cordeiro AS, Patil-Sen Y, Shivkumar M, et al. Nanovaccine Delivery Approaches and Advanced Delivery Systems for the Prevention of Viral Infections: From Development to Clinical Application. Pharmaceutics. 2021; 13(12): 2091. doi: 10.3390/pharmaceutics13122091
65. Mittal G, Sahana DK, Bhardwaj V, et al. Estradiol loaded PLGA nanoparticles for oral administration: Effect of polymer molecular weight and copolymer composition on release behavior in vitro and in vivo. Journal of Controlled Release. 2007; 119(1): 77-85. doi: 10.1016/j.jconrel.2007.01.016
66. Hrib J, Sirc J, Hobzova R, et al. Nanofibers for drug delivery - incorporation and release of model molecules, influence of molecular weight and polymer structure. Beilstein Journal of Nanotechnology. 2015; 6: 1939-1945. doi: 10.3762/bjnano.6.198
67. Lee CC, Gillies ER, Fox ME, et al. A single dose of doxorubicin-functionalized bow-tie dendrimer cures mice bearing C-26 colon carcinomas. Proceedings of the National Academy of Sciences. 2006; 103(45): 16649-16654. doi: 10.1073/pnas.0607705103
68. Löbenberg R, Maas J, Kreuter J. Improved Body Distribution of14C-labelled AZT bound to Nanoparticles in Rats determined by Radioluminography. Journal of Drug Targeting. 1998; 5(3): 171-179. doi: 10.3109/10611869808995872
69. Goldberg DS, Vijayalakshmi N, Swaan PW, et al. G3.5 PAMAM dendrimers enhance transepithelial transport of SN38 while minimizing gastrointestinal toxicity. Journal of Controlled Release. 2011; 150(3): 318-325. doi: 10.1016/j.jconrel.2010.11.022
70. Brewer E, Coleman J, Lowman A. Emerging Technologies of Polymeric Nanoparticles in Cancer Drug Delivery. Journal of Nanomaterials. 2011; 2011: 1-10. doi: 10.1155/2011/408675
71. Liu Z, Fan AC, Rakhra K, et al. Supramolecular Stacking of Doxorubicin on Carbon Nanotubes for In Vivo Cancer Therapy. Angewandte Chemie International Edition. 2009; 48(41): 7668-7672. doi: 10.1002/anie.200902612
72. Begines B, Ortiz T, Pérez-Aranda M, et al. Polymeric Nanoparticles for Drug Delivery: Recent Developments and Future Prospects. Nanomaterials. 2020; 10(7): 1403. doi: 10.3390/nano10071403
73. Pandya M, Saran R. Application of Nanoparticles in Medicine. Journal of ISAS. 2022; 1(2): 1-21. doi: 10.59143/isas.jisas.1.2/mvsb9110

74. Ucar B, Acar T, Arayici PP, et al. A nanotechnological approach in the current therapy of COVID-19: model drug oseltamivir-phosphate loaded PLGA nanoparticles targeted with spike protein binder peptide of SARS-CoV-2. Nanotechnology. 2021; 32(48): 485601. doi: 10.1088/1361-6528/ac1c22
75. Miranda RR, Ferreira NN, Souza EE de, et al. Modulating Fingolimod (FTY720) Anti-SARS-CoV-2 Activity Using a PLGA-Based Drug Delivery System. ACS Applied Bio Materials. 2022; 5(7): 3371-3383. doi: 10.1021/acsabm.2c00349
76. Struzek AM, Scherließ R. Quality by Design as a Tool in the Optimisation of Nanoparticle Preparation—A Case Study of PLGA Nanoparticles. Pharmaceutics. 2023; 15(2): 617. doi: 10.3390/pharmaceutics15020617
77. Thomas C, Rawat A, Hope-Weeks L, et al. Aerosolized PLA and PLGA Nanoparticles Enhance Humoral, Mucosal and Cytokine Responses to Hepatitis B Vaccine. Molecular Pharmaceutics. 2011; 8(2): 405-415. doi: 10.1021/mp100255c
78. Oliveira CL, Veiga F, Varela C, et al. Characterization of polymeric nanoparticles for intravenous delivery: Focus on stability. Colloids and Surfaces B: Biointerfaces. 2017; 150: 326-333. doi: 10.1016/j.colsurfb.2016.10.046
79. Xu L, Zhang X, Chu Z, et al. Temperature-Responsive Multilayer Films Based on Block Copolymer-Coated Silica Nanoparticles for Long-Term Release of Favipiravir. ACS Applied Nano Materials. 2021; 4(12): 14014-14025. doi: 10.1021/acsanm.1c03334
80. Tan RSL, Hassandarvish P, Chee CF, et al. Chitosan and its derivatives as polymeric anti-viral therapeutics and potential anti-SARS-CoV-2 nanomedicine. Carbohydrate Polymers. 2022; 290: 119500. doi: 10.1016/j.carbpol.2022.119500
81. Xu L, Chu Z, Zhang J, et al. Steric Effects in the Deposition Mode and Drug-Delivering Efficiency of Nanocapsule-Based Multilayer Films. ACS Omega. 2022; 7(34): 30321-30332. doi: 10.1021/acsomega.2c03591
82. Surnar B, Kamran MZ, Shah AS, et al. Clinically Approved Antiviral Drug in an Orally Administrable Nanoparticle for COVID-19. ACS Pharmacology & Translational Science. 2020; 3(6): 1371-1380. doi: 10.1021/acsptsci.0c00179
83. Surnar B, Kamran MZ, Shah AS, et al. Orally Administrable Therapeutic Synthetic Nanoparticle for Zika Virus. ACS Nano. 2019; 13(10): 11034-11048. doi: 10.1021/acsnano.9b02807
84. Puiggalí-Jou A, Cejudo A, del Valle LJ, et al. Smart Drug Delivery from Electrospun Fibers through Electroresponsive Polymeric Nanoparticles. ACS Applied Bio Materials. 2018; 1(5): 1594-1605. doi: 10.1021/acsabm.8b00459
85. Tabatabaei Mirakabad FS, Nejati-Koshki K, Akbarzadeh A, et al. PLGA-Based Nanoparticles as Cancer Drug Delivery Systems. Asian Pacific Journal of Cancer Prevention. 2014; 15(2): 517-535. doi: 10.7314/apjcp.2014.15.2.517
86. Food and Drug Administration. Inactive ingredient search for approved drug products. Available online: https://catalog.data.gov/dataset/inactive-ingredient-search-for-approved-drug-products (accessed on 1 April 2024).
87. Qiu F, Meng T, Chen Q, et al. Fenofibrate-Loaded Biodegradable Nanoparticles for the Treatment of Experimental Diabetic Retinopathy and Neovascular Age-Related Macular Degeneration. Molecular Pharmaceutics. 2019; 16(5): 1958-1970. doi: 10.1021/acs.molpharmaceut.8b01319
88. Groenendaal L, Jonas F, Freitag D, et al. Poly(3,4-ethylenedioxythiophene) and Its Derivatives: Past, Present, and Future. Advances Materials. 2000; 12: 481-494. doi: 10.1002/(SICI)1521-4095(200004)12:7<481::AID-ADMA481>3.3.CO;2-3
89. Shi H, Liu C, Jiang Q, et al. Effective Approaches to Improve the Electrical Conductivity of PEDOT: PSS: A Review. Advanced Electronic Materials. 2015; 1(4). doi: 10.1002/aelm.201500017
90. Aradilla D, Estrany F, Alemán C. Symmetric Supercapacitors Based on Multilayers of Conducting Polymers. The Journal of Physical Chemistry C. 2011; 115(16): 8430-8438. doi: 10.1021/jp201108c
91. Fan X, Cheng H, Wang X, et al. Thermoresponsive Supramolecular Chemotherapy by "V"-Shaped Armed β-Cyclodextrin Star Polymer to Overcome Drug Resistance. Advanced Healthcare Materials. 2017; 7(7). doi: 10.1002/adhm.201701143
92. Pu XQ, Ju XJ, Zhang L, et al. Novel Multifunctional Stimuli-Responsive Nanoparticles for Synergetic Chemo-Photothermal Therapy of Tumors. ACS Applied Materials & Interfaces. 2021; 13(24): 28802-28817. doi: 10.1021/acsami.1c05330
93. Douglas D. Pharmaceutical Nanotechnology: A Therapeutic Revolution. International Journal of Pharmaceutical Sciences and Developmental Research. 2020; 6(1): 009-011. doi: 10.17352/ijpsdr.000027
94. Moncalvo F, Martinez Espinoza MI, Cellesi F. Nanosized Delivery Systems for Therapeutic Proteins: Clinically Validated Technologies and Advanced Development Strategies. Frontiers in Bioengineering and Biotechnology. 2020; 8. doi: 10.3389/fbioe.2020.00089
95. De Clercq E. Remdesivir: Quo vadis? Biochemical Pharmacology. 2021; 193: 114800. doi: 10.1016/j.bcp.2021.114800
96. Shah LK, Amiji MM. Intracellular Delivery of Saquinavir in Biodegradable Polymeric Nanoparticles for HIV/AIDS. Pharmaceutical Research. 2006; 23(11): 2638-2645. doi: 10.1007/s11095-006-9101-7

97. Alshabanah LA, Hagar M, Al-Mutabagani LA, et al. Hybrid Nanofibrous Membranes as a Promising Functional Layer for Personal Protection Equipment: Manufacturing and Antiviral/Antibacterial Assessments. Polymers. 2021; 13(11): 1776. doi: 10.3390/polym13111776
98. Demchenko V, Mamunya Y, Kobylinskyi S, et al. Structure-Morphology-Antimicrobial and Antiviral Activity Relationship in Silver-Containing Nanocomposites Based on Polylactide. Molecules. 2022; 27(12): 3769. doi: 10.3390/molecules27123769
99. Macchione MA, Guerrero-Beltrán C, Rosso AP, et al. Poly(N-vinylcaprolactam) Nanogels with Antiviral Behavior against HIV-1 Infection. Scientific Reports. 2019; 9(1). doi: 10.1038/s41598-019-42150-9
100. Milane L, Amiji M. Clinical approval of nanotechnology-based SARS-CoV-2 mRNA vaccines: impact on translational nanomedicine. Drug Delivery and Translational Research. 2021; 11(4): 1309-1315. doi: 10.1007/s13346-021-00911-y
101. Anselmo AC, Mitragotri S. Nanoparticles in the clinic: An update. Bioengineering & Translational Medicine. 2019; 4(3). doi: 10.1002/btm2.10143
102. Zhang D, Liu L, Wang J, et al. Drug-loaded PEG-PLGA nanoparticles for cancer treatment. Frontiers in Pharmacology. 2022; 13. doi: 10.3389/fphar.2022.990505
103. Anselmo AC, Mitragotri S. Nanoparticles in the clinic: An update post COVID-19 vaccines. Bioengineering & Translational Medicine. 2021; 6(3). doi: 10.1002/btm2.10246

Characterization and Application of Nanomaterials 2024, 7(1), 5834.
https://doi.org/10.24294/can.v7i1.5834

Review

Advancements in water splitting for sustainable energy generation: A review

Razu Shahazi[1], Amirul Islam Saddam[1], Srabani Majumdar[1], Md. Rakibul Islam[1],
Mohammed Muzibur Rahman[2,3], Md. Mahmud Alam[1,2,*], Ajoy Kumer[4], Giti Paimard[5]

[1] Department of Chemical Engineering, Z. H. Sikder University of Science and Technology (ZHSUST), Shariatpur 8024, Bangladesh
[2] Center of Excellence for Advanced Materials Research (CEAMR), King Abdulaziz University, Jeddah 21589, Saudi Arabia
[3] Chemistry Department, Faculty of Science, King Abdulaziz University, Jeddah 21589, Saudi Arabia
[4] Department of Chemistry, College of Arts and Sciences, IUBAT-International University of Business Agriculture and Technology, Dhaka 1230, Bangladesh
[5] Laboratory of Nanoscale Biosensing and Bioimaging (NBAB), School of Ophthalmology and Optometry, School of Biomedical Engineering, State Key Laboratory of Ophthalmology Optometry, and Vision Science, Wenzhou Medical University, Wenzhou 325027, China
*** Corresponding author:** Md. Mahmud Alam, alam-mahmud@hotmail.com, mmalam@zhsust.ac.bd

CITATION

Shahazi R, Saddam AI, Majumdar S, et al. Advancements in water splitting for sustainable energy generation: A review. Characterization and Application of Nanomaterials. 2024; 7(1): 5834.
https://doi.org/10.24294/can.v7i1.5834

ARTICLE INFO

Received: 16 April 2024
Accepted: 6 May 2024
Available online: 31 May 2024

Abstract: Water splitting, the process of converting water into hydrogen and oxygen gases, has garnered significant attention as a promising avenue for sustainable energy production. One area of focus has been the development of efficient and cost-effective catalysts for water splitting. Researchers have explored catalysts based on abundant and inexpensive materials such as nickel, iron, and cobalt, which have demonstrated improved performance and stability. These catalysts show promise for large-scale implementation and offer potential for reducing the reliance on expensive and scarce materials. Another avenue of research involves photoelectrochemical (PEC) cells, which utilize solar energy to drive the water-splitting reaction. Scientists have been working on designing novel materials, including metal oxides and semiconductors, to enhance light absorption and charge separation properties. These advancements in PEC technology aim to maximize the conversion of sunlight into chemical energy. Inspired by natural photosynthesis, artificial photosynthesis approaches have also gained traction. By integrating light-absorbing materials, catalysts, and membranes, these systems aim to mimic the complex processes of natural photosynthesis and produce hydrogen fuel from water. The development of efficient and stable artificial photosynthesis systems holds promise for sustainable and clean energy production. Tandem cells, which combine multiple light-absorbing materials with different bandgaps, have emerged as a strategy to enhance the efficiency of water-splitting systems. By capturing a broader range of the solar spectrum, tandem cells optimize light absorption and improve overall system performance. Lastly, advancements in electrocatalysis have played a critical role in water splitting. Researchers have focused on developing advanced electrocatalysts with high activity, selectivity, and stability for the oxygen evolution reaction (OER) and hydrogen evolution reaction (HER). These electrocatalysts contribute to overall water-splitting efficiency and pave the way for practical implementation.

Keywords: water splitting; oxygen evolution reaction (OER); hydrogen evolution reaction (HER); photoelectrochemical (PEC) cells; scarce materials; catalyst

1. Introduction

In the quest for sustainable energy generation, the development of efficient and clean technologies is of paramount importance. Among the various renewable energy sources, hydrogen has emerged as a promising candidate due to its high energy content and versatility. Water splitting, a process that involves separating water into its constituent elements, hydrogen and oxygen, offers a viable pathway for the production of hydrogen as a clean fuel [1,2]. Traditionally, water splitting has relied on electrolysis, a process that utilizes electricity to drive the reaction. However, electrolysis methods have faced challenges in terms of energy efficiency and cost-effectiveness, limiting their large-scale implementation [3,4]. To overcome these barriers, researchers and scientists around the world have been working diligently to break new ground in water splitting technology. In recent years, significant advancements have been made in the field of water splitting, leading to the development of novel and efficient approaches. These breakthroughs have the potential to revolutionize the renewable energy landscape and pave the way for a sustainable future [5,6].

One of the key areas of focus in water splitting research has been the development of catalysts. Catalysts play a crucial role in facilitating the water splitting reaction by reducing the energy requirements and increasing the reaction rates. Traditional catalysts, such as platinum, are effective but expensive, hindering their widespread adoption. However, researchers have made remarkable progress in developing low-cost and earth-abundant catalysts, such as transition metal oxides and molecular catalysts, which exhibit excellent catalytic activity and stability [7–9]. Another significant advancement in water splitting technology is the exploration of photoelectrochemical (PEC) cells. PEC cells utilize semiconductor materials to harness solar energy and drive the water splitting reaction. By combining light absorption and catalytic activity in a single device, PEC cells offer a promising approach to achieve solar-driven water splitting. Researchers have been actively investigating various semiconductor materials, such as metal oxides and perovskites, to enhance the efficiency and stability of PEC cells [10–12].

Furthermore, advancements in nanotechnology have opened up new avenues for improving water splitting efficiency. Nanostructured materials provide a high surface area, improved charge transport, and enhanced light absorption, making them ideal candidates for water splitting applications. Nanoparticles, nanowires, and nanotubes have demonstrated remarkable performance in catalyzing the water splitting reaction, offering unparalleled opportunities for efficient and cost-effective hydrogen production [13–15]. Moreover, the integration of water splitting technologies with renewable energy sources, such as wind and solar, holds tremendous potential for sustainable energy generation. By utilizing excess electricity generated from renewable sources during off-peak hours, water splitting can store the energy in the form of hydrogen, which can be used later for power generation or as a clean fuel for transportation [16–18].

Countries such as Japan, the United States, Germany, China, and South Korea have been actively researching and developing water splitting technologies [19]. They have made notable advancements in terms of increasing efficiency, reducing costs, and developing new materials for electrocatalysts [20]. Japan has a strong research community and has been actively collaborating with universities, research institutes, and industries to advance sunlight-driven water splitting technology [21]. Institutions such as the University of Tokyo, Kyoto University, and the National Institute of Advanced Industrial Science and Technology (AIST) have been at the forefront of this research. Japanese researchers have been working on the development of efficient and stable photoelectrochemical (PEC) cells and photoelectrodes for water splitting. The

United States has a vibrant research community dedicated to advancing water splitting technology. Many universities, national labs, and private research institutions have been conducting research to improve the efficiency, durability, and cost-effectiveness of water splitting systems [22]. Electrolysis, particularly proton exchange membrane (PEM) electrolysis and solid oxide electrolysis cells (SOEC), has been an area of focus in the USA. Besides this, researchers have been working on developing efficient and stable photoelectrodes, exploring new materials, and improving light absorption and charge separation processes. In addition, Germany, China, and South Korea have been actively researching and developing water splitting technologies [23,24].

In a short, advancements in water splitting technology are breaking the barriers that have hindered its widespread implementation for sustainable energy generation. The development of efficient catalysts, exploration of photoelectrochemical cells, utilization of nanostructured materials, and integration with renewable energy sources are propelling the field forward. These advancements offer a promising pathway towards a clean and sustainable future, where hydrogen can play a vital role in meeting our energy needs while minimizing environmental impact.

2. Development of efficient and cost-effective catalysts for water splitting

Water splitting is a promising technology for producing clean and renewable hydrogen fuel. It involves the separation of water into hydrogen and oxygen gases through electrochemical reactions. The process typically requires the use of catalysts to enhance the reaction rates and efficiency. Over the years, researchers have been working on developing efficient and cost-effective catalysts for water splitting.

2.1. Platinum group metals (PGMs)

PGMs, particularly platinum and iridium, have traditionally been used as catalysts for water splitting. However, their high cost and limited availability hinder large-scale applications. Researchers are exploring ways to reduce or replace the use of PGMs with more abundant and cost-effective materials [25–27].

2.2. Earth-abundant catalysts

Efforts have been focused on developing catalysts based on earth-abundant elements, such as transition metal oxides, sulfides, phosphides, and nitrides. These materials offer the advantages of low cost and scalability. For example, metal oxides like iron oxide (Fe_2O_3) and cobalt oxide (Co_3O_4) have shown promising catalytic activity [28–30]. An illustration of catalysis by earth-abundant materials is shown in **Figure 1**.

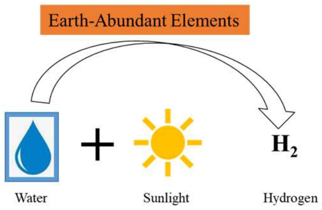

Figure 1. Water splitting with earth-abundant elements.

2.3. Bimetallic and alloy catalysts

Combining different metals into bimetallic or alloy catalysts can enhance their catalytic properties. For instance, combining nickel (Ni) with iron (Fe) or cobalt (Co) has shown improved activity for water splitting. These catalysts can be synthesized using various methods, including electrochemical deposition, sol-gel techniques, and physical mixing [31–33].

2.4. Molecular catalysts

Researchers are also exploring molecular catalysts, especially based on abundant and inexpensive organic compounds. These catalysts typically contain metal complexes with ligands that facilitate the water splitting reactions. A molecular catalytic reaction is demonstrated in **Figure 2**. Molecular catalysts offer precise control over the catalytic properties and can be designed to optimize efficiency [34–36].

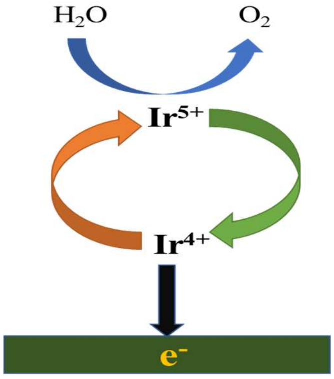

Figure 2. Schematic diagram of homogeneous catalysis with soluble molecular catalyst.

2.5. Nanostructured catalysts

Nanostructured catalysts, such as nanoparticles, nanowires, and nanotubes, have attracted attention due to their high surface area and unique electronic properties. These structures can enhance catalytic activity by providing more active sites and improving charge transport. Examples include metal nanoparticles supported on conductive substrates or semiconductor nanomaterials [37–40]. Several nanoparticles and nanowires are shown in **Figure 3**.

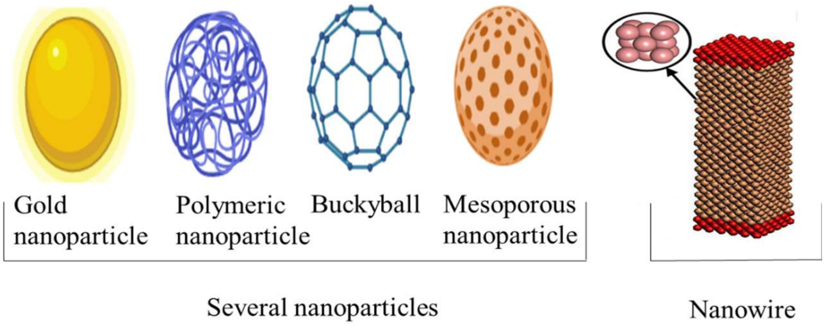

Figure 3. An illustration of nanoparticles and nanowire.

2.6. Computational design

Advances in computational modeling and machine learning have enabled the rational design of catalysts with enhanced activity. By simulating the electronic structure and reaction kinetics, researchers can identify promising catalyst candidates for experimental validation, accelerating the discovery process [41–43].

3. Solar energy to drive the water-splitting reaction

Utilizing solar energy to drive the water-splitting reaction is a promising approach for sustainable hydrogen production. It involves harnessing the energy from sunlight and converting it into chemical energy stored in the form of hydrogen gas. There are two common methods for using solar energy in water splitting:

3.1. Photovoltaic (PV) electrolysis

This method involves using photovoltaic cells, commonly known as solar cells, to directly convert solar energy into electricity. The generated electricity is then used to power an electrolyzer, which splits water into hydrogen and oxygen gases. The electrolyzer consists of two electrodes (cathode and anode) immersed in an electrolyte solution. When an electric current is applied, water molecules at the cathode are reduced to produce hydrogen gas (H_2), while water molecules at the anode are oxidized to produce oxygen gas (O_2). Catalysts are employed at the electrodes to enhance the reaction rates and improve overall efficiency [44–46].

3.2. Photoelectrochemical (PEC) water splitting

PEC water splitting combines the principles of solar cells and electrolysis into a single device. A photoelectrochemical cell is used, which typically consists of a semiconductor electrode immersed in an electrolyte solution [47]. A schematic diagram of photoelectrochemical water splitting is depicted in **Figure 4**. The semiconductor electrode absorbs photons from sunlight, generating electron-hole pairs. The excited electrons participate in the reduction reaction (hydrogen evolution), while the holes contribute to the oxidation reaction (oxygen evolution) [48–51]. Catalysts are essential in PEC cells to facilitate the reaction kinetics and improve efficiency. Both PV electrolysis and PEC water splitting have their advantages and challenges:

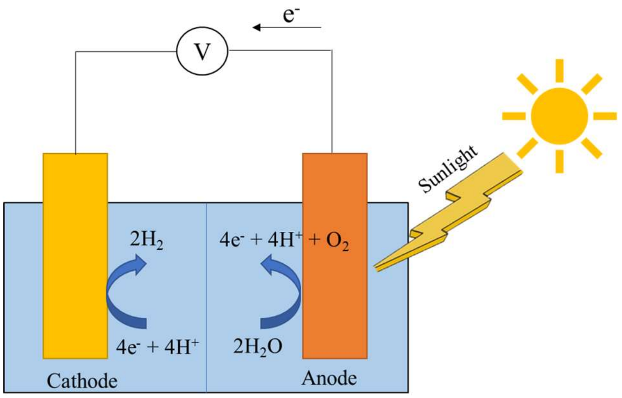

Figure 4. Schematic diagram of photoelectrochemical water splitting.

3.2.1. Advantages

- Utilization of abundant and renewable solar energy.
- Production of clean and sustainable hydrogen fuel.
- Compatibility with existing infrastructure for hydrogen storage and utilization.
- Potential for decentralized hydrogen production.

3.2.2. Challenges

- Efficiency: Maximizing the efficiency of solar energy conversion and the water-splitting reaction to maximize hydrogen production.
- Catalysts: Developing efficient and stable catalysts that can enhance the reaction rates and reduce energy losses.
- Materials: Exploring and optimizing semiconductor materials with desirable properties for efficient solar energy absorption and charge separation.
- Durability: Ensuring the long-term stability and durability of the materials and catalysts under harsh operating conditions.
- Cost: Reducing the cost of materials, catalysts, and system components to enable widespread adoption.

Ongoing research and development efforts are focused on improving the efficiency, stability, and cost-effectiveness of solar-driven water-splitting technologies. By addressing these challenges, solar energy can be harnessed to drive the water-splitting reaction, enabling the production of clean and sustainable hydrogen fuel.

4. Natural photosynthesis to hydrogen fuel

By integrating light-absorbing materials, catalysts, and membranes, artificial photosynthetic systems aim to mimic the complex processes of natural photosynthesis and produce hydrogen fuel from water. These systems, often referred to as artificial photosynthesis or artificial leaf systems, seek to harness solar energy and use it to drive the water-splitting reaction, generating hydrogen gas (H_2) as a clean and renewable fuel. Here’s a breakdown of the key components:

4.1. Light-absorbing materials

Light-absorbing materials, such as semiconductors or molecular dyes, capture sunlight and convert it into usable energy. These materials should have a broad absorption spectrum, efficient light harvesting, and good charge separation properties to generate the necessary energetic electrons [52–54].

4.2. Catalysts

Catalysts facilitate the water-splitting reaction by reducing the energy barriers and increasing the reaction rates. They are typically used at the cathode (hydrogen-evolving reaction, HER) and anode (oxygen-evolving reaction, OER) to promote the respective electrochemical reactions. Catalysts can be based on various materials, including earth-abundant metals, metal oxides, molecular complexes, or even biological enzymes [55–57].

4.3. Membranes

Membranes are employed to separate the HER and OER compartments, preventing the mixing of hydrogen and oxygen gases and enhancing the overall system efficiency. Proton-exchange membranes (PEMs) or other selective ion-conductive membranes are used to enable the transport of protons while blocking the crossover of gases [58–60].

4.4. Electron transfer pathways

Efficient pathways for electron transfer are essential to transport the generated electrons from the light-absorbing materials to the catalytic sites. Electron-conductive materials or structures, such as conductive electrodes or nanowires, are used to facilitate the movement of electrons to the respective electrodes [61–63].

By integrating these components, artificial photosynthetic systems emulate the fundamental processes of natural photosynthesis, where plants and algae convert sunlight, water, and carbon dioxide into chemical energy in the form of carbohydrates. In the case of artificial photosynthesis for hydrogen production, the focus is on generating hydrogen fuel from water using sunlight as the primary energy source. These systems hold promise for sustainable and carbon-neutral energy production, but there are still challenges to overcome, such as improving the efficiency, stability, and scalability of the components, as well as reducing costs. Extensive research and development efforts are ongoing to advance the field of artificial photosynthesis and enable its practical implementation as a viable technology for hydrogen production and energy storage.

5. Tandem cells to enhance the efficiency of water-splitting systems

Tandem cells have emerged as a strategy to enhance the efficiency of water-splitting systems in artificial photosynthesis. Tandem cells are multi-junction devices that combine multiple light-absorbing materials with different bandgaps in a stacked configuration [64–66]. This configuration allows for the efficient capture of a broader range of the solar spectrum, thereby increasing the overall energy conversion efficiency. Here's a closer look at how tandem cells work:

5.1. Bandgap combinations

Different semiconductor materials have different bandgaps, which determine the range of light wavelengths they can efficiently absorb. In tandem cells, materials with varying bandgaps are carefully selected and arranged in a series to create a cascade of absorption layers. The bandgap of each layer is tailored to match the energy level of a specific portion of the solar spectrum, enabling efficient utilization of a wider range of photons [67,68].

5.2. Efficient light harvesting

As sunlight passes through the tandem cell, each layer absorbs a specific portion of the solar spectrum. The absorbed photons generate electron-hole pairs (excitons) in the respective layers, leading to the production of electrical current [69,70]. The light harvesting technique is demonstrated in **Figure 5**.

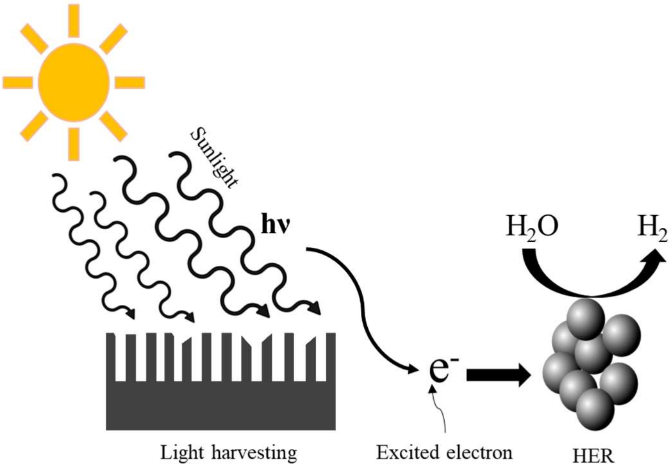

Figure 5. Light harvesting technique.

5.3. Charge separation and collection

The excited electrons and holes generated in each layer are rapidly separated due to the different bandgaps and internal electric fields. Efficient charge collection mechanisms are employed to extract the electrons and holes from each layer and direct them to their respective contacts or electrodes.

5.4. Water-splitting reactions

The separated electrons and holes can be utilized for the water-splitting reaction. The excited electrons are directed to the cathode, where they participate in the reduction reaction (hydrogen evolution) by converting protons (H^+) from water into hydrogen gas (H_2). The holes are directed to the anode, where they participate in the oxidation reaction (oxygen evolution) by oxidizing water molecules (H_2O) to produce oxygen gas (O_2).

By combining materials with different bandgaps in tandem cells, a larger portion of the solar spectrum can be effectively harvested, leading to improved light-to-hydrogen conversion efficiency. This approach allows for better utilization of solar energy and has the potential to achieve higher efficiencies compared to single-junction devices. Tandem cells are an active area of research, and scientists are exploring various material combinations, device architectures, and fabrication techniques to optimize their performance. The development of efficient and stable tandem cells is crucial for advancing the field of artificial photosynthesis and enabling more efficient solar-driven water-splitting systems for sustainable hydrogen production.

6. Development and optimization of OER and HER

The development and optimization of the oxygen evolution reaction (OER) and hydrogen evolution reaction (HER) electrocatalysts are crucial for advancing various energy conversion and storage technologies. Here are some key aspects involved in the development and optimization of OER and HER processes:

6.1. Catalyst screening and design

Initial stages involve screening and evaluation of various catalyst materials to identify candidates with high activity for OER and HER. The catalyst design considers factors such as electronic structure, surface area, crystal structure, and surface chemistry to enhance catalytic activity and stability. Computational modeling and high-throughput screening techniques are often employed to accelerate catalyst discovery [71,72].

6.2. Nano-structuring and surface modifications

Nano-structuring techniques, such as nanoparticle synthesis, thin-film deposition, or nanowire fabrication, are employed to increase the surface area and expose more active sites. Surface modifications, such as doping, alloying, or surface functionalization, can tailor the catalyst's electronic properties and surface reactivity, leading to improved performance [73–75]. Surface functionalization of catalysts is illustrated in **Figure 6**.

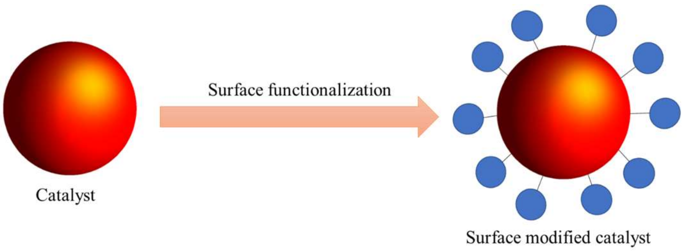

Figure 6. Surface functionalization of catalyst.

6.3. Interface engineering

The catalyst-support interface plays a crucial role in the overall catalytic activity and stability. Interface engineering techniques, such as optimizing the catalyst-support interaction, introducing interlayers, or using conductive substrates, can enhance electron transfer kinetics and catalytic performance [76–78].

6.4. Co-catalysts and synergy effects

Co-catalysts, such as metal nanoparticles, metal oxides, or molecular complexes, can be combined with the primary catalyst to enhance catalytic performance. Synergistic effects between different catalyst components can promote electron transfer, modify reaction kinetics, and improve overall efficiency [79,80].

6.5. Ion and mass transport

Efficient ion and mass transport within the electrochemical system is crucial for optimizing OER and HER. Strategies to enhance mass transport include designing porous electrode structures, optimizing electrolyte composition, and improving gas diffusion pathways [81,82].

6.6. Stability and durability

Long-term stability and durability of OER and HER catalysts are essential for practical applications. Researchers focus on understanding degradation mechanisms, developing strategies to mitigate catalyst degradation (e.g., corrosion resistance), and exploring protective coatings or encapsulation techniques [83,84].

6.7. Advanced characterization techniques

Advanced characterization techniques, such as scanning electron microscopy (SEM), transmission electron microscopy (TEM), X-ray photoelectron spectroscopy (XPS), and in-situ spectroscopy, provide insights into catalyst structures, active sites, and reaction mechanisms. These techniques help in understanding the structure-activity relationships and guide catalyst optimization efforts.

The development and optimization of OER and HER catalysts involve a multidisciplinary approach, combining materials science, surface chemistry, electrochemistry, and computational modeling. Continued research efforts aim to enhance catalytic activity, selectivity, stability, and cost-effectiveness to enable efficient and sustainable energy conversion and storage systems.

7. Catalyst for OER and HER

Researchers have indeed focused on developing advanced electrocatalysts with high activity, selectivity, and stability for the oxygen evolution reaction (OER) and hydrogen evolution reaction (HER). These electrocatalysts play a critical role in facilitating efficient and sustainable water splitting, which is essential for various applications, including artificial photosynthesis and renewable energy storage. Here’s an overview of the advancements in electrocatalyst development for the OER and HER:

7.1. Oxygen evolution reaction (OER)

7.1.1. Metal oxides and mixed metal oxides

Metal oxides, such as ruthenium oxide (RuO_2), iridium oxide (IrO_2), and manganese oxide (MnO_x), have shown excellent catalytic activity for the OER. Researchers have been exploring the synthesis of nanostructured and well-defined metal oxide catalysts to enhance their surface area and expose more active sites. Mixed metal oxides, combining different elements, can exhibit improved OER activity and stability compared to single-metal oxides [85–87] (**Table 1**).

Table 1. Comparison of oxygen evolution reaction (OER) performance with various transition metal oxide and hydroxide [88].

Materials	pH	Overpotential for 10 mA cm^{-2}/V	Tafel Slope/mV decade^{-1}
MnCo-G	14	0.33	48
RuO_2	14	0.3	42
Ni_5Mn-LDH-MWCNT	14	0.35 (iR-corrected)	83
Co_5Mn-LDH-MWCNT	14	0.3 (iR-corrected)	74
CoNi-LDH/Fe-PP-M	14	0.32	53
$CuCo_2O_4$/N-rGO	14	0.36	64
Co_3S_4@MoS_2	14	0.33	59
$CoMoO_4$	14	0.31	56
CoP	14	0.36	66
CoFe LDH	13	0.36	49
NiFe LDH	14	0.33	41

7.1.2. Perovskite oxides

Perovskite oxides, with a general formula of ABO_3, have garnered significant attention for OER electrocatalysis. Materials such as strontium titanate ($SrTiO_3$), strontium iridate ($SrIrO_3$), and barium strontium cobalt iron oxide (BSCF) have demonstrated promising OER activity. Doping, surface modification, and nano structuring techniques are employed to optimize the performance of perovskite oxides [89–92].

7.1.3. Earth-Abundant talysts

To overcome the cost and scarcity associated with noble metals, researchers are actively exploring earth-abundant catalysts for the OER. Materials like cobalt-based compounds (e.g., Co_3O_4), nickel-iron-based compounds (e.g., NiFe layered double hydroxides), and metal phosphides (e.g., nickel phosphide, cobalt phosphide) have shown promising OER activity [93,94].

7.2. Hydrogen evolution reaction (HER)

7.2.1. Platinum group metals (PGMs)

PGMs, particularly platinum (Pt) and palladium (Pd), are highly efficient HER catalysts due to their excellent activity and stability. Researchers are working on developing advanced Pt- and Pd-based catalysts with enhanced activity through alloying, nano structuring, and developing hybrid materials.

7.2.2. Earth-abundant catalysts

To address the cost and sustainability issues associated with PGMs, researchers are actively exploring earth-abundant alternatives for HER. Materials such as transition metal sulfides (e.g., molybdenum sulfide, nickel-molybdenum sulfide) and metal phosphides (e.g., nickel phosphide, cobalt phosphide) have shown promising HER activity [93,94]. Several earth-abundant catalysts and their properties are shown in **Table 2**.

Table 2. Examples of earth-abundant HER electrocatalysts.

Catalyst material	η at $-10\,\mathrm{mAcm^{-2}}$ (mV)	Tafel slope (mV per decade)	pH	Faradaic yield
NiMo	200 (100 $\mathrm{mAcm^{-2}}$)	122	14.8	NA
CoMo	170 (100 $\mathrm{mAcm^{-2}}$)	92	14.8	NA
NiMo	185 (100 $\mathrm{mAcm^{-2}}$)	112	14.8	NA
NiMo	70 (20 $\mathrm{mAcm^{-2}}$)	NA	14.3	NA
NiMo	34 (20 $\mathrm{mAcm^{-2}}$)	NA	14	NA
MoS_2	260	50	0	NA
Pt	50	140–150	13	NA
Ni	58	81.6	14	NA
Mo	65	76	14	NA
MoS_2	200 (15 $\mathrm{mAcm^{-2}}$)	40	−0.3	100%*
MoS_2	~150	41	0	NA
MoS_2	170	60	0.2	NA
CoS_2	145	51	0	NA

Table 2. (*Continued*).

Catalyst material	η at −10 mAcm^{-2}(mV)	Tafel slope (mV per decade)	pH	Faradaic yield
CoS_2	~175	93	7	100%
CoMoSx	250	85	7	−100%
WS_2	~250	60	0	NA
$CoSe_2$	90	39	0	NA
MoS1.0Sel.0	~200	56	0	100%*
$NiSe_2$	~140	49	0	NA
Ni_2P	130 (20 mAcm^{-2})	46	0	100%*
CoP	85 (20 mAcm^{-2})	50	0	100%*
FeP	55	38	0	100%
MoP	64	NA	0	100%
CoNx	170	75	14	NA
CoNx	140	30	0	NA
NiMoNx	225 (5 mAcm^{-2})	35.9	1	NA
α-MoB	~225(20 mAcm^{-2})	55	−0.3	100%
Mo_2C	130	53	0	NA
MoC	124	43	0	NA
MoC	77	50	14	NA
Ni/C	34	41	0	100%*
$Cu_{95}Ti_5$	60	110	13	NA

7.2.3. Molecular catalysts

Molecular catalysts, typically based on metal complexes or metalloporphyrins, offer precise control over the active sites and electronic properties. Researchers are designing and synthesizing molecular catalysts with tailored structures to optimize HER activity, selectivity, and stability.

The development of advanced electrocatalysts with high activity, selectivity, and stability is crucial for improving the overall efficiency and commercial viability of water-splitting technologies. Researchers continue to explore new materials, catalyst designs, and strategies to enhance the performance of electrocatalysts for the OER and HER, aiming to enable efficient and sustainable hydrogen production.

8. Conclusion

In conclusion, significant progress has been made in the development and optimization of catalysts and technologies for water splitting, which has advanced the production of sustainable energy. Catalysts based on abundant and inexpensive materials, such as nickel, iron, and cobalt, have shown improved performance and stability, reducing the need for costly materials. Photoelectrochemical (PEC) cells, which utilize novel materials like metal oxides and semiconductors, aim to maximize the conversion of solar energy into chemical energy for water splitting. Artificial photosynthesis approaches, inspired by natural photosynthesis, integrate light-absorbing materials, catalysts, and membranes to produce hydrogen fuel from water, offering a potential solution for clean energy production. Tandem cells, which combine multiple light-absorbing materials, optimize light absorption and enhance system efficiency. Furthermore, advancements in electrocatalysis have led to the development of advanced electrocatalysts with high activity, selectivity, and stability for the oxygen evolution reaction (OER) and hydrogen evolution reaction (HER). These advancements collectively pave the way for the practical implementation of water splitting in various energy conversion and storage systems, bringing us closer to a sustainable and clean energy future.

Conflict of interest: The authors declare no conflict of interest.

References

1. Hota P, Das A, Maiti DK. A short review on generation of green fuel hydrogen through water splitting. International Journal of Hydrogen Energy. 2023; 48(2): 523-541. doi: 10.1016/j.ijhydene.2022.09.264
2. Mohsin M, Ishaq T, Bhatti IA, et al. Semiconductor Nanomaterial Photocatalysts for Water-Splitting Hydrogen Production: The Holy Grail of Converting Solar Energy to Fuel. Nanomaterials. 2023; 13(3): 546. doi: 10.3390/nano13030546
3. Gong Y, Yao J, Wang P, et al. Perspective of hydrogen energy and recent progress in electrocatalytic water splitting. Chinese Journal of Chemical Engineering. 2022; 43: 282-296. doi: 10.1016/j.cjche.2022.02.010
4. Rafique M, Mubashar R, Irshad M, et al. A Comprehensive Study on Methods and Materials for Photocatalytic Water Splitting and Hydrogen Production as a Renewable Energy Resource. Journal of Inorganic and Organometallic Polymers and Materials. 2020; 30(10): 3837-3861. doi: 10.1007/s10904-020-01611-9
5. Li Y, Sun Y, Qin Y, et al. Recent Advances on Water-Splitting Electrocatalysis Mediated by Noble-Metal-Based Nanostructured Materials. Advanced Energy Materials. 2020; 10(11). doi: 10.1002/aenm.201903120
6. Wang YZ, Yang M, Ding Y, et al. Recent Advances in Complex Hollow Electrocatalysts for Water Splitting. Advanced Functional Materials. 2021; 32(6). doi: 10.1002/adfm.202108681
7. Shamsah SMI. Earth-Abundant Electrocatalysts for Water Splitting: Current and Future Directions. Catalysts. 2021; 11(4): 429. doi: 10.3390/catal11040429
8. Hayat A, Sohail M, Ali H, et al. Recent Advances and Future Perspectives of Metal-Based Electrocatalysts for Overall Electrochemical Water Splitting. The Chemical Record. 2022; 23(2). doi: 10.1002/tcr.202200149
9. Li S, Li E, An X, et al. Transition metal-based catalysts for electrochemical water splitting at high current density: current status and perspectives. Nanoscale. 2021; 13(30): 12788-12817. doi: 10.1039/d1nr02592a
10. Hamdani IR, Bhaskarwar AN. Recent progress in material selection and device designs for photoelectrochemical water-splitting. Renewable and Sustainable Energy Reviews. 2021; 138: 110503. doi: 10.1016/j.rser.2020.110503
11. Sivagurunathan AT, Adhikari S, Kim DH. Strategies and implications of atomic layer deposition in photoelectrochemical water splitting: Recent advances and prospects. Nano Energy. 2021; 83: 105802. doi: 10.1016/j.nanoen.2021.105802
12. Ali M, Pervaiz E, Noor T, et al. Recent advancements in MOF- based catalysts for applications in electrochemical and photoelectrochemical water splitting: A review. International Journal of Energy Research. 2020; 45(2): 1190-1226. doi: 10.1002/er.5807
13. Pratibha, Kapoor A, Rajput JK. Nanostructured materials for the visible-light driven hydrogen evolution by water splitting: A review. International Journal of Hydrogen Energy. 2022; 47(40): 17544-17582. doi: 10.1016/j.ijhydene.2022.03.232
14. Wang Y, Zhang J, Liang W, et al. Plasmonic Metal Nanostructures as Efficient Light Absorbers for Solar Water Splitting. Advanced Energy and Sustainability Research. 2021; 2(11). doi: 10.1002/aesr.202100092
15. Samanta B, Morales-García Á, Illas F, et al. Challenges of modeling nanostructured materials for photocatalytic water splitting. Chemical Society Reviews. 2022; 51(9): 3794-3818. doi: 10.1039/d1cs00648g
16. Mohamed HH. Green processes and sustainable materials for renewable energy production via water splitting. In: Cheong KY, Apblett A (editors). Sustainable Materials and Green Processing for Energy Conversion. Elsevier; 2022. pp. 169-212. doi: 10.1016/b978-0-12-822838-8.00007-7
17. Hosseini SE, Wahid MA. Hydrogen from solar energy, a clean energy carrier from a sustainable source of energy. International Journal of Energy Research. 2020; 44(6): 4110-4131. doi: 10.1002/er.4930
18. Ashraf M, Ayaz M, Khan M, et al. Recent Trends in Sustainable Solar Energy Conversion Technologies: Mechanisms,

Prospects, and Challenges. Energy & Fuels. 2023; 37(9): 6283-6301. doi: 10.1021/acs.energyfuels.2c04077

19. Han N, Race M, Zhang W, et al. Perovskite and related oxide based electrodes for water splitting. Journal of Cleaner Production. 2021; 318: 128544. doi: 10.1016/j.jclepro.2021.128544
20. Wang Y, Seo B, Wang B, et al. Fundamentals, materials, and machine learning of polymer electrolyte membrane fuel cell technology. Energy and AI. 2020; 1: 100014. doi: 10.1016/j.egyai.2020.100014
21. Kawawaki T, Kawachi M, Yazaki D, et al. Development and Functionalization of Visible-Light-Driven Water-Splitting Photocatalysts. Nanomaterials. 2022; 12(3): 344. doi: 10.3390/nano12030344
22. Vilanova A, Dias P, Lopes T, et al. The route for commercial photoelectrochemical water splitting: a review of large-area devices and key upscaling challenges. Chemical Society Reviews. 2024; 53(5): 2388-2434. doi: 10.1039/d1cs01069g
23. Jolaoso LA, Duan C, Kazempoor P. Life cycle analysis of a hydrogen production system based on solid oxide electrolysis cells integrated with different energy and wastewater sources. International Journal of Hydrogen Energy. 2024; 52: 485-501. doi: 10.1016/j.ijhydene.2023.07.129
24. Qahtan TF, Alade IO, Rahaman MS, et al. Mapping the research landscape of hydrogen production through electrocatalysis: A decade of progress and key trends. Renewable and Sustainable Energy Reviews. 2023; 184: 113490. doi: 10.1016/j.rser.2023.113490
25. Salonen LM, Petrovykh DY, Kolen’ko YuV. Sustainable catalysts for water electrolysis: Selected strategies for reduction and replacement of platinum-group metals. Materials Today Sustainability. 2021; 11-12: 100060. doi: 10.1016/j.mtsust.2021.100060
26. Hughes AE, Haque N, Northey SA, et al. Platinum Group Metals: A Review of Resources, Production and Usage with a Focus on Catalysts. Resources. 2021; 10(9): 93. doi: 10.3390/resources10090093
27. Liu J, Li Y, Zhou X, et al. Positively charged Pt-based cocatalysts: an orientation for achieving efficient photocatalytic water splitting. Journal of Materials Chemistry A. 2020; 8(1): 17-26. doi: 10.1039/c9ta10568a
28. Karuppasamy L, Gurusamy L, Ananan S, et al. Metal-organic frameworks derived interfacing Fe_2O_3/$ZnCo_2O_4$ multimetal oxides as a bifunctional electrocatalyst for overall water splitting. Electrochimica Acta. 2023; 449: 142242. doi: 10.1016/j.electacta.2022.142242
29. Warsi MF, Shaheen N, Sarwar MI, et al. A comparative study on photocatalytic activities of various transition metal oxides nanoparticles synthesized by wet chemical route. Desalination And Water Treatment. 2021; 211: 181-195. doi: 10.5004/dwt.2021.26463
30. Cao Q, Li Q, Pi Z, et al. Metal–Organic-Framework-Derived Ball-Flower-like Porous Co_3O_4/Fe_2O_3 Heterostructure with Enhanced Visible-Light-Driven Photocatalytic Activity. Nanomaterials. 2022; 12(6): 904. doi: 10.3390/nano12060904
31. Jeghan SMN, Kim D, Lee Y, et al. Designing a smart heterojunction coupling of cobalt-iron layered double hydroxide on nickel selenide nanosheets for highly efficient overall water splitting kinetics. Applied Catalysis B: Environmental. 2022; 308: 121221. doi: 10.1016/j.apcatb.2022.121221
32. Yu M, Budiyanto E, Tüysüz H. Principles of Water Electrolysis and Recent Progress in Cobalt-, Nickel-, and Iron-Based Oxides for the Oxygen Evolution Reaction. Angewandte Chemie International Edition. 2021; 61(1). doi: 10.1002/anie.202103824
33. Yaseen W, Ullah N, Xie M, et al. Ni-Fe-Co based mixed metal/metal-oxides nanoparticles encapsulated in ultrathin carbon nanosheets: A bifunctional electrocatalyst for overall water splitting. Surfaces and Interfaces. 2021; 26: 101361. doi: 10.1016/j.surfin.2021.101361
34. Zhang B, Zheng Y, Ma T, et al. Designing MOF Nanoarchitectures for Electrochemical Water Splitting. Advanced Materials. 2021; 33(17). doi: 10.1002/adma.202006042
35. Yao D, Gu L, Zuo B, et al. A strategy for preparing high-efficiency and economical catalytic electrodes toward overall water splitting. Nanoscale. 2021; 13(24): 10624-10648. doi: 10.1039/d1nr02307a
36. Li Z, Hu M, Wang P, et al. Heterojunction catalyst in electrocatalytic water splitting. Coordination Chemistry Reviews. 2021; 439: 213953. doi: 10.1016/j.ccr.2021.213953
37. Huang J, Jiang Y, An T, et al. Increasing the active sites and intrinsic activity of transition metal chalcogenide electrocatalysts for enhanced water splitting. Journal of Materials Chemistry A. 2020; 8(48): 25465-25498. doi: 10.1039/d0ta08802a
38. Huang H, Cho A, Kim S, et al. Structural Design of Amorphous CoMoPx with Abundant Active Sites and Synergistic Catalysis Effect for Effective Water Splitting. Advanced Functional Materials. 2020; 30(43). doi: 10.1002/adfm.202003889

39. Raheema MH, Jaber GS. Synthesis of Carbon Nanotubes Using Modified Hummers Method for Cathode Electrodes in Dye-Sensitized Solar Cell. Baghdad Science Journal. 2023; 20(6): 2290-2299. doi: 10.21123/bsj.2023.7150
40. Shahazi R, Majumdar S, Saddam AI, et al. Carbon nanomaterials for biomedical applications: A comprehensive review. Nano Carbons. 2023; 1(1): 448. doi: 10.59400/n-c.v1i1.448
41. Chen Y, Zheng W, Murcia-López S, et al. Light management in photoelectrochemical water splitting – from materials to device engineering. Journal of Materials Chemistry C. 2021; 9(11): 3726-3748. doi: 10.1039/d0tc06071b
42. Moon C, Shin B. Review on light absorbing materials for unassisted photoelectrochemical water splitting and systematic classifications of device architectures. Discover Materials. 2022; 2(1). doi: 10.1007/s43939-022-00026-2
43. Kawase Y, Higashi T, Domen K, et al. Recent Developments in Visible-Light-Absorbing Semitransparent Photoanodes for Tandem Cells Driving Solar Water Splitting. Advanced Energy and Sustainability Research. 2021; 2(7). doi: 10.1002/aesr.202100023
44. Liu HY, Cody CC, Jayworth JA, et al. Surface-Attached Molecular Catalysts on Visible-Light-Absorbing Semiconductors: Opportunities and Challenges for a Stable Hybrid Water-Splitting Photoanode. ACS Energy Letters. 2020; 5(10): 3195-3202. doi: 10.1021/acsenergylett.0c01719
45. Yang G, Yu S, Kang Z, et al. Building Electron/Proton Nanohighways for Full Utilization of Water Splitting Catalysts. Advanced Energy Materials. 2020; 10(16). doi: 10.1002/aenm.201903871
46. Liu PF, Yin H, Fu HQ, et al. Activation strategies of water-splitting electrocatalysts. Journal of Materials Chemistry A. 2020; 8(20): 10096-10129. doi: 10.1039/d0ta01680b
47. Zeng C, Dai L, Jin Y, et al. Design strategies toward transition metal selenide-based catalysts for electrochemical water splitting. Sustainable Energy & Fuels. 2021; 5(5): 1347-1365. doi: 10.1039/d0se01722a
48. Gahlot S, Kulshrestha V. Graphene based polymer electrolyte membranes for electro-chemical energy applications. International Journal of Hydrogen Energy. 2020; 45(34): 17029-17056. doi: 10.1016/j.ijhydene.2019.06.047
49. Li C, Baek JB. The promise of hydrogen production from alkaline anion exchange membrane electrolyzers. Nano Energy. 2021; 87: 106162. doi: 10.1016/j.nanoen.2021.106162
50. Du N, Roy C, Peach R, et al. Anion-Exchange Membrane Water Electrolyzers. Chemical Reviews. 2022; 122(13): 11830-11895. doi: 10.1021/acs.chemrev.1c00854
51. Tiwari JN, Singh AN, Sultan S, et al. Recent Advancement of p- and d-Block Elements, Single Atoms, and Graphene-Based Photoelectrochemical Electrodes for Water Splitting. Advanced Energy Materials. 2020; 10(24). doi: 10.1002/aenm.202000280
52. Li B, Tian Z, Li L, et al. Directional Charge Transfer Channels in a Monolithically Integrated Electrode for Photoassisted Overall Water Splitting. ACS Nano. 2023; 17(4): 3465-3482. doi: 10.1021/acsnano.2c09659
53. Ng WC, Chong MN. Organic-inorganic p-type PEDOT: PSS/CuO/MoS_2 photocathode with in-built antipodal photogenerated holes and electrons transfer pathways for efficient solar-driven photoelectrochemical water splitting. Sustainable Materials and Technologies. 2023; 38: e00749. doi: 10.1016/j.susmat.2023.e00749
54. Ašmontas S, Mujahid M. Recent Progress in Perovskite Tandem Solar Cells. Nanomaterials. 2023; 13(12): 1886. doi: 10.3390/nano13121886
55. Martinho F. Challenges for the future of tandem photovoltaics on the path to terawatt levels: a technology review. Energy & Environmental Science. 2021; 14(7): 3840-3871. doi: 10.1039/d1ee00540e
56. Kumar P, Thokala S, Singh SP, et al. Research progress and challenges in extending the infra-red absorption of perovskite tandem solar cells. Nano Energy. 2024; 121: 109175. doi: 10.1016/j.nanoen.2023.109175
57. He R, Ren S, Chen C, et al. Wide-bandgap organic–inorganic hybrid and all-inorganic perovskite solar cells and their application in all-perovskite tandem solar cells. Energy & Environmental Science. 2021; 14(11): 5723-5759. doi: 10.1039/d1ee01562a
58. Ullah F, Chen CC, Choy WCH. Recent Developments in Organic Tandem Solar Cells toward High Efficiency. Advanced Energy and Sustainability Research. 2021; 2(4). doi: 10.1002/aesr.202000050
59. Wang Y, Shi H, Cui K, et al. Reversible electron storage in tandem photoelectrochemical cell for light driven unassisted overall water splitting. Applied Catalysis B: Environmental. 2020; 275: 119094. doi: 10.1016/j.apcatb.2020.119094
60. Zhang D, Cho H, Yum J, et al. An Organic Semiconductor Photoelectrochemical Tandem Cell for Solar Water Splitting. Advanced Energy Materials. 2022; 12(42). doi: 10.1002/aenm.202202363
61. Zhou B, Gao R, Zou J, et al. Surface Design Strategy of Catalysts for Water Electrolysis. Small. 2022; 18(27). doi:

10.1002/smll.202202336

62. Li J, Liu Y, Chen H, et al. Design of a Multilayered Oxygen-Evolution Electrode with High Catalytic Activity and Corrosion Resistance for Saline Water Splitting. Advanced Functional Materials. 2021; 31(27). doi: 10.1002/adfm.202101820
63. Almomani F, Shawaqfah M, Alkasrawi M. Solar-driven hydrogen production from a water-splitting cycle based on carbon-TiO2 nano-tubes. International Journal of Hydrogen Energy. 2022; 47(5): 3294-3305. doi: 10.1016/j.ijhydene.2020.12.19
64. Lee JU, Kim JH, Kang K, et al. Bulk and surface modified polycrystalline $CuWO_4$ films for photoelectrochemical water oxidation. Renewable Energy. 2023; 203: 779-787. doi: 10.1016/j.renene.2022.12.129
65. Joseph M, Kumar M, Haridas S, et al. A review on the advancements of graphitic carbon nitride-based photoelectrodes for photoelectrochemical water splitting. Energy Advances. 2024; 3(1): 30-59. doi: 10.1039/d3ya00506b
66. Singh B, Indra A. Surface and interface engineering in transition metal–based catalysts for electrochemical water oxidation. Materials Today Chemistry. 2020; 16: 100239. doi: 10.1016/j.mtchem.2019.100239
67. Gu H, Shi G, Chen HC, et al. Strong Catalyst–Support Interactions in Electrochemical Oxygen Evolution on Ni–Fe Layered Double Hydroxide. ACS Energy Letters. 2020; 5(10): 3185-3194. doi: 10.1021/acsenergylett.0c01584
68. Yang X, Guo R, Cai R, et al. Engineering transition metal catalysts for large-current-density water splitting. Dalton Transactions. 2022; 51(12): 4590-4607. doi: 10.1039/d2dt00037g
69. Zhou X, Wang P, Li M, et al. Synergistic effect of phosphorus doping and MoS_2 co-catalysts on g-C_3N_4 photocatalysts for enhanced solar water splitting. Journal of Materials Science & Technology. 2023; 158: 171-179. doi: 10.1016/j.jmst.2023.02.041
70. Xiao N, Li S, Li X, et al. The roles and mechanism of cocatalysts in photocatalytic water splitting to produce hydrogen. Chinese Journal of Catalysis. 2020; 41(4): 642-671. doi: 10.1016/S1872-2067(19)63469-8
71. Luo Y, Zhang Z, Chhowalla M, et al. Recent Advances in Design of Electrocatalysts for High-Current-Density Water Splitting. Advanced Materials. 2022; 34(16). doi: 10.1002/adma.202108133
72. Sun H, Xu X, Kim H, et al. Electrochemical Water Splitting: Bridging the Gaps Between Fundamental Research and Industrial Applications. Energy & Environmental Materials. 2023; 6(5): 12441. doi: 10.1002/eem2.12441
73. Luo F, Guo L, Xie Y, et al. Iridium nanorods as a robust and stable bifunctional electrocatalyst for pH-universal water splitting. Applied Catalysis B: Environmental. 2020; 279: 119394. doi: 10.1016/j.apcatb.2020.119394
74. Luo F, Hu H, Zhao X, et al. Robust and Stable Acidic Overall Water Splitting on Ir Single Atoms. Nano Letters. 2020; 20(3): 2120-2128. doi: 10.1021/acs.nanolett.0c00127
75. Qin R, Chen G, Feng X, et al. Ru/Ir-Based Electrocatalysts for Oxygen Evolution Reaction in Acidic Conditions: From Mechanisms, Optimizations to Challenges. Advanced Science. 2024; 11(21): 2309364. doi: 10.1002/advs.202309364
76. Pascuzzi MEC, Goryachev A, Hofmann JP, et al. Mn promotion of rutile TiO_2-RuO_2 anodes for water oxidation in acidic media. Applied Catalysis B: Environmental. 2020; 261: 118225. doi: 10.1016/j.apcatb.2019.118225
77. Zhang Y, Yan R, Xu X, et al. Next Generation Noble Metal-Engineered Catalysts: From Structure Evolution to Structure-Reactivity Correlation in Water Splitting. Advanced Functional Materials. 2023; 34(4). doi: 10.1002/adfm.202308813
78. Bao J, Xie J, Lei F, et al. Two-Dimensional Mn-Co LDH/Graphene Composite towards High-Performance Water Splitting. Catalysts. 2018; 8(9): 350. doi: 10.3390/catal8090350
79. Patial S, Hasija V, Raizada P, et al. Tunable photocatalytic activity of $SrTiO_3$ for water splitting: Strategies and future scenario. Journal of Environmental Chemical Engineering. 2020; 8(3): 103791. doi: 10.1016/j.jece.2020.103791
80. Yu J, Wu X, Guan D, et al. Monoclinic $SrIrO_3$: An Easily Synthesized Conductive Perovskite Oxide with Outstanding Performance for Overall Water Splitting in Alkaline Solution. Chemistry of Materials. 2020; 32(11): 4509-4517. doi: 10.1021/acs.chemmater.0c00149
81. Zhang L, Jang H, Li Z, et al. $SrIrO_3$ modified with laminar Sr_2IrO_4 as a robust bifunctional electrocatalyst for overall water splitting in acidic media. Chemical Engineering Journal. 2021; 419: 129604. doi: 10.1016/j.cej.2021.129604
82. Aegerter D, Borlaf M, Fabbri E, et al. Tuning the Co Oxidation State in $Ba_{0.5}Sr_{0.5}Co_{0.8}Fe_{0.2}O_3$-δ by Flame Spray Synthesis Towards High Oxygen Evolution Reaction Activity. Catalysts. 2020; 10(9): 984. doi: 10.3390/catal10090984
83. Peng X, Jin X, Gao B, et al. Strategies to improve cobalt-based electrocatalysts for electrochemical water splitting. Journal of Catalysis. 2021; 398: 54-66. doi: 10.1016/j.jcat.2021.04.003
84. Lei L, Huang D, Zhou C, et al. Demystifying the active roles of NiFe-based oxides/(oxy)hydroxides for electrochemical water splitting under alkaline conditions. Coordination Chemistry Reviews. 2020; 408: 213177. doi: 10.1016/j.ccr.2019.213177

85. Bodhankar PM, Sarawade PB, Kumar P, et al. Nanostructured Metal Phosphide Based Catalysts for Electrochemical Water Splitting: A Review. Small. 2022; 18(21). doi: 10.1002/smll.202107572
86. Feng Y, Zhu L, Pei A, et al. Platinum–palladium-on-reduced graphene oxide as bifunctional electrocatalysts for highly active and stable hydrogen evolution and methanol oxidation reaction. Nanoscale. 2023; 15(42): 16904-16913. doi: 10.1039/d3nr04014c
87. Jebaslinhepzybai BT, Prabu N, Sasidharan M. Facile galvanic replacement method for porous Pd@Pt nanoparticles as an efficient HER electrocatalyst. International Journal of Hydrogen Energy. 2020; 45(19): 11127-11137. doi: 10.1016/j.ijhydene.2020.02.059
88. Lyu Z, Zhang X, Liao X, et al. Two-Dimensionally Assembled Pd–Pt–Ir Supernanosheets with Subnanometer Interlayer Spacings toward High-Efficiency and Durable Water Splitting. ACS Catalysis. 2022; 12(9): 5305-5315. doi: 10.1021/acscatal.2c00859
89. Roger I, Shipman MA, Symes MD. Earth-abundant catalysts for electrochemical and photoelectrochemical water splitting. Nature Reviews Chemistry. 2017; 1(1). doi: 10.1038/s41570-016-0003
90. Lobinsky AA, Tolstoy VP, Kodinzev IA. Electrocatalytic properties of γ-NiOOH nanolayers, synthesized by successive ionic layer deposition, during the oxygen evolution reaction upon water splitting in the alkaline medium. Nanosystems: Physics, Chemistry, Mathematics. 2018; 9(5): 669-675. doi: 10.17586/2220-8054-2018-9-5-669-675
91. Shinagawa T, Garcia-Esparza AT, Takanabe K. Insight on Tafel slopes from a microkinetic analysis of aqueous electrocatalysis for energy conversion. Scientific Reports. 2015; 5(1). doi: 10.1038/srep13801
92. Antipin D, Risch M. Calculation of the Tafel slope and reaction order of the oxygen evolution reaction between pH 12 and pH 14 for the adsorbate mechanism. Electrochemical Science Advances. 2022; 3(6). doi: 10.1002/elsa.202100213
93. Lin L, Lin Z, Zhang J, et al. Molecular-level insights on the reactive facet of carbon nitride single crystals photocatalysing overall water splitting. Nature Catalysis. 2020; 3(8): 649-655. doi: 10.1038/s41929-020-0476-3
94. Liu W, Zhang H, Li C, et al. Non-noble metal single-atom catalysts prepared by wet chemical method and their applications in electrochemical water splitting. Journal of Energy Chemistry. 2020; 47: 333-345. doi: 10.1016/j.jechem.2020.02.020

EnPress Publisher, LLC

Add: 9650 Telstar Avenue, Unit A, Suite 121, El Monte, CA 91731
Email: contact@enpress-publisher.com